The Dissertation Committee for Li Ji Certifies that this is the approved version of the following dissertation:

GEOMECHANICAL ASPECTS OF FRACTURE GROWTH IN A POROELASTIC, CHEMICALLY REACTIVE ENVIRONMENT

Committee:

Jon E. Olson, Supervisor

Matthew T. Balhoff, Co-Supervisor

Larry W. Lake

Kamy Sepehrnoori

Stephen E. Laubach

GEOMECHANICAL ASPECTS OF FRACTURE GROWTH IN A POROELASTIC, CHEMICALLY REACTIVE ENVIRONMENT

by

Li Ji, B.S.; M.S.

Dissertation

Presented to the Faculty of the Graduate School of

The University of Texas at Austin

in Partial Fulfillment

of the Requirements

for the Degree of

Doctor of Philosophy

The University of Texas at Austin

August 2013

Dedication

To my dear parents, Baoquan Ji and Jinhua Zhang,

for their endless love, patience and support.

Acknowledgements

First, I would like to express my gratitude and appreciation to my supervisor, Dr. Jon E. Olson for his guidance, support, patience and willingness to share his knowledge and experience. I also would like to thank my co-supervisor, Dr. Matthew T. Balhoff for his time and patience helping me with my research work. I also own many thanks to all my dissertation committee members, Dr. Larry Lake, Dr. Kamy Sephehrnoori and Dr. Stephen Laubach for their help and valuable suggestions.

I would like to thank several professors and researchers who supported and helped my research and study at UT, particularly Dr. Quoc Nguyen, Dr. Gary Pope and Dr. Upali P. Weerasooriya. I am sincerely thankful for all the wonderful professors and lectures who provide me such valuable courses and lectures at UT.

I also thank the financial support from the Fracture Research and Application Consortium (FRAC) of the University of Texas at Austin and grant DE-FG02-03ER15430 from Chemical Sciences, Geosciences and Biosciences Division, Office of Basic Energy Sciences, Office of Science, U.S. Department of Energy.

I owe special thanks to all my friends in Austin for making my life here interesting and fun. Thank you all for your care and love. No matter where we will go after leaving Austin, I always remember you guys and those memories deep in my heart.

To my dad and mum, thank you for your patience and encouragement through all these years. Without your love and support, I would not go this far on this journey.

GEOMECHANICAL ASPECTS OF FRACTURE GROWTH IN A POROELASTIC, CHEMICALLY REACTIVE ENVIRONMENT

Li Ji, Ph.D.

The University of Texas at Austin, 2013

Supervisor: Jon E. Olson

Co-Supervisor: Matthew T. Balhoff

Natural hydraulic fractures (NHFs) are fractures whose growths are driven by fluid loading. The fluid flow properties of the host rock have a primary, but hitherto little appreciated control on the NHF propagation rates. This study focuses on investigating the impacts of host rock fluid flow on the propagation and pattern development of multiple NHF in a poroelastic media. A realistic geomechanical model is developed to combine both the fluid flow and mechanical interactions between multiple fractures.

The natural hydraulic fracture propagation is observed to consist of a series of crack-seal processes indicating incremental stop-start growth. Growth timing is on the scale of millions of years based on recent natural fracture growth reconstructions. These time scales are compatible with some model scenarios. My newly developed numerical model captures the crack-seal process for multiple NHF propagation. A sensitivity study conducted to investigate the impacts of different fluid flow properties on NHF propagation shows that permeability is a predominate influence on the timescale of NHF development. In low-permeability rocks, fractures have more stable initiation and much longer propagation timing compared to those in high-permeability rocks.

Another aspect of great interest is the influence of fluid flow on fracture spacing and pattern development for multiple NHFs propagation in a poroelastic environment. My new poroelastic geomechanial model combines the natural hydraulic fracturing mechanism with the mechanical interactions between fractures. The numerical results show that as host rock permeability decreases, more fractures can propagate and a much smaller spacing is reached for a given fracture set. The low permeability slows down the propagation of long fractures and prevents them from dominating the fracture pattern. As a result, more fractures are able to grow at a similar speed and a more closely spaced fracture pattern is achieved for either regularly spaced or randomly distributed multiple fractures in low-permeability rocks.

Investigation is also conducted in analyzing the distributions of fracture attributes (length, aperture and spacing) in low- and high-permeability rocks. For shales with high subcritical index, low permeability helps the fractures propagate more closely spaced instead of clustering. Meanwhile, in low-permeability rocks, factures have relatively smaller apertures, which lead to a slower fracture opening rate. The competition between the slow fracture opening rate and quartz precipitation rate will affect the effective permeability and porosity of the naturally fractured reservoir. However, the competition is trivial in high-permeability rocks. Other factors, such as reservoir boundary condition, layer thickness, subcritical index and pattern development stage, all have considerable impact on fracture pattern development and attribute distribution in a poroelastic media.

Table of Contents

List of Tables

List of Figures

Chapter 1: Introduction

1.1 OBJECTIVE

Over the past decade natural gas reserves have become an emerging asset worldwide, especially in the United States, Canada, Europe, Australia, Russia and China (Halliburton, 2008). Nearly half of the natural gas reserves are unconventional, a term which commonly is taken to refer to their low permeability (NPR reports, 2007). Engineers and scientists seek to characterize this type of reservoir and to optimize the production from the low-permeability rocks. Evidence shows that many low-permeability rocks are naturally fractured (Warpinski and Teufel, 1987; Gale et al., 2007; Lash and Engelder, 2008; Gale and Holder, 2008, 2010). The existence of natural fractures could affect hydraulic fracturing treatments depending on the interaction process between natural fractures and hydraulic fractures. Natural fractures may reactivate during hydraulic fracturing treatments (Arash and Olson, 2009). Moreover, the effective permeability of low-permeability rock is strongly affected by the fracture pattern geometry and attribute distribution (fracture length, aperture and spacing), which are all associated with natural fracture propagation process (Philip, et al., 2005). Thus, it is important to study the geomechanical aspects of fracture growth and to characterize the natural fracture systems in real reservoir environments with the existence of fluid flow and active chemicals.

Core samples and image logs are the common tools used to measure the subsurface natural fracture geometry directly; however, the measurements are limited to the near wellbore region and the information may not be representative and sufficient to study the fracture system distributed in the massive reservoir matrix. Geostatistical techniques are also widely used: randomly populating natural fractures in a field based on fracture attribute populations obtained from the core or log measurement data. This

method requires massive sampling to obtain fracture length, aperture, spacing and orientation to produce a reasonable population distribution (Kulatilake, 1993). An alternative to geostatistical techniques is the geomechanical method, where the solution of boundary value problems is based on the physics of fracture, pertinent geologic boundary conditions and material properties. The geomechanical model can deterministically predict the time-sequence of fracture propagation and the final distributions of fracture attributes (Olson, 1993, 1997, 2004).

Geomechanical modeling studies on natural fracture propagation have been mainly focused on the mechanical aspects of fractures, geological loading history and mechanical properties of rocks. The growth rates of natural fractures are controlled not only by the state of stress around the fracture tip, but also limited by the rate of fluid flow from the saturated porous medium into the void space created during the fracture propagation process (Secor, 1969; Renshaw and Harvey, 1994). For conventional sandstones and limestones, high permeability ensures a fast flow rate and sufficient fluid for pressure recovery, resulting in a negligible effect of permeability on fracture growth rate. However, for rocks encountered in unconventional resource plays, such as tight gas sandstones, mudstones and shales, low permeability leads to a slow internal fracture fluid pressure recovery process, which will significantly limit fracture growth rate, delay fracture propagation timing and affect fracture pattern development.

The primary objective of this study is to build up a realistic geomechanical model to study multiple natural fracture propagation in a poroelastic medium. A simplified two-dimensional reservoir model coupled with the effective media theory is first developed to study the transient behavior of fracture internal fluid pressure during the propagation process and consequent influences on multiple fracture development (Segall, 1984; Renshaw and Harvey, 1994). Moreover, the mechanical interactions between multiple

fractures and the heights of natural fractures have strong impacts on the stress state around each fracture tip. Both features are captured by a boundary element model, which is coupled with a fluid flow model to study the pseudo three-dimensional multiple fracture propagation with both mechanical interactions and fluid flow interferences. The new model enables the investigation of fracture pattern development and fracture attribute distribution in rocks with different permeability and other rock properties.

The dissertation is organized as below.

1.2 OVERVIEW

1.2.1 The overview on the timescale of natural hydraulic fracture development

Natural hydraulic fracture (NHF) refers to a type of fracture whose propagation is driven by an internal fluid pressure purge and follows a crack-seal growing process. The conjecture of natural hydraulic fracturing mechanism comes from the extensive field evidence, such as the plumose structure with arrest marks, synkinematic cements and fluid inclusion in fracture bridges (Hodgson, 1961; Pollard and Aydin, 1988; Beach, 1977; Laubach, 1988, 2004; Bechker et al., 2010; Fall et al., 2012).

Secor (1965) first pointed out that fluid pressure is important in the opening mode fracture development. Later, Renshaw and Harvey (1994) studied the quasi-static fracture propagation process for a single NHF in a poroelastic media by investigating the coupling effect between pore pressure and stress field. The partially and fully decoupled simulations were found to yield similar results to those obtained from fully coupled model. In addition, several key factors are found to control fracture growth rate: rock permeability, porosity and initial fracture length. The conclusions were based on the assumption that a single NHF propagates at critical condition, which means the mode I

stress intensity factor K_I is always equal to fracture toughness K_{IC}. Segall (1984) proposed an effective media theory to consider the fracture population effect, where the analysis was focused on the propagation of an arbitrary fracture in the fracture set and the mechanical effects of all other fractures were expressed in the material stiffness, $\tilde{E}$. This theory showed the final fracture geometry was highly affected by the remote strain history and initial fracture density. However, the changes in internal pore pressure, the initial fracture length distribution and the mechanical interactions between multiple fractures were not considered in this model.

In Chapter 2, a new model is developed based on Renshaw and Harvey's work on single NHF growth problem and Segall's effective media theory to weight fracture population. Unlike the prescribed reservoir conditions, the fluid flows were determined from numerical reservoir simulation using the finite difference method. This new model provides detailed insights into fluid flow effects on multiple NHF propagation, especially in the low-permeability rocks. Preliminary simulation results showed that the pore pressure transient behavior was important and cannot be neglected during the multiple NHF propagation process. Reservoir permeability has a significant effect on controlling the timescale of natural fracture development. Other important factors include the boundary conditions, initial fracture density, tectonic strain rate, fracture approximation model and subcritical index. Consideration should be taken for all these factors to characterize the subsurface natural fracture patterns, especially in low-permeability rocks.

1.2.2 The overview on the impact of permeability on the fracture spacing to mechanical layer thickness relationship

The opening mode fractures observed in outcrops are often confined by layered rocks and parallel or subparallel to each other within the same set (Pollard and Aydin, 1988; Helgeson and Aydin, 1991; Olson, 1993; Narr and Suppe, 1991; Gross, 1993). In

many sedimentary rocks, a linear correlation is found between fracture spacing and the layer thickness. The field measurement data shows the spacing to layer thickness ratio (S/T) range from 0.1 to 10 (Narr and Lerche, 1984; Narr, 1991; Narr and Suppe, 1991). The extremely low value of S/T ratio corresponds to the very closely spaced fracture set observed in some low-permeability rocks (McQuillan, 1973; Ladeira and Price, 1981; Becker and Gross, 1996; Fisher et al., 1995; Engelder and Lash, 2007, 2009) and coal cleats as well (Tremain et al., 1991; Law, 1993; Laubach, 1993).

Simulation work has been conducted on a set of regularly spaced fractures bounded by a single layer. The modeling results state that the minimum fracture spacing is approximately the value of the bounded layer thickness (Wu and Pollard, 1995). Additional fracture propagation is prevented because of the compressive stress generated by the stress shadow in the areas between the close-spaced fractures (Bai and Pollard, 2000a). The controversy between simulation results and field observations of the wide range of S/T ratio indicates that the current numerical models are neglecting key physics or mechanisms. One of the possible explanations for the low S/T ratio is natural hydraulic fracturing mechanism, also known as the fluid flow process between saturated rock and propagating fractures (Ladeira and Price, 1981).

In Chapter 2, the elastic interaction between cracks, which is expected to influence fracture growth significantly, is not considered in the new effective media model. In Chapter 3, the geomechanical aspects of fractures will be fully described, especially the stress state around the fracture tip. Many researchers showed that there exists a stress relief area around a pre-existing opening mode fracture, which mechanically influences any fracture located inside this regime (Pollard and Segall, 1987; Olson and Pollard, 1989, 1991). For multiple fractures, the stress shadow of each fracture will overlap and influence the stress state of each other (Olson, 1993). Most current

geomechanical modeling work of natural fracture propagation assumes that the internal fluid pressure is always at the initial constant value. Their conclusions state that the remote differential stress, fracture propagation mode, bed thickness and rock mechanical properties all strongly influence the final fracture geometry (Olson, 1989, 1993, 2004).

The primary goal of Chapter 3 is to develop a new pseudo three-dimensional geomechanical model, which couples fluid flow and fracture mechanical interactions. Boundary element method (Crouch and Starfield, 1983; Olson, 1989, 1993; Renshaw and Pollard, 1994) and subcritical growth law (Atkinson and Meredith, 1984; Atkinson, 1987) will be used to model fracture propagation. An approximate correction factor was incorporated later to account for the fracture height effect (Olson, 2004). In the new model, fluid pressure changes with time and space inside reservoir. Validation work is conducted by setting permeability at a sufficiently large value to represent the constant internal fluid pressure condition. A sensitivity study on a set of multiple regularly spaced fractures is conducted to evaluate the permeability influences on the fracture pattern development and fracture spacing to layer thickness ratio. Other factors, such as subcritical index, reservoir boundary condition and initial fracture half-length, are also investigated in this chapter.

1.2.3 The overview on the influence of formation permeability on fracture pattern development and fracture attribute distribution

Fracture patterns observed in outcrops are often used to interpret the fracture network in subsurface. Various techniques are proposed to characterize fracture patterns and fracture attribute distributions. From the field observations in many outcrops, natural fracture set usually contains fractures with a wide range of fracture attributes (Engelder et al., 2009). Fracture attributes, commonly referred as fracture orientation, planarity, length, aperture and spacing, are widely regarded as a proper representation of the

fracture pattern development. Different functions have been proposed to describe fracture attribute distribution according to whether the fractures are bounded or not and which stage of fracture pattern is developed, well or poorly (Laubach, 1991). These functions include power-law, normal, log-normal and negative exponent (Gillespie, 1999).

There exist three kinds of fracture pattern characterization method: outcrop or core observation (Rives, 1992; Laubach, 1997; Ortega and Marrett, 2000), geostatistical models (Kulatilake et al., 1993) and geomechanical modeling (Qiu, 2002; Olson, 2004). Field observations are direct and simple, but suffer from sampling size and bias issues. Geostatistical models are based on the inherent statistical nature of rock and all the parameters are inherently statistical, which makes it questionable for quantitative prediction of joint properties. Geomechanical modeling work is based on the underlying mechanisms associated with fracture propagation process; however, it requires some basic knowledge of the fracture set, host rock and field stress/loading history.

Meanwhile, it is desired to present all the mechanisms involved in the pattern development process. The foundation of the geomechanical modeling work is linear elastic fracture mechanics (Ingraffea, 1981; Segall, 1984; Olson, 1989). Research focus has been set on studying the influence of mechanical interactions and geological settings on multiple fracture propagation (Olson, 1993, 1997, 2004; Bai and Pollard, 2000b). The past studies show that fracture attribute distribution and pattern development are mainly controlled by the subcritical fracture growth (Segall, 1984; Olson, 1993; Renshaw and Park, 1997) and mechanical layer thickness (Olson, 1997, 2001, 2004).

With the new poroelastic model developed in Chapter 3, permeability established its importance in controlling fracture spacing to layer thickness ratio for regularly spaced fractures. It is of great interest to investigate the influences of formation permeability on randomly distributed multiple fracture propagation and pattern development. The new

poroelastic models developed in Chapter 2 and 3 will be applied to simulate multiple NHF propagation process in Chapter 4. The fracture pattern, the distributions of fracture attribute will all be analyzed to evaluate the impacts from permeability, bed thickness, boundary conditions and subcritical index. The hypothesis is that significant differences are expected in multiple NHF pattern development under various reservoir and rock properties, especially between the low- and high-permeability rocks.

In order to better interpret the natural fracture systems in outcrop or deep in the reservoir, a better understanding and description are required for the physical processes and mechanisms which contribute to NHF propagation in the realistic chemically reactive environment. Fluid flow is a key factor which controls the fracture internal pressure and the fracture intensity factor around its tip. The flow rate is related to the physical and chemical conditions of the saturated porous media where natural fracture propagation occurs over millions of years.

The research in this dissertation focuses on studying the influences of the reservoir properties, especially the reservoir permeability and boundary conditions, on the natural fracture propagation in the porous media. Modified effective media model is a simple and straightforward method to study the fluid effect on large population fracture set. Pseudo3D DDM coupled with fluid flow model fully describes the mechanical interaction and fluid flow interference effects among multiple fractures; therefore this model is more complete and accurate. Both new models show that fluid flow is important for multiple natural hydraulic fracture propagation, the attribute distribution and pattern development. Moreover, very closely spaced fracture patterns, as observed in many outcrops, are observed in the numerical simulations for multiple NHF propagation in low-permeability rocks confined by thick bedding layers.

The numerical results confirm the hypothesis that permeability has significant impacts on fracture propagation timing and pattern development. Natural hydraulic fracturing mechanism is the key to explain the observations of extremely long fracture growth timing and very closely spaced fracture set in low-permeability rocks.

Chapter 2: The Timescale of Natural Hydraulic Fracture Development

Natural fracture propagation can be driven by earthquake rupture or remote tectonic loading or internal fluid pressure purge. The fluid-driven fracture growth is called natural hydraulic fracturing process (Secor, 1965; Beach, 1977; Engelder, 1985; Engelder and Lacazette, 1990; Renshaw and Harvey, 1994). In this chapter, the crack-seal process of natural hydraulic fracture (NHF) growth will be modeled. A study will be performed to examine the effects of flow rate from a saturated porous media into a fracture void on the propagation rate of NHF. Moreover, the fracture population will influence the stiffness of porous media and control NHF growth rate consequently (Segall, 1984). A numerical simulation model is set up by coupling the effective media theory and a two-dimensional fluid flow for the multiple NHF development. The modeling results show that the permeability of the porous medium affects the timescale of NHF development significantly. Other factors, like initial fracture density, tectonic loading rate, fracture shape and fracture distribution, have strong influences as well.

2.1 NATURAL HYDRAULIC FRACTURING OBSERVATIONS

2.1.1 Plumose structure with arrest marks

The surface morphology of a joint records the information about the propagation process (Woodworth, 1896). Plumes, also called plumose structures, are a feature of joint surface morphology, capturing the joint propagation direction from initiation through arrest (Parker, 1942; Hodgson, 1961). As a product of crack development, plumose structures have been used as an important tool to interpret the joint propagation direction, velocity and arresting points (Bahat and Engelder, 1984; Savalli and Engelder, 2005).

Bahat and Engelder (1984) described plumose patterns in the Upper Devonian shales and siltstones of the Appalachian plateau in New York and Pennsylvania. Among the various geometries observed, some patterns had repeated fans along a joint surface as shown in Figure 2.1. They were called rhythmic plumes, and their pattern illustrates that the crack propagation process can be a cyclic process consisting of propagation and arrest.

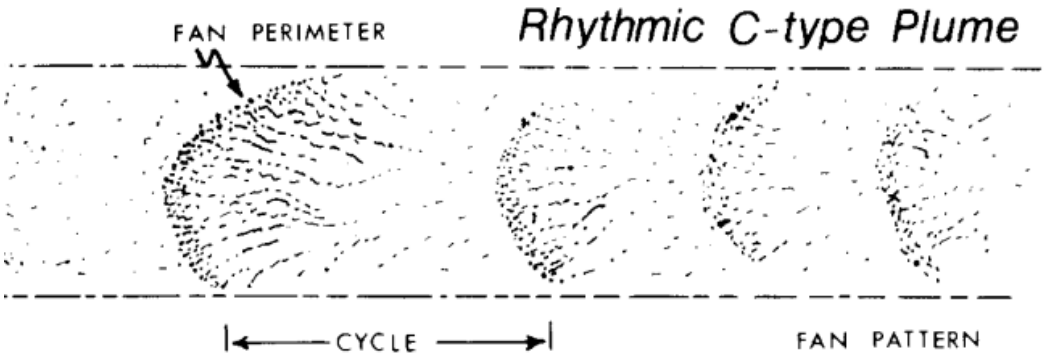

Figure 2.1 - Rhythmic plumes observed on the siltstones of Appalachian Plateau (from Bahat and Engelder, 1984).

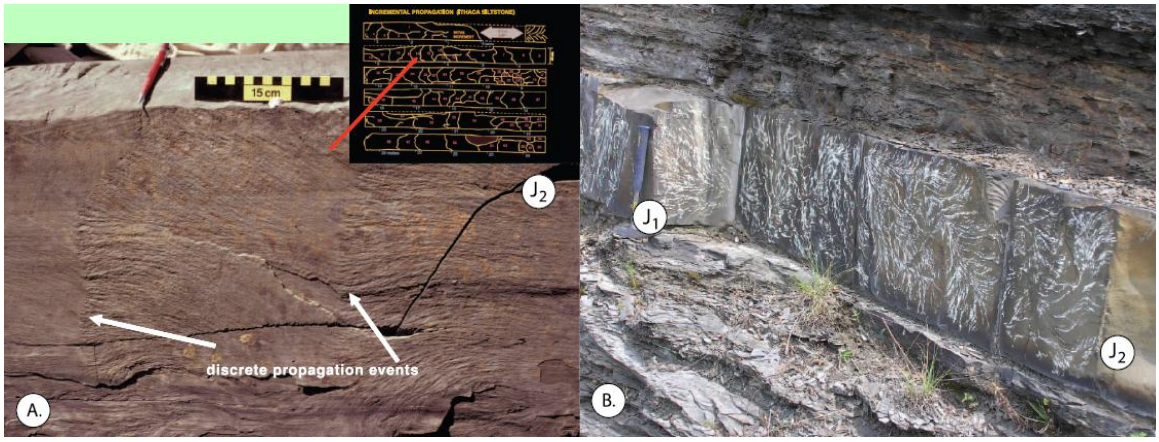

Figure 2.2 - (A) Plume structure with discrete NHF propagation events in the Ithaca siltstone in southwest Watkins Glen, New York (from Engelder et al., 2009). The insert includes 68 increments of propagation mapped on the joint surface. (B) Plume structure mapped on joint surface in a bed of the Devonian Brallier Formation at Huntingdon, Pennsylvania (from Ruf et al., 1998).

The rhythmic plumes shown in Figure 2.2 are widely observed in the field (Ruf et al, 1998; Engelder et al, 2009). The mapped plumose structure on Figure 2.2A shows a series of incremental propagation and arrest events along the joint propagation direction. Figure 2.2B shows more irregular propagation direction along the smooth joint plane, indicating a slower subcritical growth. Both mapped plumose patterns present episodic and incremental propagation of joints. The proposed mechanism for these field observations is fluid loading of natural joints or called natural hydraulic fracturing (Secor, 1965, 1969; Lacazette and Engelder, 1992; Engelder and Fischer, 1996). It was also reported that the joint propagation was driven by the built-up fluid pressure in the black shale, which is heavily overpressured during the later stage of Alleghanian tectonic cycle (Lash and Engelder, 2005).

2.1.2 Synkinematic cements

Beach (1977) reported that the massive vein arrays found in S.W. England were filled with quartz and siderite. These drusy growth fabrics indicated the cements were carried into the fracture voids with the infilling fluid. From the core samples from East Texas basin, Laubach (1988) found the subsurface fractures in sandstone had quartz precipitation and cementation. Later, it was discovered that virtually all fractures created under high temperature and reactive fluid environment have minerals, like quartz, calcite or dolomite, precipitated and dissolute on their surfaces over geologically-long periods of time (Laubach, 2004). The attributes of the fractured rocks depend on the coupling effects of fracturing and diagenesis on nucleation surface area because the cements will fill in the porosity to some extent (Lander et al., 2002; Laubach, 2004).

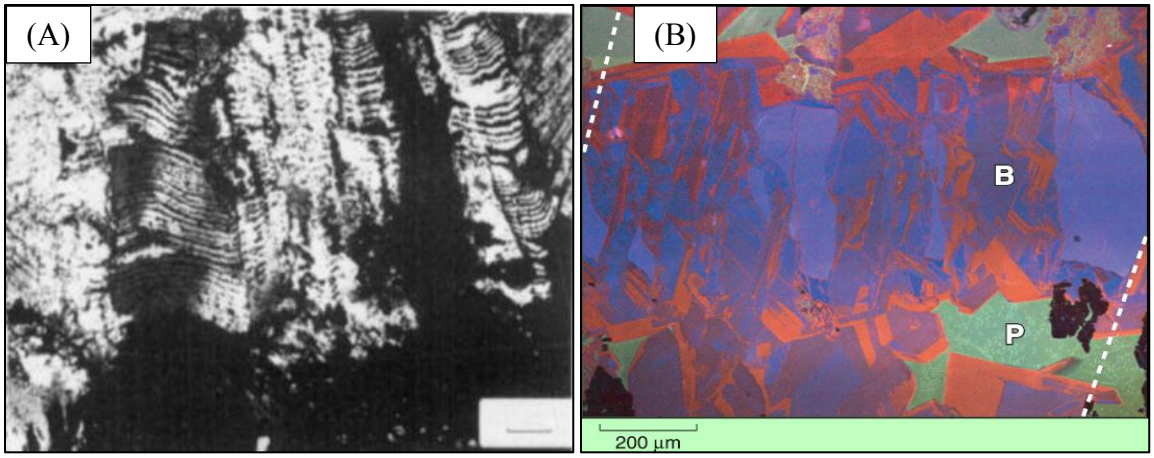

Figure 2.3 - (A) Inclusion bands are parallel to the vein wall on this thin section for crack-seal veins from the Windgallen (from Ramsay, 1980). (B) Scanned CL image shows bridge (B) with crack-seal texture for natural fracture at depth of 20,000 ft in Cretaceous Frontier Formation, Wyoming (from Laubach, 2003). Fracture walls are parallel to the dotted line and P is the residual porosity.

The crack-seal mechanism is described by Ramsay (1980) for vein growth and by Laubach (1988, 2003) for quartz cementation in sandstone as shown in Figure 2.3. Fractures in some dolomite samples also have the crack-seal texture (Gale et al., 2004). In addition, some microfractures, which are the fractures having aperture smaller than 0.1 mm, tend to have crack-seal feature as well (Laubach, 2004). When the cracking and diagenesis occur simultaneously on the fracture, the process is called synkinematic cementation (Laubach, 1988, 2003). The synkinematic cement can correlate the diagenetic history of formation and the quartz precipitation sequence. This indicates the fluid drive initiated the fracture propagation and carried cement into the fracture during its opening process. With this concept, the timing of natural hydraulic fracturing can be inferred from the synkinematic cement (Lander and Walderhaug, 1999; Lander et al., 2002; Laubach, 2004).

2.1.3 Fluid inclusions in fracture bridges

During fracture opening, the fracture-filling cement contains information which can be used to track fracture growth timing and conditions. Fluid inclusions in fracture cements can be integrated to some known diagenetic cement sequence (Laubach, 1988, 2003) or a known thermal history (Narr and Currie, 1982; Laubach, 2003; Laubach et al., 2004; Hanks, 2006) to build up the fracture propagation history. With the modern material characterization tools, the pressure-temperature-composition (P-T-X) evolution history of pore fluid can be reconstructed by analyzing the synkinematic bridge cements and applying crosscutting and overlapping growth relations between quartz cement and crack-seal cement layers (Parris et al., 2003; Becker et al., 2010; Fall et al., 2012). The most recent work suggests that an individual fracture development propagated over a period of 35 my (Fall et al., 2012) to 48 my (Becker et al., 2010) with the aperture opening rates varying from 16 to 23 microns/my. The slow opening rate and long opening period suggest the fracture was actively conducting fluid from surrounding formations and maintaining propagation over the geologically-long period of time.

All the above field and lab evidence shows that natural hydraulic fractures do exist and are highly influenced by the internal fluid pressure changes. The natural hydraulic fracturing process can be very slow and last an extremely long period of time under the chemically-reactive environment. Hence, it is important to develop a model capturing the fluid and mechanical aspects of the natural hydraulic fracture development.

2.2 MECHANISMS FOR NATURAL HYDRAULIC FRACTURE GROWTH

2.2.1 Effective stress

Fracturing is controlled by the effective stress normal to the fracture plane, which was defined by Terzaghi (1943) in the study of soils. The effective stress is the difference between external compressive stress and internal fluid pressure (Secor, 1965; Engelder and lacazette, 1990). In subsurface rocks, all the stresses are compressive and joints are natural hydraulic fractures. Most subsurface rocks are porous media filled with water. The pore fluid pressure may raise or even exceed the hydrostatic pressure if the porous medium is mechanically weak or of very low permeability. Some associated geological events may occur when the rock is under a deformation process, like deposition, burial and compaction (Hubbert and Rubey, 1959; Price, 1975). The fluid pressure, which affects the effective stress on the fracture, is critical during the fracturing process. When the fluid pressure excesses the normal stress on the fracture, the fracture propagates. Overwhelming evidence suggests that joints form in extension rather than shear in subsurface (Narr and Currie, 1982; Engelder, 1985; Pollard and Aydin, 1988).

2.2.2 LEFM propagation concepts

In linear elastic fracture mechanics theory, fracture propagation depends on the stress intensity factors, K_I and K_{II}, which characterize the stress concentration at the fracture tip for normal and shear displacement modes respectively. K_{IC} is a material property called fracture toughness and it represents a material's resistance for a crack to propagate inside. For mode I fracture propagation, the stress intensity factor is expressed as (Lawn and Wilshaw, 1975):

$$K_I = \Delta\sigma\sqrt{\pi a}, \tag{2.1}$$

where a is the fracture half-length and $\Delta\sigma$ is the driving stress which is assumed to be uniformly applied along the fracture surface.

The energy release rate (Evans, 1972) is another term associated with crack propagation conditions. It is related to the stress intensity factor for plane strain condition as:

$$G = \frac{K_I^2 + K_{II}^2}{E^*}, E^* = \frac{E}{1-\gamma^2}, \quad (2.2)$$

where E and v are Young's modulus and Poisson's ratio respectively. In order to generate an increment of growth at the crack tip, the required energy release rate needs to be equal to or larger than the work required to create the additional new crack surface, a material property defined as the fracture surface energy per unit area.

2.2.3 Subcritical and critical crack growth theories

Wiederhorn (1967) created a log-log plot of crack propagation velocity versus stress intensity factor. On this plot (Figure 2.4), three principle regions were recognized for crack growth.

In region I, the slope of the curve is nearly constant, indicating a power-law relationship between crack propagation velocity and stress intensity factor. The power-law exponent, n, is strongly related to rock type and crack propagation environment. In region II, the crack propagation velocity is almost constant over a small range of K_I. The crack velocity strongly depends on the delivery rate of the active species to the crack tip by diffusion or transport. In region III, the propagation velocity accelerates as K_I approaches K_{IC}, where critical fracture propagation happens and it is controlled by the rupture velocity. K_{IC} is the upper threshold for stress intensity factor. The lower threshold on the Figure 2.4, K_I^*, is somewhere speculative, suggesting no crack extension occurs by stress corrosion below this value (Atkinson and Meredith, 1987a). This threshold value is

related to the fracture properties and environmental conditions. Atkinson chose 0.2 times fracture toughness K_{IC} for quartz and Olson chose 0.1 times fracture toughness K_{IC} in his model (Atkinson, 1984; Olson, 1993).

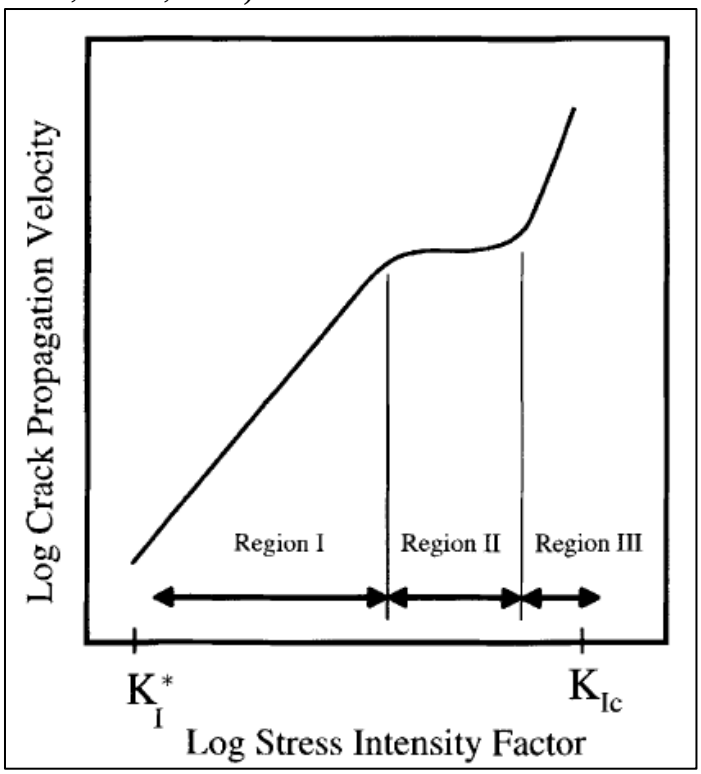

Figure 2.4 - Log-log plot of propagation velocity vs. stress intensity factor (K_I) for subcritical crack growth. K_I^* is the minimum stress intensity factor below which there is no propagation. K_{IC} is the fracture toughness of the material, at which propagation becomes critical (from Olson, 2004).

Critical crack growth

Critical crack growth occurs when K_I is equal to K_{IC}, which requires a driving stress of

$$\Delta\sigma_{IC} = K_{IC}/\sqrt{\pi a}. \quad (2.3)$$

This shows propagation is inherently unstable because once initiated, it takes a declining amount of stress to continue (Lawn and Wilshaw, 1975; Pollard and Aydin, 1988).

Therefore, mode I critical crack propagation depends on the loading, crack size, boundary conditions and material properties.

Subcritical growth

Subcritical crack growth is often observed in rocks and minerals, especially when they are experiencing long-term or cyclic loading or high temperature. Over a long period of time, cracks can propagate when stress intensity factor is lower than the critical value, K_{IC}. This is called subcritical crack growth. Atkinson (1984) concluded that the main mechanism for subcritical growth is stress corrosion. This occurs when crack tip is under a chemically-active environment. An active chemical component reacts with the crack tip, reducing the energy requirement for crack growth (Atkinson and Meredith, 1987b).

The power-law relationship between crack subcritical velocity and stress intensity factor is expressed in the form of

$$V = Vmax\left({K_I}/{K_{IC}}\right)^n, \tag{2.4}$$

where V_{max} is a constant and n is the subcritical index (Charles, 1958; Pletka, 1979).

2.2.4 Aperture versus length data

The fracture aperture is defined as the maximum opening displacement along fracture walls. For noninteracting, mode I fractures under 2D plane strain conditions in a homogenous and isotropic body, the LEFM relationship between fracture aperture (d_{max}) and fracture total length (L) is expressed as (Pollard and Segall, 1987)

$$d_{max} = \Delta\sigma_I \frac{2(1-\gamma^2)}{E} L. \tag{2.5}$$

If constant driving stress propagation is assumed, a linear aperture-to-length scaling is expected:

$$\frac{d_{max}}{L} = \Delta\sigma_I \frac{2(1-\gamma^2)}{E}. \tag{2.6}$$

Olson (2003) suggested that constant stress intensity factor propagation is more realistic for geological loading conditions, and consequently, the aperture-to-length relationship becomes

$$d_{max} = \frac{K_{IC}(1-\gamma^2)}{E\sqrt{\pi/8}}\sqrt{L}, \quad (2.7)$$

which predicts fracture aperture scales with the square root of fracture length. The possible mechanisms for the falling driving stress with propagation required to maintain constant stress intensity factor propagation could be natural hydraulic fracturing (Renshaw and Harvey, 1994) or elastic relaxation due to fixed displacement loading at the remote boundaries (Segall, 1984).

2.2.5 Models for natural hydraulic fracture growth

The numerical modeling work of natural fracture propagation involves the dynamic diffusion of fluid flow in porous media and the stress-induced deformations of fractures, or the so-called poroelastic theory formulated by Biot (1941) and modified by Rice and Cleary (1976). Secor (1965) proposed a classic model of natural hydraulic fracturing with consideration of internal fluid pressure. He argued that although the stresses in the subsurface are all compressive, effective tension is possible due to pore pressure, and the depth to which effective tension is possible increasing with increasing pore pressure gradient. He also proposed that failure could occur repeatedly in an environment of increasing pore pressure gradient due to burial.

The growth of macroscopic tension fractures consists of two stages (Renshaw and Harvey, 1994): a short period of crack extension at crack tip, followed by a longer period during which the pore fluid flows into the crack to recover the internal fluid pressure. Assuming the remote stress values remain constant, the rate of crack propagation is mainly controlled by fluid flow properties of the rock.

2.2.6 Range of permeability for host rocks

A tight gas reservoir is defined as rock with a permeability lower than 0.1 mD and higher than 0.001 mD (Sonnenberg, 2011). The permeability range of shale gas reservoirs is generally lower than 1 microdarcy but roughly higher than 1 nanodarcy (Soeder, 1988). Conventional gas reservoirs have permeability as high as 1 mD to 1 Darcy. The demonstration is shown in Figure 2.5.

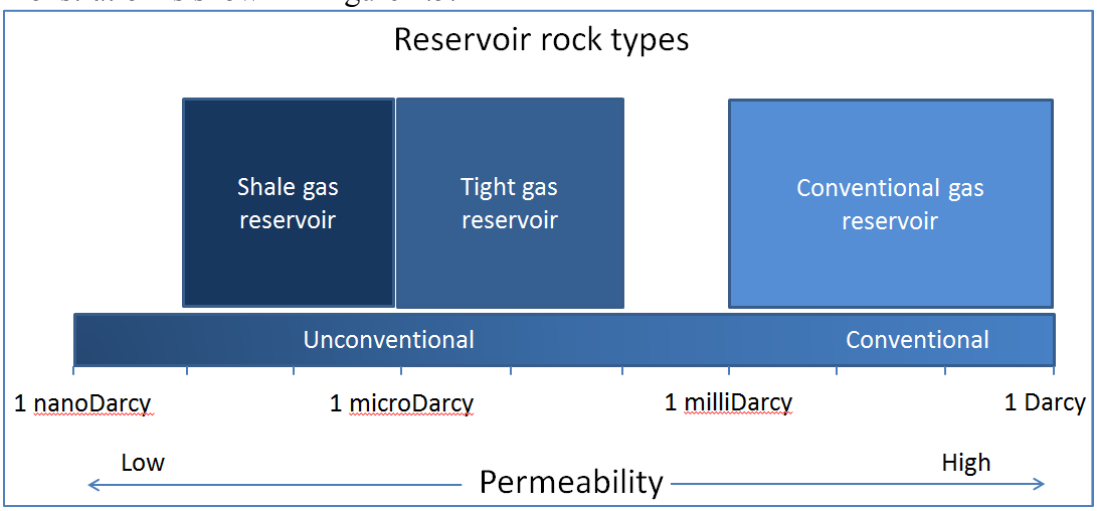

Figure 2.5 - Scale of permeability for shale gas, tight gas and conventional gas reservoir rocks.

2.2.7 Models for layer bounded fracture shape

In reality, fractures are three-dimensional features but they are often approximated using two-dimensional analysis. Plane strain is a two-dimensional, elastic approximation when the strain in the direction of the longest dimension is constrained and can be assumed as zero. For example, if no deformation variation is observed in the out-of-plane direction (z-direction), the 3D calculation problem is reduced to a 2D problem in the x-y plane. There are two main types of 2D approximation that come from the hydraulic fracturing literature: the PKN model (Perkins and Kern, 1961; Sneddon and Elliot, 1946) and the KGD model (Khristianovic and Zheltov, 1955; Geertsman and de

Klerk, 1969). In the geological literature, these shapes are referred to as blade-like and slot-like (Olson, 1993). The out-of-plane direction is the height direction for the KGD fracture and the length direction for the PKN fracture.

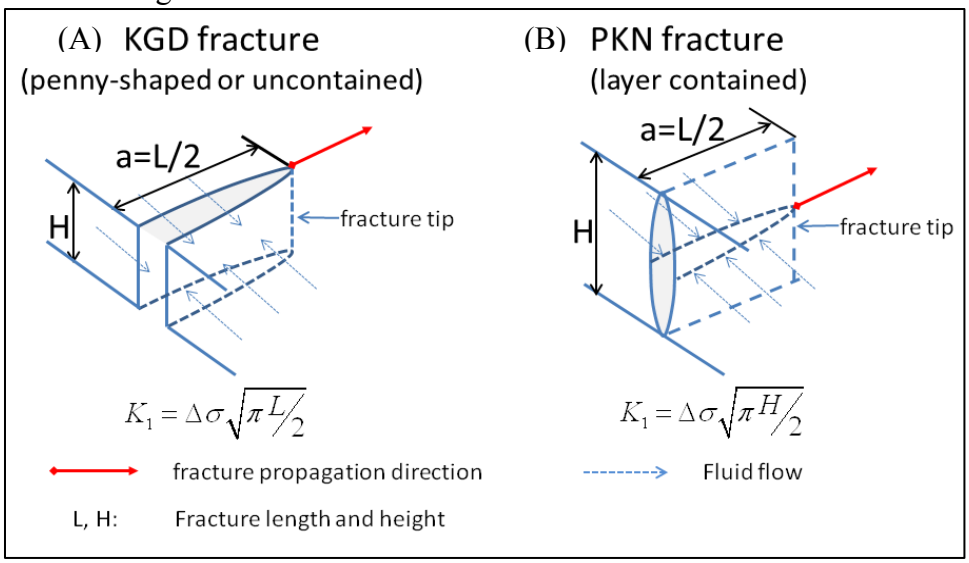

Figure 2.6 - Demos of two types for 2D fracture approximation: (A) KGD fracture (B) PKN fracture.

The major difference between the PKN and the KGD models is the assumption the model makes to convert a 3D problem into a 2D plane strain model. In the PKN model, the shape of fracture at the vertical cross section is assumed elliptical and each cross-section along the length of the fracture is mechanically independent of the others. Fracture compliance depends solely on the height of the PKN fracture. This is true if the fracture length is much greater than fracture height. The KGD model assumes opening is uniform over the height of the fracture while it varies elliptically along the length. Consequently, the compliance of the fracture is a function of the length for KGD fracture.

2.3 MODELING NATURAL HYDRAULIC FRACTURE GROWTH

2.3.1 Renshaw and Harvey's work

Renshaw and Harvey (1994) studied natural hydraulic fracturing process in poroelastic media using numerical simulation. Single opening mode fracture propagation was investigated in a 2D saturated, linear elastic medium with constant remote stress and boundary pressure. The local normal stress and fracture internal fluid pressure were updated from the numerical calculation. Critical propagation was assumed, indicating the fracture internal fluid pressure was always equal to the critical value to maintain the propagation criteria. Furthermore, the compressibility of the fluid inside the fracture was assumed to be zero. In other words, the fluid flow volume from surrounding media into the fracture was equal to the volume change of the fracture. Renshaw and Harvey (1994) tried three different methods for the poroelastic analysis: coupled, partially coupled and completely decoupled models. All gave similar results, but the partially coupled and completely decoupled models were computationally more efficient than the coupled model. The numerical simulation results showed that fracture growth rate scales with permeability and is also controlled by reservoir porosity, initial fracture half-length and rock mechanical properties. Furthermore, the fracture growth accelerates in poroelastic materials.

Renshaw and Harvey (1994) studied an isolated mode I fracture growth under critical propagation conditions. However, the field evidence shows that most fracture's growths are subcritical. Moreover, instead of single fracture, a set of NHFs should be studied for the population effect.

2.3.2 Segall's model for critical growth of fracture populations

Based on the strain energy conservation, Walsh (1965) conducted a theoretical analysis of the relationship between elastic moduli of the material and crack density for a single crack in a material at different loading conditions. The crack was assumed as plane strain cracks and no crack interaction was considered. E is the initial value of the Young's modulus of the material and E_{eff} is the changed value after the material is cracked. The relationships between E and E_{eff} are shown in equation (2.8a) for plane strain and equation (2.8b) for plan stress:

$$E/E_{eff} = 1 + \frac{4\pi}{3}(1-\gamma^2)\rho, \tag{2.8a}$$

$$E/E_{eff} = 1 + \frac{4\pi}{3}\rho. \tag{2.8b}$$

The fracture density, ρ, is defined as

$$\rho = \frac{\sum_{n=1}^{N} a_n^2}{A} = \frac{N \cdot a^2}{A}. \tag{2.9}$$

Segall (1984) proposed an effective media model for a set of N non-interacting mode-I natural fractures with the same half-length a in a reservoir with area A following Walsh's analysis (1965). In Segall's theoretical model, fracture propagation was driven by a uniaxial extension to the reservoir, and the Young's modulus was softened as

$$\tilde{E} = \frac{E}{1+2\pi(1-\upsilon^2)\rho}. \tag{2.10}$$

In other words, one fracture is modeled and the fracture population effects are considered through effective modulus, $\tilde{E}$. This model gives stable fracture growth under uniform strain rate conditions. The analytical derivation for fracture propagation is expressed as

$$\frac{G}{2\Gamma^*} = \frac{\kappa_I^2+\kappa_{II}^2}{\kappa_{I0}^2+\kappa_{II0}^2}\left[\frac{\frac{\tilde{E}\Delta\varepsilon}{1-\upsilon^2\tilde{E}/E}+\Delta P}{\frac{\tilde{E}_0\Delta\varepsilon_0}{1-\upsilon^2\tilde{E}_0/E}+\Delta P_0}\right]^2\left(\frac{a}{a_0}\right), \tag{2.11}$$

where $\frac{G}{2\Gamma^*}$ is the dimensionless crack extension force. Five factors affect fracture propagation: the change in applied strain $\Delta\varepsilon$, changing elastic interaction among cracks

$\kappa_I^2 + \kappa_{II}^2$, crack half-length a, internal fluid pressure ΔP and changing effective modulus $\tilde{E}$. Generally,

$$\upsilon \sim 0.2, \frac{\tilde{E}}{E} < 1, 1 - \upsilon^2 \frac{\tilde{E}}{E} \approx 1, \tag{2.12}$$

which leads to an approximation of

$$\frac{G}{2\Gamma^*} \propto [\tilde{E}\Delta\varepsilon + \Delta P]^2 \left(\frac{a}{a_0}\right). \tag{2.13}$$

As fracture growth criterion is known as $\frac{G}{2\Gamma^*}$ being equal to larger than 1, equation (2.13) indicates fracture growth is strongly influenced by the internal fluid pressure, especially when ΔP is comparable to $\tilde{E}\Delta\varepsilon$. This happens either at the early stage when $\Delta\varepsilon$ is small or during the later stage of multiple fracture growth when $\tilde{E}$ becomes smaller.

However, Segall's model neglects fluid flow effects by assuming constant fluid pressure. This assumption will not be valid for low-permeability rocks where the internal pore pressure is changing with fluid flow all the time. Both fluid flow and fracture population should be considered for multiple NHF propagation.

2.4 NEW POROELASTIC EFFECTIVE MEDIA MODEL

To study multiple natural fracture propagation in poroelastic media, a new realistic geomechanical model is developed to quantify the dynamic growing process of multiple opening mode NHFs in a homogenous, isotropic saturated and linear elastic porous media. Effective media theory is adapted to this new model to consider the fracture population effect. A sensitivity study is conducted to examine the influence of various factors, the permeability's effect in particular, on fracture growth timing.

2.4.1 New model description

The basic geometry of this problem is illustrated in Figure 2.7. Planar, KGD fractures of the same length *L* are oriented perpendicular to the least compressive remote

stress, S_{hmin}, and the fluid pressure P_f is uniform in the fracture. The initial pressure in the reservoir and the fractures is $P_i = S_{hmin}$. Reservoir boundaries are held at constant pressure. Once fracture propagation starts, the fluid pressure distribution is computed using the diffusivity equation: $\frac{\phi\mu C_t}{k}\frac{dP}{dt} = \frac{\partial^2 P}{\partial x^2} + \frac{\partial^2 P}{\partial y^2} + q_f$. The finite difference method is employed to solve the fluid flow problem through time. The simulation area is discretized into square elements as shown in Figure 2.7.

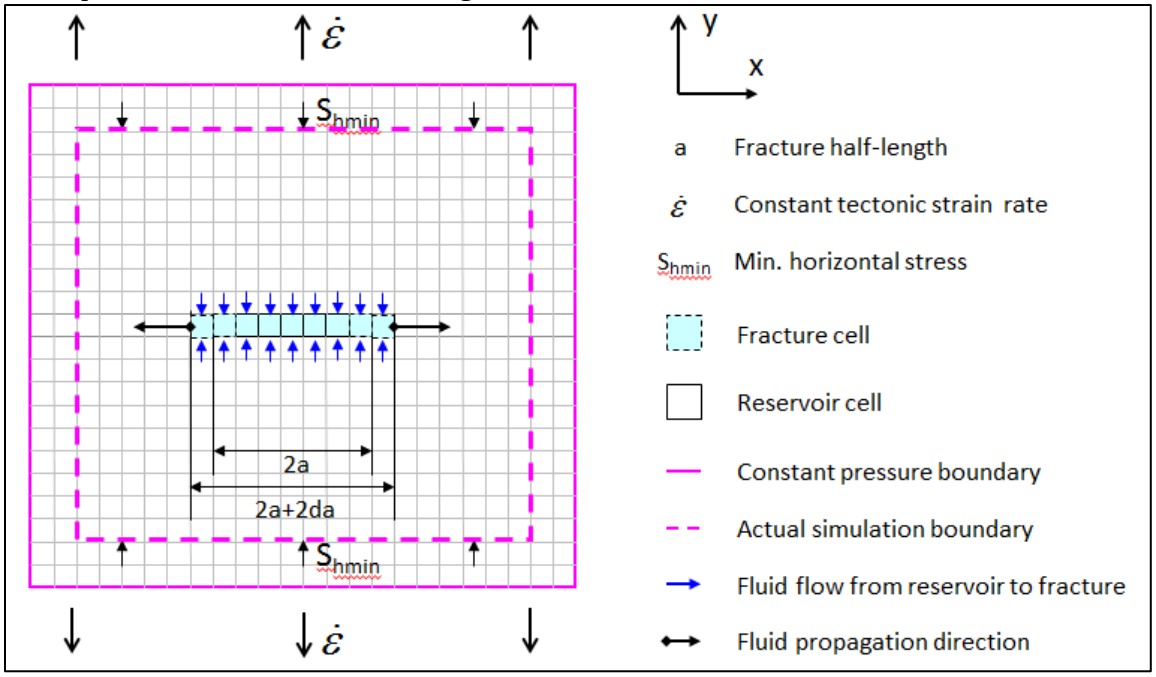

Figure 2.7 - Coordinate system and two-dimensional geometry of reservoir and fracture system.

With a uniform strain continuously applied to the media at a constant rate $\dot{\varepsilon}$, S_{hmin} will drop and meet the fracture propagation criterion after a certain period of time. The onset condition for crack propagation meets when K_I equals K_{IC}, where

$$K_I = (P_f - S_{hmin})\sqrt{\pi L/2}. \quad (2.14)$$

Once the propagation initiates, the internal fluid pressure drops, which draws the fluid from the saturated porous medium into the newly generated void space created by

fracture propagation. This process is called the pressure recovery stage. The volume of fluid flow from the porous medium is equal to the volume change of the natural fracture. Therefore, the fluid transfer process along the fracture walls is time-dependent and can be described as

$$\frac{k_y h}{\mu}\int_{-a}^{a}\left(\frac{\partial P}{\partial y}\right)\Big|_{y=0} dx = \frac{dV_f}{dt}. \tag{2.15}$$

The pressure recovery stage ends once the effective stress reaches the criterion again and leads to another fracture growth stage. One increment element will be added to fracture tip parallel to fracture propagation direction accounting for one growth event. As fractures grow, fracture density increases and effect modulus softens as analytically described in equation (2.10). Appendix A includes all the details on discretization of the diffusivity equation and modeling flow chart for Chapter 2.

2.4.2 Parameters and variables

The parameters used in the simulations are listed in Table 2.1.

Table 2.1 Values of some basic parameters used in the new effective media model.

Parameters	**Values**
Strain rate	$1.2 \times 10^{-19}\ s^{-1}$
Young's modulus, E	20 GPa
Poisson's ratio, υ	0.2
Fracture toughness, K_{IC}	1.5 $MPa \cdot m^{1/2}$
Fluid compressibility, C_t	0.58 GPa^{-1}
Fluid viscosity, μ	1 cP
Reservoir porosity, $\emptyset$	0.1
Initial fracture half-length, a	0.05 m

The KGD fracture shape is assumed for these preliminary runs. The flaws are located in a finite body with an x-dimension of 10 m, a y-dimension of 10 m and a layer thickness of 1 m. Fracture heights are constant and equal to layer thickness. The growth of flaws is excluded from within 1 m of the boundaries to prevent unwanted edge effects. Planar propagation normal to S_{hmin} is also assumed.

2.5 MODEL VERIFICATION

2.5.1 Segall's work

To verify the new model against Segall's work, the reservoir permeability is set to 1 Darcy to represent high-permeability host rocks. Figure 2.8 exhibits the normalized crack extension force versus normalized crack length for various initial fracture densities. Solid lines are the published analytical results from Segall (1984) and symbols are numerical simulation results from this work. The excellent match implies that a permeability of 1 Darcy is essentially equivalent to constant pressure in the fractures for the strain and fracture propagation rates examined here. When dimensionless crack extension force is larger than 1, fracture growth is unstable, where there is a jump in crack length at fixed applied strain. As crack propagation continues, the dimensionless crack extension force drops below 1, which is a stable propagation condition - as the fracture grows, its energy for continuing decreases. Initial fracture densities (ρ_0) smaller than 0.05 lead to unstable crack growth followed by stable growth, while for initial densities (ρ_0) higher than 0.05, crack growth is stable throughout.

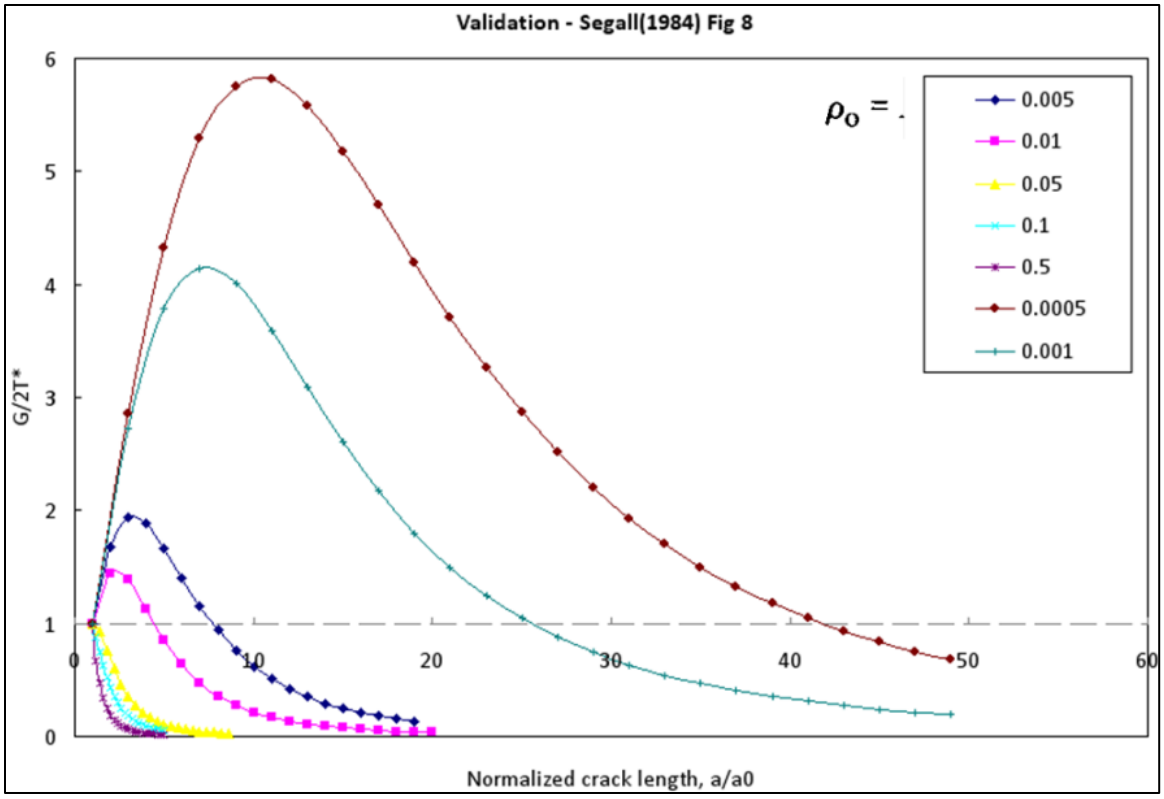

Figure 2.8 - Model verification: curves of normalized fracture extension force vs. normalized fracture half-length for various initial fracture density for both Segall's work (solid line) and our model (data points).

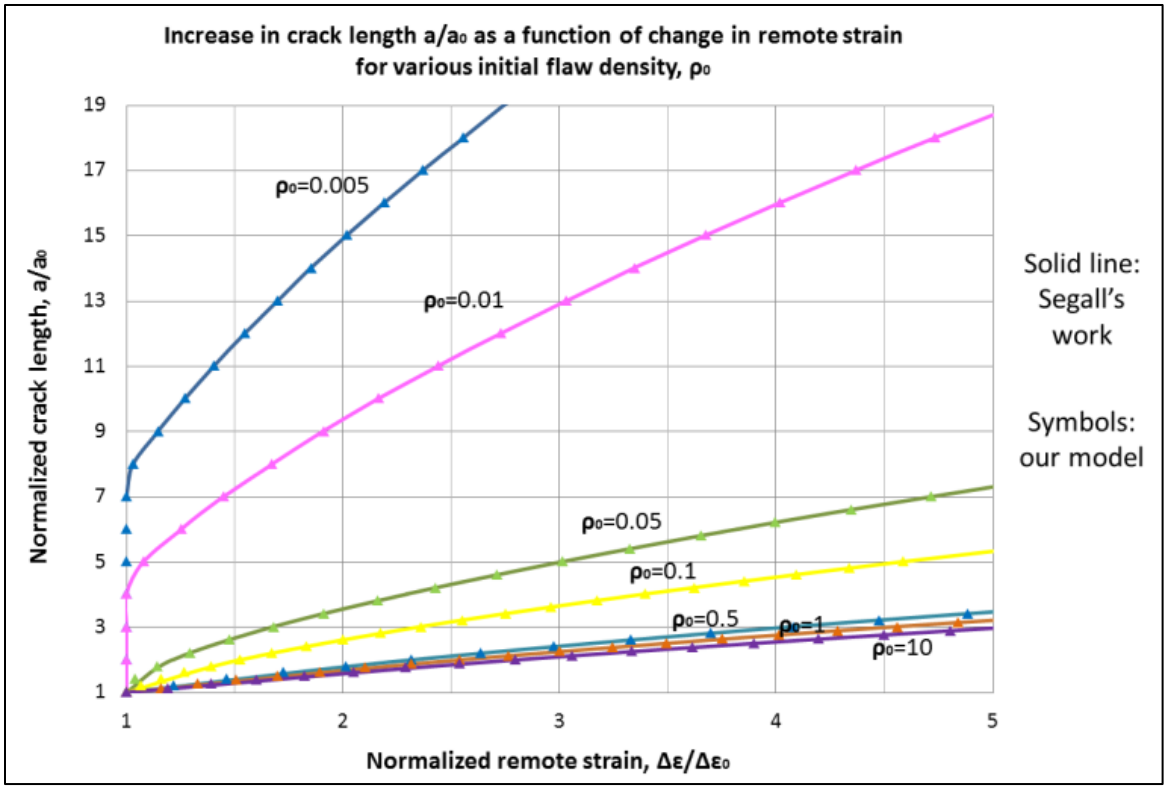

Figure 2.9 - Model verification: curves of normalized fracture length vs. normalized remote strain for both Segall's work (solid lines) and our model (symbols).

Compared to Segall's analytical results shown in Figure 2.9, the same results were obtained in our model for a/a_0 vs $\Delta\varepsilon/\Delta\varepsilon_0$ curves at various initial fracture densities. For small ρ_0 cases, our results also demonstrated that fracture length jumped once fracture propagation initiates, implying unstable initial growth. The initial growth turned to be stable for large ρ_0 cases. Figure 2.9 not only verifies the accuracy of our model, but also indicates that Segall's analytical theory can be applied fairly well to conventional sandstone and limestones with high permeabilities.

2.5.2 Comparison with Renshaw and Harvey (1994)

Renshaw and Harvey (1994) examined a case study based on the Ruhr sandstone. The pertinent material properties are given in Table 2.2. The two models match well

when looking at the fracture half-length versus time curve (Figure 2.10) for a single NHF propagation in a 4 m by 4 m reservoir area.

Table 2.2 Values of material properties of Ruhr Sandstone.

Parameters	**Values**
Young's modulus, E	29 GPa
Poisson's ratio, υ	0.12
Fracture toughness, K_{IC}	1 $MPa \cdot m^{1/2}$
Initial fracture half-length, a	0.1 m
Fluid compressibility, C_t	0.58 GPa^{-1}
Maximum velocity, V_{max}	0.6 m/s
Permeability, k	$2 \times 10^{-16}\ m^2$
Strain rate	$1.2 \times 10^{-19}\ s^{-1}$
Fluid viscosity, μ	1 cP
Reservoir porosity, $\emptyset$	0.1

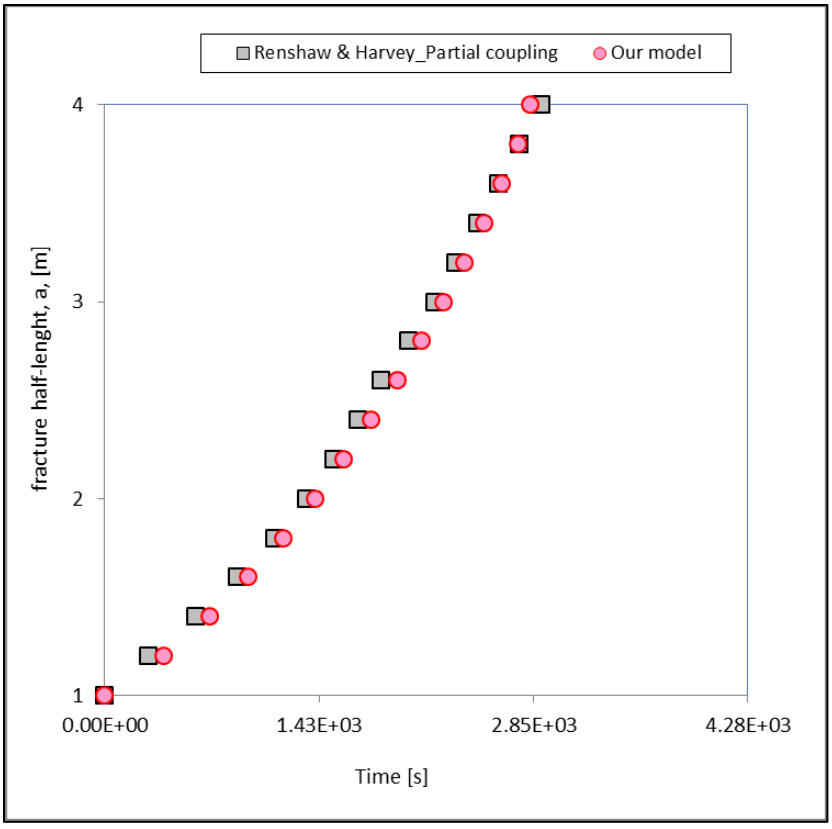

Figure 2.10 - Model validation: curves of fracture half-length vs. fracture growth time for the work done by Renshaw and Harvey (1994) and my model.

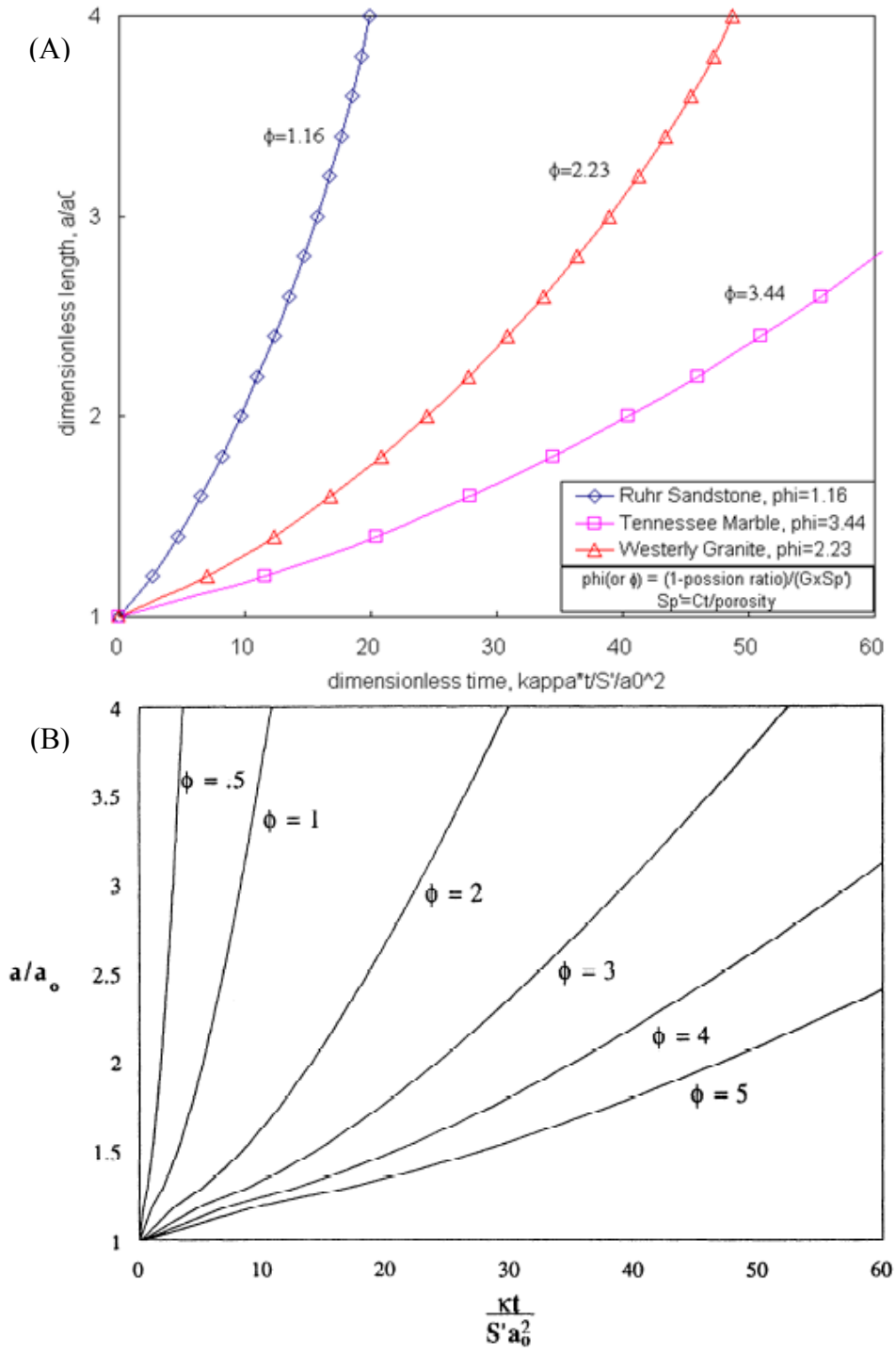

Figure 2.11 - Model validation: curves of dimensionless fracture half-length vs. dimensionless time for various ϕ using (A) current model, (B) Renshaw and Harvey's model (from Renshaw and Harvey, 1994).

Similar results are presented in the plots of dimensionless fracture half-length (a/a_0) vs. dimensionless time (t_D) using the new model (Figure 2.11A) and Renshaw and Harvey's model (Figure 2.11B). The dimensionless time (t_D) is defined as

$$t_D = \frac{\kappa t}{S' a_0^2}, S' = S'_p \cdot \rho g, \tag{2.17}$$

where S'_p is the storage and κ is the hydraulic conductivity of the reservoir. t_D is proportional to κ, which means it scales with reservoir permeability. The variable ϕ characterizes the ratio of the amount of water required to maintain crack propagation to the amount of water actually available in reservoir. The lower the reservoir porosity (higher ϕ), the longer time it takes for water to flow into fracture and the slower the crack growth rate. Figure 2.11 also shows that the fracture growth accelerates as fracture length gets longer, indicating KGD geometry natural hydraulic fracture growth is unstable.

2.6 RESULTS

2.6.1 Permeability effect for critical propagation

Renshaw and Harvey (1994) demonstrated the process of natural hydraulic fracturing in their dimensionless analysis, but did not fully investigate the implications for fracture propagation duration and rate for rocks over a wide range of permeability. In order to investigate rock types varying from shale to sandstone, simulations were run changing the reservoir permeability from $1x10^{-12}$ D (1 pD) to 1 D to represent different rock types. As stated in Section 2.2.6, the permeability of conventional sandstone and limestone is at the scale of Darcy to milliDarcy, while that of shales is on the order of tens of nanoDarcies or less. The permeability of siltstone and tight gas sandstone may

range from milliDarcy to nanoDarcy. A set of 200 KGD flaws were employed to evaluate the permeability effect on multiple fracture growth.

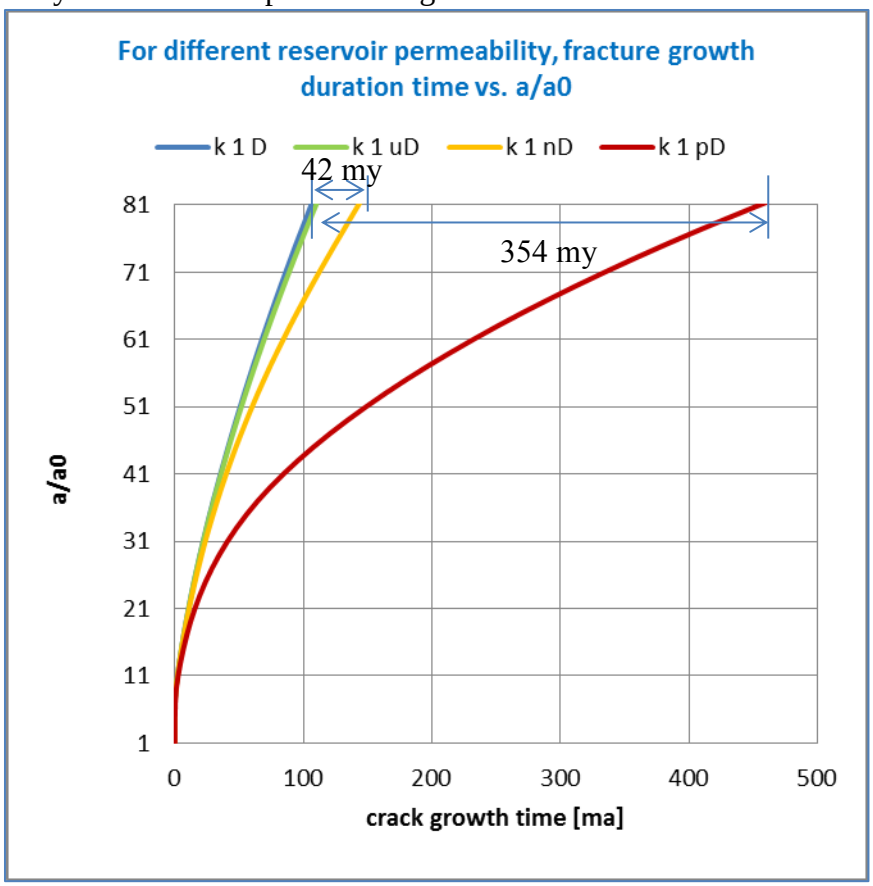

Figure 2.12 - Permeability effect: normalized fracture length vs. fracture growth duration (my) for various reservoir permeabilities.

Figure 2.12 shows the normalized crack length versus time for reservoir permeabilities from 1 D to 1 pD. The high permeability case, which is the same as assuming constant pressure in the fractures, takes a little over 100 my for the average fracture length to reach 81 times the original flaw size. Reducing the permeability all the way down to a microDarcy makes surprisingly little difference in fracture propagation time. However, nano-Darcy permeability for the matrix delays the propagation process by about 42 my, while pico-Darcy permeability causes a 354 my delay. Consequently, the

lower reservoir permeability, the slower the fracture propagation, but extreme changes in permeability are required to cause noticeable effects.

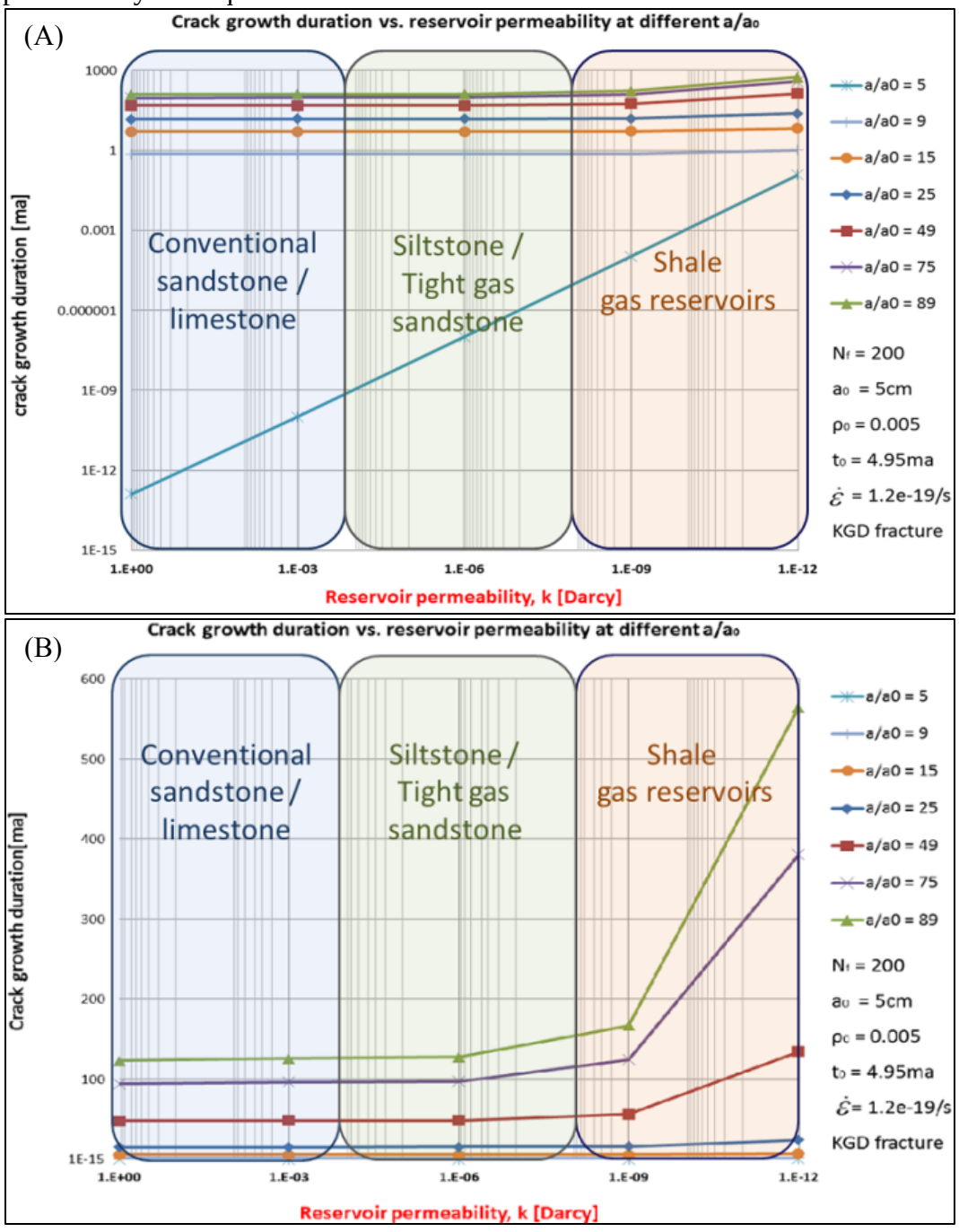

Figure 2.13 - Permeability effect: fracture growth duration vs. reservoir permeability at various normalized fracture length: (A) log-log plot (B) semi-log plot.

Figure 2.13 illustrates the crack growth time required to reach different normalized fracture half-length as controlled by permeability. Each curve on the plot represents a given normalized half-length stage (a/a_0 = 5 is the shortest plotted and a/a_0 = 89 is the longest), with the x-axis being permeability and the y-axis being propagation time since initiation. The reference initiation time is t_0 = 4.95 my, which is the elapsed time since the application of strain for the initiation of growth. The log-log plot (Figure 2.13A) shows that early in the growth history, it takes 10^{-13} my to reach a normalized fracture half-length of a/a_0 = 5 in the highest-permeability case (1 D), while in the lowest-permeability case (1 pD) it takes 0.1 my. At later stages, this seemingly large factor of timing difference goes away for the permeability range of 1 D to 1 μD. For instance, it takes 47.6 my to reach a/a_0 = 49 for 1D case and 48.4 my for 1 μD case (Figure 2.13B). The 1 nD case is starting to lag behind, taking 55.7 my to reach the same half-length, and the 1 pD case is significantly delayed at 134 my. Finally, for the a/a_0 = 89 growth stage, the difference between the 1 D (123 my) and 1 pD (565 my) case is a factor of 5, yet the μD case is still keeping up with growth pace of the 1 D case. Consequently, the important threshold value for permeability where flow lag starts to impact fracture propagation rate is on the order of nD.

2.6.2 Other factors

2.6.2.1 Initial fracture density effect for critical propagation

Initial fracture density (ρ_0) is the parameter used to characterize the initial fracture geometry in this model. Segall (1984) stated the initial fracture geometry and remote strain history were the two factors controlling final fracture geometry, given the fluid effects were neglected. The influence of initial fracture geometry is investigated by varying ρ_0 from 0.0005 to 0.01 and keeping the remote strain rate at $1.2 \times 10^{-19}\, s^{-1}$.

Two permeability values, 1 D and 1 nD, were chosen to represent the high- and low-permeability rocks.

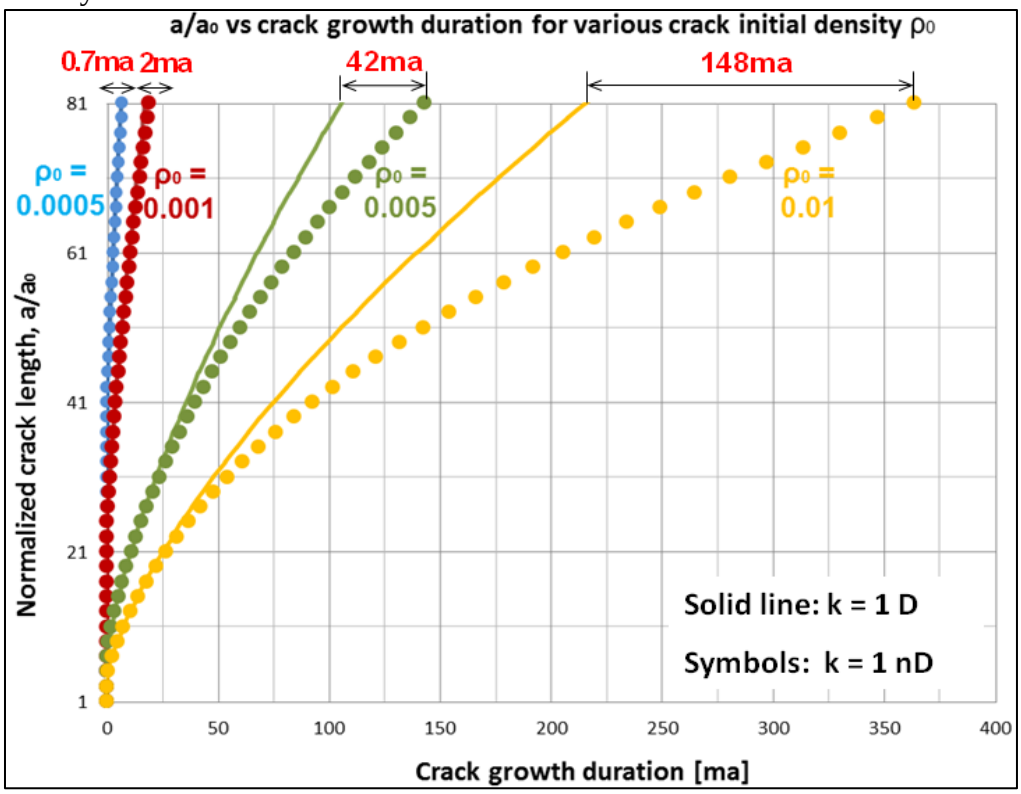

Figure 2.14 - Initial fracture density effect: normalized fracture length vs. fracture growth duration for various initial fracture densities. Solid lines are for 1 D reservoir and symbols are for 1 nD reservoir.

Figure 2.14 illustrates the normalized crack half-length versus time for ρ_0 range from 0.0005 to 0.01. The high-permeability cases (1 D) are demonstrated by solid lines and the low-permeability cases (1 nD) by symbols. Each color represents a specific ρ_0 value. As ρ_0 increases, longer time is required for fracture to reach the same propagation stage in both high- and low-permeability rocks. Generally, fracture growths are lagging behind in low-permeability rocks, compared to those in high-permeability ones. The timing difference between 1 D and 1 nD to reach $a/a_0 = 81$ is labeled for each

ρ_0 value on the top of the plot. An increasing timing difference is observed for higher ρ_0. For example, with ρ_0 = 0.0005, there is only a 0.7 my lag between 1 nD and 1 D cases, and the lag in timing increases to 148 my for ρ_0 = 0.01 case. The initial fracture density has a predominate impact on the fracture growth for both 1 D and 1 nD cases. The timing difference between 1 D and 1 nD cases is trivial for small ρ_0 case, but very significant when ρ_0 is large. The combining effects of reservoir permeability and the initial fracture density are important for NHF propagation timing.

2.6.2.2 Strain rate effect for critical propagation

Remote strain rate is changed from high (1.2×10^{-13}/s) to low (1.2×10^{-19}/s) values to study the influence of remote strain history on fracture growth in low-permeability rock (1 nD). In high-permeability rock, the fluid pressure remains almost constant throughout. The effective media theory (Segall, 1984) states that the fracture growth is a function of normalized strain, not strain rate, assuming the pressure is constant. For low-permeability rock, fluid flow rate is really small and consequently, the fracture growth slows down, resulting in a possible lag in time of millions of years. The applied strain rate may have a notable influence during such a long lagging timing.

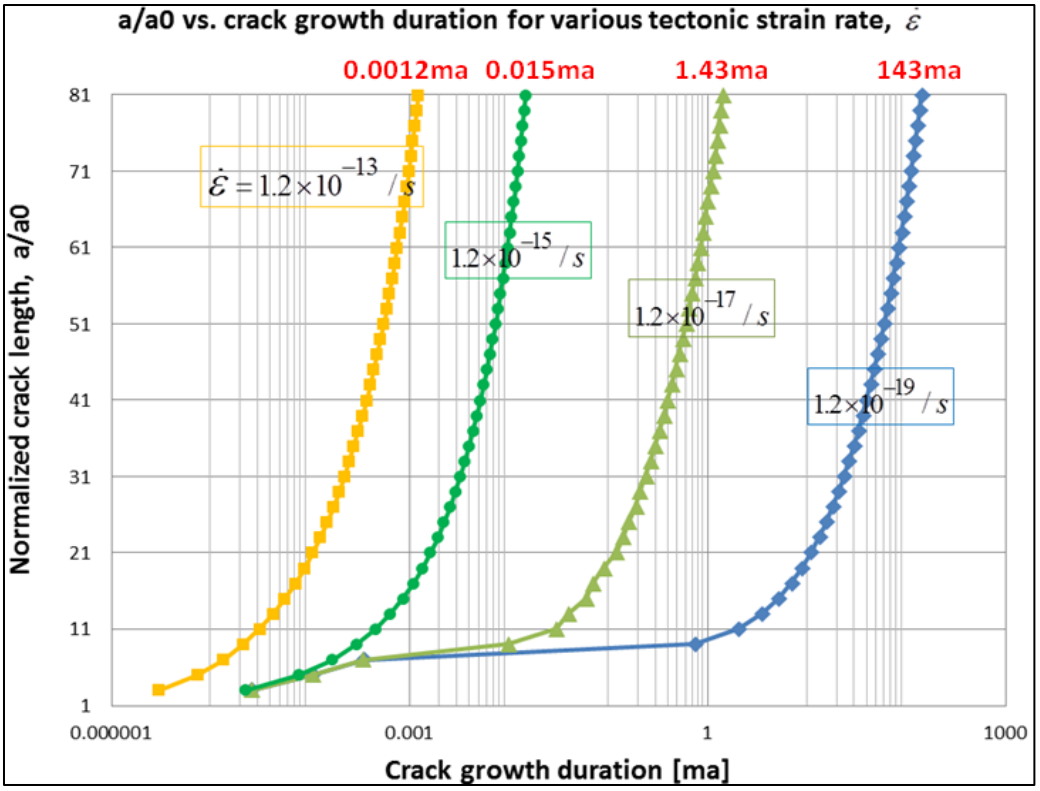

Figure 2.15 - Remote strain rate effect: normalized fracture length vs. fracture growth duration for various applied strain rates for 1 nD reservoir.

A semi-log plot of normalized fracture half-length vs. fracture growth duration is illustrated in Figure 2.15 for the strain rate effect in 1 nD rock. The initial fracture density is 0.005. Consider the low strain rate case ($1.2 \times 10^{-19}\ s^{-1}$) for example, fracture propagation starts at 4.95 my and it takes 143 my to reach a/a_0 = 81 since the initiation. For the large strain rate case ($1.2 \times 10^{-13}\ s^{-1}$), the initiation starts at 4.95 years and the propagation time is 0.0012 my to reach the same a/a_0 ratio of 81. The initiation time is linearly correlated to the remote strain rate and not a function of permeability at all; whereas the correlation is nonlinear between the remote strain rate and the propagation time required to reach a specific a/a_0 ratio 1nD rock. In other words,

the remote strain rate has a noticeable effect on fracture growth timing for low-permeability rocks mainly.

2.6.2.3 Fracture shape effect for critical propagation

Different 2D geomechanical models are used to approximate the fracture geometries. For the KGD fracture, the stress intensity factor K_I is a function of both effective stress and fracture half-length, which results in a faster growth as the fracture propagates. For the PKN fracture, K_I is only a function of effective stress because the fracture height is constant during the whole propagation process; therefore, a slower, but more stable, growth is expected.

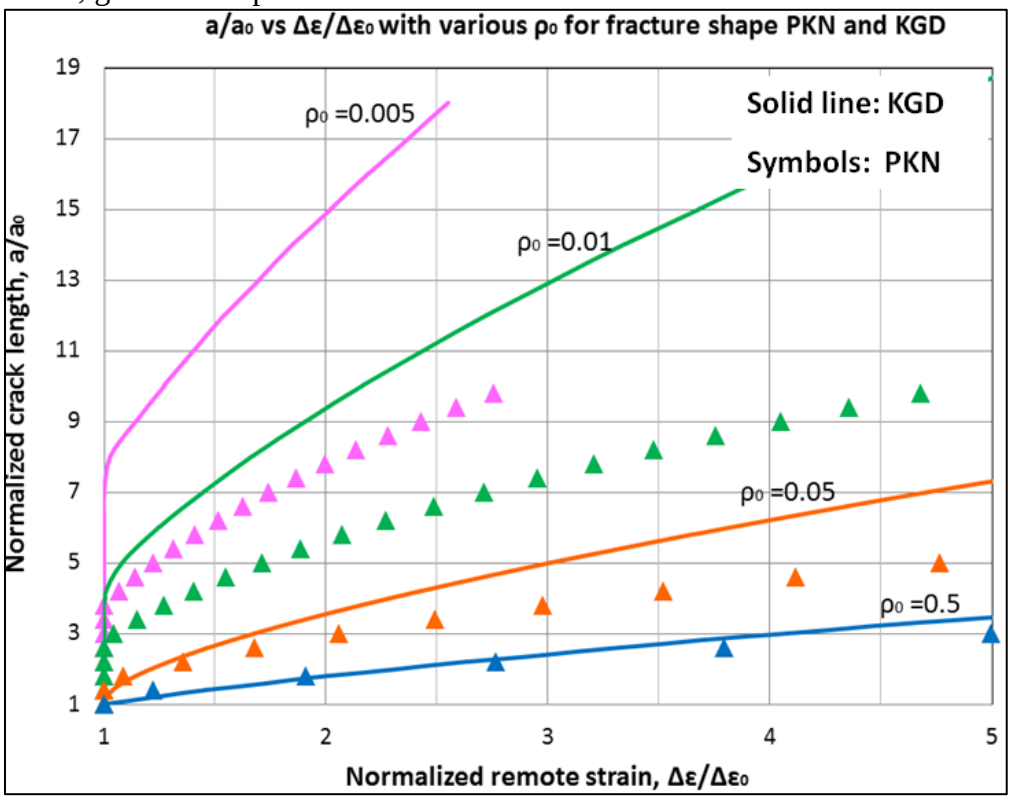

Figure 2.16 - Fracture shape effect: normalized fracture length vs. normalized remote strain for various initial fracture densities. Solid lines are for KGD fracture and symbols are for PKN fracture.

The reservoir permeability is set at 1 D and the remote strain rate at $1.2 \times 10^{-19}\, s^{-1}$ for the plots shown in Figure 2.16. Each color represents a specific initial fracture density (ρ_0) value, ranging from 0.5 (the blue-colored plots) to 0.005 (the purple-colored plots). For a specific ρ_0 case, both the KGD (demonstrated by lines) and the PKN (demonstrated by symbols) models are applied to study the relation between normalized fracture half-length and normalized remote strain. As expected, the results show that the PKN fracture has a more stable but slower growth than the KGD fracture. For a low initial fracture density case (ρ_0 = 0.005), both KGD and PKN fractures have unstable growths when the propagation is initiated, but the KGD fracture growth turns stable when a/a_0 is higher than 8 and the turning point for the PKN fracture is at a/a_0 = 4. In addition, to reach a/a_0 = 8, only a slight increase in the normalized remote strain ($\Delta\varepsilon/\Delta\varepsilon_0$) is needed for the KGD fracture, while $\Delta\varepsilon/\Delta\varepsilon_0$ is required to be as large as 2.2 for the PKN fracture. Given the strain rate and $\Delta\varepsilon_0$ are the same for both fracture models, higher $\Delta\varepsilon/\Delta\varepsilon_0$ represents large $\Delta\varepsilon$, corresponding to longer fracture growth time. On the other hand, for a high ρ_0 case (ρ_0 = 0.5), $\Delta\varepsilon/\Delta\varepsilon_0$ is required to be higher than 5 for both KGD and PKN fractures to reach a/a_0 = 4. A subtle difference is observed between the two fracture models for high ρ_0 case and $\Delta\varepsilon/\Delta\varepsilon_0$ range from 1 to 5. This implies the fracture approximation model has a negligible effect on fracture growth timing for the large ρ_0 case, but significantly influences the small ρ_0 case when the $\Delta\varepsilon/\Delta\varepsilon_0$ value is lower than 5.

2.6.2.4 Boundary condition effect for critical propagation

Fluid flow behavior is strongly influenced by the reservoir boundary conditions, especially during the semi-steady and steady state period. When fluid flow is in the transient period, the pressure disturbance caused by fracture growth has not interfered

with reservoir boundary yet. Therefore, the fracture propagation rate depends mainly on the reservoir permeability, rock properties and fracture configuration as what have been discussed so far. When the fluid flow passes the transient region, the boundary condition will affect the pressure distribution within the reservoir and impact fracture propagation accordingly. Constant pressure and no-flow boundary conditions will be studied and compared for fracture propagation in low-permeability rocks.

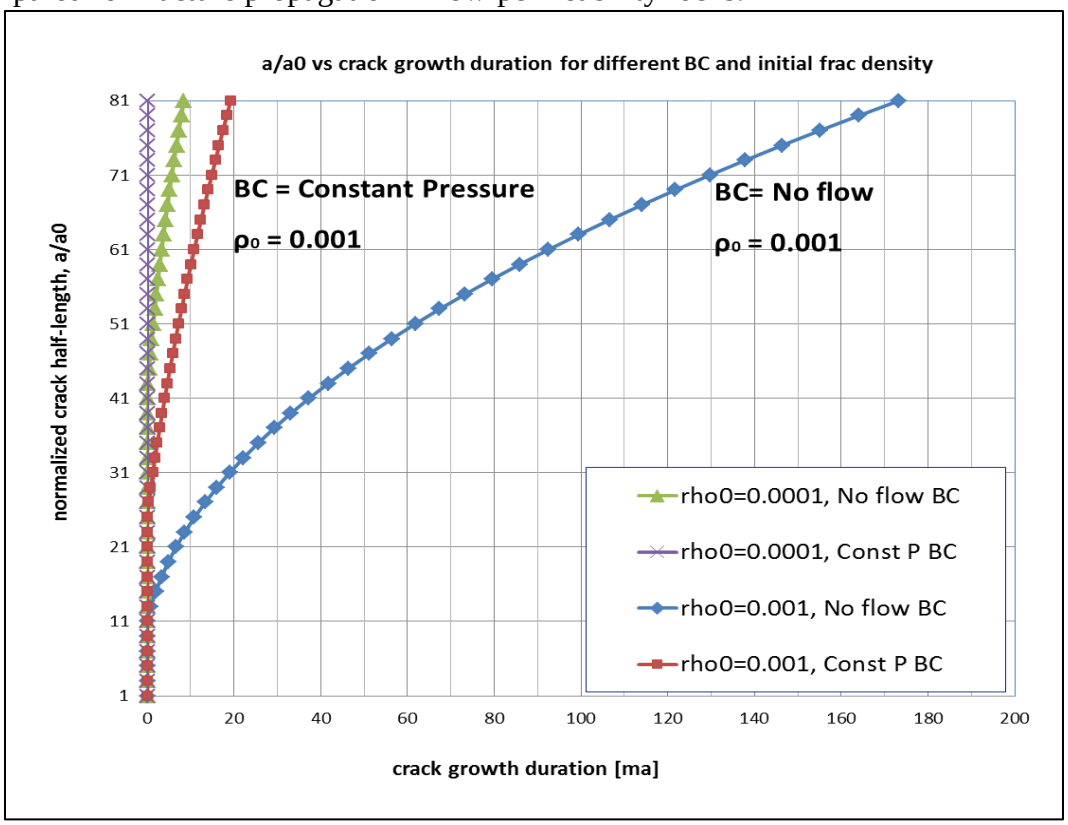

Figure 2.17 - Reservoir boundary condition effect: normalized fracture length vs. fracture growth duration (my) for various initial fracture density and reservoir boundary condition. Cases are for the KGD fracture propagation at strain rate of 1.2×10^{-19} s^{-1} in 1 nD rock.

Four cases are illustrated in Figure 2.17 to investigate boundary condition effect on fracture growth at low and high ρ_0 conditions in 1 nD rock. Both the red and blue

curves refer to the high ρ_0 case (ρ_0 = 0.001). After the fracture initiation, the growth timing is 20 my for fracture's half-length to reach a/a0 = 81 with the constant boundary condition and 175 my with the no-flow boundary condition, resulting in a lag of 155 my. The difference in elapsed timing is only about 10 my for low ρ_0 case (ρ_0 = 0.0001). The results show that slower fracture propagation is expected with no-flow than constant pressure boundary condition. The timing difference between the different boundary condition cases becomes considerably large for the large ρ_0 case.

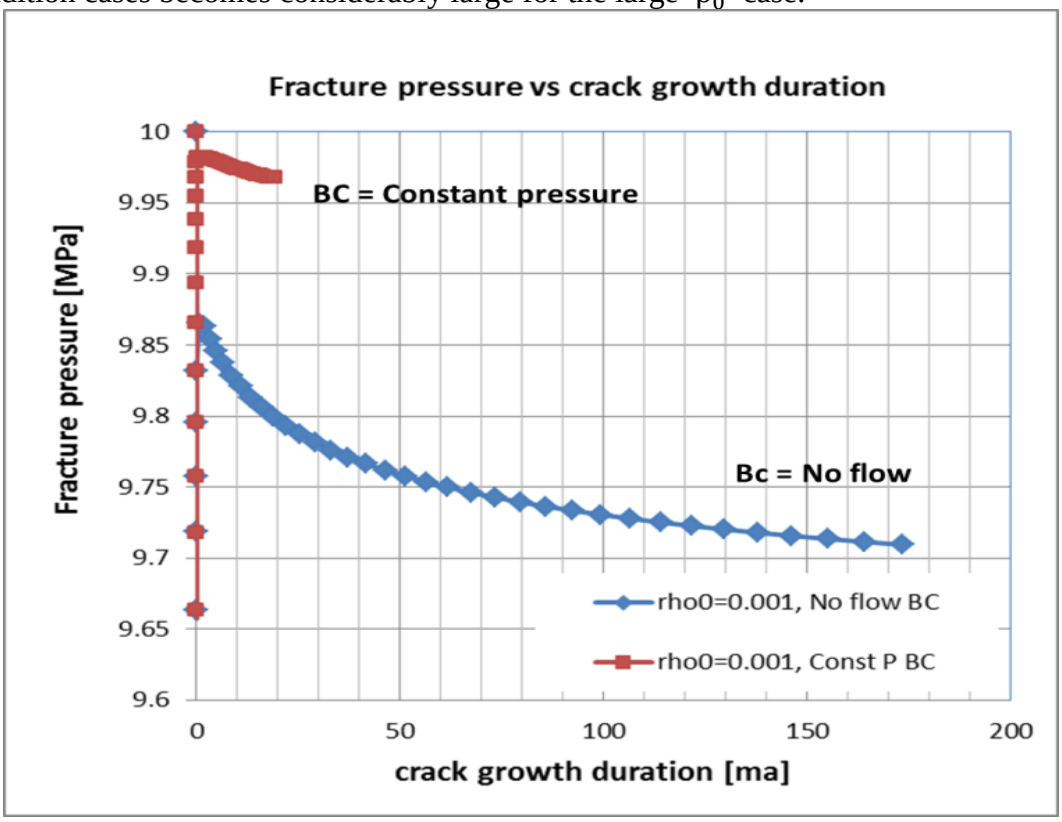

Figure 2.18 - Reservoir boundary condition effect: Fracture pressure vs. fracture growth duration (my) for different reservoir boundary conditions. Cases are for the KGD fracture propagation at strain rate of 1.2×10^{-19} s^{-1} and initial fracture density of 0.001 in 1 nD rock.

Figure 2.18 records the transient behavior of the fracture internal fluid pressure versus crack growth duration with ρ_0 = 0.001 at constant pressure (red-colored curve) or

no flow (blue-colored curve) boundary condition. The fluid pressure inside the fracture is generally higher with constant pressure than no-flow boundary condition. The fracture propagation arrests when a/a_0 = 81 is achieved. After 20 my propagation time, the internal fluid pressure is around 9.97 MPa with a constant pressure boundary condition. For the no-flow boundary condition case, the internal fluid pressure is about 9.71 MPa at the growth timing of 175 my. Consistent differences are observed in the propagation timings and the internal fluid pressure values. Some geological representation may help explain the disparity of this problem. For the constant pressure boundary case, such as when an aquifer or source rock exists around the host rock, the fracture can get sufficient fluid supplies from the porous medium although its propagation duration may differ due to the influences from other factors discussed in previous sections. For the no-flow boundary case, the sufficiency of fluid supplies from porous media to fracture becomes more dominating and the fracture propagation will slow down because of zero fluid flux from reservoir boundaries.

2.6.2.5 Subcritical growth index effect

For all the previous discussions, fracture growths are assumed at critical propagation condition, which corresponds to the upper limit in the subcritical growth regime (n = 1, Figure 2.4). Some fractures grow at a velocity far below the critical value, referring to the subcritical region (n > 1, Figure 2.4). Subcritical index affects the fracture propagation velocity and the ultimate growth timing as illustrated in Figure 2.19. The reservoir has a permeability of 1 nD and boundary at constant pressure condition. The applied strain rate is 1.2×10^{-19} s^{-1} and initial fracture density is 0.001.

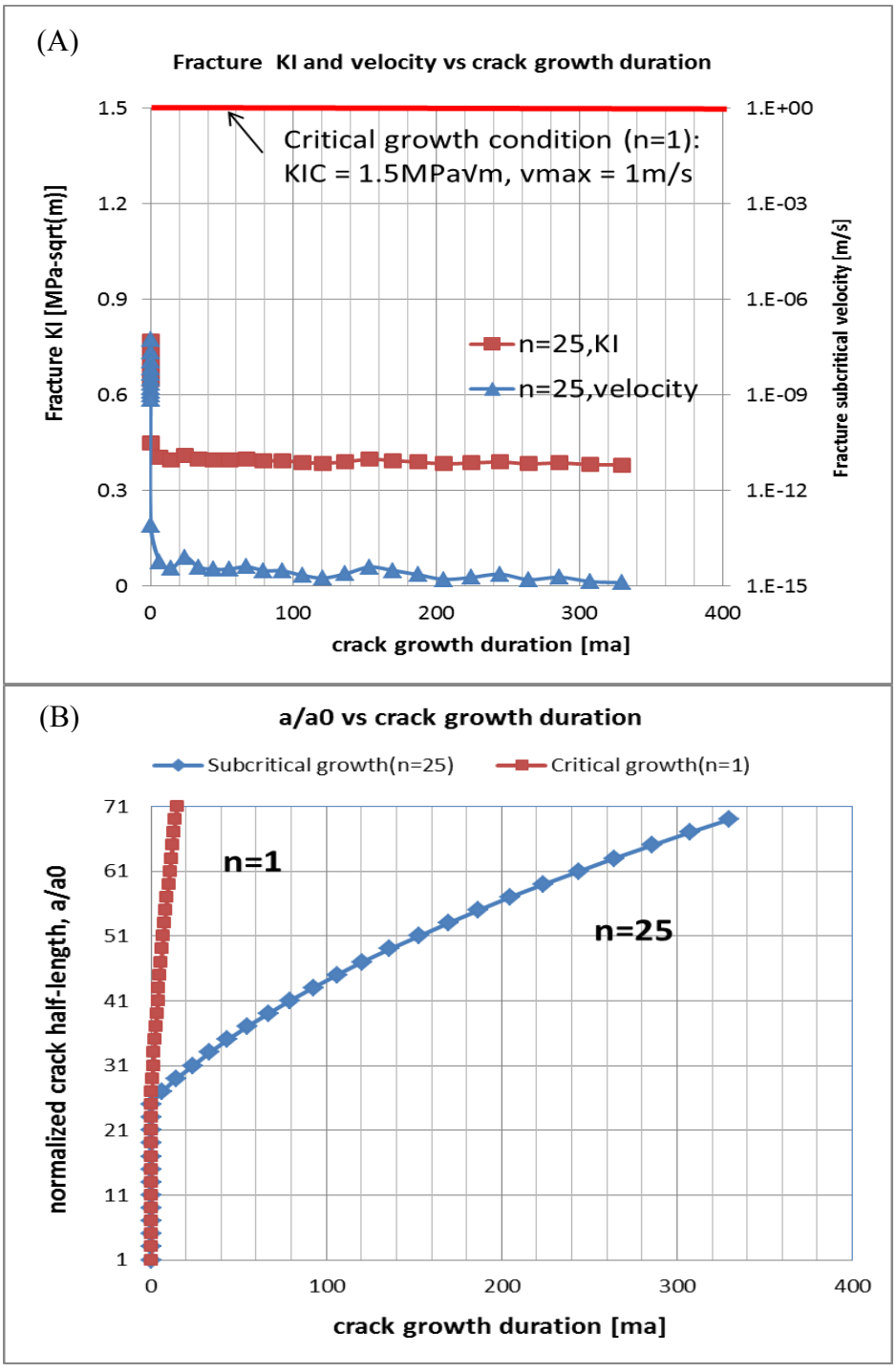

Figure 2.19 - Growth region effect: (A) fracture K_I and subcritical index vs. fracture growth duration (my); (B) dimensionless fracture half-length vs. fracture growth duration (my) for n = 1 and n = 25. Cases are for the KGD fracture.

Fracture velocities and stress intensity factors are recorded in Figure 2.19A. Each data points represent the values of v and K_I at each fracture growth event. For the critical growth case ($n = 1$), both v and K_I are at critical values, 1 m/s and 1.5 MPa√m, respectively. For subcritical growth case ($n = 25$), v is around 1×10^{-19} m/s and K_I is about 0.4 MPa√m, which are far below the critical values. A much smaller propagation rate is observed for the subcritical growth case, which affects the fracture growth duration as shown in Figure 2.19B. The lag in fracture growth timing is significant between the critical and subcritical propagation cases since the propagation becomes stable. For the subcritical case ($n = 25$), it takes about 340 my for the fracture to reach the desired dimensionless half length ($a/a_0 = 71$), whereas the timing is only 20 my for the critical growth case ($n = 1$) (Figure 2.19B). The difference between the critical (20 my) and subcritical (340 my) case is a factor of 17. These results suggest the subcritical index has a remarkable impact on fracture growth duration in low-permeability rocks.

2.7 CONCLUSIONS ABOUT NHF DEVELOPMENT TIMESCALE

To study the influence of fluid flow on multiple natural fracture propagation, a numerical model is developed to simulate the fracture crack-seal propagation process in a poroelastic medium. The fracture internal fluid pressure is updated based on the fluid flux from the porous medium to the fractures. Fracture population effect is considered via evaluating the effective modulus of the poroelastic medium. The numerical results show that the fluid pressure inside fracture does not maintain constant throughout the fracture's crack-seal process in low-permeability rocks, but instead, it is a function of both the fluid flow properties of host rock and the fracture geometry and population. This new model is

also applied to study the impacts of several key factors on NHF growth. The corresponding key findings are summarized as follows:

1. The numerical results for the high-permeability rocks agree with the analytical results which neglect the fluid flow effects by assuming the fluid pressure is constant throughout.
2. Fracture initiation is more stable in the lower-permeability rocks, but fracture growth timing is much shorter in the higher-permeability rocks. High permeability, range from 1D to 1μD, show little influence on fracture propagation, whereas low permeability, especially on the order of nD, significantly affects the fracture propagation because of the flow lag in very low-permeability rocks.
3. Initial fracture density (ρ_0) is used to characterize the fracture geometry in this study. The lag in timing between high- and low-permeability rocks is negligible for small ρ_0 case, but very significant for large ρ_0 case. The coupling effects of ρ_0 and permeability are notable on the fracture growth timing.
4. Remote strain rate determines the strain loading history of the reservoir rock. The initiation time is linearly correlated to the remote strain rate. For the high-permeability rocks, the correlation is linear between the remote strain rate and the propagation timing to reach a specific normalized fracture half-length (a/a_0); however, the correlation becomes less linear with decreasing rock permeability. Fracture propagation is a nonlinear function of the remote strain rate in low-permeability rocks.
5. For the normalized $\Delta\varepsilon/\Delta\varepsilon_0$ range from 1 to 5, little difference is observed between the KGD and PKN fracture propagation for the large ρ_0 case.

The difference shows up for small ρ_0 case as the PKN fracture has a slower but more stable growth than the KGD fracture.

6. A lower fracture internal fluid pressure and longer fracture growth timing are expected for fracture propagation under no flow than constant pressure boundary condition. The lag in timing between the different boundary condition cases becomes noticeably large for the high ρ_0 case.
7. For fractures undergoing subcritical propagation, a much smaller growth rate is observed, which leads to a much longer growth duration than for critical propagation case. The lag in fracture growth timing is remarkably large between the two cases at the late stage of fracture propagation.

In summary, the new model provides new insights into the fluid flow effects on multiple NHF propagation. The permeability effect on the timescale of multiple NHF development is more significant in less permeable rocks, especially those with permeability on the scale of tens of nD or less. In addition, the fracture growth timing strongly depends on the initial fracture density, remote strain rate, fracture approximation model, reservoir boundary condition and fracture subcritical index. However, this model does not consider some key factors which affect multiple NHF pattern development, such as the mechanical interactions between fractures, the remote loading strain history and the fractured layer thickness. More discussion will be addressed in the following chapters.

Chapter 3: The Impact of Permeability on The Fracture Spacing to Mechanical Layer Thickness Relationship

In this chapter, I combine a new fluid flow model with a pseudo three-dimensional displacement discontinuity boundary element method (DDM) to study the fracture spacing to layer thickness relationship under different reservoir and mechanical conditions. This model will also be used in Chapter 4 to analyze fracture pattern development and the statistical distribution of fracture attributes (length, aperture and spacing).

3.1 NATURAL FRACTURE SPACING OBSERVATIONS

Opening mode fractures, called joints, have some interesting features as found in the outcrops, like the fracture orientation, spacing and size distribution. Fractures within the same set are often observed parallel or subparallel to each other (Pollard and Aydin, 1988; Helgeson and Aydin, 1991; Olson, 1993). Their formation is considered under the same tectonic and reservoir conditions. Fracture spacing is measured to characterize fracture density along some scanline in the outcrop (Narr and Suppe, 1991; Gross, 1993; Bai and Pollard, 2000a, b). The relationship between fracture spacing and bed layer thickness is of great interest to many geologists and engineers. By studying the relationship between fracture spacing and layer thickness, one can obtain more understanding of physical and geological processes of the fracture propagation and pattern evolution.

3.1.1 Strata-bound fractures

Many of the opening mode fractures observed in the sedimentary rocks are confined in layered sedimentary rocks (Pollard and Aydin, 1988; Helgeson and Aydin,

1991; Olson, 1993; Narr and Suppe, 1991; Gross, 1993). The siltstone outcrop surface in Appalachian Plateau, central New York showed that each siltstone layer had its independent complete fracturing event as indicated from the plumose structure shown in Figure 3.1 (Helgeson and Aydin, 1991). The fracture propagations were initiated from the top of each layer and terminated by the impermeable layers adjoined vertically, which suggest the propagation was a sequential process.

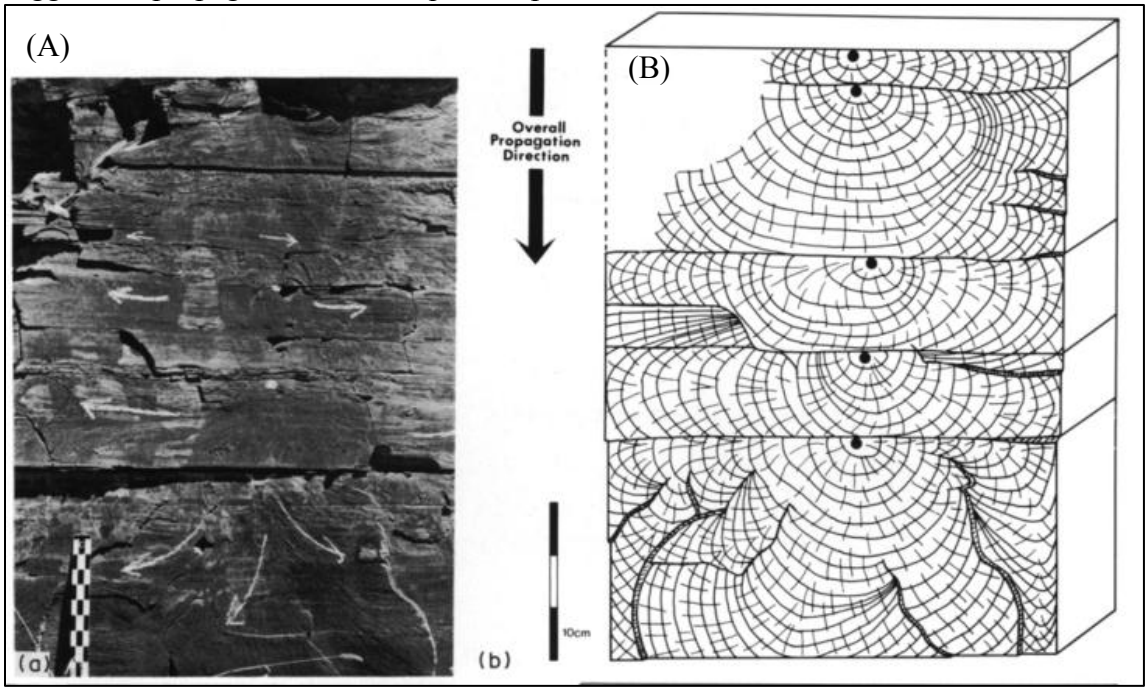

Figure 3.1 - (A) The outcrop of siltstone layers in Appalachian Plateau, central New York. (B) Schematic illustration of the outcrop face in (A) with the associated initiation points, hackle traces and fracturing fronts for the fracture propagation in each siltstone layer. The overall propagation direction is systematically downward (from Helgeson and Adyin, 1991).

3.1.2 Spacing versus bed thickness

Measuring the spacing between the strata-bound fractures is a common approach to study the fracture set in the layered sedimentary rocks. There are also two standard methods to measure fracture spacing: line method (Narr and Suppe, 1991; Gross, 1993)

and area method (Wu and Pollard, 1995). In this study, the line method is used for spacing calculation and the mathematical formula is expressed below:

$$D = \frac{l}{n+1}, \quad (3.1)$$

where l is the length of scanline and n is the number of fractures which intersect with this specific scanline. The value of spacing (D) varies with the position of the scanline, which is normally picked perpendicular to the average orientation of the joint set.

Various kinds of research work have been carried on to study fracture spacing, especially its relationship with respect to layer thickness (Lachenbruch, 1961; Hobbs, 1967; McQuillan, 1973; Sowers, 1973; Ladeira and Price, 1981; Narr, 1991; Narr and Suppe, 1991; Gross, 1993; Becker and Gross, 1996; Rives, 1992; Wu and Pollard, 1992, 1995; Bai and Pollard, 2000). Current findings conclude that fracture spacing in layered rocks is proportional to the layer thickness(Narr and Lerche, 1984) and the ratio of fracture spacing to layer thickness have been found to vary dramatically. The correlation of $S = a \times T$, (3.2)

is proposed to represent this linear relationship between fracture spacing (S) and layer thickness (T). The slope (a) is assumed to be a function of the rock properties and the location of outcrop in the field (Lachenbruch, 1961; Hobbs, 1967; Sowers, 1973; Narr, 1991; Narr and Suppe, 1991; Gross, 1993), not a function of layer thickness (T). From the literature, the value of slope (a) varies from 0.1 to 10.

3.2 LAYER THICKNESS AND FRACTURE SPACING RELATIONSHIP

Fracture saturation occurs when fracture spacing to layer thickness ratio is not changing with applied strain, which is first discovered in the field observation of rock saturated with joints (Cobbold, 1979; Narr, 1991, Narr and Suppe, 1991). Similar results

have also been observed in laboratory experiments (Rives, 1992; Wu and Pollard, 1991, 1992, 1995). The lab experiments are conducted to investigate the evolution process of hundreds of fractures in a brittle coating with a controlled loading sequence, so that the real-time observation can be made to monitor the different stages of fracture pattern development. The experimental results show that in the early stage, fracture spacing decreases rapidly with the applied strain. As time evolves, the spacing decreases less rapidly and eventually reaches a constant value, referred to as fracture saturation. This also demonstrates that laboratory experiments can be used to interpret the field data and to understand the physical process of fracture pattern evolution which cannot be observed in subsurface directly.

3.2.1 Theoretical explanations

There are some theoretical and numerical models proposed to study the *S-T* relationship and to explain the fracture saturation phenomena observed in field outcrops and lab experiments (Hobbs, 1967; Pollard and Segall, 1987; Narr and Suppe, 1991; Zeller and Pollard, 1992; Gross, 1993; Gross, 1995). Most of the models investigate the two-dimensional fracture propagation in the plane perpendicular to the bedding without considering the growth in height.

Hobbs (1967) modified Cox's (1952) stress transfer model and proposed the sequential infilling model to study the fracture growth process in layered rocks. The model proposed the *S-T* relationship as a function of Young's modulus of fractured layer (E) and shear modulus of neighboring layers (G) as expressed in equation (3.3):

$$\frac{S}{T} = \left(\frac{1}{2}\right)^{n} \left(\frac{E}{G}\right)^{\frac{1}{2}} \cosh^{-1}\left(\frac{\varepsilon_{ave}}{\varepsilon_{ave}-\varepsilon_{T}}\right) , \qquad (3.3)$$

where the average strain ε_{ave} and maximum tensile strain ε_T are given. This model is not based on the equilibrium equations, so it fails to explain the fracture saturation and the results are not consistent with lab or field observations (Gross, 1993).

Another model is proposed, called stress shadow model, in which a stress shadow is created around the opening fracture (Narr, 1982; Gross, 1995; Pollard and Segall, 1987). The stress increases from zero at opening mode fracture surface to the remote stress value at a certain distance. At distance *S*, the fracture normal stress is at the percentage *c* of the remote stress value. Stress shadow zone is defined as the area within that specific distance *S*. No new fracture can grow within that distance. The relationship between the distance *S* and layer thickness *T* is proposed as a function of the constant *c* as

$$\frac{S}{T} = \frac{1}{2}\frac{c^{\frac{1}{3}}}{\sqrt{1-c^{\frac{2}{3}}}}. \tag{3.4}$$

Sowers (1972) and Cherepanov (1997) later proposed a model based on studying the limiting equilibrium state of failure in the bed. They claimed that it was the periodic stress-strain field that led to a periodic fracture pattern in layered rocks to achieve a limiting equilibrium state from the initial elastic state. This process made the fracture infilling process possible. The model provides an analytical solution of *S*-*T* correlation as a function of the Poisson's ratio (γ) of the rock layer:

$$\frac{S}{T} = \frac{\sqrt{3}}{2}\frac{\pi}{\sqrt{(1+\gamma)^2-3\gamma}}. \tag{3.5}$$

However, the model cannot explain the wide range of S/T ratio from 0.1 to 10, which are observed in field.

3.2.2 Stress shadow and fracture spacing

Bai and Pollard (2000) classified the field data of *S*/*T* ratio into four ranges: Range I (unsaturated cases): *S*/*T* >1.2; Range II (critical cases, saturation level): 0.8< *S*/*T*

<1.2; Range III: 0.3< S/T <0.8; Range *IV*: S/T <0.3. Numerical simulations were conducted to investigate the stress state transition between fractures which are equally spaced in a two-dimensional layered model with 2D finite element code (FRANC). The results show that the stress transits from tensile to compressive when the S/T ratio falls below some critical value, which is normally around 1. The stress transition prohibits any more fracture infillings in that area if no other fracture growth mechanism is considered. This explains S/T ratio cannot go lower than 0.8 in Range II. The vertical growth of flaws at the layer boundaries contributes more fracture infillings, which explains the lower limit of S/T at 0.3 in Range III. However, the numerical model cannot explain the extreme low S/T ratio in Range IV. The stress state transition study concludes that no additional fracture can form between two fractures if the S/T ratio is lower than some critical value. The additional fracture infilling process requires explanations from other mechanisms, such as hydraulic fractures.

3.3 ANOMALOUSLY CLOSE SPACING IN FRACTURES

3.3.1 Swarms (fracture clustering)

Swarms are zones of anomalously closely spaced fractures. They are observed as fracture clusters with fracture spacing to layer thickness ratio less than 0.1 as demonstrated in the field shown in Figure 3.2 (Hennings et al., 2000; Olson, 2004).

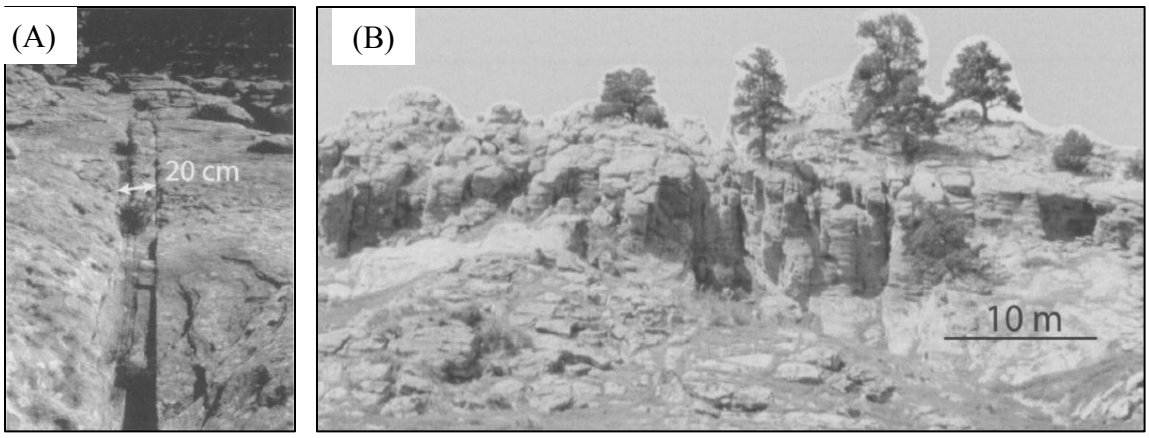

Figure 3.2 - Field demonstration of swarms: (A) a fracture cluster in the Triassic Wingate sandstone on Comb Ridge, Utah, USA. Fracture clustering lies within a 20 cm-wide zone between three and five long fractures, whose spacing scales with the thickness of the fractured layer. (B) a large fracture swarm in the Cretaceous Frontier sandstone at oil mountain, Wyoming, USA. The spacing of the cross-fold fractures is less than 10% of layer thickness (from Hennings et al., 2000; Olson, 2004)

The linear correlation between fracture spacing and stress zone size cannot explain fracture swarms where the local fracture spacing is much smaller than layer thickness. Olson (1993) developed a new geomechanical model to predict fracture swarms by involving fracture subcritical growth and incorporated pseudo three-dimensional effects (Olson, 2004) in the calculation of fracture mechanical interactions. The simulation results illustrate three regimes of fracture spacing to layer thickness ratio. For low subcritical index regime ($n \sim 5$), fractures are irregularly spaced and the spacing in the swarm is much smaller than the layer thickness as those shown in Figure 3.2B. In the high subcritical index regime ($n \sim 80$), fractures form a clustering pattern similar to that in Figure 3.2A, where fractures are very closely spaced in clusters and all the clusters are widely spaced to each other. For the intermediate subcritical index regime ($n \sim 20$), fracture spacing is proportional to the layer thickness due to the stress shadow effect.

3.3.2 Coal cleats

Opening mode fractures in coals are another example of closely-spaced fractures (Laubach, 1993). These vertical systematic natural fractures sets are also named cleats (Dron, 1925). Most cleats are confined by coal beds or maceral layers. For a specific cleat set, two kinds of cleat exist: face cleats as the dominating ones and butt cleats which sit orthogonal to face cleats and stop propagation when meeting face cleats. Similar to other layered sedimentary rocks, cleat spacing increases with increasing coal bed thickness (McQuillan, 1973; Close and Mavor, 1991; Tremain et al., 1991; Law, 1993). There are some cleats very closely spaced to each other as well (Figure 3.3A).

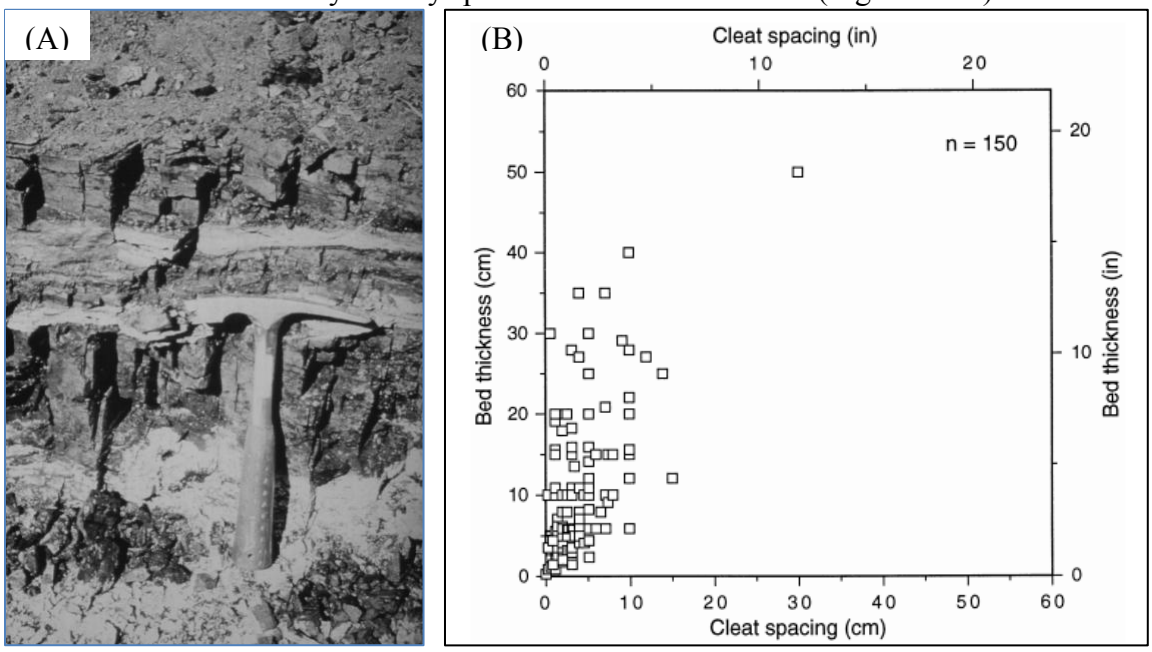

Figure 3.3 - The outcrop of Cretaceous Fruitland formation, northwestern San Juan Basin: (A) Cleats in coal with rock hammer for scale; (B) Cleat spacing versus bed thickness of medium-brightness coals (from Tremain et al., 1991).

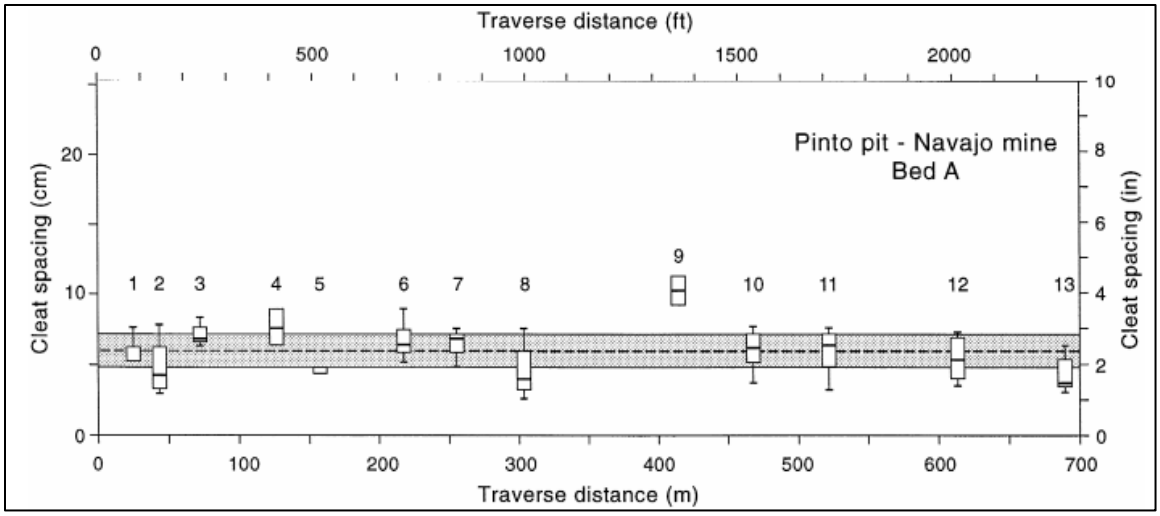

Figure 3.4 - The plot of cleat spacing versus traverse distance for a bed in San Juan Basin, New Mexico (from Laubach. et. al., 1998).

For a given confined coal layer, the size of cleats are defined by the coal bed thickness. The spacing distribution is surprisingly uniform over a long distance, shown in Figure 3.4 (Tremain et al., 1991; Laubach et al., 1998). It was found that cleat spacing is slightly less than the layer thickness as shown in Figure 3.3B. The major influencing factors include coal rank, coal lithology, and layer thickness (Dawson et al., 2010). It was also suggested that the cooling rate of coal strongly affects fracture propagation and results in a closer spaced cleat set of a given size (DeGraff and Aydin, 1993).

3.3.3 Fracture sets in shales

Closely spaced joints have been observed and studied in Marcellus black shales in Appalachian basin by many geologists for decades (Fisher, 1995; Engelder and Lash, 2007, 2009). The formation of these joints has been considered as a result of natural hydraulic fracturing process (Secor, 1964; Engelder and Lacazette, 1990).

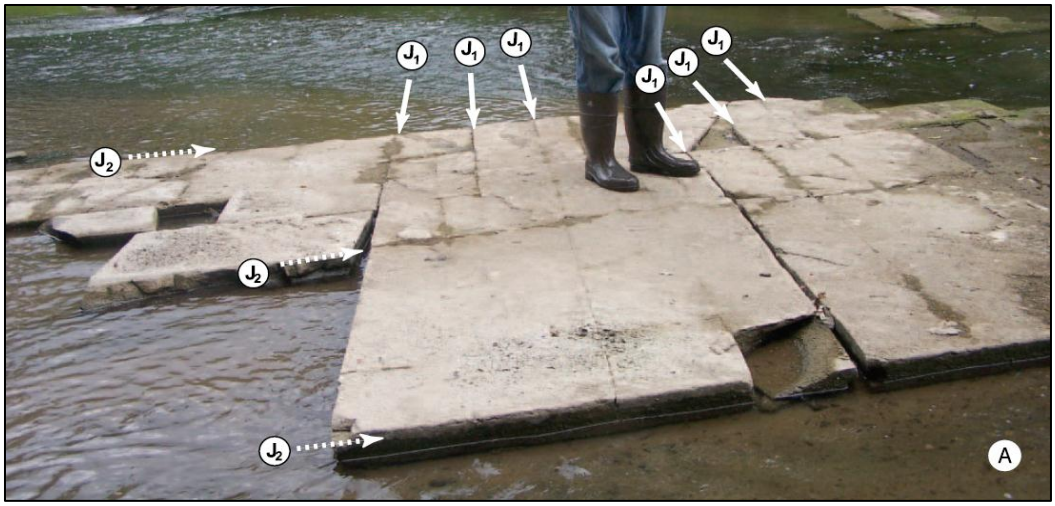

Figure 3.5 - The crosscutting joint sets, J_1 and J_2, in the Marcellus black shale in Oatka Creek, Le Roy, New York (from Engelder and Lash, 2009).

Two sets of joints, often referred as J_1 and J_2 in Figure 3.5, are systematically observed and cross cutting each other in the same bed in the Appalachian basin (Engelder and Geiser, 1980; Lash et al., 2004; Lash and Engelder, 2007, 2009). The NW J_1 set is more closely spaced than ENE J_2 set which exist more massively throughout the basin (Engelder et al. 2009).

Figure 3.6 - Tall and closely spaced J_1 joints at the contact (white dashed line) of the Dunkirk shale and underlying Hanover shale on Eighteenmile Creek (from Lash and Engelder, 2007). White bar is 1 m.

The J_1 set is of particular interest because its strike direction is approximately parallel to S_{Hmax} of the contemporary tectonic stress field. As observed in Figure 3.6, they are very tall and confined by the black shale above and gray shale beneath them (Lash and Engelder, 2007). In addition, these joints are very closely spaced compared to their heights. This observation is consistent with the observed deep-formed vertical joints driven by fluid loading (Fischer, 1995), which provides further evidence for natural hydraulic fracture mechanism (Ladeira and Price, 1981; Engelder and Fischer, 1996).

3.3.4 Very closely spaced fracture sets

The most accepted mechanisms for natural opening mode fractures are based on linear elastic fracture mechanics theory (Bai and Pollard, 2000; Olson, 2004, 2007).

Though the mechanical model validates some field observations, it fails to explain the low *S*/*T* ratio (Figure 3.7) in Range IV (Bai and Pollard, 2000).

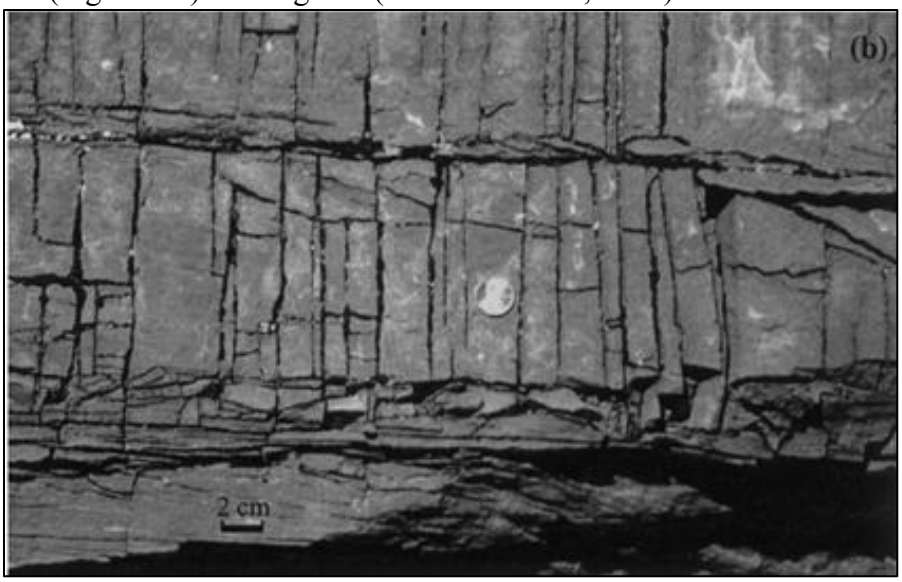

Figure 3.7 - Field observation (plane view) of closely spaced joints in the limestone layers of the Carmel Formation, Chimney Rock, Utah, with S/T ratio less than 0.8 (from Bai and Pollard, 2000).

These extreme low *S*/*T* ratios represent very closely spaced fracture sets in fields, such as the fracture sets in Asmari limestone in Iran, Portuguese greywacke and UK and those in limestone layers in south Israel (McQuillan, 1973; Price and Cosgrove, 1990; Becker and Gross, 1996) (Figure 3.8A). Hobbs (1967) proposed that more fracture infilling occurs possibly when the changes in internal fluid pressure or overburden stress drive more flaws to grow.

The measurement data on Figure 3.8A (Ladeira and Price, 1981) shows a very small fracture spacing in some fields, where the layer thickness is generally high, up to 12 m, and the measured S/T ratio is less than 0.11, almost close to zero. This is unlike most field studies conducted in thin beds; thus, Ladeira and Price (1981) studied the S-T relationship with the field data from McQuillan (1973). Instead of the linear

relationship which is observed in most thin layers, a bilinear correlation between S and T is observed (Figure 3.8B).

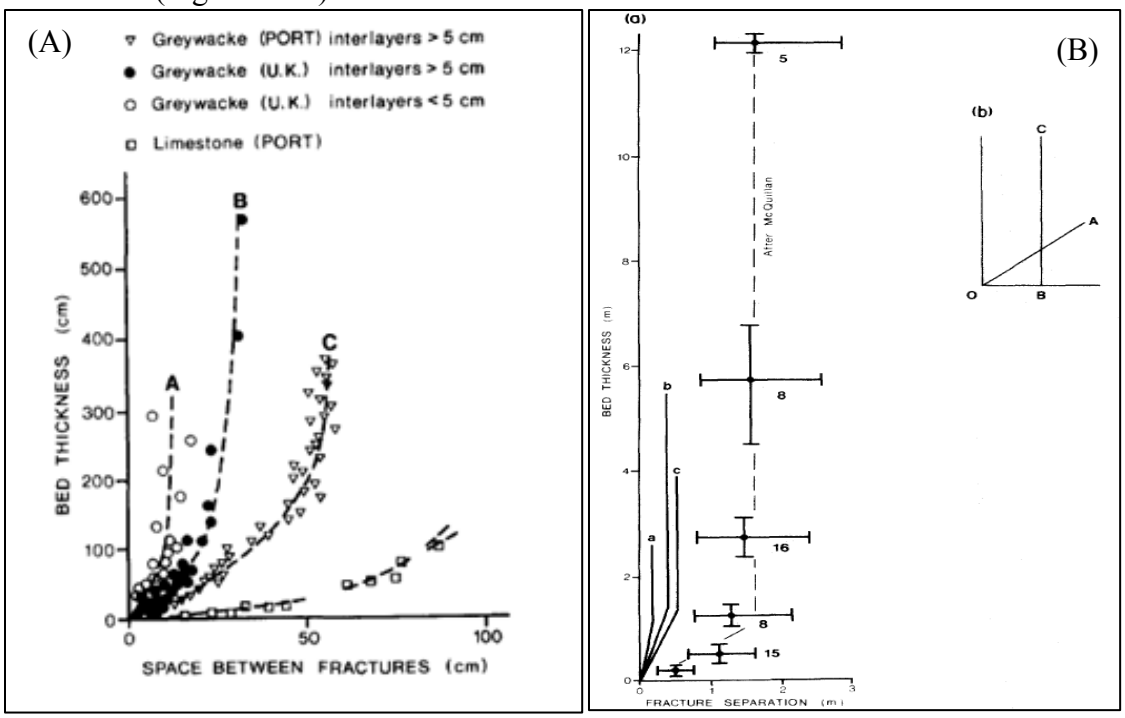

Figure 3.8 - (A) The relationship between bed thickness vs. fracture spacing for greywacke and limestones. Each point represents the mean of at least 50 readings. (B) Bilinear relationship between fracture spacing and bed thickness from field data in different rock types. The numbers are the number of groups of readings (from Ladeira and Price, 1981).

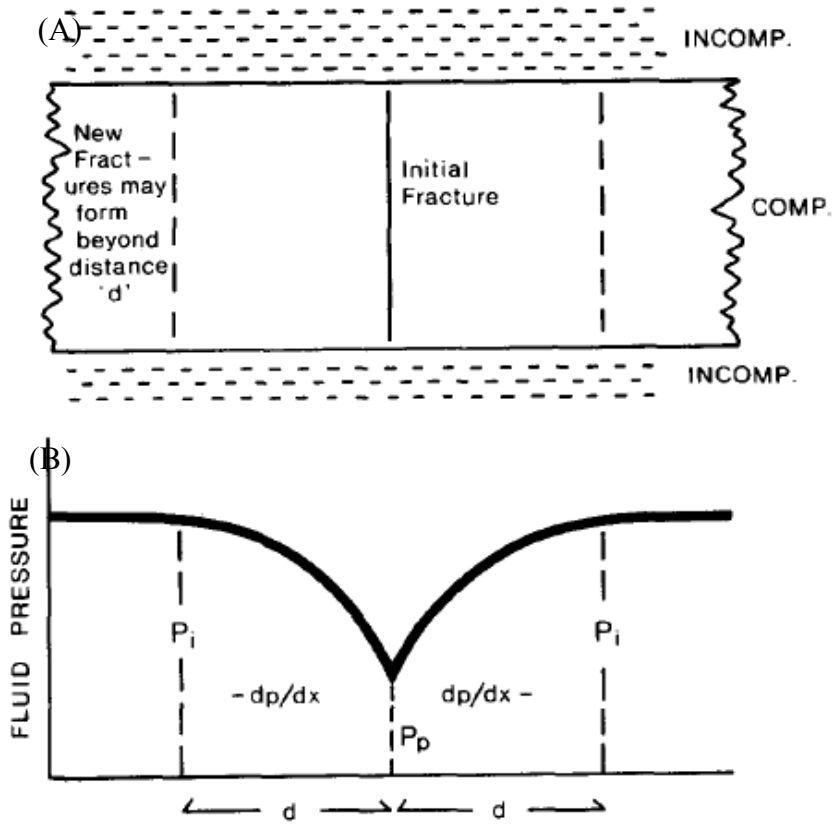

Figure 3.9 - (A) Demonstration of the position of initial fracture and possible new fractures forming beyond distance '*d*'. (B) Indication of the disruption in fluid pressure distribution caused by the existence of initial fracture. No fracture can develop within the distance '*d*' (from Ladeira and Price, 1981).

Natural hydraulic fracturing mechanism is proposed to explain the nonlinear *S-T* correlation in thick beds, where fracture spacing is independent of bed thickness (Ladeira and Price, 1981; Price and Cosgrove, 1990). It becomes important in thick beds because the fracture internal fluid pressure fails to remain constant during the propagating process. When a fracture propagates, the internal fluid pressure decreases, resulting in a fluid pressure gradient from low pressure inside the fracture to remote pressure value at a certain distance, *d* (Figure 3.9B). The fluid pressure of any fracture siting within the distance *d* will be affected. Other fractures located beyond the distance *d* will not be

influenced by the pressure gradient and are possibly able to grow and infill the unfractured area (Figure 3.9A). Both the fracture propagation rate and rock permeability affect the fluid pressure gradient in thick rock layers. The Greywacke beds, where low *S/T* ratio is observed, are much less permeable than limestone (Figure 3.8A); therefore, *d* is smaller around a growing fracture in Greywacke, allowing more flaws to grow to achieve a smaller fracture spacing. This field observation is consistent with the hypothesis of hydraulic fracture mechanism for very closely spaced natural fractures in low-permeability thick rock layers.

3.4 NEW POROELASTIC MODEL INCORPORATING MECHANICAL FRACTURE INTERACTION

One of the drawbacks of the Ladeira and Price's idea (1981) for permeability control of fracture spacing is that it did not include mechanical crack interaction or stress shadow effects. In Chapter 2, fluid flow has established strong influence on multiple NHF propagation, but the mechanical interaction between fractures is not considered. To better investigate the process of fluid flow and mechanical interaction, the non-interacting NHF model of Chapter 2 has been modified to include stress shadow effects.

This new geomechanical model incorporates two-dimensional, plane strain, displacement discontinuity method (2D DDM) (Crouch and Starfield, 1983), where a fracture is represented as a series of line elements connected end to end. This model is coupled with the 2D finite difference diffusivity solution of Chapter 2.

3.4.1 Model description

Unlike the finite difference and finite element methods which divide the whole region into a network of elements, the boundary element method only divides the boundary contour into an array of elements (Crouch and Starfield, 1983). This results in a

simpler solution for the discontinuous displacement for each element. Given a single curved crack in an infinite elastic body as shown in Figure 3.10, the crack is divided into *N* elements joined end to end. Each element is a straight line and its position and orientation can be described with respect to the *x, y* Cartesian coordinate system. Boundary conditions, either displacement or stress, are also prescribed for each boundary element and a system of algebraic equations are set up correspondingly to find the discontinuity solution that satisfies these boundary conditions.

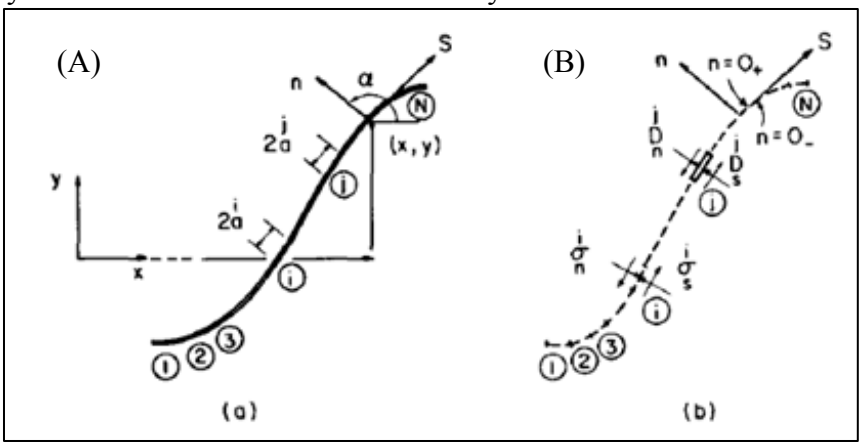

Figure 3.10 - Representation of (A) a crack by N elemental displacement discontinuities; (B) a single elemental displacement discontinuity at the j[th] segment of the crack (from Crouch and Starfield, 1983).

Based on the principle of superposition, the normal and shear stresses (σ_n^i and σ_s^i, separately) at i^{th} element are influenced by all the other elements in the body. The influence of the j^{th} element's opening and shearing displacement discontinuities (D_n^j and D_s^j, respectively) on normal and shear stresses at the i^{th} element, are given by Crouch (1979) as

$$\sigma_s^i = \sum_{j=1}^{N} A_{ss}^{ij} D_s^j + \sum_{j=1}^{N} A_{sn}^{ij} D_n^j \,, \tag{3.6a}$$

$$\sigma_n^i = \sum_{j=1}^{N} A_{ns}^{ij} D_s^j + \sum_{j=1}^{N} A_{nn}^{ij} D_n^j, \tag{3.6b}$$

$$i = 1 \; to \; N,$$

where A_{ss}^{ij}, A_{sn}^{ij}, A_{ns}^{ij} and A_{nn}^{ij} are the influence coefficients, depending on the position and orientation of each element in the system.

Once the displacement discontinuity D_n^i and D_s^i are calculated, fracture propagation direction can be expressed as

$$\theta^i = 2\tan^{-1}\left(\frac{1}{4}\left(K_I^i/K_{II}^i \mp \sqrt{\left(K_I^i/K_{II}^i\right)^2 + 8}\right)\right), \tag{3.7}$$

and the mode I and II stress intensity factors can be calculated as

$$K_I^i = 0.806\left(\frac{E\sqrt{\pi}}{4(1-\gamma^2)\sqrt{\Delta a}}\right)D_n^i, \tag{3.8a}$$

$$K_{II}^i = 0.806\left(\frac{E\sqrt{\pi}}{4(1-\gamma^2)\sqrt{\Delta a}}\right)D_s^i. \tag{3.8b}$$

When K_{II} is zero, θ is equal to 0, which indicates fracture planar propagation in the pure opening mode (mode I). Previous simulation and experimental work showed that when the remote differential stress ($S_{Hmax} - S_{hmin}$) parallel to the crack is large, the fracture propagation path tends to be straight (Cotterell and Rice; 1980; Olson, 1989; Thomas and Pollard, 1993). For simplicity, this study will focus on the straight propagation paths only.

In the absence of fluid flow effects, subcritical crack growth has been used to estimate natural fracture propagation velocity. Subcritical propagation obeys the power-law function (Atkinson, 1984; Swanson, 1984) described in equation (2.4) with $K_I = K_{tip}$. K_{tip} is calculated as

$$\mathrm{K_{tip}^i} = \cos^2\left(\frac{\theta^i}{2}\right)\left[\mathrm{K_I^i}\cos\left(\frac{\theta^i}{2}\right) - 3\mathrm{K_{II}^i}\sin\left(\frac{\theta^i}{2}\right)\right]. \tag{3.9}$$

During the time increment Δt, the i[th] crack element will grow the length of

$$\Delta L^i = V^i \times \Delta t. \tag{3.10}$$

Once it reaches the prespecified growth increment length, one boundary element will be added to the i^{th} crack element to represent one growth event.

Olson (1997, 2004) proposed an important addition to the 2D DDM model to account for 3D stress shadow effects for laterally propagating fractures. Based on 2D plane strain equations from Pollard and Segall (1987), a factor, G, is used to represent the fracture height effect on stresses, dependent on fracture layer thickness h, distance d_{ij} and two parameters α, β:

$$G^{ij} = 1 - \frac{d_{ij}^{\beta}}{\left[d_{ij}^2 + (h/\alpha)^2\right]^{\beta/2}}. \quad (3.11)$$

For a very long fracture, the mechanical interaction distance scales with the fracture height h. When d_{ij} is much larger than h, G_{ij} goes to zero, leading to little mechanical interaction between widely spaced fractures. When d_{ij} is much smaller than h, G_{ij} is close to 1, indicating fracture length becomes the dominating factor which controls the mechanical interaction distance. The choice of α and β are $\alpha = 1$ and $\beta = 2.3$ in the following sections (Olson, 1997, 2004). Appendix C contains the details in coupling P3D DDM with fluid model and the associated modeling flow chart for Chapter 3.

3.5 MODEL VERIFICATION

The implication of the pseudo-3D correction factor G was validated against published results from Olson (2004) and Wu and Olson (2012). For a single fracture with fixed height of 2 m and uniformly distributed internal pressure, the relationship between the normalized aperture and normalized length over height is plotted in Figure 3.11. G-factor proposed by Olson (2004) is used in the numerical model to approximate the layer thickness effect (α = 2 and β = 2). A good match is obtained between the numerical results and published results.

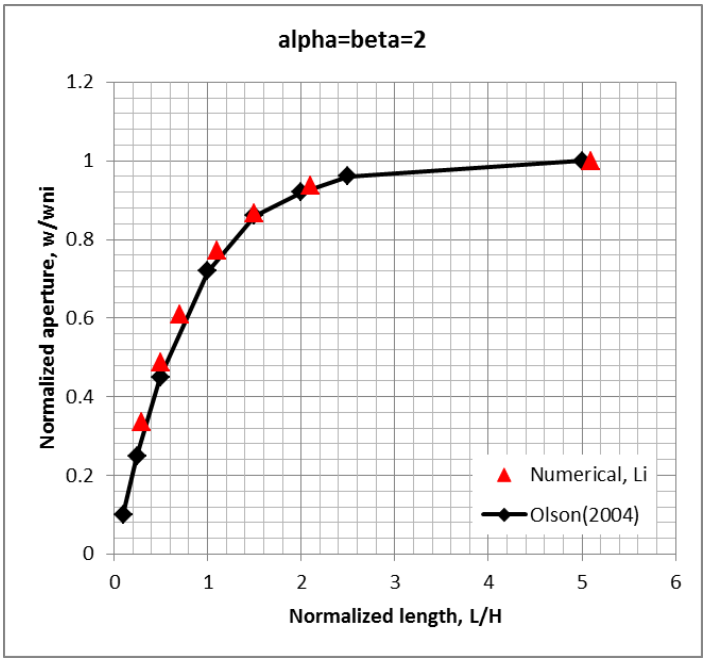

Figure 3.11 - The normalized fracture aperture vs. normalized length for a single isolated fracture.

Another verification is performed for a set of three parallel fractures (Germanovich and Astakhov, 2004; Meyer and Bazan, 2011). These fractures with the same half-length of 1.5 m and fixed height of 3 m are propagating under constant internal pressure. Fracture spacing is the variable changing from 0.5 to 10 m.

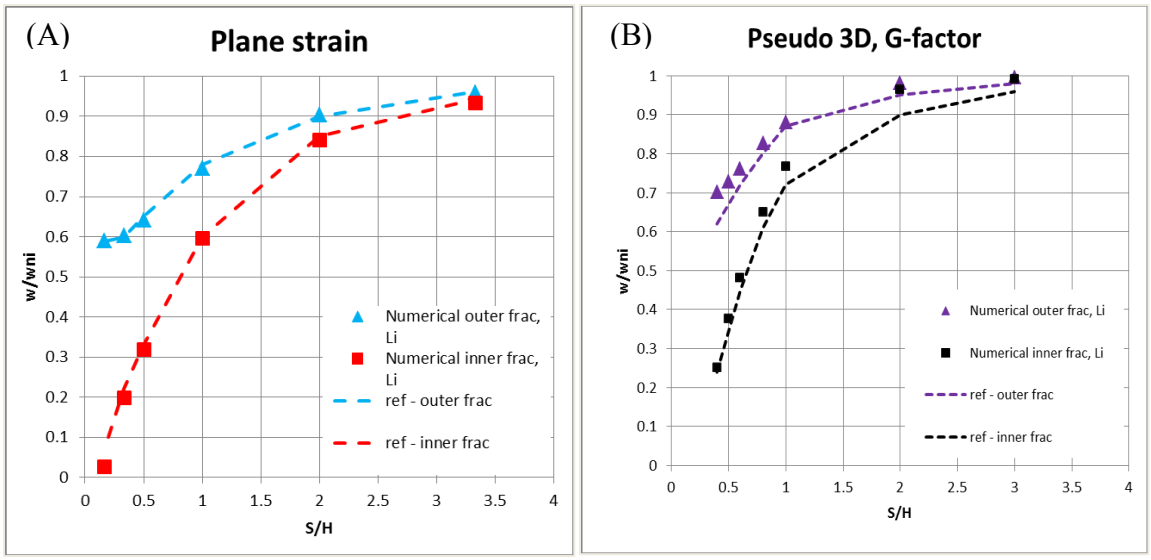

Figure 3.12 - The normalized aperture for outer and inner fracture vs. fracture spacing to layer thickness ratio under (A) plane strain; (B) Pseudo 3D condition.

Results in Figure 3.12 show that the newly developed poroelastic model produces accurate and consistent results for multiple fracture propagation. Additional verification cases are illustrated in Appendix D. In the next section, this new model will be applied to study how the permeability and some other factors affect the fracture growth. Their influences on fracture pattern development will be discussed in Chapter 4 in detail.

3.6 RESULTS

Pure opening mode (mode I) cracks are considered in all the application cases. The loading strain history is prescribed and kept the same for all the cases. The values of some basic parameters are listed in Table 3.1. Several key variables will be investigated for multiple natural hydraulic fracture propagation: reservoir permeability, fracture subcritical growth index, fracture spacing to layer thickness ratio, the initial crack half-length and boundary conditions.

Table 3.1 Values of some basic parameters used in the new poroelastic P3D DDM model.

Parameters	**Values**
Young's modulus, E	20 GPa
Poisson's ratio, υ	0.2
Fracture toughness, K_{IC}	1.5 $MPa \cdot m^{1/2}$
Fluid compressibility, C_t	0.58 GPa^{-1}
Fluid viscosity, μ	1 cP
Reservoir porosity, $\emptyset$	0.1
Initial fracture half-length, a	0.2 m

3.6.1 Closely spaced fractures under plane strain condition

To examine fracture spacing development, a series of simulations were performed using a common basic parameter set (Table 3.1). The first example starts with a set of 38 flaws regularly spaced 1 m in a 10 m thick layer. The traverse distance is 40 m. Subcritical index is 20 and a constant strain of 5×10^{-5} is applied to initiate the fracture propagation. The reservoir boundary is at constant pressure of 10 MPa and the permeability varies from 1 D to 1 nD. The fracture propagations differ in different permeable rocks, resulting in different final fracture spacings.

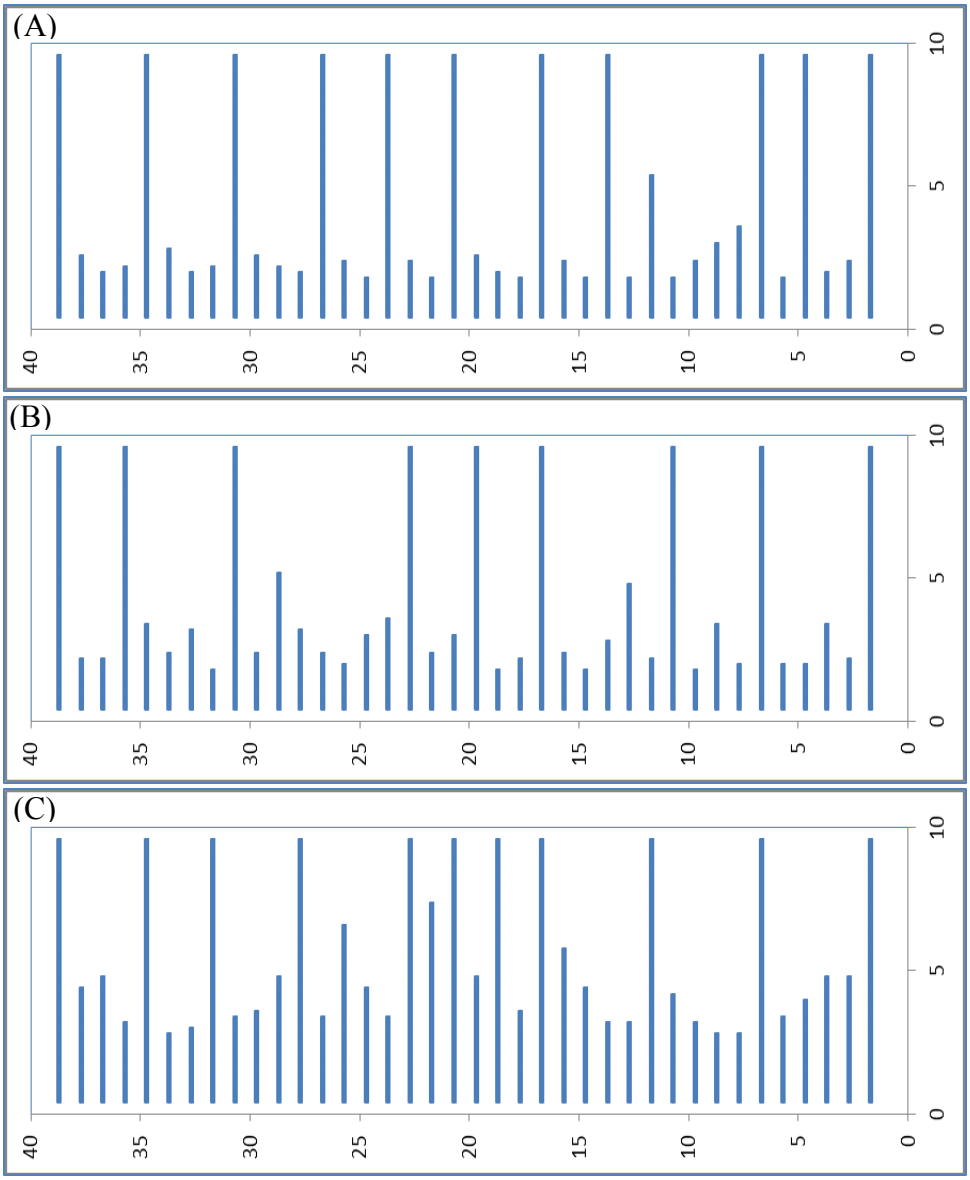

Figure 3.13 - Fracture trace map in rocks with permeability of (A) 1 D, (B) 1 mD, (C) 1 nD at 13.2 my propagation time under plane strain condition. The fractured region is bounded by $0 < x < 10$ and $0 < y < 40$, where x is the fracture parallel direction.

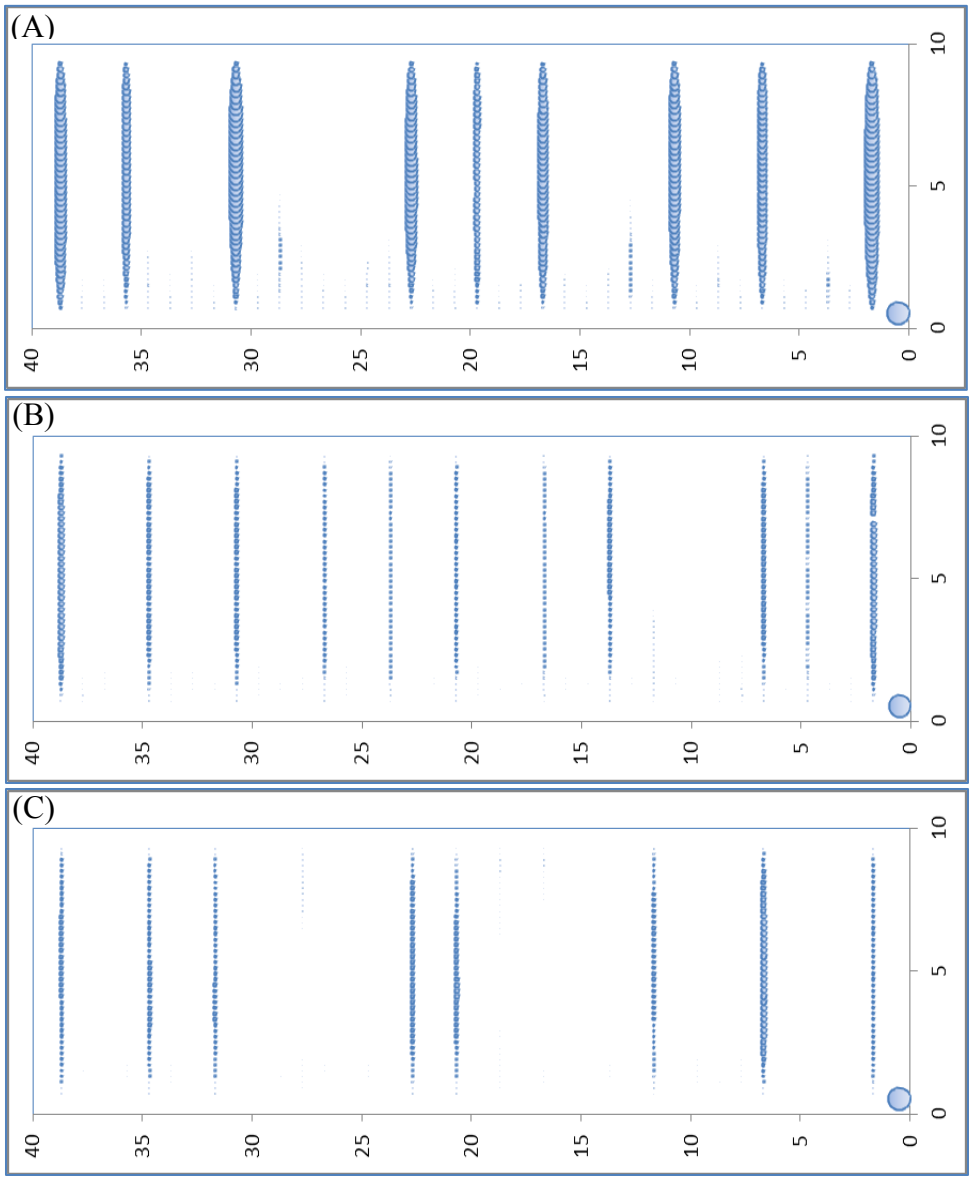

Figure 3.14 - Fracture aperture map in rocks with permeability of (A) 1 D, (B) 1 mD, (C) 1 nD at 13.2 my propagation time under plane strain condition. The diameter of the reference bubble is 1×10^{-3} m. The fractured region is bounded by $0 < x < 10$ and $0 < y < 40$, where x is the fracture parallel direction.

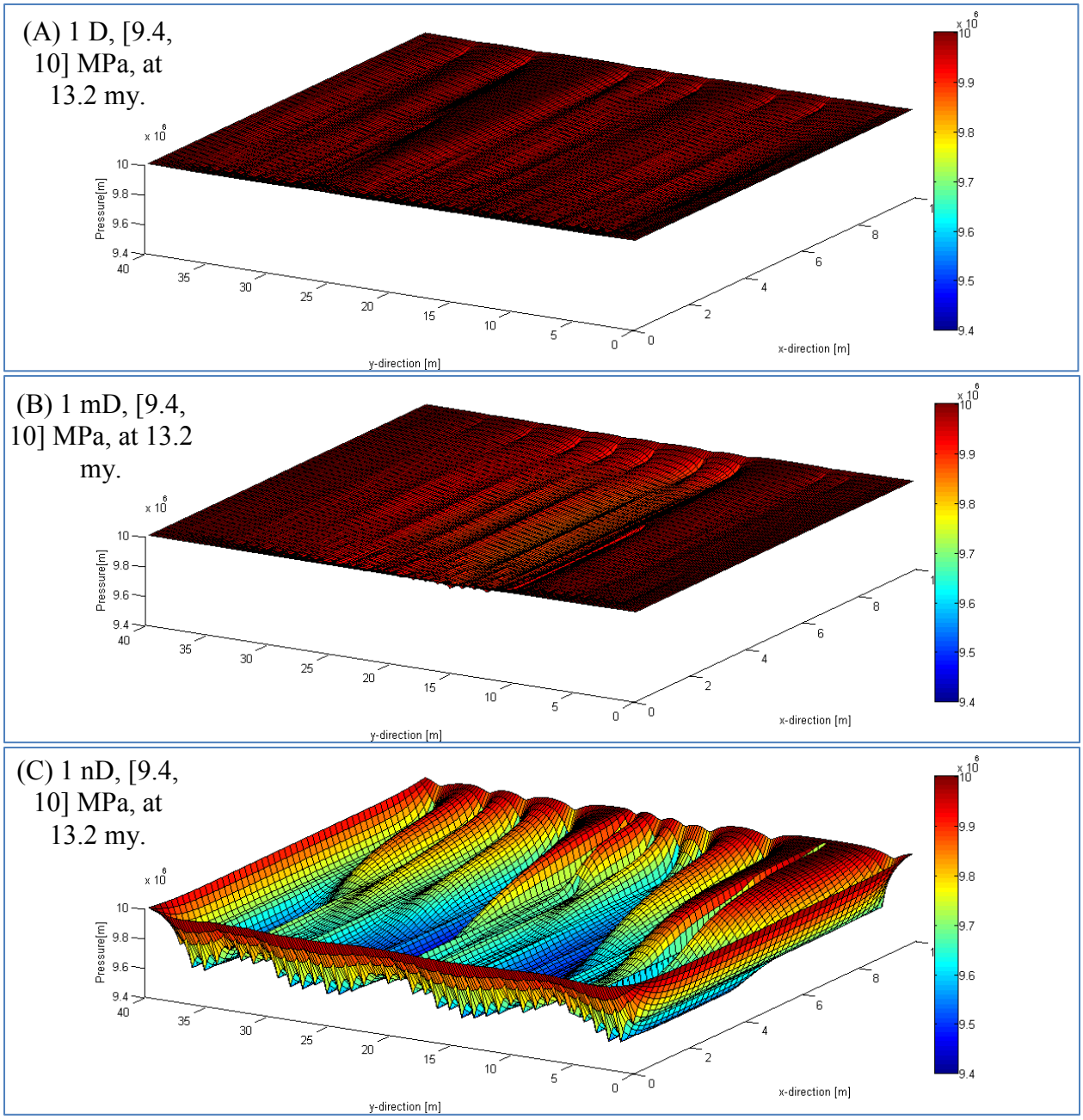

Figure 3.15 - Pressure profiles in rocks with permeability of (A) 1 D, (B) 1 mD, (C) 1 nD at 13.2 my propagation time under plane strain condition.

Figures 3.13 and 3.14 are the fracture trace map and aperture map for the set of 38 fractures after a growth period of 13.2 my in 1 D, 1 mD and 1 nD rocks. The fractures developed in high-permeability rocks (1 D) are more widely spaced to each other and their apertures are large. In low-permeability rocks (1 nD), more fractures propagate and they are more closely spaced to each other, though the fractures are relatively skinnier compared to those in 1 D rocks. Fracture aperture depends on the internal fluid pressure, which is correlated to the fluid flow properties in the host rock. The 3D pressure profiles at the growth timing of 13.2 my are shown in Figure 3.15, where the average pressure in 1 D rock is approximately at 10 MPa (Figure 3.15A) and it is only 9.5 MPa in 1 nD rock (Figure 3.15C).

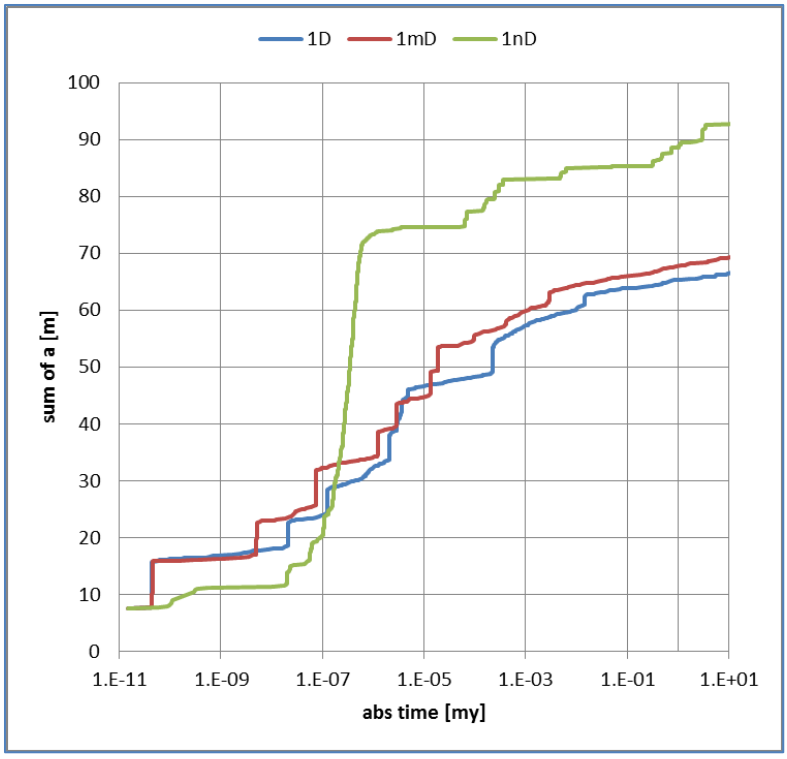

Figure 3.16 - The summation of fracture half-length vs. fracture propagation duration in rocks with permeabilities of 1 D, 1 mD and 1 nD at 13.2 my propagation time under plane strain condition.

Figure 3.16 represents the total fracture half-length versus fracture propagation duration for different permeability rocks. In the early stage when growth timing is less than 0.1 year, fracture propagation is slower in low-permeability rock. Beyond 0.1 year, more fractures propagate in low-permeability rock than the high-permeability case, leading to a higher total fracture half-length at the later stage.

Table 3.2 Fracture spacing measured along the scanning line (intersecting the mid-point of x-axis)

Scanning range along y-axis	**1 D**	**1 mD**	**1 nD**
0 ~ 40 m	4 m	3.1 m	2.7 m
5 ~ 35 m	3 m	3 m	2.3 m
10 ~ 30 m	2.9 m	2.9 m	2 m
15 ~ 25 m	**2.5 m**	**2.5 m**	**1.25 m**

At 13.2 my, the fracture spacing is calculated for the patterns in Figure 3.13 by line method and the results are summarized in Table 3.2. The position of the scanline is chosen at the mid-point of bed thickness and perpendicular to the fracture growth direction. Four different scanning ranges are chosen along the traverse direction (y-axis): 0 ~ 40 m means the whole traverse distance are scanned, while 15 ~ 25 m means only the center 10 m area along the traverse distance is scanned to avoid the boundary effect. Generally, the fracture spacing is smaller in less permeable rocks no matter which regime along the traverse distance is examined. For the scanning range from 15 to 25 m, the fracture spacing is 1.25 m in 1 nD rock and 2.5 m in 1 mD and 1 D rock. There is no difference in fracture spacing for permeability range of 1 D to 1 mD. The results show the more fractures propagate in less permeable rocks and the fracture spacing is high-permeability rock can be twice that in low-permeability rock. This indicates hydraulic fracturing mechanism can lead to the closely-spaced fracture pattern in low-permeability rocks.

3.6.2 Closely-spaced fractures under pseudo 3D condition

The case study in section 3.6.1 did not consider the fracture height effect. The developed pseudo 3D model will be used in this section to study the fracture spacing to layer thickness ratio (S/T ratio) for a set of nine stratabound fractures. The nine flaws are evenly spaced at a distance of 2 m within a reservoir area with size of 10 m by 40 m. A strain of 5×10^{-5} is applied in perpendicular to flaw propagation direction to initiate their growth. The initial fluid pressure is equal to the remote stress in y-direction everywhere in the reservoir. The settings of other parameters are shown in Table 3.2.

3.6.2.1 Permeability effect: fracture spacing versus layer thickness (n = 20)

First, the reservoir permeability effect on S/T ratio is examined by evaluating fracture propagation in 1 nD and 1 D rock with layer thickness (T) range from 2, 4 to 8 m. Subcritical index is chosen at 20 and reservoir boundary is at constant pressure condition.

High-permeability rock (k = 1 D): fracture pattern vs. layer thickness (n = 20)

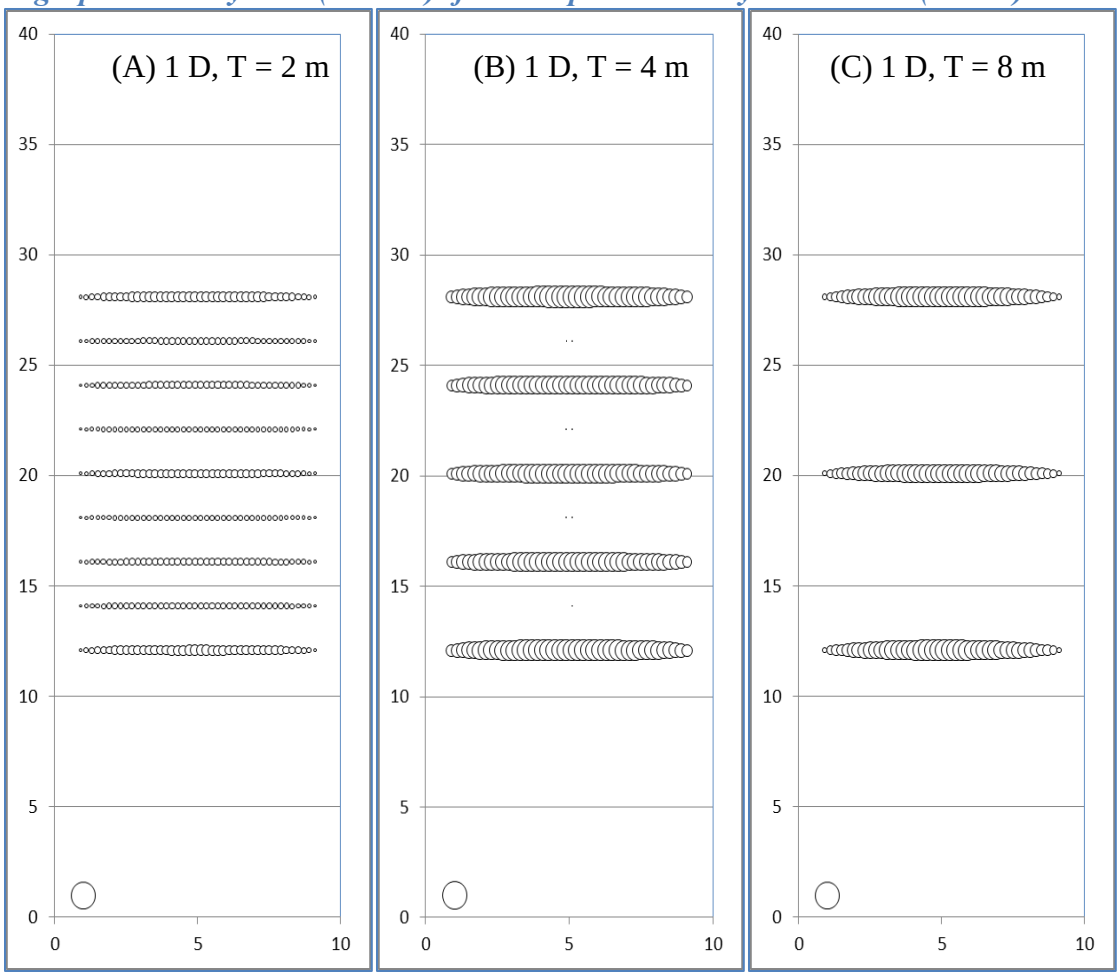

Figure 3.17 - Fracture aperture maps in 1 D rock with layer thickness of (A) 2 m, (B) 4 m, (C) 8 m at 13.2 my propagation time. The fractured region is bounded by $0 < x < 10$ and $0 < y < 40$, where x is the fracture parallel direction.

Low-permeability rock (k = 1 nD): fracture pattern vs. layer thickness (n = 20)

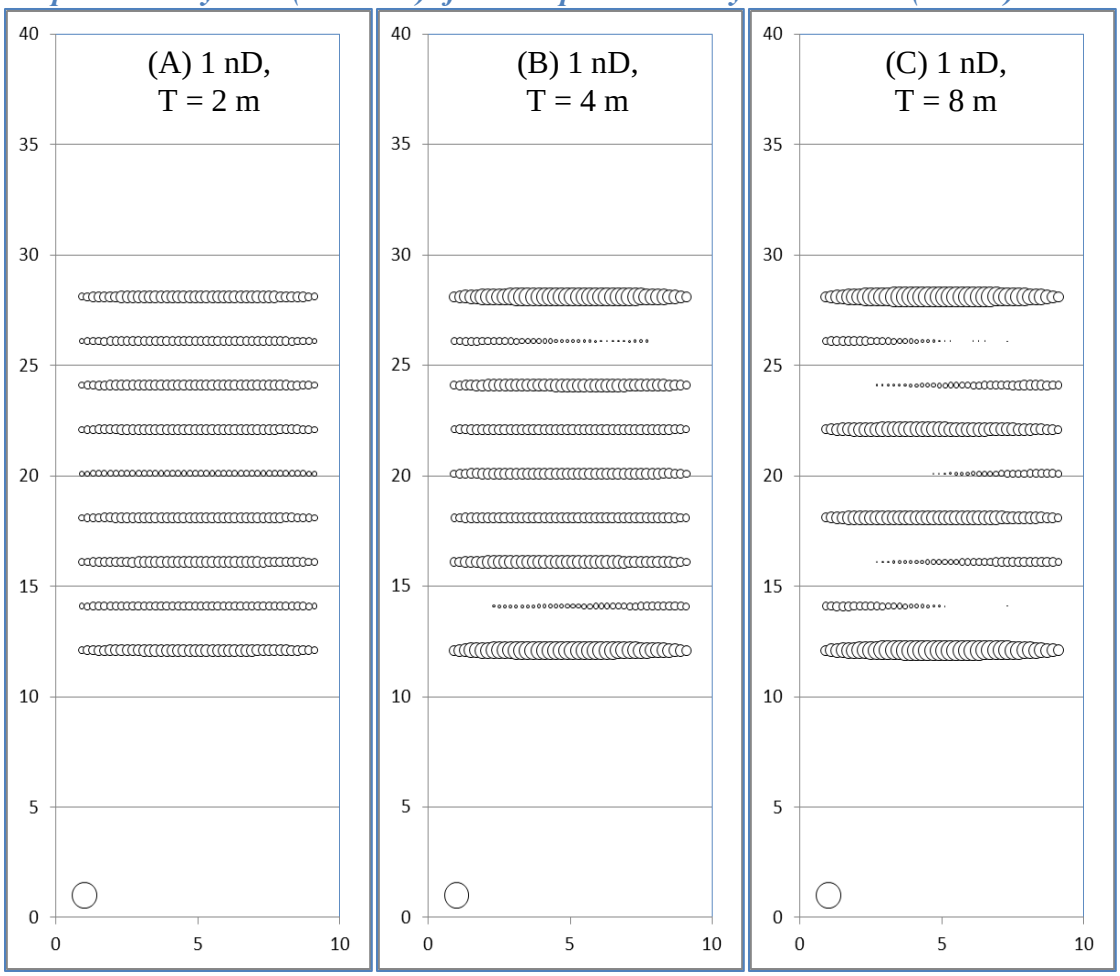

Figure 3.18 - Fracture aperture mapw in 1 nD rock with layer thickness of (A) 2 m, (B) 4 m, (C) 8 m at 13.2 my propagation time. The fractured region is bounded by $0 < x < 10$ and $0 < y < 40$, where x is the fracture parallel direction.

Figure 3.18 shows the fracture aperture maps developed in 1 D rock with the layer thickness varying from 2, 4 to 8 m at the growth timing of 13.2 my. For the thin bed case (T = 2 m), all nine fractures developed to the full length (around 8 m). However, in thicker bed case, few fractures can grow to the full length, only five fractures in T = 4 m case and three fractures in T = 8 m case. The patterns in 1 D rock demonstrate clearly the relative fracture spacing scales with the layer thickness (T). The fracture spacing is also

an indication of the size of stress shadow around the developed fractures. No additional fractures can propagate within this distance. These results are consistent with the conclusions from a previous geomechanial model which assumes fracture internal pressure is always constant (Olson, 2004). This assumption is valid for high-permeability rocks because high permeability ensures fast pressure recovery and maintains the fracture internal pressure roughly constant.

The final fracture patterns are quite different in low-permeability rock (1 nD) as shown in Figure 3.18, where the fracture spacing does not scale with the layer thickness (T). In the thin bed (T = 2 m), all nine fractures reach the boundary. In thicker beds, fewer fractures can grow to full length and their apertures are different based on their locations inside the reservoir. For example, in the 8 m bed, all nine fractures propagate, but only four fractures grow to full length. The other five fractures, which are located in the interior area of the four long fractures, still propagate, but there are slightly shorter and skinner than the four long fractures. The low permeability of the rock slows down the fluid pressure recovery rate inside the long fractures; thus, the stress shadow effect is less dominant and the fluid depletion zone is relatively smaller. This enables more neighboring fractures to grow. Meanwhile, the longer the fracture grows, the less driving stress is required. Therefore, less fluid interference and weaker mechanical interaction exist between multiple fractures in low-permeability rock. This also illustrates that more fracture propagations are possible in low-permeability rock, which lead to a small S/T ratio in thick bed.

High-permeability rock (k = 1 D): Pressure profiles

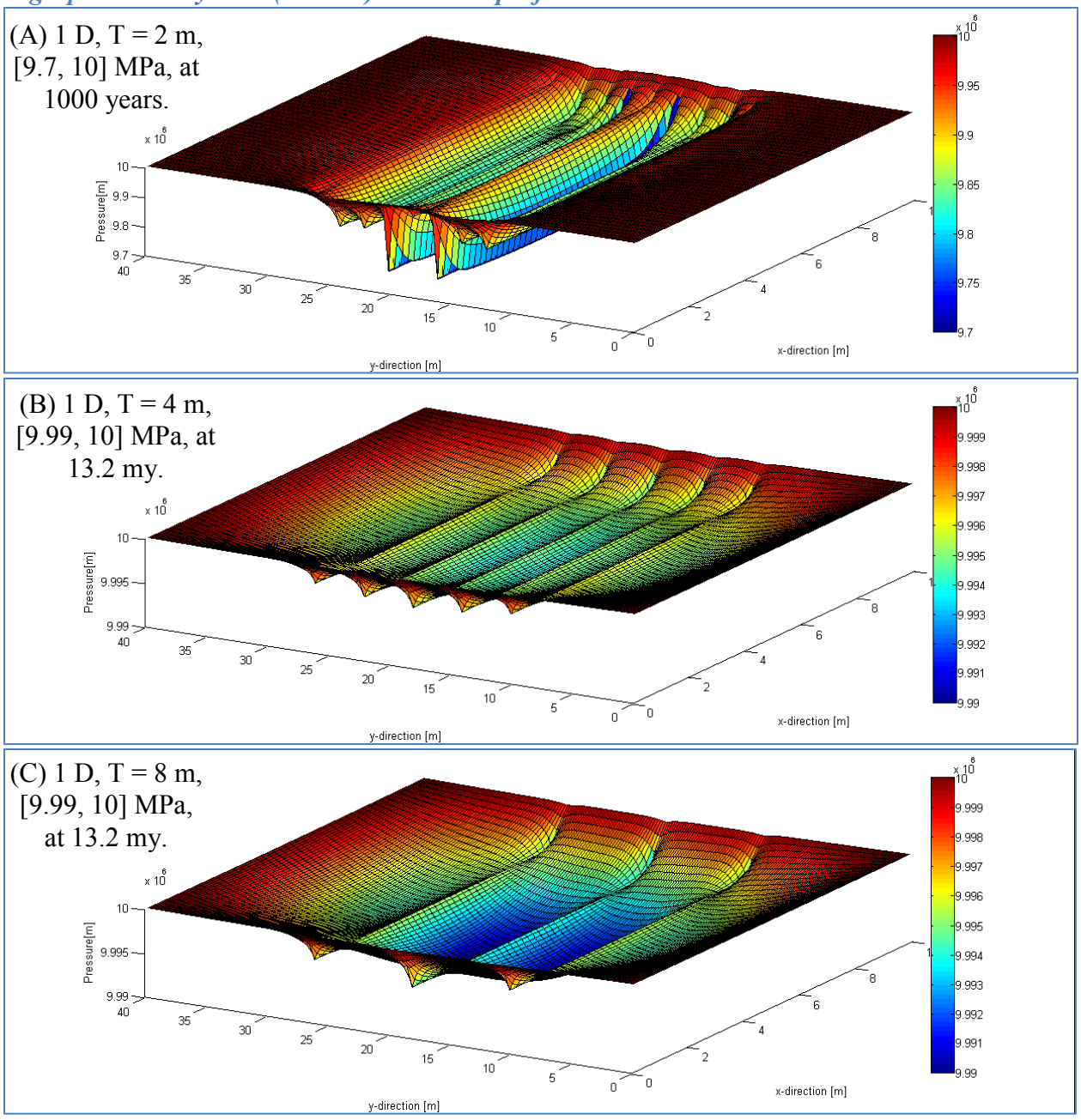

Figure 3.19 - Pressure profiles in 1 D rock with layer thickness of (A) 2 m at 1000 years, range as [9.7, 10] MPa, (B) 4 m at 13.2 my range as [9.99, 10] MPa, (C) 8 m at 13.2 my, range as [9.99, 10] MPa.

Low-permeability rock (k = 1 nD): Pressure profiles

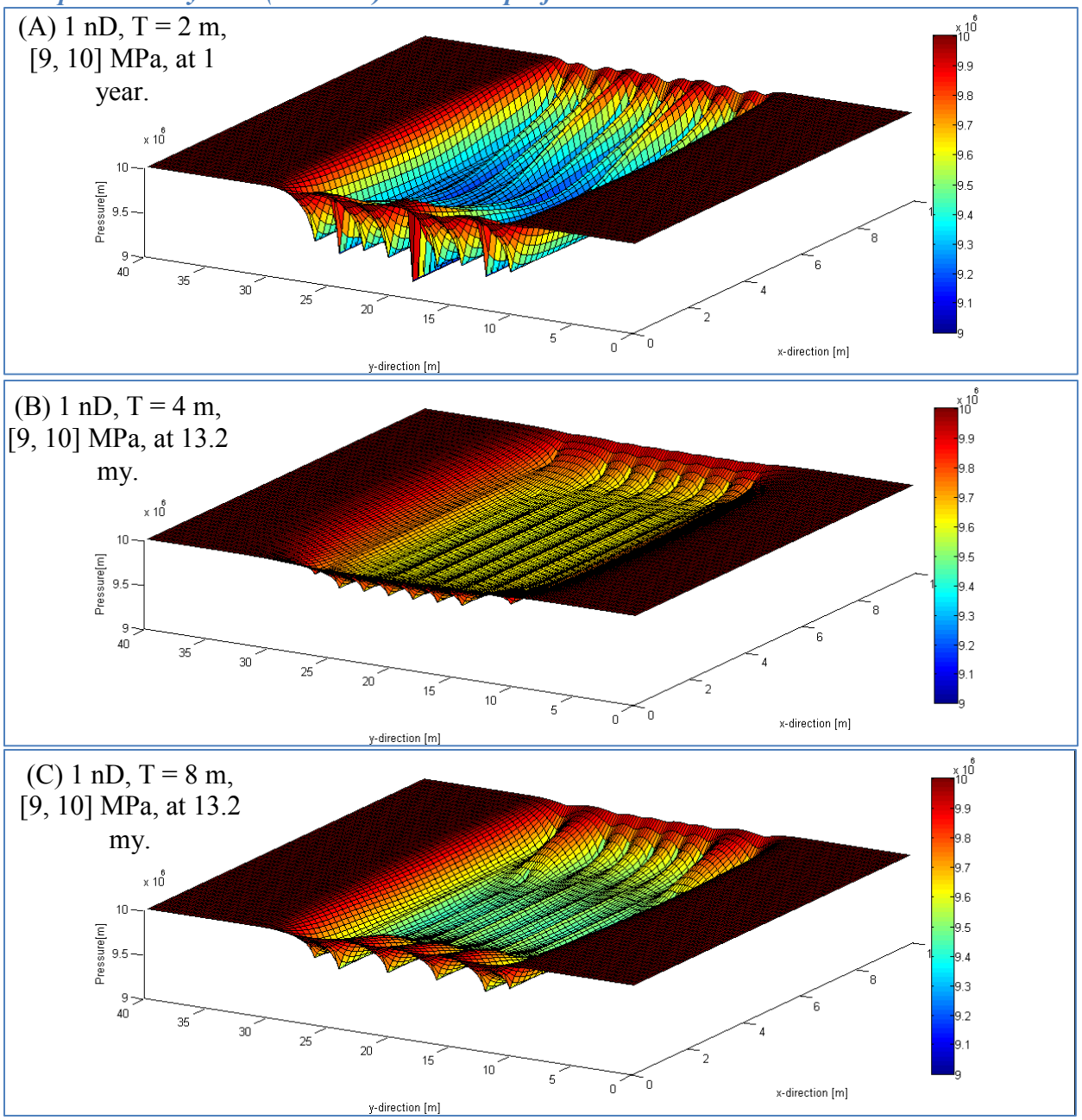

Figure 3.20 - Pressure profiles in 1 nD rock with layer thickness of (A) 2 m at 1 year, (B) 4 m at 13.2 my, (C) 8 m at 13.2 my. Pressure ranges are all [9, 10] MPa.

The pressure profiles are illustrated in Figures 3.19 and 3.20, corresponding to the fracture patterns shown in Figures 3.17 and 3.18. Generally, lower average pressure and smaller fluid drainage area are observed in low-permeability rocks than the high-permeability cases. In low-permeability rock, the low fluid pressure slows down fracture propagation; meanwhile, the small fluid drainage area allows more fractures to propagate at a closer distance. On the other hand, in high-permeability rocks, fractures can grow faster because of the fast fluid recovery rate, which leads to large pressure drainage distance and significant stress shadow area around the long fractures, which arrest any neighboring fractures' propagation. Therefore, the fracture propagation and spacing are significantly controlled by the combined effects from fluid flow and mechanical interactions.

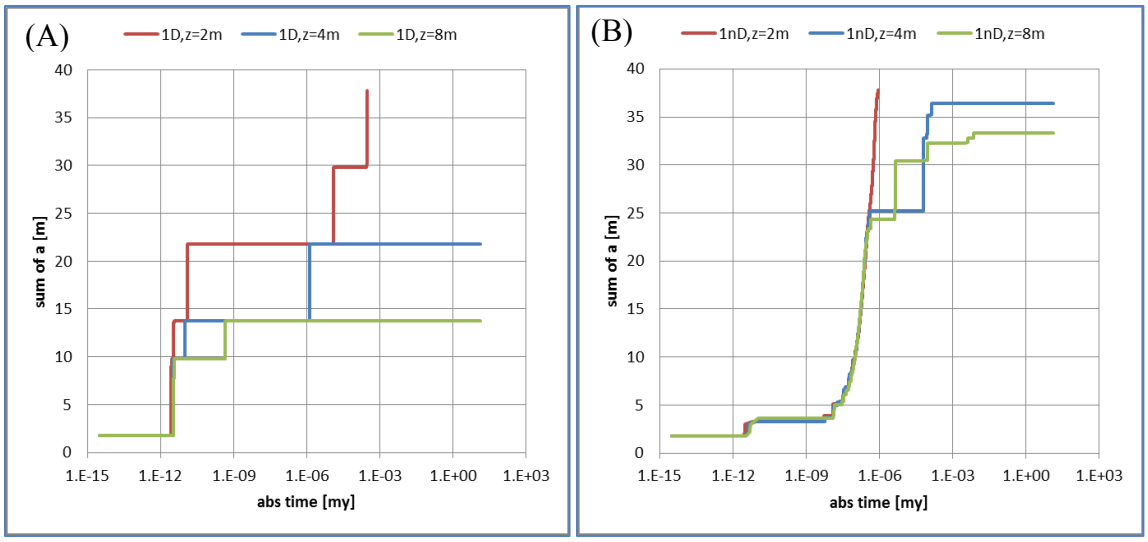

Figure 3.21 - The summation of fracture half-length vs. crack propagation duration for (A) 1 D, and (B) 1 nD rocks. The layer thickness varies from 2, 4 to 8 m. The subcritical index n is 20.

Figure 3.21 exhibits the total fracture half-length versus growth timing for different *T* cases. Each curve corresponds to a case with specific layer thickness *T*. In 1

nD rock (Figure 3.21B), the divergence between the three curves shows up when the total fracture half-length reaches 25 m. Before that point, the fracture growth is insensitive to the layer thickness *T*. All the fractures are propagating at similar pace with no extreme long fracture dominating the whole pattern. Beyond this point, as *T* increases, the increase in total fracture half-length slows down. Eventually, some shorter fractures stop propagation for the large *T* case. In 1 D rock (Figure 3.21A), the growth curves vary dramatically from those for 1 nD case. The divergence of three curves appears at total fracture half-length of 10 m, corresponding to the stage when two exterior fractures reach the boundary. Beyond that point, fewer fractures can grow in thicker beds due to the stress shadow effect.

Therefore, for a given population of starting cracks, high-permeability rocks are expected to have a few extremely long and fat fractures with a majority of very short and skinny cracks which are unable to propagate. In contrast, in low-permeability rocks, majority of the fractures can grow at a similar pace and a larger total fracture half-length can be achieved. In sum, hydraulic fracturing mechanism explains the possibility of generating the very closely spaced fracture patterns in low-permeability rocks with large layer thickness.

3.6.2.2 Permeability effect: fracture spacing versus subcritical index (*T* = 4 m)

Natural fractures are generally subcritical growing under long term loading and chemically- active environments. Subcritical index controls the crack growth velocity. In order to study its effect on fracture spacing, subcritical index (*n*) is changed from 1, 20 to 100 for 1 nD and 1 D cases. Layer thickness (*T*) is maintained at 4 m.

High-permeability rock (k = 1 D): fracture spacing versus subcritical index (T = 4 m)

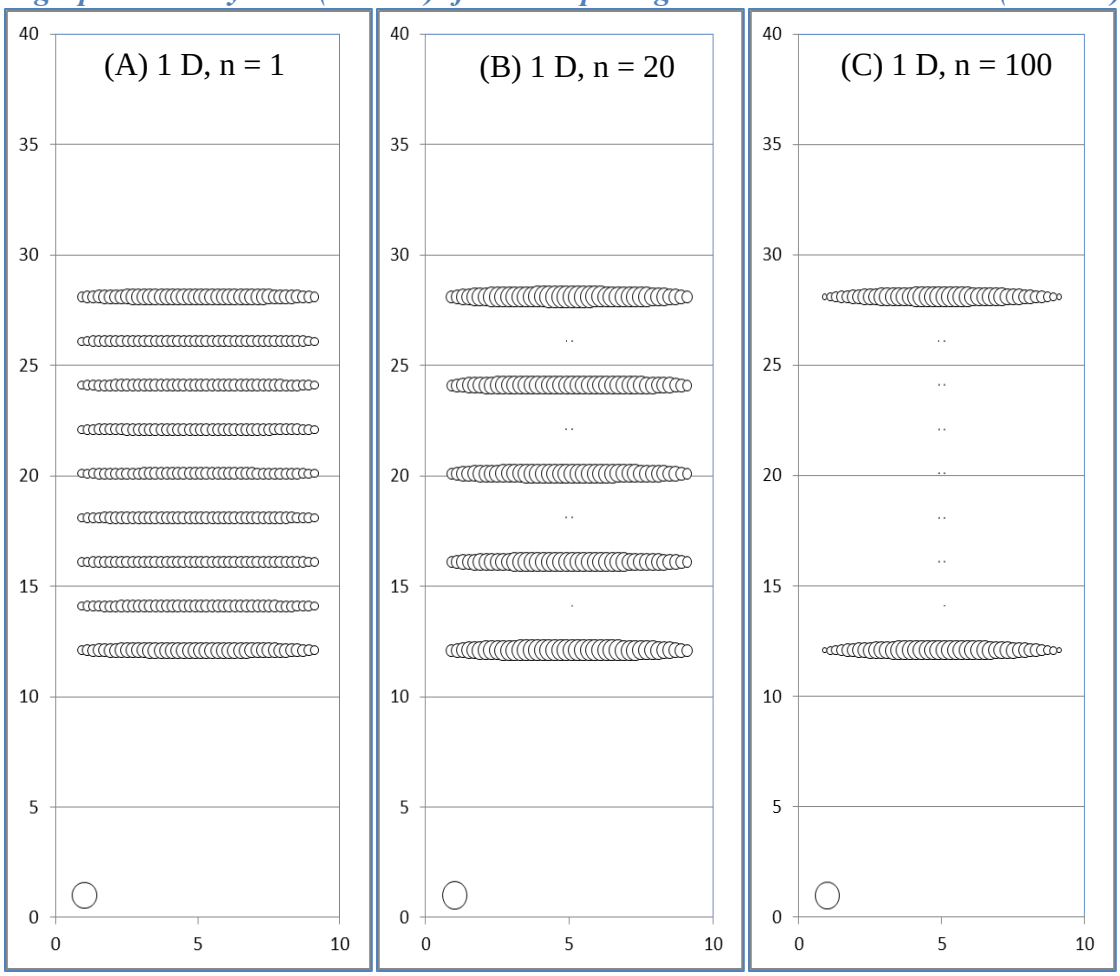

Figure 3.22 - Fracture aperture maps in 1 D rock with subcritical index (n) of (A) 1, (B) 20, (C) 100 at 13.2 my propagation time. The fractured region is bounded by $0 < x < 10$ and $0 < y < 40$, where x is the fracture parallel direction. The small dots represent the unpropagated fracture segments.

Low-permeability rock (k = 1 nD): fracture spacing versus subcritical index (T = 4 m)

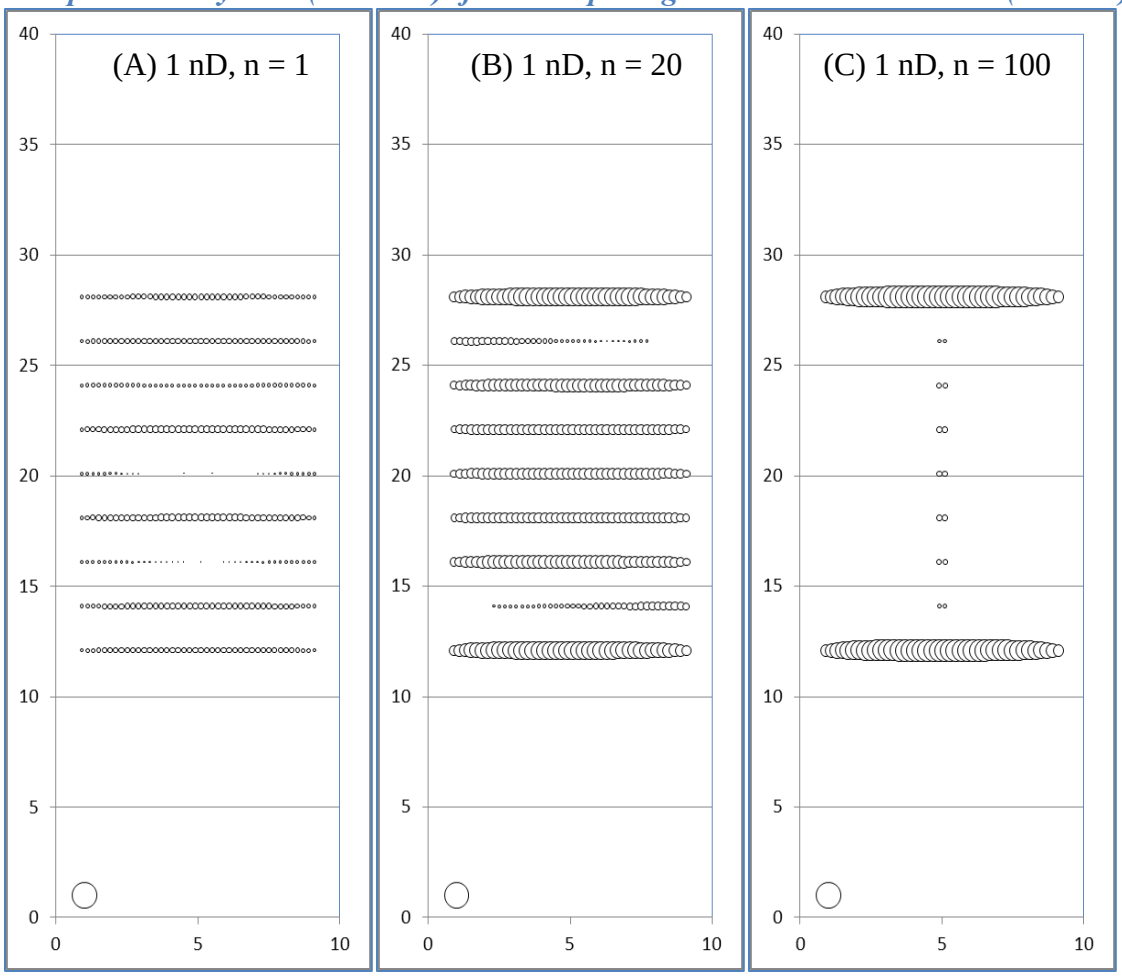

Figure 3.23 - Fracture aperture maps in 1 nD rock with subcritical index (*n*) of (A) 1, (B) 20, (C) 100 at 13.2 my propagation time.

The fracture aperture maps for various *n* cases are shown in Figure 3.22 for high-permeability rock (1 D) and Figure 3.23 for low-permeability rock (1 nD). For both 1 D and 1 nD cases, fewer cracks grow when the subcritical index increases from 1 to 100. In 1 D rock, there are nine, five and three fractures grow to full length, corresponding to the subcritical index of 1, 20 and 100 respectively (Figure 3.22). The stress shadow and fluid depletion areas created by the long fractures limit other fracture's propagation. The

influences become more significant when the subcritical index is higher. This leads to a larger fracture spacing of the pattern with fewer long and wide fractures and more unpropagated fractures for high *n* cases.

In 1 nD rock, the fracture pattern looks similar to that for 1 D case when $n = 100$, but quite different when $n = 1$ and 20. When $n = 1$, all nine fractures propagate to full length, but three of them are relatively thinner than the others (Figure 3.23A). For the $n = 20$ case, all nine fractures grow, but only seven of them grow to full length (Figure 3.23B). The other two fractures are slightly shorter and thinner than others. The results indicate cracks can grow at similar velocity for small subcritical index cases in low-permeability rocks. Once the subcritical index is high, the contrast in fracture velocities becomes more significant and affects fracture propagation rate significantly, which leads to a larger fracture spacing ultimately. Moreover, at a very high subcritical index, permeability does not have a controlling influence on fracture spacing and pattern for the simple case studied here (Figure 3.22C, 3.23C).

High-permeability rock (k = 1 D): Pressure profiles

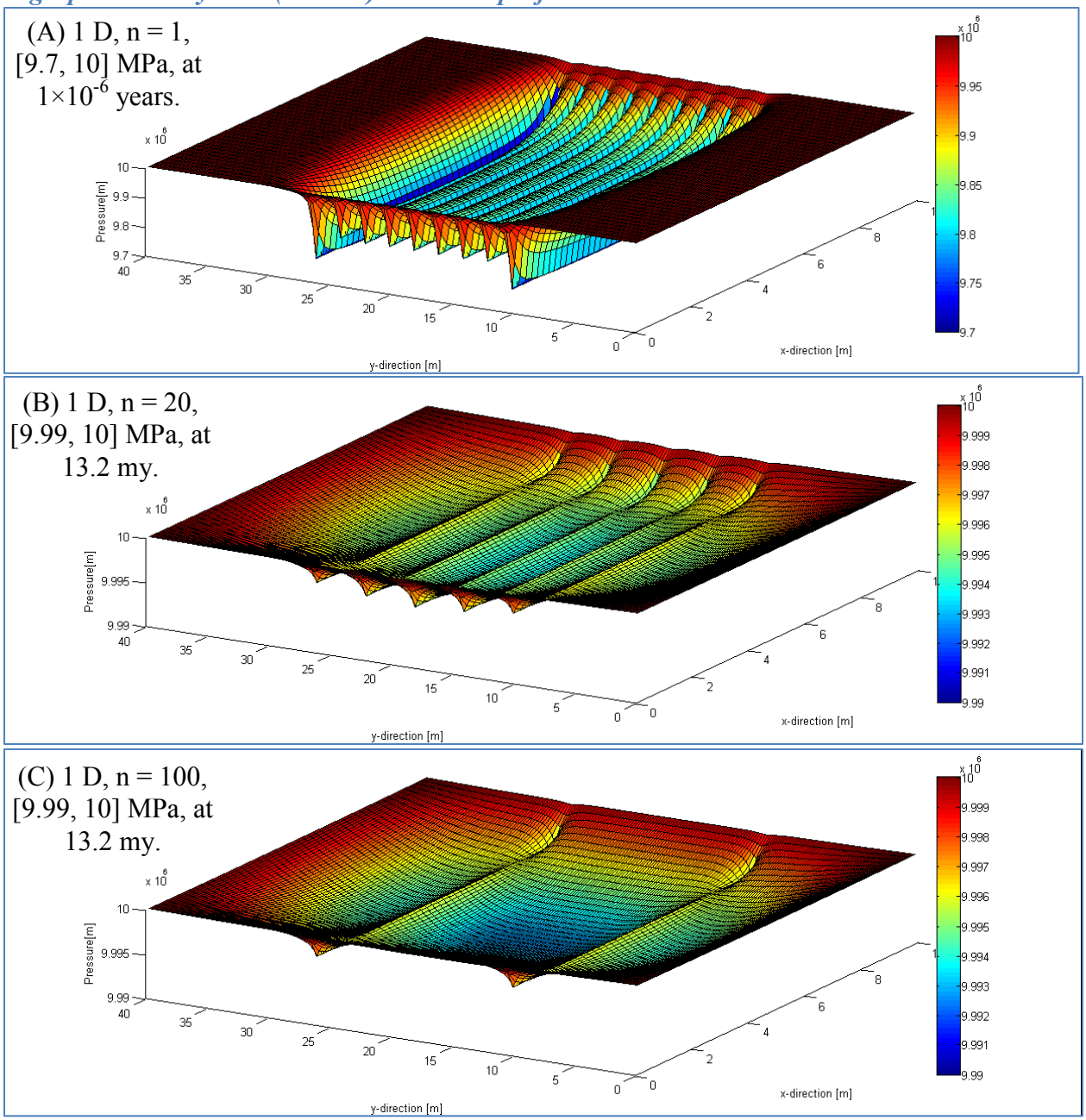

Figure 3.24 - Pressure profile in 1 D rock with subcritical index of (A) 1 at 1×10^{-6} yeras, range as [9.7, 10] MPa, (B) 20 at 13.2 my, range as [9.99, 10] MPa, (C) 100 at 13.2 my, range as [9.99, 10] MPa.

Low-permeability rock (k = 1 nD): Pressure profiles

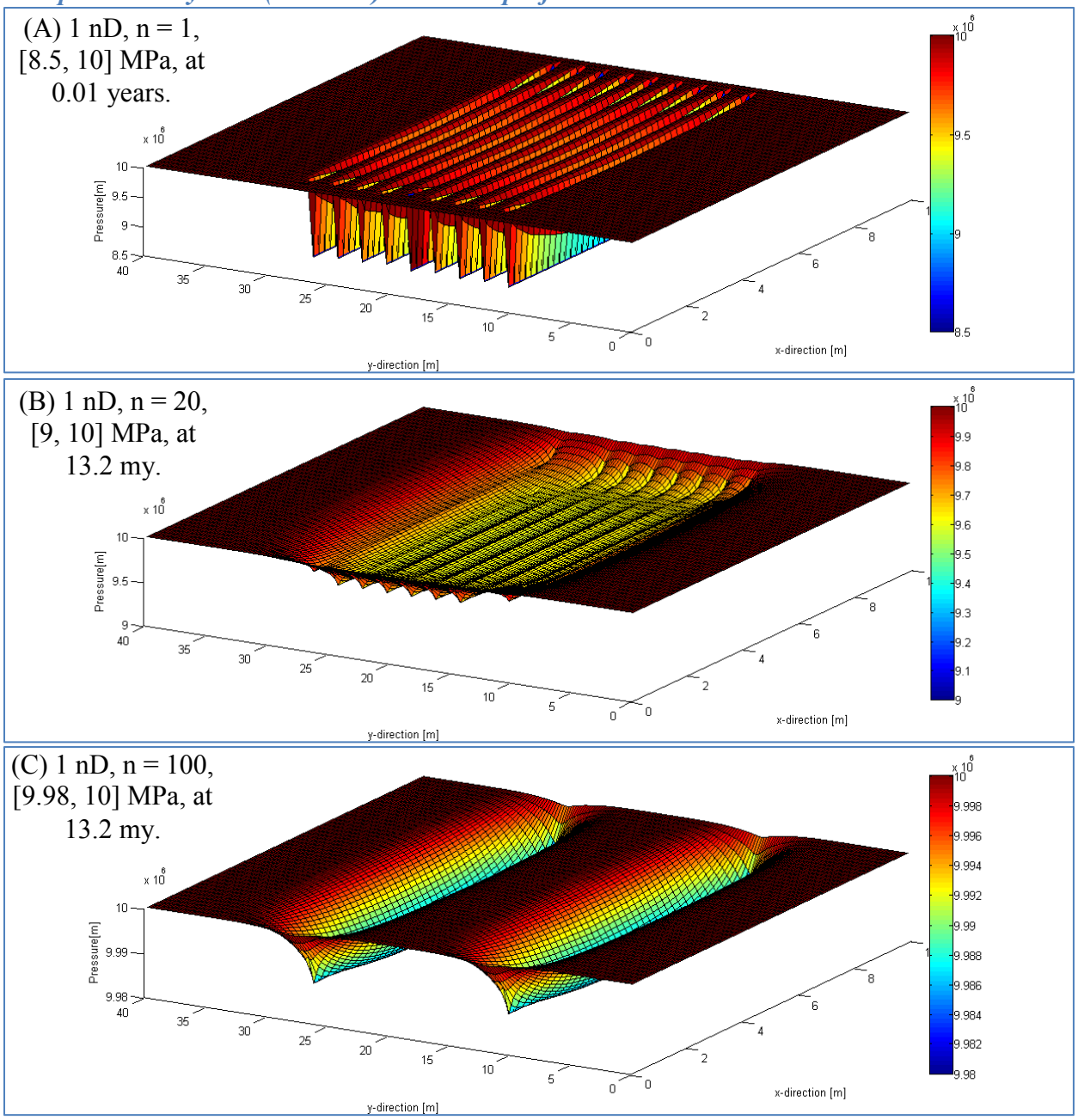

Figure 3.25 - Pressure profile in 1 nD rock with subcritical index of (A) 1 at 0.01 yeras, range as [8.5, 10] MPa, (B) 20 at 13.2 my, range as [9, 10] MPa, (C) 100 at 13.2 my, range as [9.98, 10] MPa.

Figures 3.24 and 3.25 clearly show that the fluid pressure is much higher in high-permeability rocks than low-permeability ones for all subcritical index cases. Shorter growth timing is required for low *n* cases, resulting in a lower fluid pressure distribution and smaller fluid depletion area for both 1 D and 1 nD cases. As *n* increases to 20, longer growth time is needed for fractures to propagate to full length. Permeability has a stronger controlling effect on the fluid depletion area and fracture propagation speed, therefore, more fractures propagate to long length in low-permeability rocks than high-permeability ones. When *n* is extremely high, two long fractures dominate the fracture pattern by creating both large pressure depletion and stress shadow areas, which prevent any neighboring fracture from propagating.

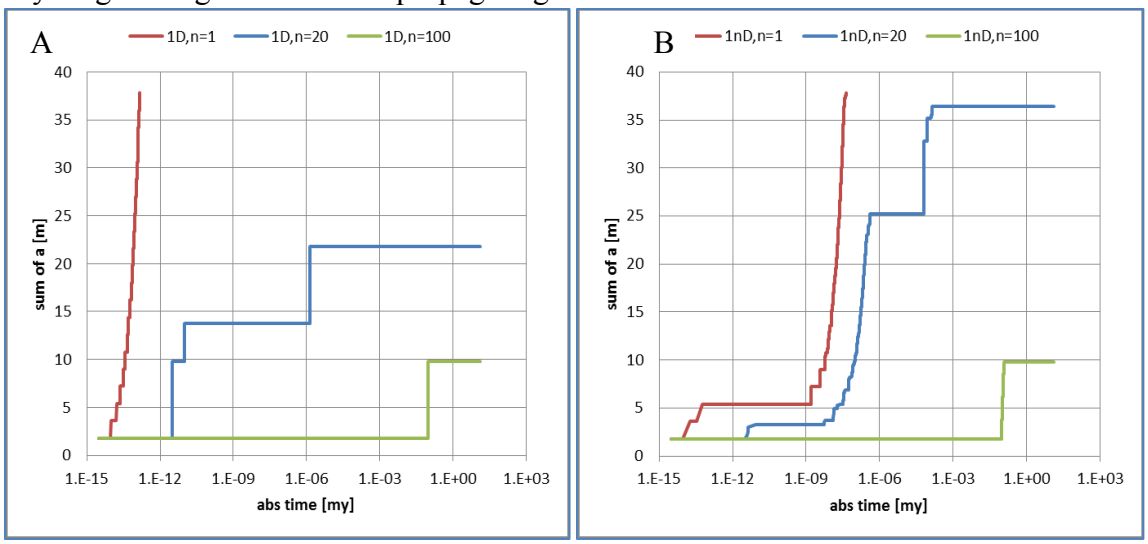

Figure 3.26 - The summation of fracture half-length vs. crack propagation duration for (A) 1 D and (B) 1 nD rocks. The subcritical index n varies from 1, 20 to 100.

Figure 3.26 is the plot of the total fracture half-length versus the fracture growth time with *n* varying from 1, 20 to 100 in 1 D and 1 nD rocks. Generally, the fracture propagation rate is higher for small subcritical index cases in both high- and low-

permeability rocks. For the n = 1 case, longer growth timing is required for all nine fracture to grow to full length in 1 nD than 1 D rocks. For the n = 20 case, fractures grow slower in lower permeability rocks, but the ultimate total fracture half-length is much higher in low-permeability rocks at growth timing at 13.2 my. When n is as high as 100, the total half-length versus growth time curves look the same for both high- and low-permeability rocks. The results indicate that permeability has a more controlling effect for low subcritical index case for the regularly spaced fracture set studied here.

3.6.2.3 Boundary condition effect

As discussed in chapter 2, reservoir boundary conditions are important for fluid flow at later stage, i.e. pseudo-steady or steady states. For fracture propagation in a saturated porous medium, the fluid flow from porous media into fracture voids not only depends strongly on the permeability, but also on the reservoir boundary conditions. The effect of boundary conditions, constant pressure or no flow, is studied in this section for both 1 D and 1 nD rocks. The subcritical index is 20 and layer thickness is 4 m.

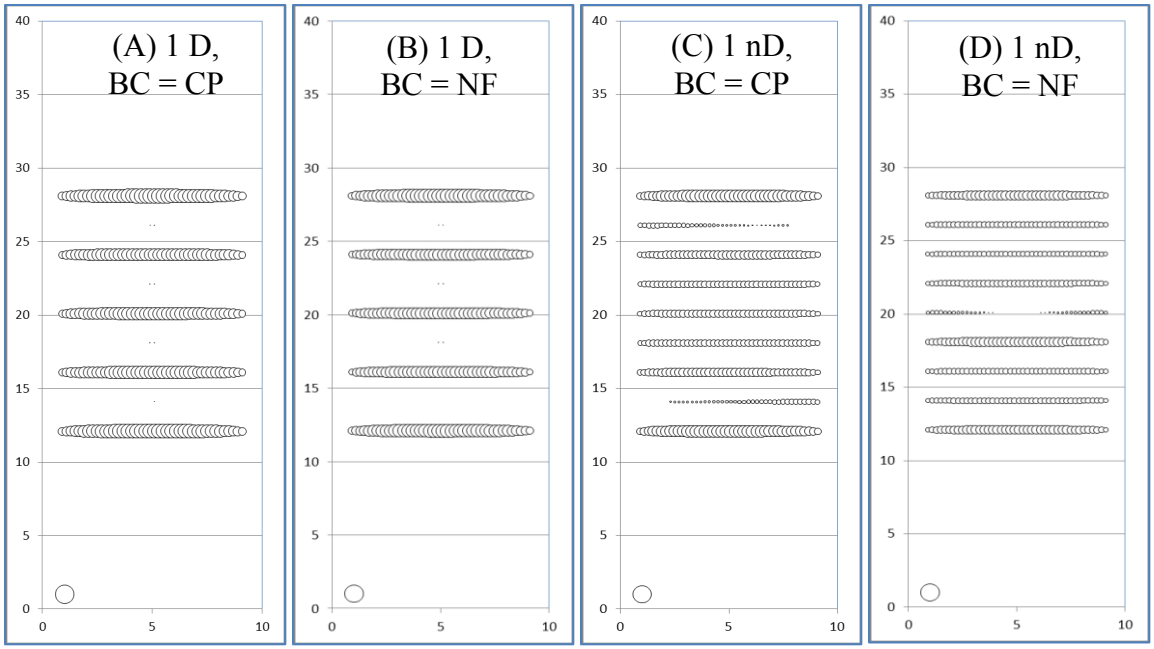

Figure 3.27 - Fracture aperture maps in (A, B) 1 D rock with constant pressure and no flow boundary conditions (C, D) 1 nD rock with constant pressure and no flow boundary conditions. BC = boundary condition, CP = constant pressure, NF = no flow.

Figures 3.27A, B illustrate the fracture pattern developed in high-permeability rock (1 D) under constant pressure and no flow boundary conditions. The aperture maps show the same fracture spacing, aperture and pattern with the two different boundary conditions, indicating boundary condition has a negligible effect on fracture propagation in high-permeability rocks for regularly spaced fracture sets. For the low-permeability rock case (Figure 3.27C, D), fracture spacing is the same, but the aperture distribution look different for the two different boundary condition cases.

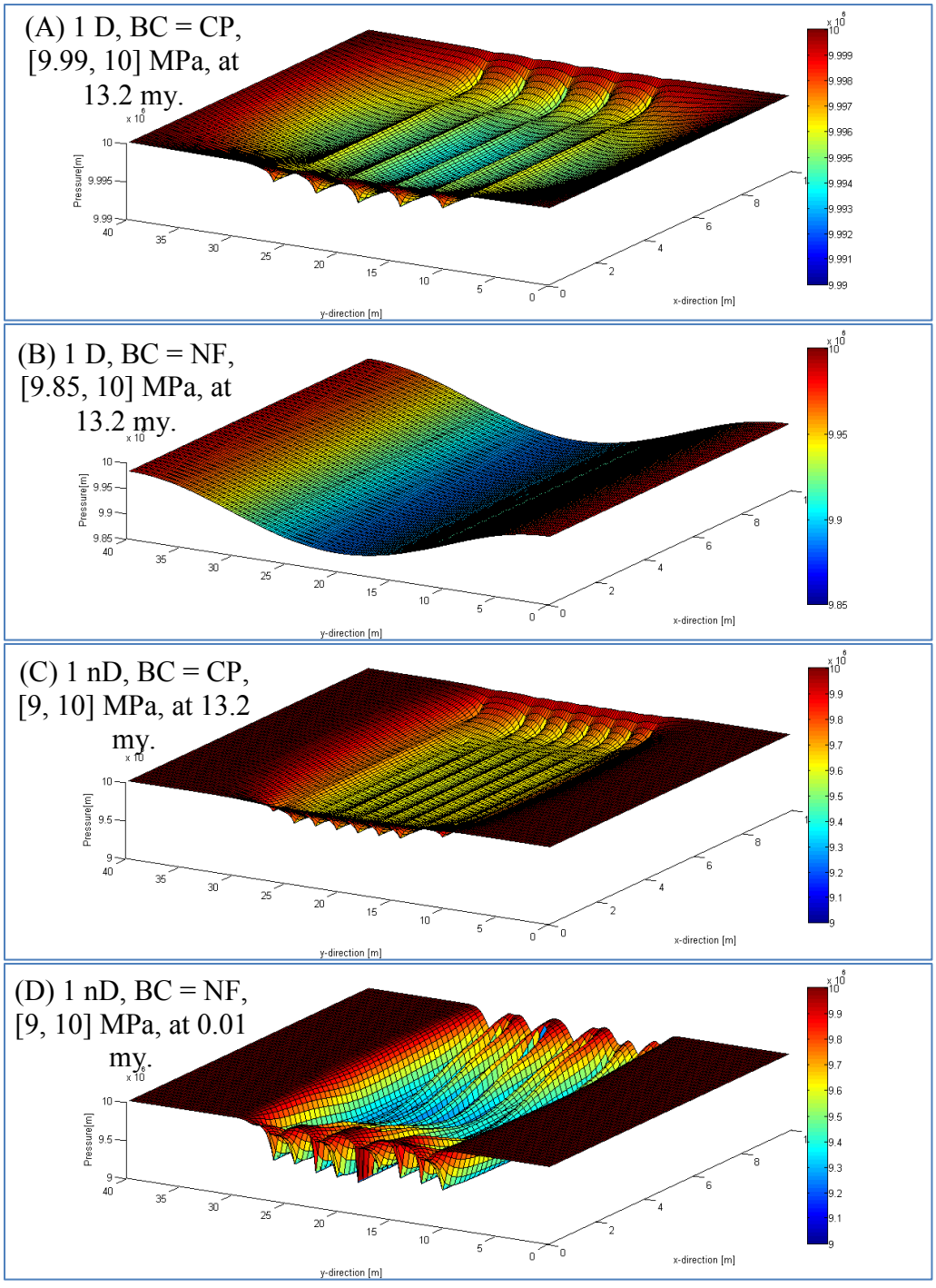

Figure 3.28 - Pressure profiles in (A, B) 1D rock with constant pressure and no flow boundary conditions (C, D) 1nD rock with constant pressure and no flow boundary conditions.

Figure 3.28 shows the corresponding 3D pressure profiles for fracture patterns shown in Figure 3.27. The boundary condition dramatically changes the pressure distribution inside the reservoir and the average pressure is generally much lower under no-flow than constant pressure condition. In high-permeability rock, the no-flow boundary creates a larger fluid depletion zone around the propagated fractures compared to the constant pressure case (Figure 3.28A, B). For low-permeability rocks, the pressure distribution inside reservoir is less influenced by the boundary condition as a result of the slow fluid flow rate associated with the low reservoir permeability. In addition, the fluid depletion area is always smaller in low-permeability than high-permeability rocks. This explains the differences observed in fracture aperture maps (Figure 3.27).

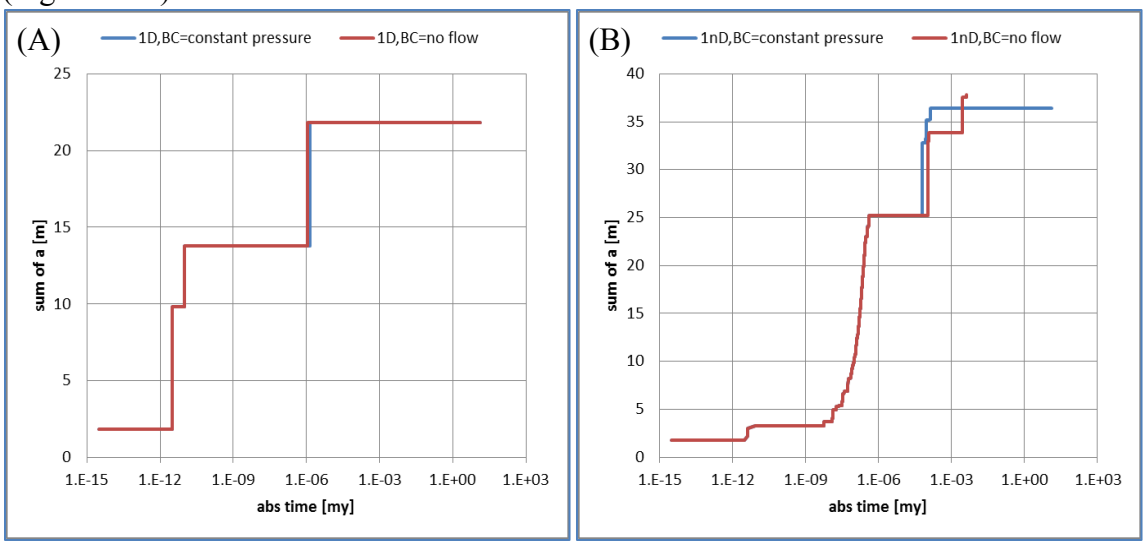

Figure 3.29 - The summation of fracture half-length vs. crack propagation duration for (A) 1 D, and (B) 1 nD rocks. The boundary condition varies as constant pressure and no flow.

Figure 3.29 are the summation of fracture half-length versus crack propagation duration plots under different boundary conditions for 1 D (Figure 3.29A) and 1 nD

(Figure 3.29B). In high-permeability rocks (Figure 3.29A), five fractures grow to full length immediately after the propagation initiated for both constant pressure and no-flow cases. The other neighboring fractures, located within the long fracture's stress shadow, are unable to grow in length or aperture. The fast propagation rates for the five fractures make the total fracture half-length growth curve insensitive to boundary condition for high-permeability rock case.

For low-permeability rocks (Figure 3.29B), the total fracture half-length growth curves look the same before the total length reaches 25 m, indicating the fracture propagations are not yet affected by the boundary condition . Beyond this point, fractures grow slower for the no-flow boundary case compared to constant pressure case. However, with constant pressure condition, the ultimate total fracture half-length is 36.4 m and no increment is observed beyond 1×10^{-4} my. With the no-flow condition, the ultimate total fracture half-length reaches 37.8 m at 4×10^{-3} my. The results indicate slower fluid rate makes more fractures propagate in length, though the growth timing will be longer. The no-flow boundary condition leads to more fracture propagation in low-permeability rocks.

3.6.2.4 Initial fracture half-length effect

Another factor of interest is the initial fracture half-length (a_0), which is used to characterize the initial fracture density in chapter 2 and shows strong influences on fracture propagation timing. To study the effect of a_0, it is varied from 0.2 m to 1m for 1 D and 1 nD rock. The other parameters are n = 20, T = 4 m and boundary is at constant pressure condition.

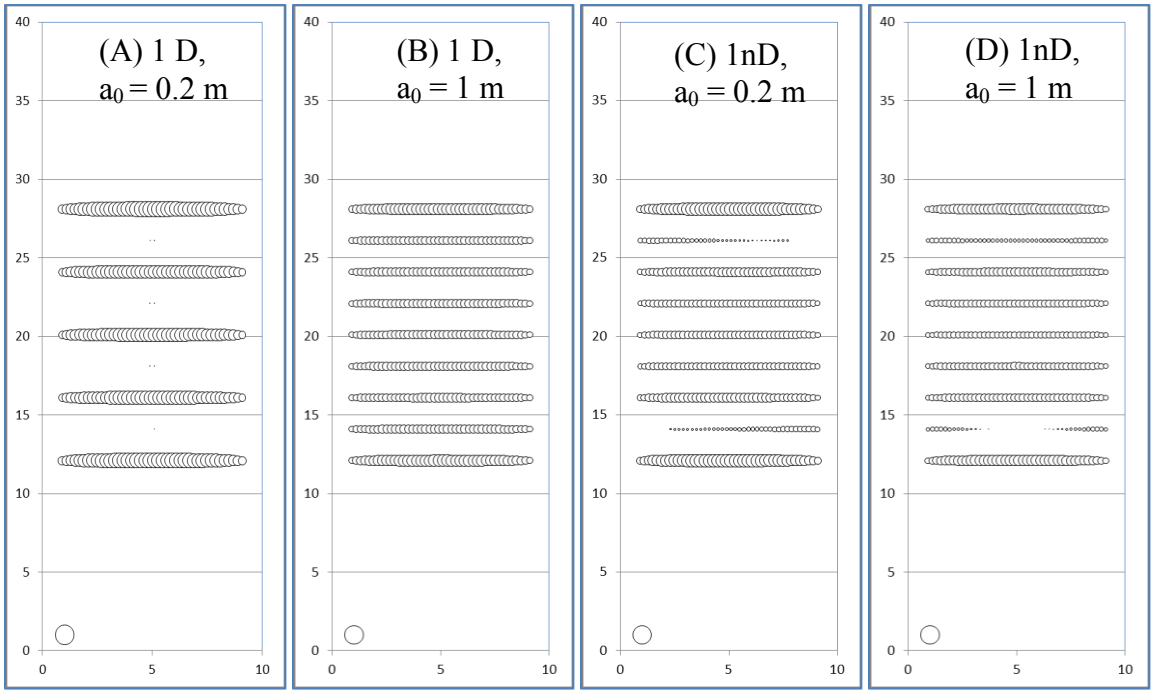

Figure 3.30 - Fracture aperture maps in (A, B) 1 D rock with a_0 = 0.2 m and a_0 = 1 m, (C, D) 1 nD rock with a_0 = 0.2 m and a_0 = 1 m.

For a_0 = 1 m case, all nine fractures grow to full length in both 1 D and 1 nD rocks as shown in Figure 3.30B, D. The fracture apertures are slightly skinnier for a_0 = 1 m case than a_0 = 0.2 m case for 1 D rock (Figure 3.30A, B). For 1 nD rock, the fracture apertures are similar for both small and large a_0 cases. The corresponding pressure profiles in Figure 3.31 reveal more details of the associated fluid pressure distribution and fracture propagation timing for each pattern in Figure 3.30. For the large a_0 case, less pressure drive is required for fracture propagation and therefore, shorter propagation timing is required as indicated from Figure 3.31.

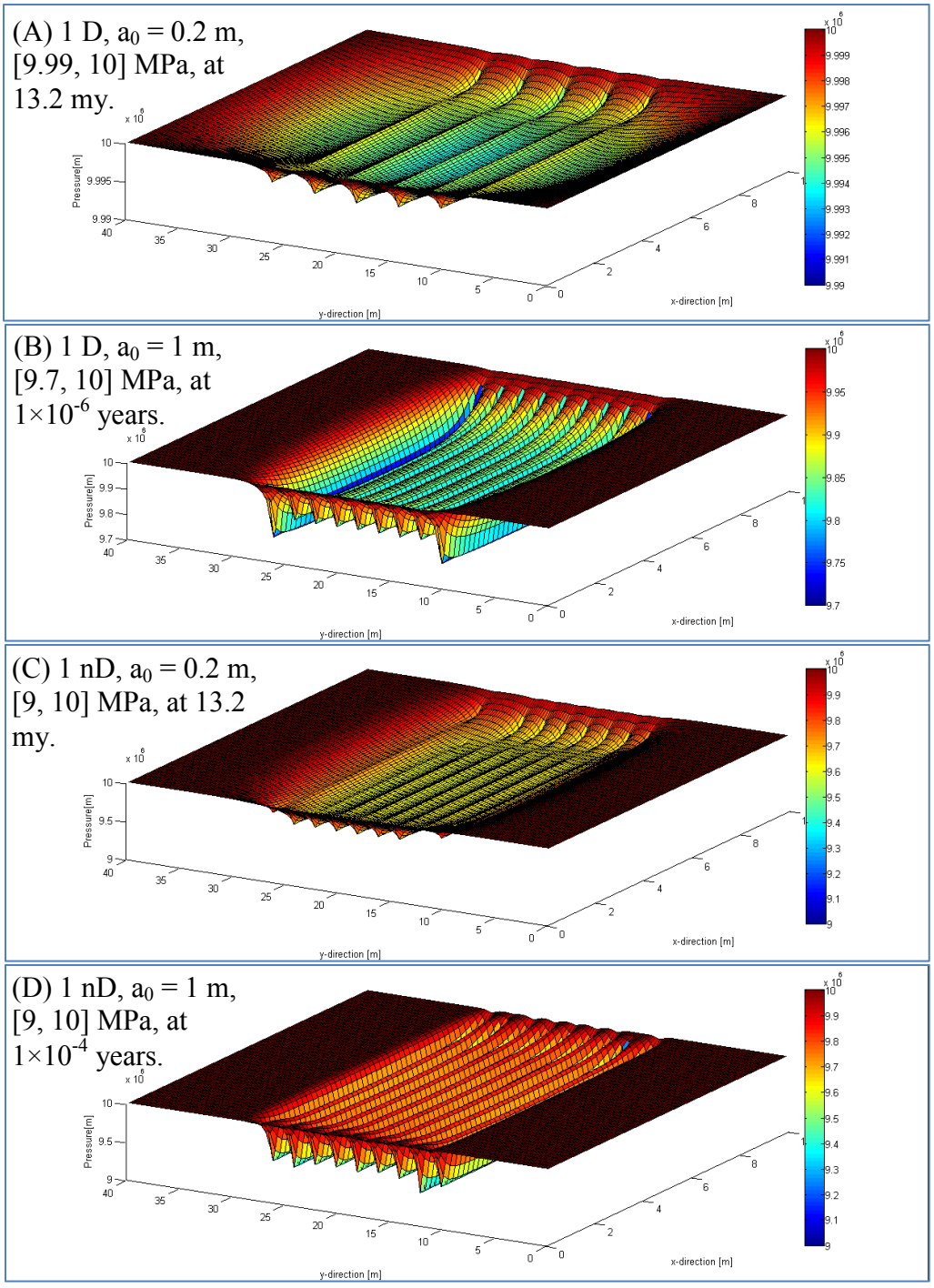

Figure 3.31 - Pressure profiles in (A, B) 1 D rock with a_0 = 0.2 m and a_0 = 1 m, (C, D) 1 nD rock with a_0 = 0.2 m and a_0 = 1 m.

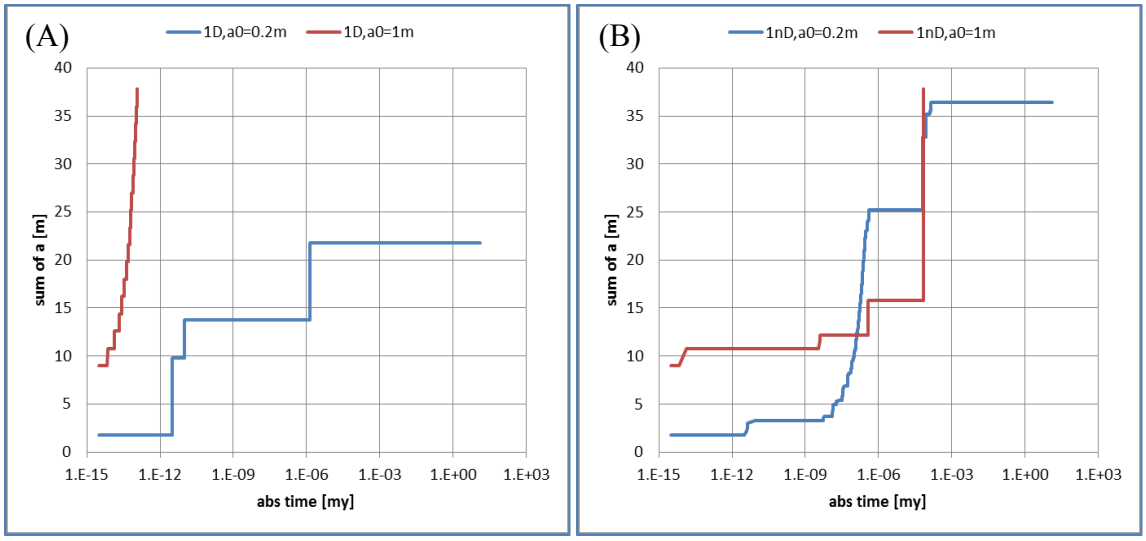

Figure 3.32 - The summation of fracture half-length vs. crack propagation duration for (A) 1 D and (B) 1 nD rocks. The initial half-length of the starter fractures varies as 0.2 m and 1 m.

For a_0 = 1 m case, all nine fractures have a fast propagation rate in both high- and low-permeability rocks as less pressure drive is required for long cracks to grow. The total crack growth timing is around 4 seconds for 1 D rock (Figure 3.32A) and 70 years for 1 nD rock (Figure 3.32B). As a_0 decreases to 0.2 m, the differences in fracture propagation and spacing become significant between high- and low-permeability rocks. Only five fractures can grow to full length and no more fracture growth is observed after 1×10^{-6} my in high-permeability rocks; whereas more fracture grow in low-permeability rocks though the total growth duration is much longer. Therefore, permeability will have a more significant influence on fracture propagation timing and spacing for flaws with smaller initial crack half-length. The smaller the initial crack half-length, the larger pressure drive is required for fracture to grow. The low permeability leads to slower fluid flow rate and less fluid and mechanical interferences, which will result in a relatively closely spaced fracture pattern in low-permeability rocks.

3.7 CONCLUSIONS ABOUT THE PERMEABILITY IMPACT ON *S/T* RATIO

Reservoir permeability, together with subcritical index and layer thickness, has a strong influence on fracture propagation process and fracture spacing for the regularly spaced fracture sets studied in this chapter. For high-permeability rocks, the simulation results are consistent with the conclusions predicted by the classic geomechanical model, where constant internal fluid pressure is assumed. In high-permeability rocks, fast flow rate ensures the internal fluid pressure remain almost constant throughout. This leads a strong controlling effect of stress shadow on the fracture propagation and spacing, mainly as a function of subcritical index and layer thickness. Higher subcritical index or larger layer thickness results in larger fracture spacing, which approximately scales with the layer thickness. For low-permeability rocks, the conclusions are totally different. For the same reservoir and geomechanical conditions, the low permeability results in a small flow rate and a slow fluid pressure recovery process inside fracture. The duration of the pressure recovery process is roughly inversely proportional to rock permeability. This prevents any fracture from growing extremely fast and dominating the whole fracture pattern. Therefore, majority of the fracture can propagate at a slow, but uniform pace. This leads to more fracture propagations and smaller fracture spacing in low-permeability rocks, though the fracture apertures are normally smaller due to the low average pressure in the less permeable rocks. The difference in fracture spacing controlled by reservoir permeability is most significant for fracture propagation with intermediate subcritical index in thick bedding layers.

Other factors, such as reservoir boundary condition and initial fracture half-length, have noticeable impacts on fracture spacing and growth timing as well. Their influences can be explained using the idea of the fluid depletion area shown in Figure 3.9. In addition to the stress shadow zone, the fluid depletion area is observed around the

propagating fractures. The size of the depletion area is related to reservoir permeability, fracture length and boundary condition. Generally, smaller fluid depletion area is observed with lower reservoir permeability, shorter fracture length and no flow boundary condition for later fracture development stage. The smaller the fluid depletion area, the less pressure interference exists between fractures. Meanwhile, the slower the fluid flows from reservoir into fracture, the longer time the crack requires to recover the internal fluid pressure to grow. Therefore, with smaller fluid depletion area and slower fluid flow rate, more fractures are able to grow at similar velocities and a closely spaced fracture pattern can be achieved.

The fracture patterns studied in this chapter are composed of regularly spaced multiple fractures, which are not very realistic in the field. Randomly distributed natural fracture patterns are more realistic. Therefore, chapter 4 will focus on investigating how reservoir permeability affects the fracture pattern development and the statistical distribution of fracture attributes of a more complicated and realistic natural fracture set.

Chapter 4: The Impact of Permeability on Fracture Pattern Development and Fracture Attribute Distribution

Fracture patterns observed in the outcrops provide useful information for interpretation of subsurface fracture patterns. An accurate and detailed description of the fracture network helps engineers quantify rock deformation and predict the fluid flow within porous media, which later acts as guidelines for oil and gas exploration and production (Snow, 1970; Long et al., 1982; Andersson and Dverstorp, 1987; Dverstorp and Andersson, 1989; Zhang et al., 1992; Gudmundsson, 2000). Research emphasis has been focused on characterizing the attributes of natural fractures and understanding the fracture pattern development process. The key fracture attributes generally include fracture orientation, planarity, length, aperture and spacing. Fracture attribute distribution is often considered as a representation of fracture pattern development; in other words, the characterization of fracture attribute distribution enables us discover the mechanism for the related process as well (Olson, 2007). Among various techniques for fracture pattern characterization, the new geomechanical modeling technique which was developed in the previous chapter will be applied to investigate the randomly-distributed natural hydraulic fracture pattern development and attribute distribution in Chapter 4.

4.1 NATURAL FRACTURE PATTERN CHARACTERIZATION

Fracture pattern development goes through several stages (Laubach, 1991). In the early stage, most fractures begin propagation and their lengths are less than or equal to the spacing between them, while in later stages, some fractures will have leading advantages in propagation and dominate the pattern as their lengths grow to be much larger than fracture spacing (Dyer, 1988; Rives, 1992). The fracture pattern is referred to

as poorly developed at the early stage and well-developed at the late stage (Wu and Pollard, 1995).

Normally, there are three types to characterize fracture network attributes: direct observation from outcrops or cores (Rives, 1992; Laubach, 1997; Ortega and Marrett, 2000), geostatistical models (Kulatilake et al., 1993) and geomechanical models (Qiu, 2002; Olson, 2004). Field observations and core sample studies are simple and direct; however, the sampling may be a potentially problem because it is challenging to gather sufficient and representative data to construct a fracture attribute distribution. Geostatistical models are based on the inherent statistical nature of rock to characterize the discontinuities inside it, like joints and bedding planes, statistically (Kulatilake et al., 1993). On the other hand, geomechanical modeling work is based on the underlying mechanisms to represent the physical process and predict the fracture attribute distribution. Meanwhile, the modeling work requires some basic knowledge of the rock properties, field stress or loading history and initial distribution of flaws (Olson, 2004).

Granitic outcrops in Sierra Nevada provide excellent exposures of sub-parallel planar fractures, whose lengths vary from centimeters to hundreds of meters (Segal and Pollard, 1983) (Figure 4.1A). Based on field mapping, the fracture length data can be described by the choice of functions. Both negative exponential and power-law functions represent well the fracture length distribution, while the power-law function provides a more accurate fit to the field data (Figure 4.1B). Similar field work has also been conducted on mapping the outcrop surface in order to measure the fracture connectivity, length and density.

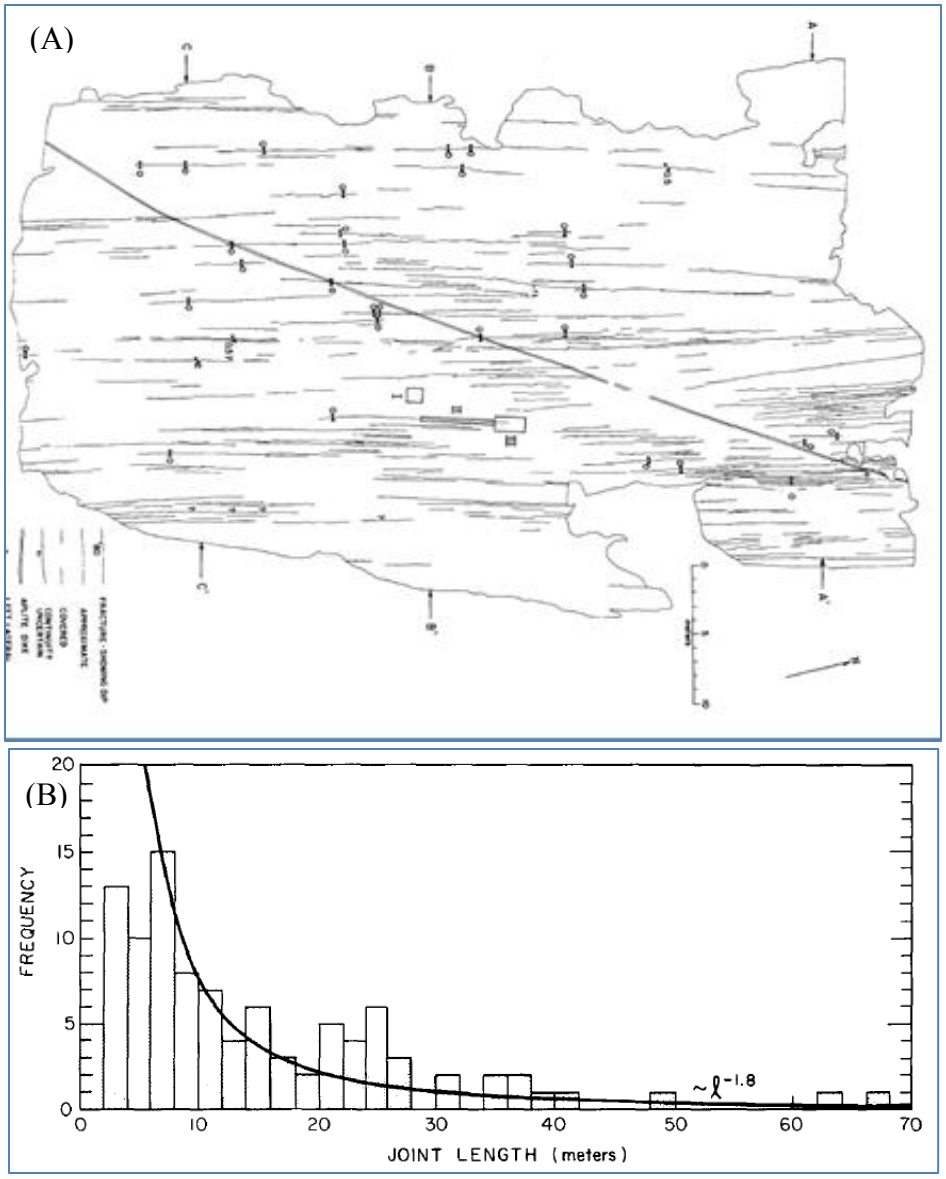

Figure 4.1- (A) Mapping the joint geometry and displacement indicators (A-A', B-B' and C-C' indicate strain traverses), (B) distribution of joint length (curve fitting by power-law function) in the Ward Lake outcrop in Sierra Nevada (from Segall and Pollard, 1983).

As most fractures in the subsurface are vertically oriented, the probability is quite small for a vertical well to intersect vertical natural fractures in the subsurface if fracture spacing is greater than wellbore diameter (Narr, 1996). Therefore, the sampling size for

core samples is small and direct observation from core samples can be biased or restricted. In addition, the information obtained from fractures in core samples is limited by the size of the core. This is the same problem for direct observations from outcrop, where fracture length and spacing are limited by outcrop size. It is also challenging to preserve the subsurface condition for core samples and interpret the distribution in subsurface from outcrop observations.

In order to interpret the fracture patterns in the subsurface, researchers show that mircrofracture observation obtained from core samples from the subsurface can upscale and serve as an analog for fracture orientation and aperture distribution at much large scales where fracture sampling is difficult (Laubach, 1997, 2000, 2003; Marrett et al., 1999; Ortega and Marrett, 2000). Microfractures are abundant in rocks (Segall and Pollard, 1983; Kranz, 1979; Tapponier and Brace, 1976) and formed under the reactive fluid environment (Lander, 1998; Milliken and Laubach, 2000), which indicates fracture and host-rock diagenesis are closely correlated. The cement deposited after fracture growth arrested is called postkinematic cements. The approach proposed by Laubach (1997, 2000, 2003) is based on analyzing the amount of postkinematic cements in the microfractures to predict fracture openness at larger scales via the degradation index. Degradation index can also be used to predict whether macrofractures are open, partially open or sealed. The orientation of the microfractures is normally consistent with that of macrofractures. However, fracture length distribution and fracture connectivity cannot be provided by this approach.

Geostatistical modeling uses the basic information about the fracture intensity, orientation, and spacing and size distributions to build up a geometry model for the specific joint set in a statistically homogenous region (Kulatilake et al., 1993). The

parameters in geostatistical models are basically statistical and its application to quantitative prediction of joint properties is questionable.

Another useful tool, Geomechanical modeling, has been extensively discussed in Chapter 3. This method has been used to predict fracture attribute distribution for the entire reservoir region or at locations where fracture sampling is challenging. However, it also requires some inputs such as subcritical index, Poisson's ratio, and Young's modulus and remote stresses/strains (Olson, 2004).

4.2. EXISTING CONCLUSIONS ON FRACTURE ATTRIBUTE DISTRIBUTION

4.2.1 Fracture length distribution

Field observations show that the fracture length distribution fits into some functions, mostly referring to the power-law function (Segall and Pollard, 983; Gudmundsson, 1987; Jamison, 1997; Odling, 1997; Marrett, 1997; Marrett et al., 1999; Ortega and Marrett, 2000), negative exponential function (Miller, 1993; Bloomfield, 1996) and log normal (Rouleau and Gale, 1985; Barton and Zaback, 1992; Miller, 1993; Renshaw, 1993; Bloomfield, 1996). Gillespie et al. (1999) also pointed out layering of the vein array influenced fracture thickness distribution and spacing.

The power-law distribution is expressed as a function of fracture length x:

$$f(x) = ce^{-n \cdot x}, \tag{4.1a}$$

where $f(x)$is the probability distribution function, n is the power-law exponent and c is a constant. For a fracture population obeys power-law distribution, the slope is $-n$ for the log-log plot of $f(x)$ versus x. For a negative exponent function, the probability distribution function is only a function of fracture length x and constant λ:

$$f(x) = \lambda e^{-\lambda x}. \tag{4.1b}$$

The probability distribution function for log normal function depends on the fracture length x and the mean and standard deviation of the fracture length distribution:

$$f(x) = \frac{1}{\sqrt{2\pi\sigma x}} e^{-\frac{(\ln x-\mu)^2}{2\sigma^2}}. \quad (4.1c)$$

In addition to the field observations, Olson (1997) applied a geomechanical model and numerically discovered negative exponent shape on the cumulative frequency of fracture length curves under uniaxial loading condition. For biaxial loading condition, the fracture length population curve follows power-law curve for the generated orthogonal type fracture pattern (Olson, 2004).

4.2.2 Fracture aperture distribution

Similar field measurement data suggests fracture aperture distributions follow power-law functions mostly (Barton and Zoback, 1992; McCaffrey, 1994; Gross and Engelder, 1995; Clark, 1995; Marrett, 1997, 1999; Ortega and Marrett, 2000). The numerical results showed that fracture aperture distribution deviates from normal to negative exponential as fracture height increases and all fracture length distributions follow negative exponential functions. This is explained by the analysis on crack tip stress intensity factor in a fracture overlap model (Pollard et al., 1981; Olson et al., 2001; Qiu, 2002).

In Austin Chalk, Gale (2002) observed power-law distribution of opening mode fractures with threshold aperture at 11 mm. It is estimated that the natural fracture population will follow power-law function in low-permeability rock as well (Gale and Holder, 2010).

4.2.3 Fracture spacing distribution

The correlation between fracture spacing and layer thickness is discussed in details in Chapter 3.

4.2.4 Fracture aperture versus length correlation

The classic linear elastic fracture mechanics assumes all fractures do not interact with each other and all of them have the same driving stress, which is regarded as irrelevant to their length. LEFM predicts a linear correlation between fracture length and maximum fracture aperture (Pollard and Segall, 1987) as shown in equation (2.5).

A sublinear scaling law was observed in the field as described in Chapter 2 (Delaney and Pollard, 1981; Vermilye and Scholz, 1995; Renshaw and Park, 1997; Moros, 1999). A sublinear relation between fracture aperture and length was proposed by Olson (2003) to explain the field observations. Instead of constant driving stress, constant stress intensity factor is assumed for all the noninteracting fractures in the host-rock or remote tectonic extension is applied to drive fracture propagation slowly. The numerical results show a square root aperture-to-length correlation as shown in equation (2.7), which resembles the field data on fracture aperture versus length (Delaney and Pollard, 1981; Vermilye and Scholz, 1995; Moros, 1999). In addition, fracture segmentation and fracture layer thickness have significant influences on fracture aperture-to-length relationship (Olson, 2003).

Superlinear aperture to length correlation is observed in two populations of tensile fractures in Krafla fissure swarm in northeast Iceland (Hatton et al., 1994). The Krafla swarm was reported to be triggered by the increase in fluid pressure during the lateral magmatic intrusion process (Einarsson, 1991). The measurement data of the two sets of fractures in this swarm revealed a power-law correlation between fracture aperture (d_{max}) and length (L) as:

$$d_{max} \propto L^n, \tag{4.2}$$

where n is the slope and its value is distinctly different when L is above and below a characteristic length of 3 m. n is around 2.2 when L is below this characteristic length,

but becomes 0.9 once L is above this characteristic length. Renshaw and Park (1997) proposed a numerical model to explain that the mechanical interactions between the closely spaced tensile fractures in the swarm added the complicity on the scaling of d_{max} and L and led to the superlinear d_{max} - L correlation. The mechanical interaction also explains the considerable scatter in the natural data.

4.3 POROELASTIC P3D GEOMECHANICAL MODEL: PERMEABILITY EFFECT

In Chapter 3, a new poroelastic geomechanical model is developed to use the natural hydraulic fracturing mechanism to explain the closely spaced fractures pattern found in field. In this chapter, this new model is used to study the distribution of fracture attributes and pattern development of multiple stratabound fracture propagation in a poroelastic media.

I start with a set of 100 flaws with initial half-length of 0.2 m, randomly distributed in a rectangle area of 8 m by 36 m centered in a 10 m by 40 m finite body. The flaws are parallel to each other and confined by a 4 m bedding layer. A uniaxial strain of 1×10^{-4} is applied through 10 discrete increments at regular time intervals in the y-direction. The strain rate is 1.2×10^{-19} per second, which leads to a total growth period of 25 my. Simulations were performed with subcritical index of 80. Reservoir boundary is at a constant pressure condition.

Reservoir permeability varies from zero, 1 nD, 1 mD to infinitely large (referred as constant pressure case). Permeability close to zero represents the situation where fluid pressure recovery is extremely slow. It is assumed in this model that it takes one million years for a fracture to fully recover the pressure drop caused by its latest propagation event. The constant pressure case is the situation when the fluid pressure inside fracture is

always constant, indicating extremely fast fluid flow from porous media to fracture. Permeability values of 1 nD and 1 mD are selected to represent the low- and high-end of permeability values for shale and tight rocks. On each fracture pattern, a reference bubble with radius of 1e-3 is located at the corner of each plot. The propagation starts around 8 million years after strain is applied.

Table 4.1 Settings of parameters used in the case study.

Parameters	**Values**
Young's modulus, E	25 GPa
Poisson's ratio, υ	0.25
Fracture toughness, K_{IC}	1.5 $MPa \cdot m^{1/2}$
Fluid compressibility, C_t	0.58 GPa^{-1}
Fluid viscosity, μ	1 cP
Reservoir porosity, $\emptyset$	0.1
Reservoir size, L_x by L_y	10 by 40 m
Boundary condition	Constant pressure
Layer thickness, T	4 m
Number of flaws	100
Initial fracture half-length, a_0	0.2 m
Subcritical index, n	80
Total strain applied, ε_f	1×10^{-4}
Strain rate, $\dot{\varepsilon}$	1.2×10^{-19}/s
Event number	10

4.3.1 Fracture patterns – trace map and aperture map

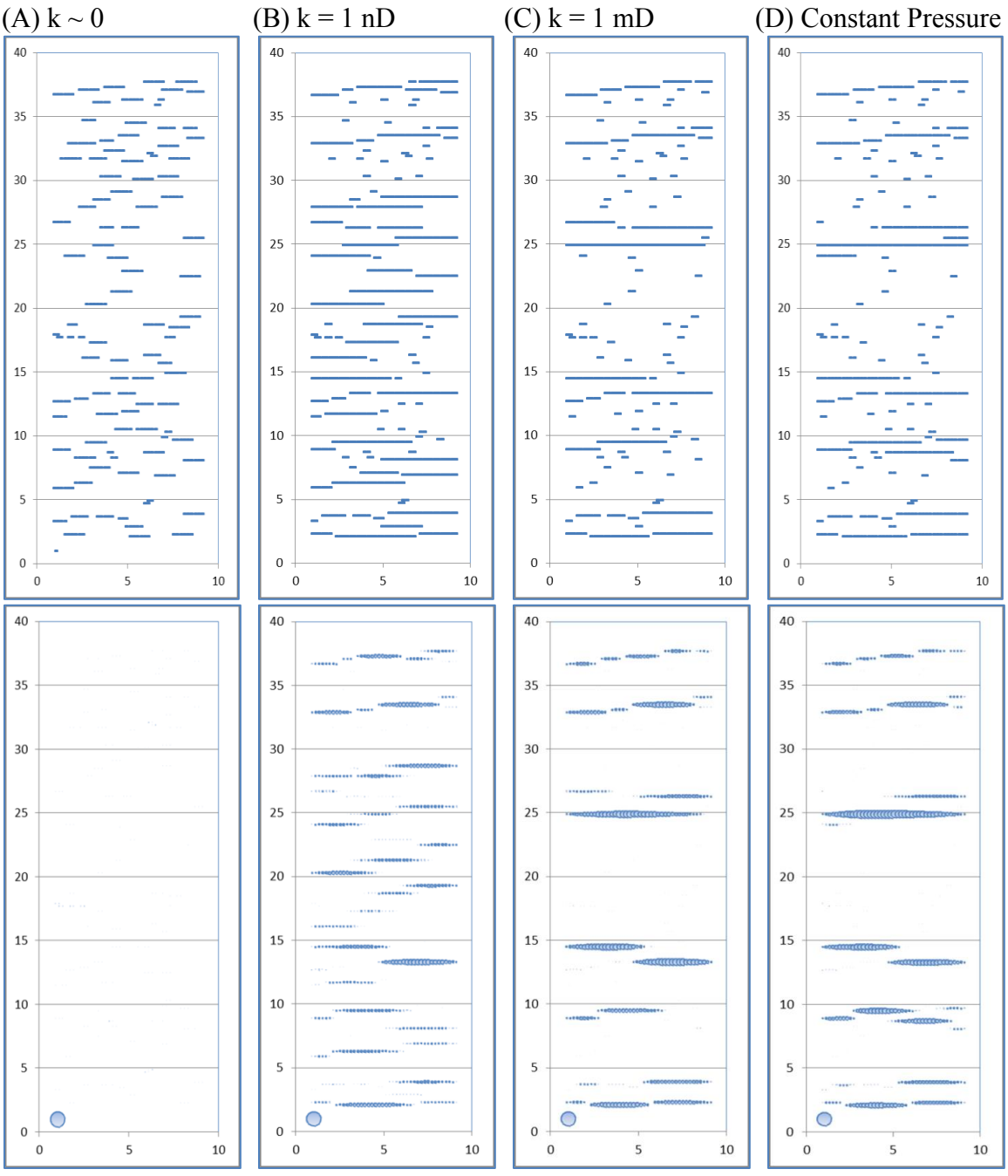

Figure 4.2 - At 11.3 my, the subcritical fracture growth patterns with n = 80, T = 4 m and constant pressure boundary condition with permeability of (A) 0, (B) 1 nD, (C) 1 mD and (D) infinitely large value (constant pressure case). The trace maps are listed in top array and aperture maps are shown in bottom array.

Figure 4.3 - At 19 my, the subcritical fracture growth patterns with n = 80, T = 4 m and constant pressure boundary condition with permeability of (A) 0, (B) 1 nD, (C) 1 mD and (D) constant pressure case. The trace maps are listed in top array and aperture maps are shown in bottom array.

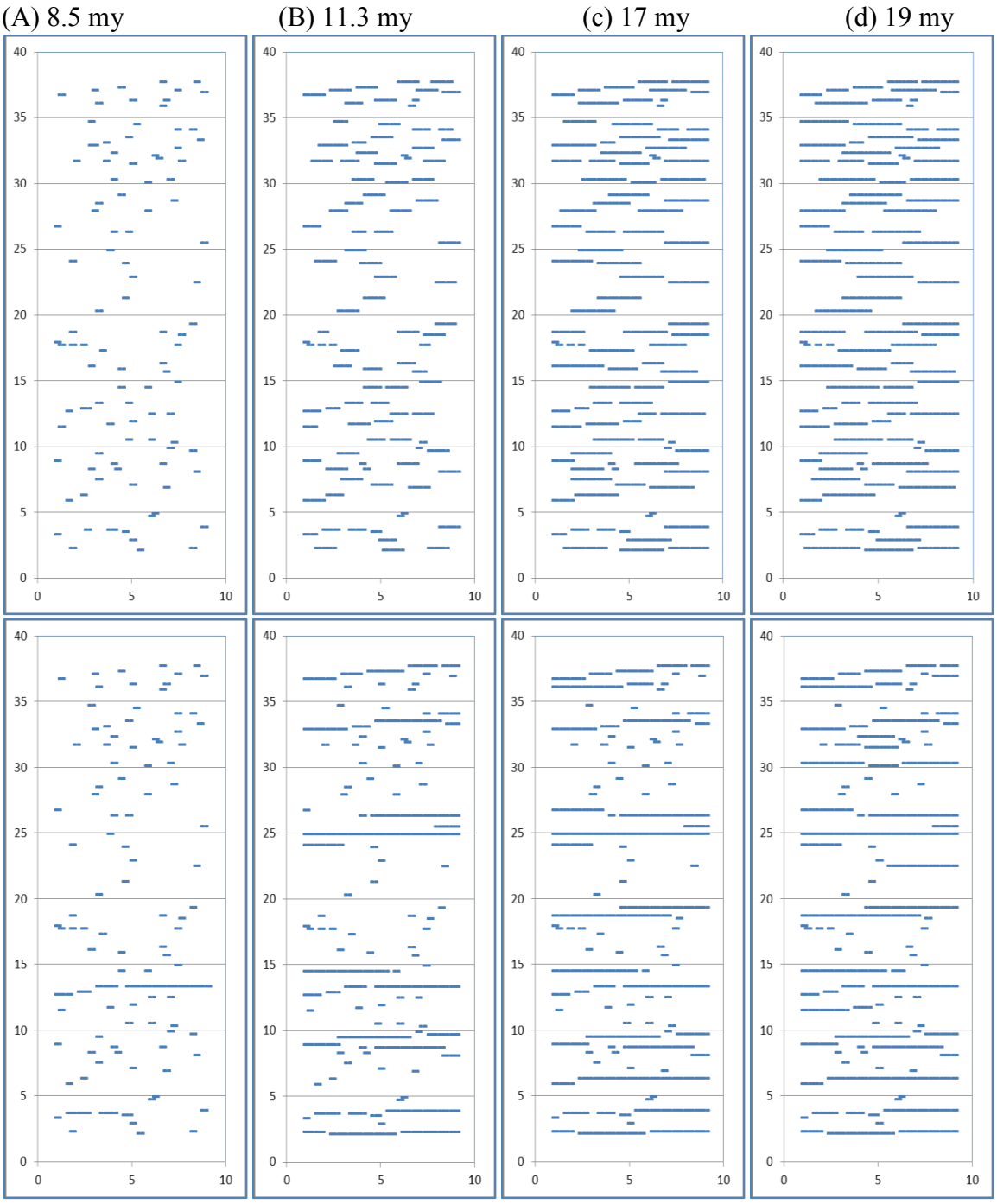

Figure 4.4 - The trace map of fracture pattern development with n = 80, T = 4 m and constant pressure boundary condition at the growth timing of (A) 8.5 my, (B) 11.3 my, (C) 17 my and (D) 19 my since the strain applied to the rock. k ~ 0 case is listed in top array and constant pressure case is in bottom array.

Figures 4.2 and 4.3 represent the fracture patterns developed at 11.3 my and 19 my in different permeability rocks. In each set of patterns, the trace maps are shown in the top array, illustrating the position and length of the growing fractures inside the rock. There are four trace maps in the top array, corresponding to four different rocks with permeability range from close to zero to infinitely large. The bubble plots in the bottom array are the aperture maps corresponding to each trace map above them. The fracture opening can be qualitatively observed from these bubble plots.

In high-permeability rocks (Figure 4.2C, D), strong fracture localization is observed and these localization zones are widely spaced to each other. In Figure 4.2A, B, localization is lacked in the low-permeability rocks, where fractures have similar length and aperture and are more closely spaced to each other. The clustering in high-permeability rock is because of the dominating mechanical interactions. High permeability ensures fast fluid recovery; thus long fractures can grow faster than others and create a stress shadow zone, generating local clusters with high subcritical index. This is consistent with the results on swarms shown by Olson (2004). In low-permeability rocks, the growth of the long fracture is hindered by the fluid lag due to low permeability. This leads most fractures to grow at a similar pace.

The pattern development at later stages is shown in Figure 4.3. Figure 4.2D and 4.3D show that more fractures fill in the spare area between clusters and the distance between them are approximately on the scale of layer thickness. Results are similar for 1 mD rock. For low-permeability rocks (Figure 4.3A), many fractures grow to a similar length and aperture and they are very closely spaced to each other, indicating the fluid flow, instead of mechanical interaction, is the dominating mechanism in this case. Moreover, as the fracture pattern continues to develop, no much change is observed in the length distribution in 1 nD rock (Figure 4.2B and 4.3B); the fracture apertures increase

significantly at late stages as more fluid recovery is achieved in low-permeability rocks at these stages.

Figure 4.4 illustrates more details of the pattern development process in extremely low-permeability rock (k ~ 0 case) and infinitely permeable rock (constant pressure case). Fractures tend to propagate at similar paces and have roughly the same length. Moreover, the fractures are very closely spaced to each other and no localization or clustering is observed. In the constant pressure case, at 8.5 my (0.5 my since propagation initiated), some fractures grow faster than others. Localization shows up quickly at 11.3 my and more swarms are generated at 17 my. It is obvious that several cracks are prevented from growing because of the stress shadow effect from the long fractures which dominate the pattern. For shales with extremely low permeability, the pattern development process would look similar to the top array plots in Figure 4.4 for k ~ 0 case, which indicates a closely spaced pattern.

The above conclusions are consistent with results in Chapter 3. The feathers of these patterns can be presented by fracture size, aperture and length, which are discussed next.

4.3.2 Fracture spacing distribution

The fracture patterns at late times (19 my) shown in Figure 4.3 indicate significant difference in fracture spacing for permeability range from almost zero to infinitely large. Therefore, fracture spacing is measured along the scanline at x = 5 m in Figure 4.3. Table 4.2 summarizes the calculated data. The cumulative frequency of fracture spacing along the scanline is plotted in Figure 4.5 for all four permeability cases.

Table 4.2 shows the average fracture spacing is around 1.7 m for both k ~ 0 and 1 nD cases, while the spacing is about 2.7 m for 1 mD and higher permeability rocks.

Moreover, as fracture pattern continues to develop, the spacing decreases indicating more fractures are filling the unfractured area until a saturation point is reached.

Table 4.2 Summary of the fracture spacing calculated with line method.

Permeability, *k*	**S[m] @ 11.3 my**	**S[m] @ 19 my**
Extremely small, ~ 0	3.3	1.7
1 nD	2.1	1.7
1 mD	4.4	2.7
Infinitely large (constant Pressure case)	4.0	2.4

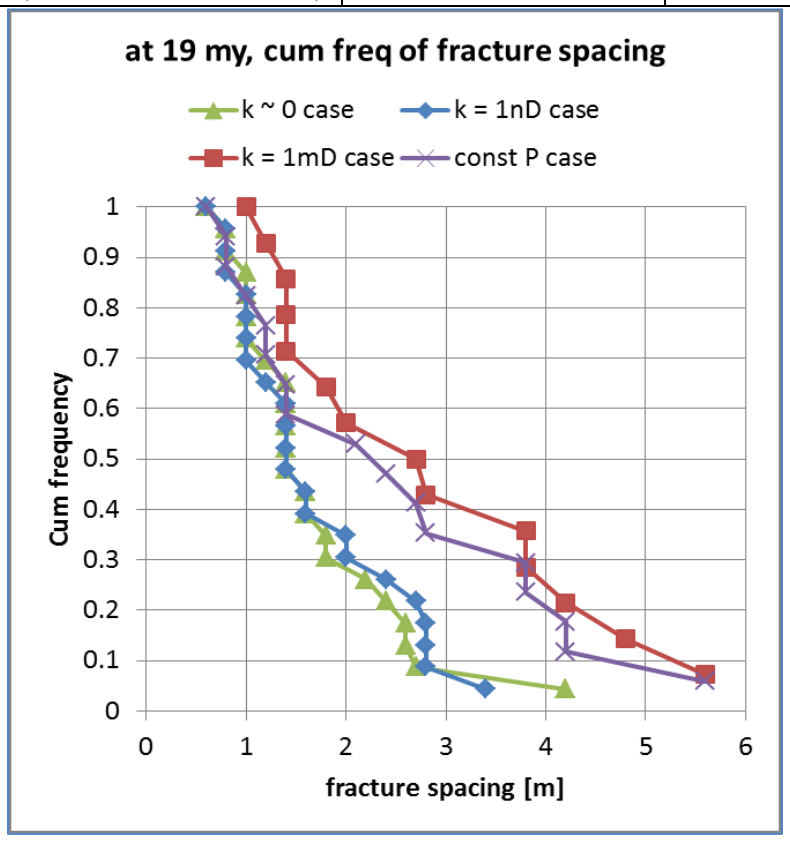

Figure 4.5 - Cumulative frequency of fracture spacing for the fracture patterns observed in Figure 4.3 based on a scanline at x = 5 m.

Figure 4.5 is the fracture spacing distribution along the scanline (x = 5 m) at 19 my of propagation time. For k ~ 0 and 1 nD cases, their distribution curves are almost

identical with spacing range from 4 m to 0.6 m. The higher-permeability rocks, 1 mD and higher, their distribution also look similar with broad spacing range, from 5.7 m to 1 m. The large fracture spacing of 5.7 m in 1 mD or higher rocks corresponds to the distance between fracture clustering sets. The lower end of the four distribution curves is around 0.6 to 1 m, which is the spacing between individual fractures and it is very small compared to the layer thickness of 4 m. The results is consistent with the field observation of closely spaced fractures in shales that low permeability makes the clustering away at high subcritical index condition, which helps the generation of closely spaced fracture pattern.

4.3.3 Fracture size distribution

4.3.3.1 Aperture and length distribution

Figure 4.2 and 4.3 are the pattern illustration of fracture length and aperture distribution. In this part, I will examine the distribution of fracture attributes, aperture (Figure 4.6A) and length (Figure 4.6B), and whether their distribution can be a good representation of the trace and aperture maps.

Figure 4.6 illustrates that fractures developed in k ~ 0 rock are very short, where the longest half-length is less than 1 m; these fractures are also thin as the maximum fracture aperture is approximately 2×10^{-4} m. In addition, the range of aperture and half-length values are smaller in low-permeability rocks, indicating fractures are growing in a similar pace and not disturbing each other significantly. On the other hand, in high-permeability rock, one long fracture can reach the boundary set by the numerical model and the aperture for this longest fracture is also large. This corresponds to the fracture located at the center of the rock shown in Figure 4.3D, where no other fractures can grow around that dominating fracture.

Generally, the distribution of fracture half-length in k ~ 0 and 1 nD rocks is less broad than that in 1 mD and infinitely large permeability rocks. This implies the majority of fractures are able to grow in low-permeability rocks; therefore, a closely spaced fracture pattern can be obtained in rocks with low permeabilities, such as shales.

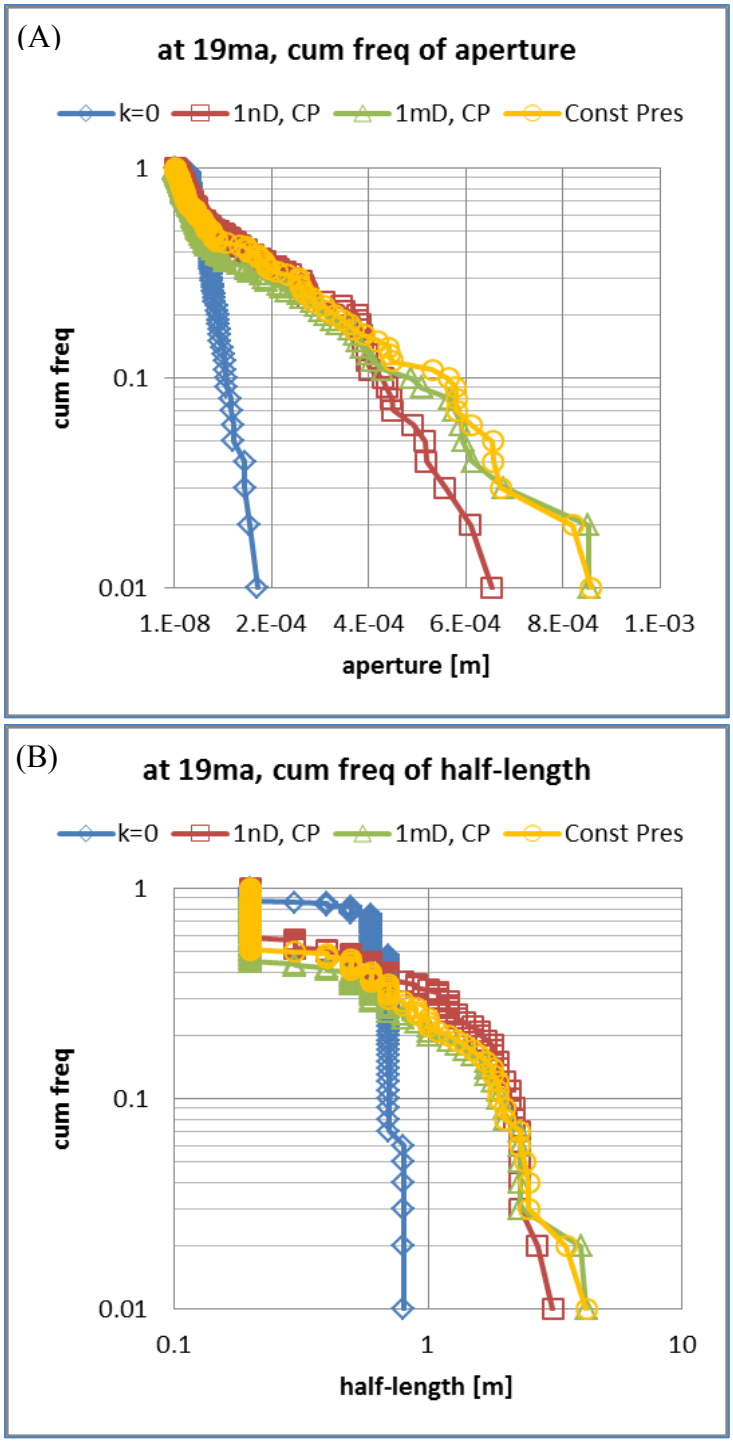

Figure 4.6 - The cumulative frequency plots of fracture attributes with n = 80, T = 4 m and constant pressure boundary condition: (A) aperture plot, (B) half-length at 19 my.

4.3.3.2 Aperture versus length correlation

Aperture to length correlation is found to follow linear, sublinear and superlinear functions as discussed in Section 4.2.4. Figure 4.7 are the fracture aperture to length plots at 11 my (Figure 4.6A) and 19 my (Figure 4.6B) respectively. Three curve fittings, with slope of 2, unit and ½, are plotted together with the aperture to length data, which correspond to the superliner, linear and sublinear correlation as predicted and observed in Section 4.2.4.

Linear correlation is predicted by LEFM theory for non-interacting fractures, which have the same driving stress for their propagation. Olson (2003) proposed a square root correlation by assuming the stress intensity factor is kept the same for the non-interacting fractures. This condition may be met during natural hydraulic fracturing process or with fixed displacement loading. Superlinear correlation is proposed by Renshaw and Park (1997) who concluded the importance of mechanical interaction between fractures, leading to the superlinear correlation between aperture and length. In this study, all the fractures are interacting with each other by mechanical interaction and fluid flow competition inside reservoir. At early stages (Figure 4.7A), the aperture to length data for 1 nD rock case is mainly located in the sublinear region between unit slope and ½ slope, indicating fractures are interacting with each other and fluid flow is the more dominating process. At late stages (Figure 4.7B), the data points are distributed in the region with superlinear correlation, indicating the mechanical interaction is more dominating the pattern now. For the low-permeability case, large scatter in natural data is obvious because of both the natural hydraulic fracturing and fracture mechanical interaction mechanisms play a significant role at different stage of the pattern development.

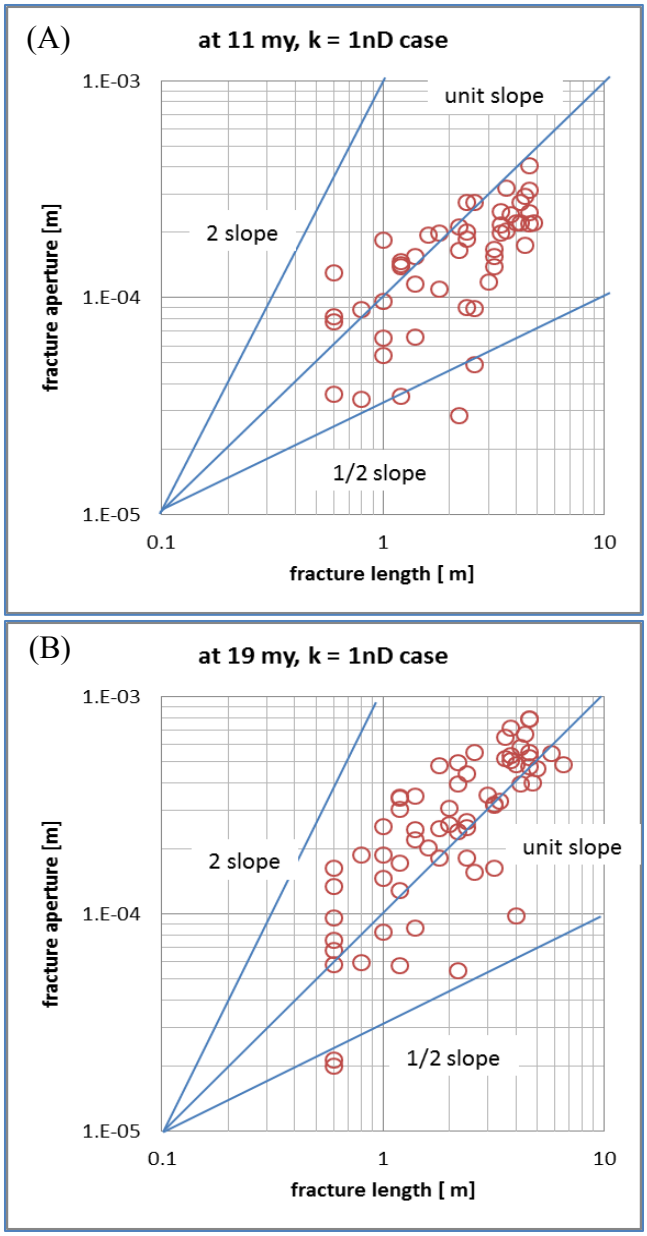

Figure 4.7 - Aperture versus fracture length plots with n = 80, h = 4 m, and constant pressure in 1 nD rocks at (A) 11 my, (B) 19 my.

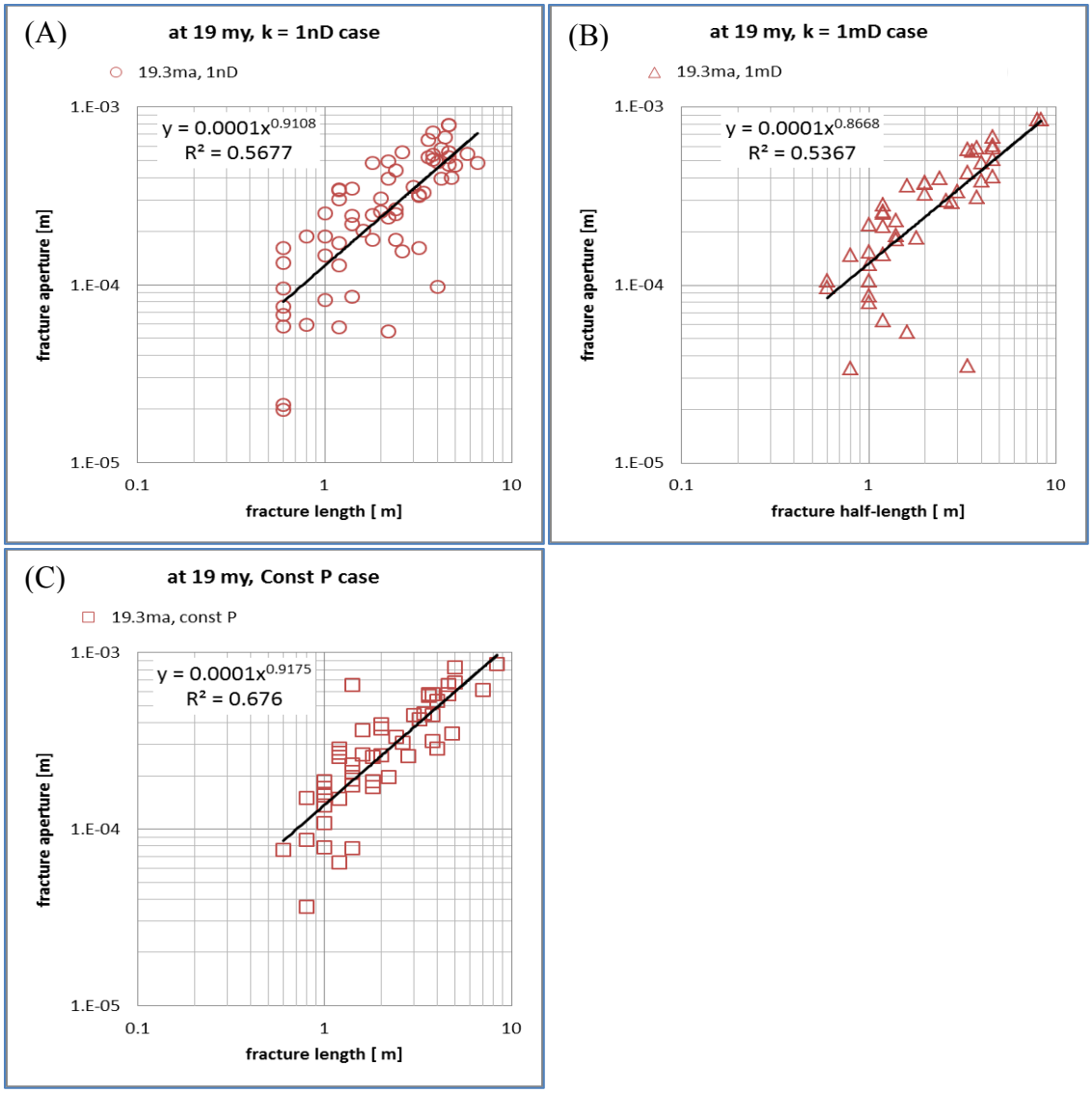

Figure 4.8 - Aperture versus length plots with n = 80, h = 4 m and constant pressure boundary condition at late stage of 19 my: (A) 1 nD, (B) k = 1 mD, (C) constant pressure case. The fitting curves follow power-law shapes.

The aperture versus fracture half-length plots in Figure 4.8 show a power-law distribution for 1 nD (Figure 4.8A), 1 mD (Figure 4.8B) and constant pressure case (Figure 4.8C) at the growth timing of 19 million years since the remote strain applied. The exponents in all three cases are quite similar, all close to one. This may be related to

the numerical limit the model set that the fractures cannot grow beyond the reservoir boundary. More scattering in data is observed in Figure 4.8A for 1 nD rock, whereas the data follows a power-law distribution in the constant pressure case (Figure 4.8C). The difference in data scattering between these two cases could be related to the rock permeability and the corresponding fracture fluid pressure recovery process. In the constant pressure case, fracture fluid pressure is constant everywhere and at all times; whereas in 1 nD case, low permeability leads to slow fluid pressure recovery rate and different fluid pressure inside each fracture. Fracture aperture is directly related to fracture fluid pressure, thus, the scattering in data is observed.

The subcritical index is chosen at 80 for this case study because it is also the value measured for some shale samples in the lab (Gale and Holder, 2010). The classic geomechanical model predicts fracture clustering (swarm) pattern would dominate the fracture pattern with broad distributions of fracture spacing, length and aperture. The study in this section shows that the low permeability makes the clustering patterns away by bringing the fluid flow effect. Lower permeability leads to slower fluid rate and fracture internal pressure recovery. This prevents long fractures from getting longer and makes other fractures less affected by the long fracture's stress shadow. This also allows short fractures more time to grow. Therefore, more fractures tend to grow at relatively similar pace and form a closely-spaced pattern, which is lack of any clustering. In high-permeability rocks, the fluid recovery is fast and constant pressure is maintained for fractures to grow. Thus, the mechanical interaction (stress shadow effect) is the more dominating factor over the pattern development.

4.4 POROELASTIC P3D GEOMECHANICAL MODEL: OTHER KEY IMPACTS

4.4.1 Bed thickness effect

Bed thickness effect will be examined in this section by adjusting its value to 2 m and keeping all other parameters the same. The fracture aperture (Figure 4.9) and half-length (Figure 4.10) distributions are shown below.

In 1 nD rock, Figure 4.9A indicates the fracture aperture distribution is not very sensitive to the layer thickness at early time. This is because at early stages, crack propagation is slow and their length is short, even compared to the layer thickness. Thus, crack growth is not confined by the layer thickness yet and its aperture is not sensitive to the layer thickness. At later stages, fractures tend to have more long fractures and a wider distribution of apertures in thicker beds. In comparison, for 1 mD rock, fracture aperture distribution is sensitive to the layer thickness at early and late stages. The trend is consistent with that observed for 1 nD rock; thicker beds will result in longer fractures and wider ranges of aperture distribution.

Figure 4.10A implies layer thickness has a small effect on fracture length distribution in 1 nD rock, whereas in 1 mD rock, more long fractures are observed in the thin bed. The classic geomechanical model claims the stress shadow size scales with layer thickness. The thinner the bed, the smaller the stress shadow, therefore more fractures can grow and more long fractures are observed in Figure 4.10B. For low permeability rock, the slow fluid rate already relaxes the stress shadow effect; thus, the thinner layer will not affect the fracture pattern significantly in 1 nD rocks.

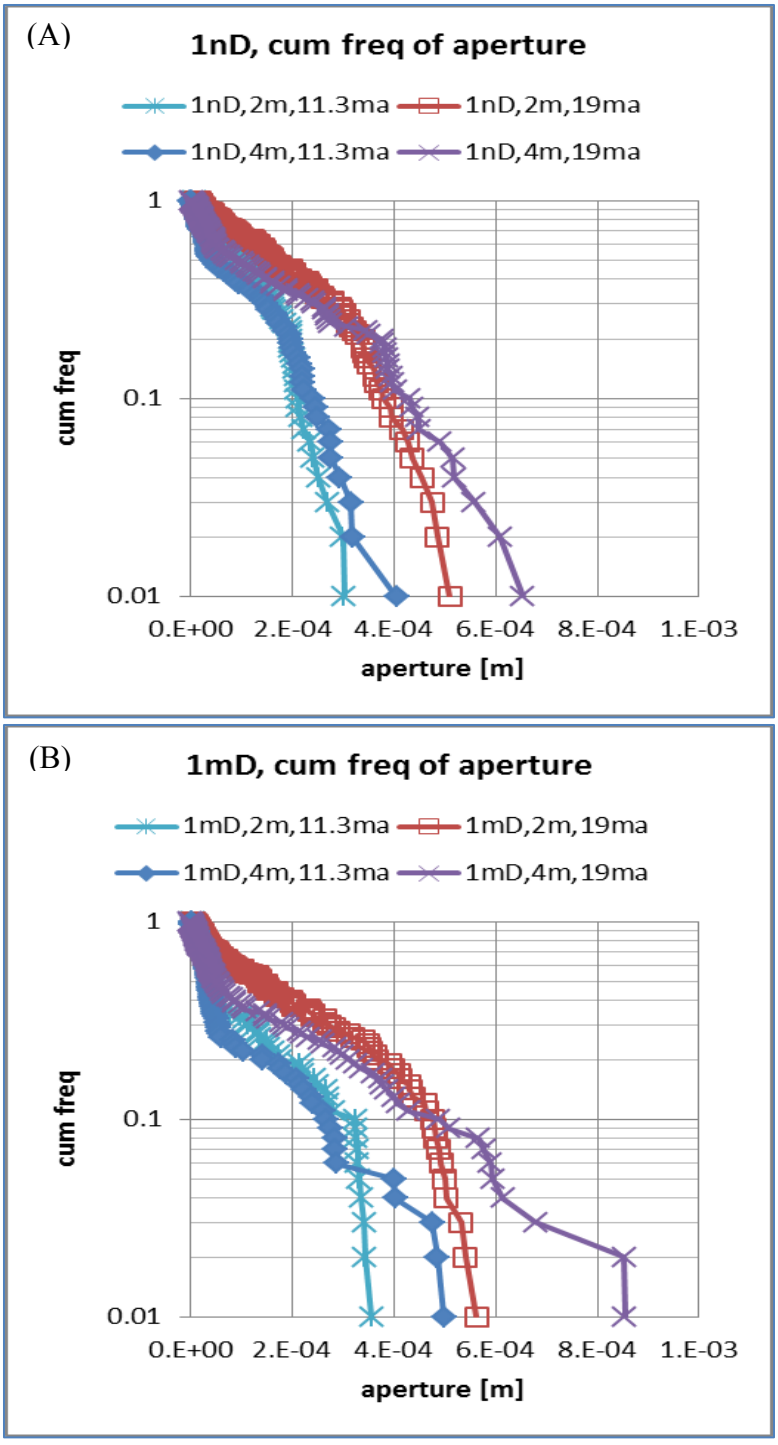

Figure 4.9 - The cumulative frequency plots of fracture aperture with n = 80, T = 2 m and constant pressure boundary condition: (A) 1 nD, (B) 1 mD at 11.3 and 19 my (ma).

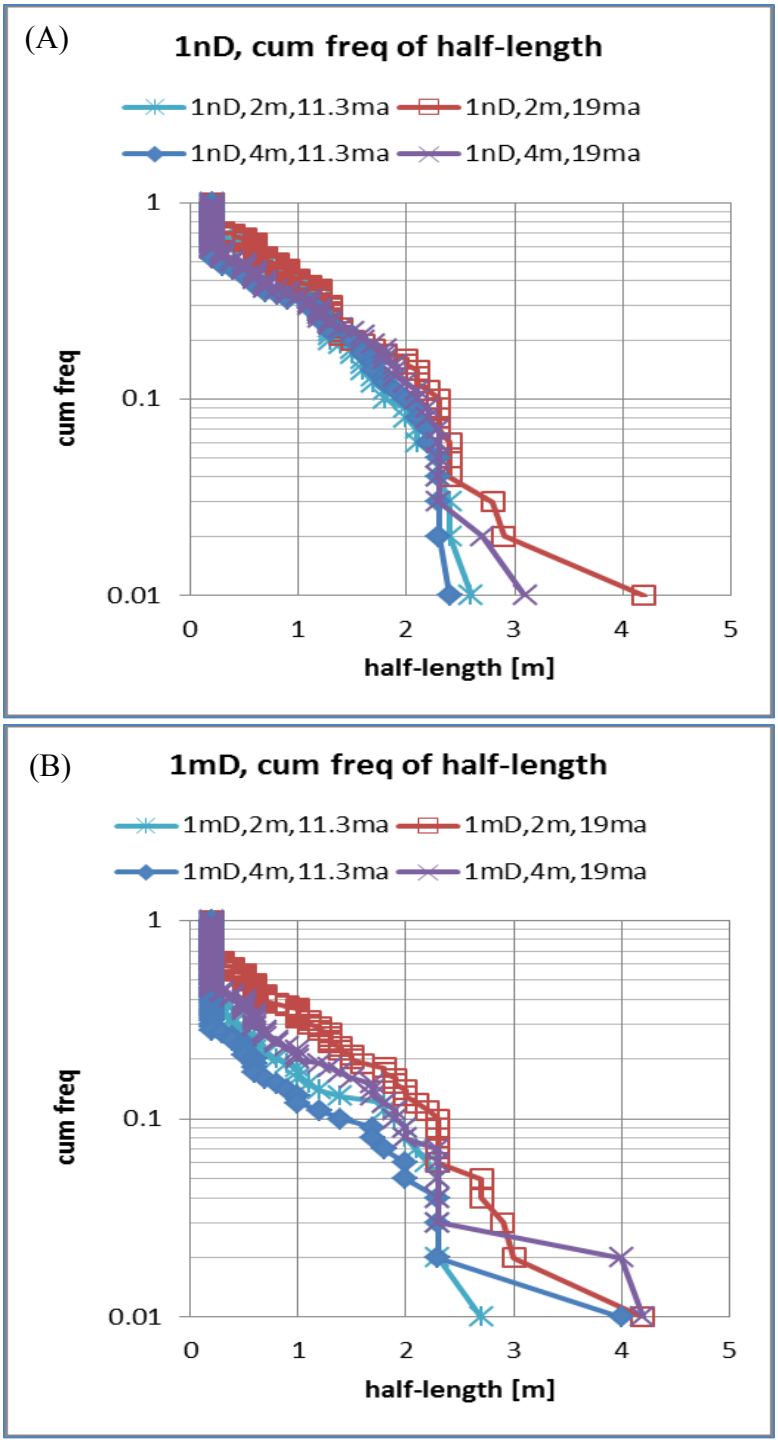

Figure 4.10 - The cumulative frequency plots of fracture half-length with n = 80, T = 2 m and constant pressure boundary condition: (A) 1 nD, (B) 1 mD at 11.3 and 19 my (ma).

4.4.2 Boundary condition effect

The importance of reservoir boundary conditions has been extensively discussed in the previous chapters. Boundary conditions not only affect the fluid flow in porous media, but also influences fracture propagation rate and the consequent pattern development for multiple fractures. The effect of boundary conditions will be tested in both low- and high-permeability rocks by varying between constant pressure and no-flow conditions.

Figures 4.11A and 4.12A imply that the boundary condition has little influence on fracture attribute distribution in 1 nD rocks, though fracture apertures are slightly smaller under a no-flow condition than a constant pressure condition at late stages.

Unlike in low-permeability rocks (1 nD), fractures in high-permeability rocks (1 mD, Figure 4.11B and 4.12B) are more sensitive to the boundary condition throughout the early and late development stage. There are fewer wide and long fractures under the no-flow condition than the constant pressure condition, indicating the limited fluid flow from reservoir boundary has a direct effect on the interior fracture propagation by affecting the fracture fluid pressure recovery rate. The influences of boundary condition on fractures in low-permeability rocks are less significant because the fluid flow is already very slow due to the low permeability of porous media.

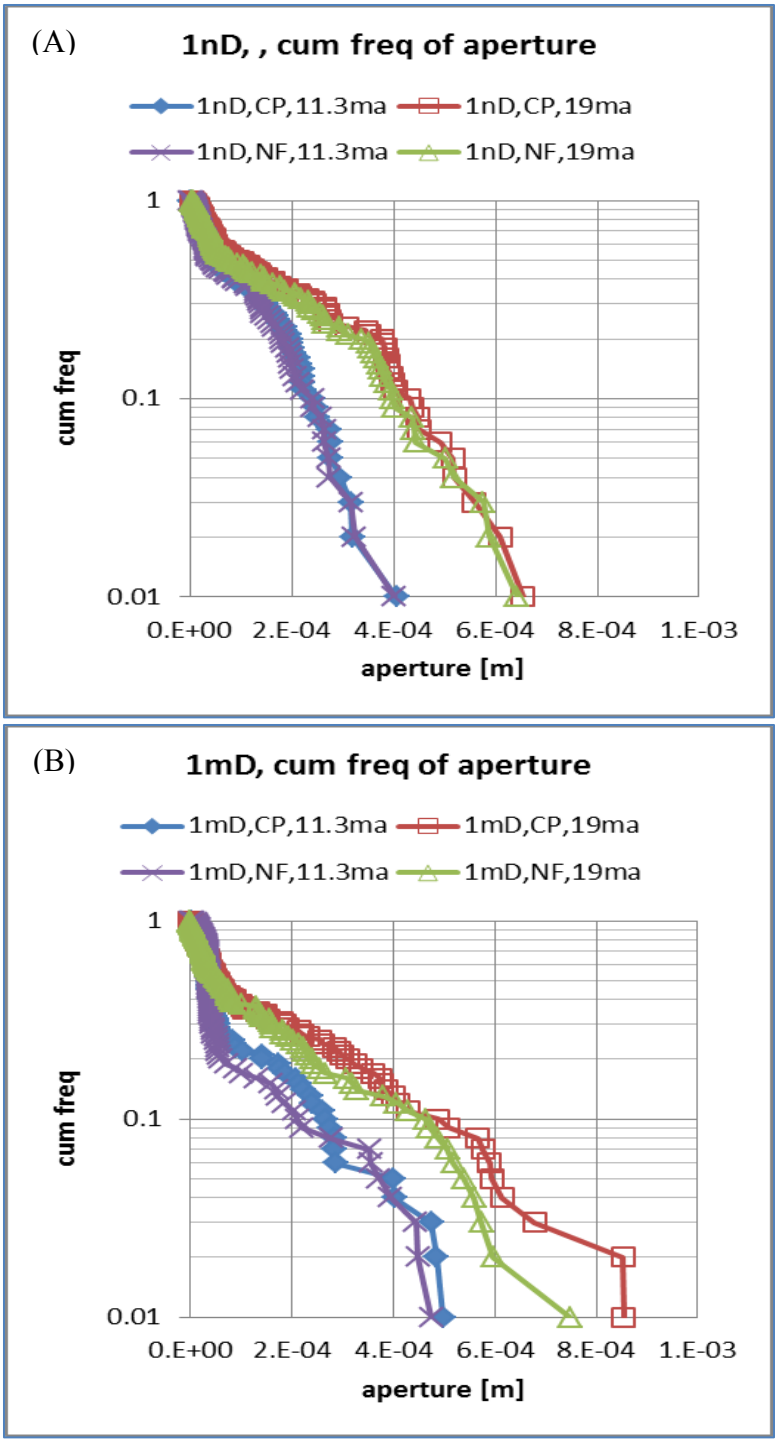

Figure 4.11 - The cumulative frequency plots of fracture aperture with n = 80, T = 4 m and no flow boundary condition: (A) 1 nD, (B) 1 mD at 11.3 and 19 my (ma).

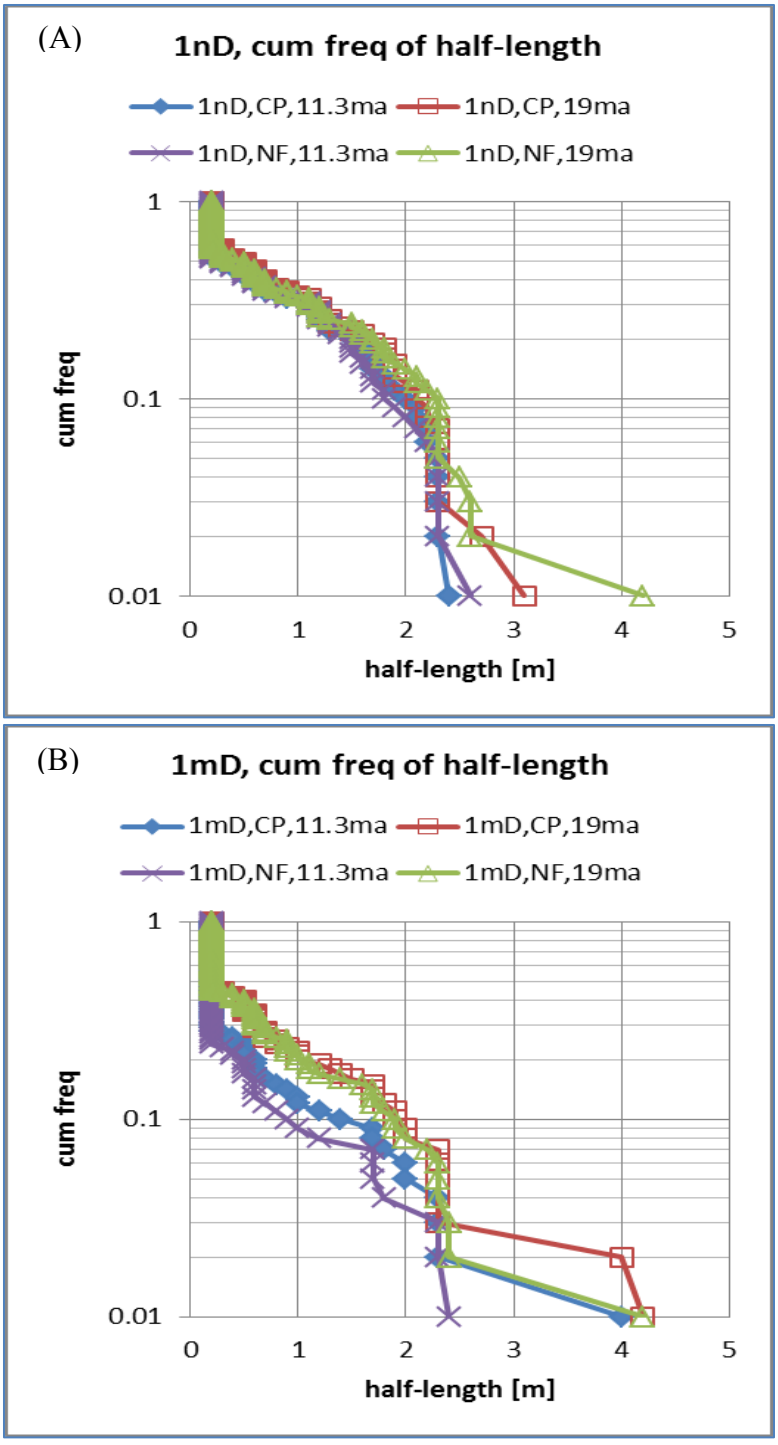

Figure 4.12 - The cumulative frequency plots of fracture half-length with n = 80, T = 4 m and no flow boundary condition: (A) 1 nD, (B) 1 mD at 11.3 and 19 my (ma).

4.4.3 Subcritical index effect

The classic geomechanical modeling work states that layer thickness and subcritical index are the two key factors controlling fracture pattern development assuming that constant pressure is maintained inside the fracture because of the sufficient fluid supplied by porous media. In reality, the fluid drive from porous media relies on the permeability of host rock. The coupling effect of rock permeability and subcritical index is examined in this section.

Figure 4.13A indicates 1 nD rock aperture distribution is almost insensitive to subcritical index, and Figure 4.14A shows subcritical index only impacts the tail part of the half-length distribution. This implies that in low-permeability rock, the fluid flow is a more dominating process over the mechanical interaction process which highly depends on subcritical index.

On the other hand, for 1 mD rock shown in Figure 4.13B and 4.14B the fracture aperture and half-length are more sensitive to the subcritical index. As explained in Section 4.4.1, mechanical interaction is more controlling the pattern development and fluid flow is less important because the high permeability of the rock set all the fractures away from fluid lag for their propagation. Therefore, subcritical index affects fracture pattern development in high-permeability rock, but not very key to the low-permeability case.

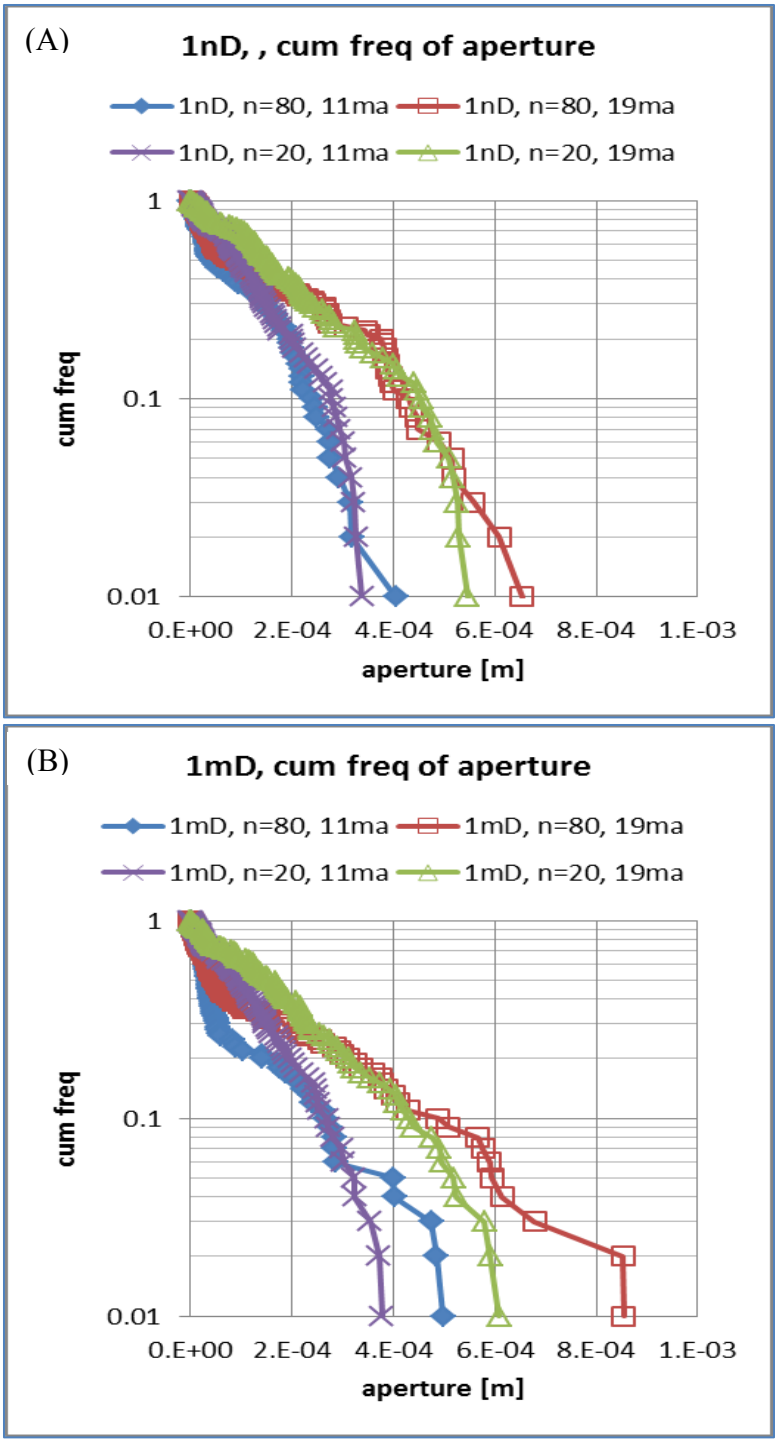

Figure 4.13 - The cumulative frequency plots of fracture aperture with n = 20, T = 4 m and constant pressure boundary condition: (A) 1 nD, (B) 1 mD at 11.3 and 19 my (ma).

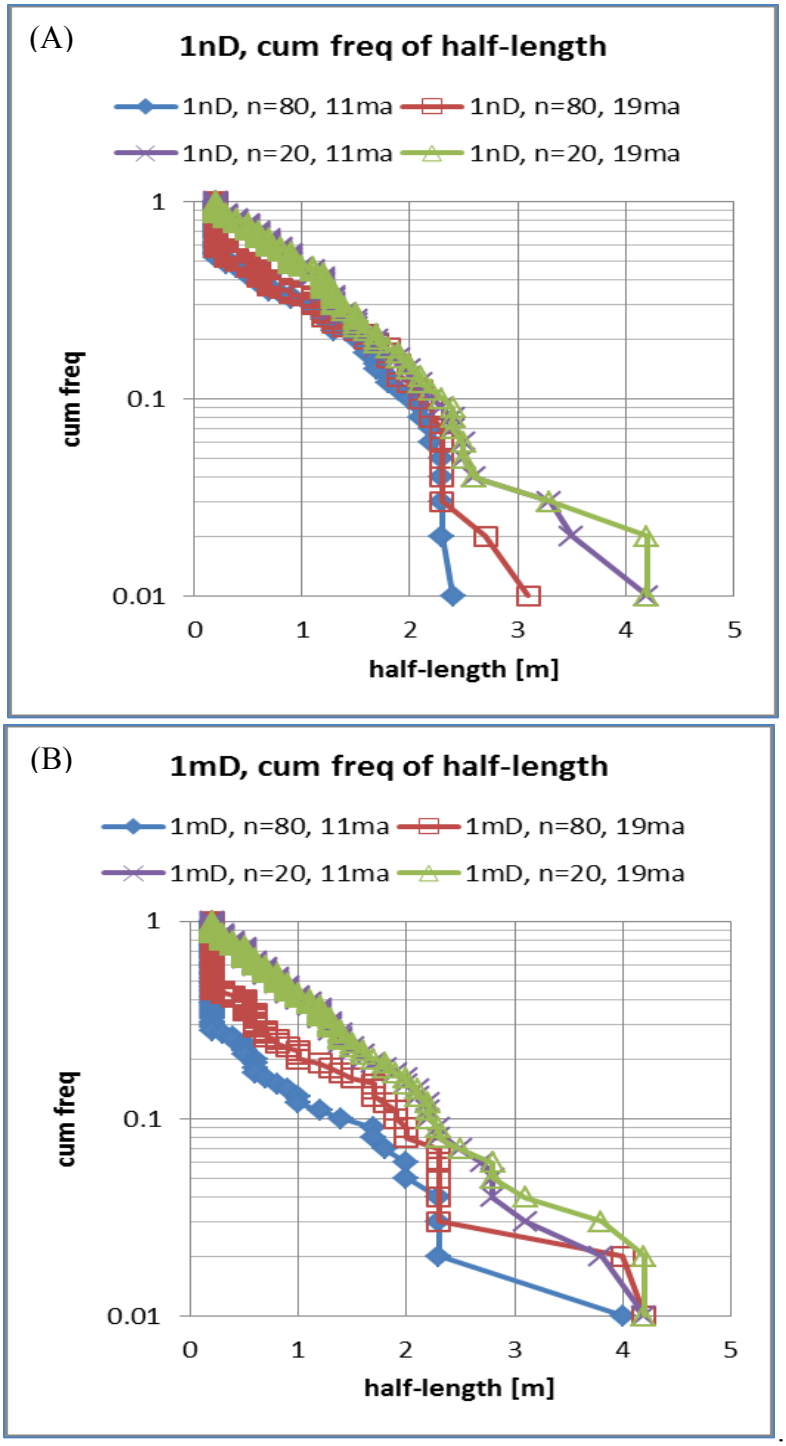

Figure 4.14 - The cumulative frequency plots of fracture half-length with n = 20, T = 4 m and constant pressure boundary condition: (A) 1 nD, (B) 1 mD at 11.3 and 19 my (ma).

4.4.4 Summary on fracture spacing

Fracture attribute distributions have been investigated regarding various bed thickness, boundary condition and subcritical index. The low and high values of the factors are defined in Table 4.3 below:

Table 4.3 Definitions of the low and high values for the parameters chosen for sensitivity study

Definition	**Low value**	**High value**
Bed thickness [m], *h*	2	4
Subcritical index, *n*	20	80
Boundary condition, *BC*	No flow (NF)	Constant pressure (CP)
Propagation duration [ma]	11.3	19

Table 4.4 Summary of the fracture spacing calculated with line method for Chapter 4.

Permeability, k	***h* [m]**	**BC**	***n***	***S* [m] @ 11.3 ma**	***S* [m] @ 19 ma**
1nD	4	CP	80	2.1	1.7
1mD	4	CP	80	4.4	2.7
1nD	2	CP	80	1.7	1.4
1mD	2	CP	80	2.5	1.7
1nD	4	NF	80	2.1	1.8
1mD	4	NF	80	5.7	2.7
1nD	4	CP	20	1.4	1.4
1mD	4	CP	20	1.5	1.5

Figure 4.15 is the plot of fracture spacing from the sensitivity study conducted in Section 4.4.1-3. Generally, fracture spacing is smaller in low- than high-permeability rocks. Moreover, fracture spacing decreases in both rock types as fracture growth duration increases.

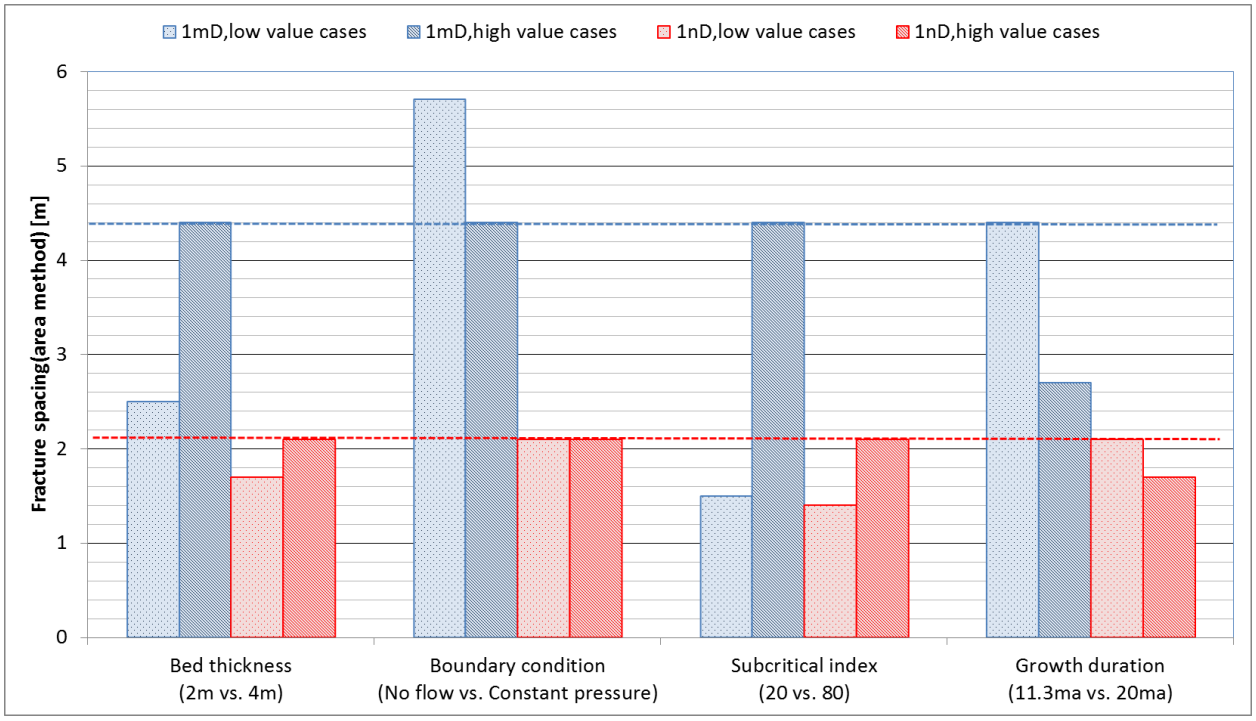

Figure 4.15 - Sensitivity plots of fracture spacing obtained via line method for both 1 nD and 1 mD rocks. Base case: subcritical index at 80, bed thickness of 4 m, and constant pressure boundary condition and growth duration at 11.3 my (ma), where average fracture spacing is 4.4 m for 1 mD rock(blue dash line) and 2.1 m for 1 nD rock(red dash line).

For fracture pattern developed at 11.3 my in high-permeability rock, the average fracture spacing decreases from 4.4 m in 4 m bed to 2.5 m in 2 m bed, suggesting a linear correlation between fracture spacing and bed thickness. In contrast, fracture spacing is much smaller in low-permeability rocks, about 2.1 m in 4 m bed and 1.7 m in 2 m bed. The difference in fracture spacing between low- and high-permeability rocks is more significant in thick bed than thin bed.

The fracture spacing in low-permeability rock appears insensitive to the reservoir boundary condition, whereas in high-permeability rock, spacing is much larger with no-flow than the constant pressure condition.

The fracture spacing in high-permeability rock is more sensitive to subcritical index than in low-permeability rock. When subcritical index is low, the difference of fracture spacing in high- and low-permeability rocks is negligible. This indicates fracture spacing is insensitive to reservoir permeability for fracture pattern developed with low subcritical index.

4.5 DISCUSSIONS

4.5.1 Fracture opening rate versus cement precipitation rate

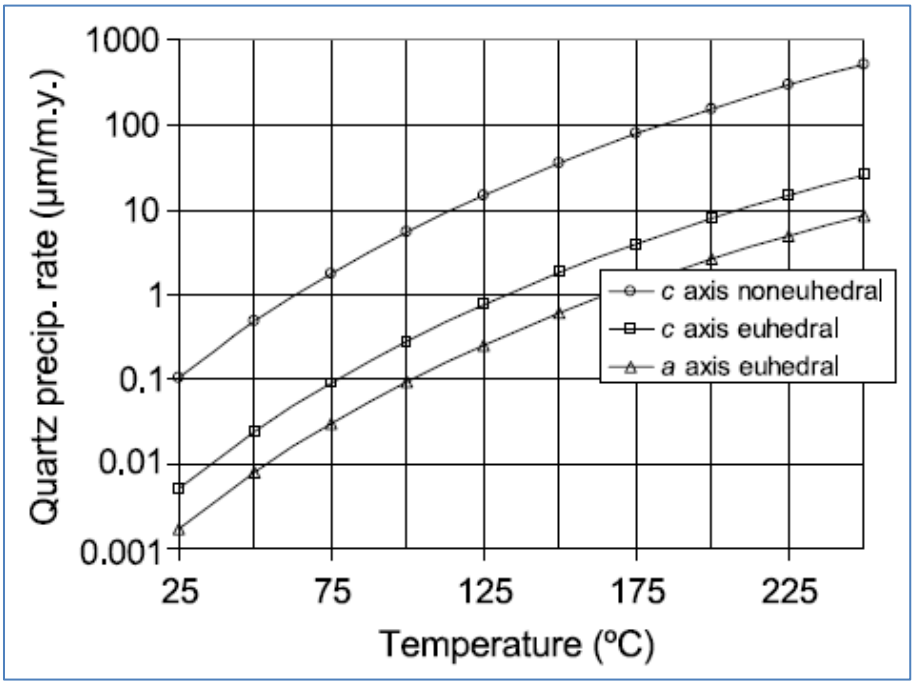

Figure 4.16 – Quartz precipitation rate (micrometers/my) as a function of temperature and three growth directions and crystal facies (from Olson, et al., 2009).

The competition between cement precipitation rate and fracture opening rate determines whether the fracture is fully or partially filled with cement. Quartz growth rate is a function of temperature and estimated by the Arrhenius expression (Walderhaug,

1994, 2000; Lander et al., 2008). Assuming the formation temperature is approximately 150 ^{0}C and quartz grows parallel to c axis on euhedral crystals, the quartz precipitation rate is approximately 5 μm/my. If the fracture opening rate is lower than quartz growth rate, the fracture will be completely filled with quartz, which leads to no fracture porosity. On the other hand, the fracture will be partially filled with cement when the fracture opens faster than the quartz precipitates. The fracture opening rate is obtained by estimating the change in fracture aperture throughout the 25 million year growth period. Figure 4.16 shows the distribution of the propagated fracture aperture vary with time in both extremely low-permeability rocks (k ~ 0 case) and infinitely permeable (constant pressure case) rocks. Three values, maximum, mean and 20% of fracture aperture, are extracted from each plot, which correspond to a specific timing during the 25 my propagation period. These aperture values are plotted as a function of propagation time in Figure 4.17, together with the quartz thickness growth curve at the constant precipitation rate of 5 μm/my.

There are eight plots on Figure 4.17A, corresponding to the aperture distribution curves at eight different stages during fracture pattern development, from initiation time around 8 my to the end of simulation at 25 my for the extremely small permeability case (k ~ 0). Figure 4.17B is the same plot but for infinitely large permeability rock. The obvious observation is the fracture aperture is distributed on a much higher end for constant pressure case than the k ~ 0 case. Moreover, aperture curves on Figure 4.17A indicate its distribution function transient from power-law to negative-exponent beyond almost 14 my. Details about the power-law distribution of aperture in low-permeability rock at early stages will be discussed in Section 4.5.2. The aperture curves on Figure 4.17B all show negative exponent distributions and they are located on the high end

indicating wide fractures are observed in high-permeability rock under constant pressure condition.

By analyzing the maximum, mean and 20% of maximum aperture values, a plot of fracture opening rate in competition with cement precipitation rate is shown in Figure 4.18. For k ~ 0 case (Figure 4.18A), fracture apertures are relatively small when fracture growth is initiated. As the fracture is opening, the cement precipitation rate may exceed some fracture's opening rate, which will lead those fractures sealed by quartz. In the constant pressure case, the fracture openings are much larger compared to the quartz precipitation rate during any stage of the propagation. Therefore, the quartz will not be able to seal the fractures.

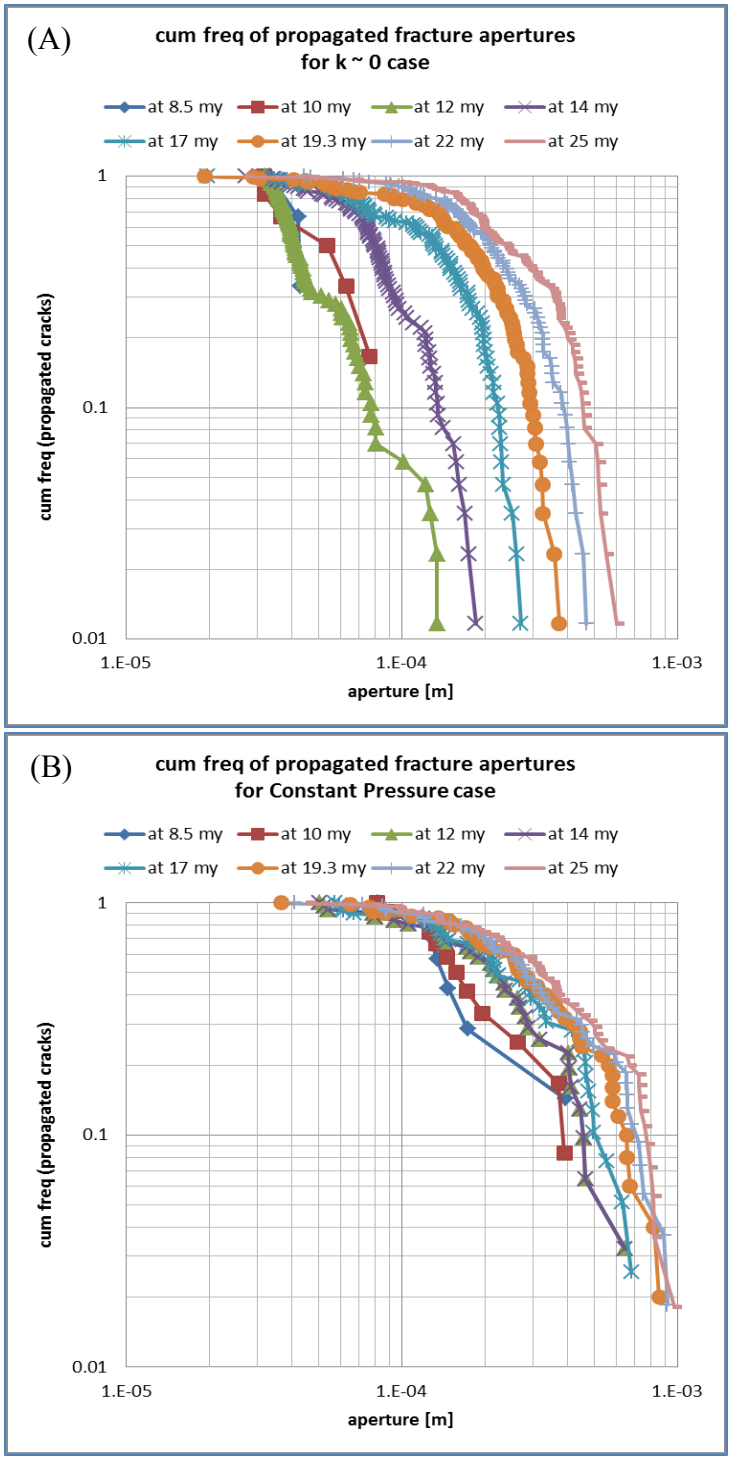

Figure 4.17 – The cumulative frequency plots of propagated fractures in (A) k ~ 0 and (B) constant pressure case throughout the 25 my growth timing.

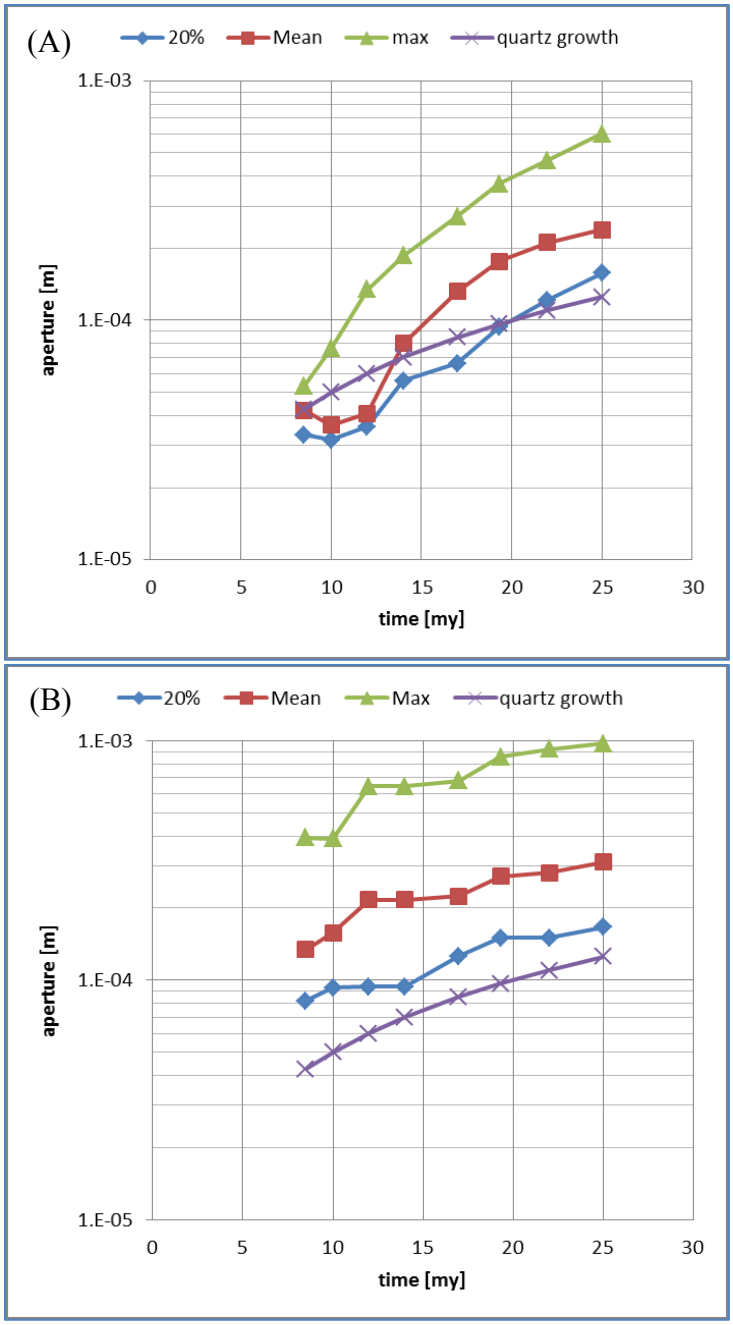

Figure 4.18 – Fracture aperture and estimated quartz thickness vs. time for the 25 my simulation conducted in Section 4.2 for (A) k ~ 0 case and (B) constant pressure case. The aperture data is summarized by plotting the maximum, mean and 20 percentage value on fracture aperture cumulative frequency plot. Quartz growth starts at the same time as fracture growth in the simulation at a constant precipitation rate of 5 μm/my.

4.5.2 Effective porosity

Effective porosity is a parameter used to characterize the relative void volume of the fractures with respect to the whole reservoir area where the fractures are propagating. The fracture volume is calculated approximately by multiplying fracture length by opening and summing the fracture volume. Fracture volume divided by reservoir volume is the effective porosity. The effective porosity is plotted as a function of grow duration for both k ~ 0 and k ~ infinitely large cases.

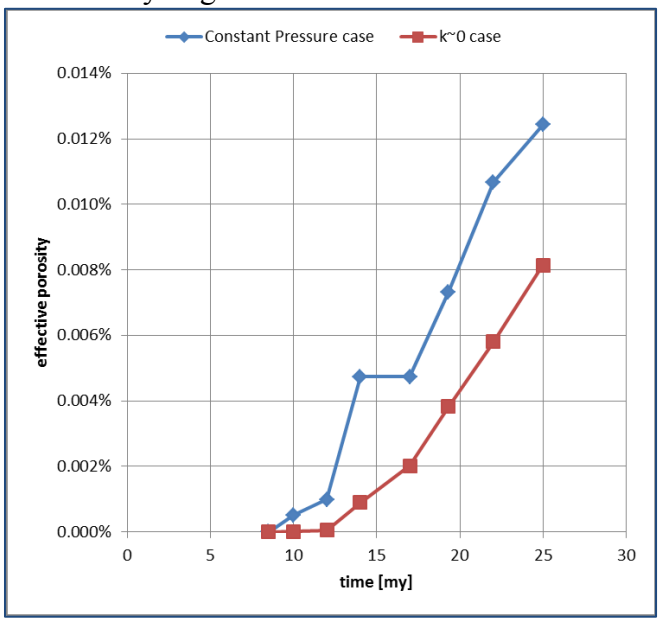

Figure 4.19 – Effective porosity calculated for the fracture patterns developed in k ~ 0 and k ~ infinitely large rocks.

Figure 4.19 indicates the effective porosity in the constant pressure case is generally larger than that in k ~ 0 cases. Initially, not much of the fracture propagated; the porosity in both cases is close to zero. At the end of the simulation, the porosity in the constant pressure case is around 0.013%, 50% higher than that of 0.008% in k ~ 0 cases. Moreover, Figure 4.18B indicates the fracture opening may be filled by cement and cannot act as a fluid conduit for fluid flow, which will lower the effective permeability

and porosity of the cemented rocks. For production in low-permeability rocks, like shale, it is important to characterize the fracture attribute distribution and estimate the fracture opening rate and cement precipitation rate, therefore a better understanding of the percentage of open or partially open or totally closed natural fractures in a given fracture set. Open or partially open fractures can act as a fluid conduit for the fluid stored inside the low-permeability rocks, like shale. An accurate description of the natural fracture opening or sealed population distribution and attribute distribution are required to estimate the effective permeability of the naturally fractured reservoir rock for the drilling and production purpose.

4.5.3 Power-law distribution for fracture aperture

The majority of the aperture distributions observed in the field follows a power-law distribution, while the numerical results tend to produce negative exponent function for aperture distribution. The curve fitting plots for aperture distribution in both k ~ 0 and constant pressure case are shown in Figure 4.20A for early stage (12 my) and Figure 4.20B for late stage (19 my). At early stage, 12 my, the fracture aperture distribution follows a power-law function (R^2 = 0.97) in k ~ 0 case. The reason is the fractures in extremely low-permeability rock are relatively short, much shorter than the layer thickness, which makes the fracture behave as unbounded. Gillespie et al. (1999) predicts that the bounded fracture aperture follow power-law distribution, while the aperture distribution becomes more negative exponent for stratabound fractures. The negative exponent function fit the aperture data both k ~ 0 (R^2 = 0.86) and constant pressure cases (R^2 = 0.96) better (Figure 4.20B).

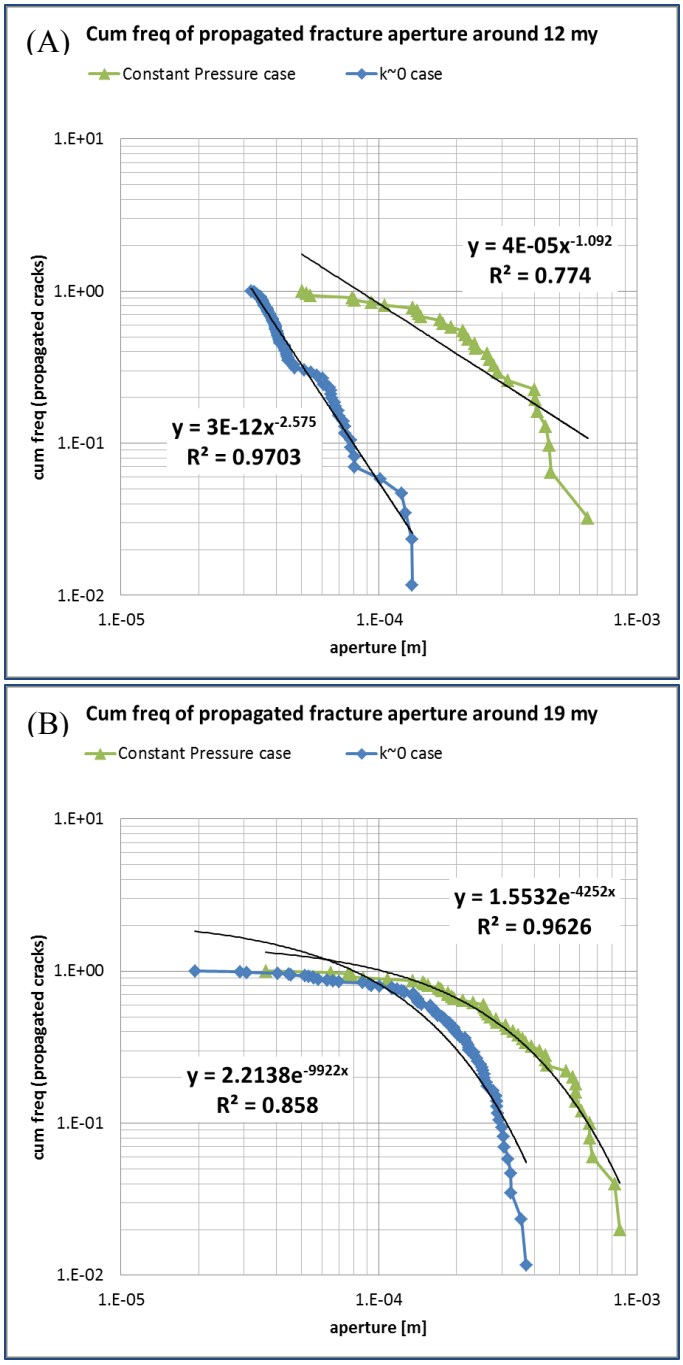

Figure 4.20 - The cumulative frequency plots of fracture aperture with n = 80, T = 4 m and constant pressure boundary condition in k ~ 0 and k ~ infinitely large rocks at (A) 12 my (B) 19 my since the strain is applied. Curve fittings are plotted on the figure too.

4.6 CONCLUSIONS ABOUT THE PERMEABILITY EFFECT ON FRACTURE PATTERN DEVELOPMENT AND ATTRIBUTE DISTRIBUTION

The coupled fluid flow and geomechanical model effectively simulates multiple natural hydraulic fracture propagation in poroelastic media. This technique enables the study of how the reservoir and geomechanial properties simultaneously affect multiple fracture pattern development and attribute distribution. The study results show that permeability is a key factor controlling fracture pattern development, especially with high subcritical index and large layer thickness. The low permeability slows the fluid flow rate from porous media into fractures, which makes the long fractures stop their propagation and wait a long period of time for the internal fluid pressure to recover for the next growth event. Therefore, small stress relief is introduced by the long fractures and all the fractures tend to propagate at similar rate in low-permeability rocks. This leads to a fracture pattern lack of clustering and consisted of more intermediate length and openness fractures in low-permeability rocks. Moreover, the fractures are more closely spaced in low-permeability rocks than in high-permeability rocks. In high-permeability rocks, the fracture patterns generated under constant pressure boundary condition look similar to those predicted by the classic genomechanical models. This indicates the constant pressure assumption in the classic models is valid for highly permeable rocks.

Other factors, such as bed thickness, reservoir boundary condition, and subcritical index and fracture growth duration, have significant influences on fracture pattern development and attribute statistics as well. Generally, fractures grow in length and aperture with time and they are spaced more closely under a constant pressure boundary condition. The bed thickness and boundary condition have much stronger influences on fracture size distribution and average spacing in high-permeability rocks. In addition, subcritical index has strong effects on fracture pattern development in both low- and

high-permeability rocks. With low *n*, fracture patterns become well-developed earlier and fractures are spaced much closer to each other. The pattern development seems insensitive to reservoir permeability with low subcritical index.

Based on the fracture attribute distribution curves, fracture opening rate can be estimated and compared to quartz precipitation rate. The competition between fracture opening and quartz precipitation determines the natural fracture open, or partially open or totally sealed. The simulation results show fractures are more likely to be sealed in low-permeability rocks. This will affect the effective permeability and total porosity of the naturally fracture reservoir and has a big influence for drilling and production, especially in very low-permeability reservoirs.

Moreover, a power-law function for aperture distribution is observed in the fracture pattern development in low-permeability rocks at 12 million years since the strain is applied. Because fractures grow very slow in low-permeability rocks due to fluid lag, their propagation speed is slow which makes the propagation duration is long and the growth in length and aperture is small as well. The aperture follows power-law function indicating the fracture sets behave like unbounded in the field. In low-permeability rock, fluid flow is the dominating factor for the pattern development at high subcritical index in low-permeability rocks.

Chapter 5: Conclusions and Recommendations

This study focuses on investigating the fluid flow's impacts on multiple natural fracture propagation and pattern development in poroelastic media. The growths of natural hydraulic fractures (NHF) are driven by fluid loading. To investigate the importance of fluid flow in natural hydraulic fracture propagation process, two new poroelastic models have been developed, which combine the effects from the fluid flow inside the reservoir and the mechanical interaction of multiple fractures. Sensitivity studies were performed to investigate the influences of reservoir permeability, boundary condition, and subcritical index and some other factors on multiple NHF growth and pattern development.

Many field observations and lab measurements indicate that the natural hydraulic fractures extensively exist in rocks and some of their growth durations are surprisingly long, on the scale of millions of years. To study the natural hydraulic fracture propagation process and timing numerically, it is desired to set up a numerical model, which can not only capture the fluid flow communication between porous media and propagating fractures, also consider the population effect of multiple fractures. Based on the two-dimensional diffusivity equation and effective media theory, the new effective media model is capable of calculating the pressure distribution within the entire reservoir, updating fracture internal fluid pressure and capturing a fracture's crack-seal process.

The sensitivity study shows that reservoir permeability has a significant influence on fracture propagation process. Fracture propagation behavior in high-permeability rocks is consistent with the analytical results where the fracture internal pressure is assumed constant throughout the entire growth duration. In low-permeability rocks, fractures have more stable initiation and much longer propagation duration compared to

those in high-permeability rocks. Reservoir boundary condition affects the average reservoir pressure, which leads to a much slower fracture growth with no flow boundary condition than constant pressure boundary condition. In addition, fractures tend to have a slower propagate rate with higher initial fracture density, slower remote strain rate, and larger subcritical index and PKN fracture geometry model. The simulation results prove the hypothesis that fluid flow affects natural hydraulic fracturing process, especially in low-permeability rocks where the growth duration can be as long as millions of years.

Though the new effective media model is a simple and direct approach to numerically predict the timing of natural hydraulic fracture propagation with specific reservoir and geological settings, the model does not consider the fracture height effect and the mechanical interaction between neighboring fractures – both have a controlling influence on the relative spacing between stratabound multiple fractures. The classic fracture mechanics studies state that larger fracture spacing is observed with higher subcritical index and larger layer thickness with the assumption of constant fracture internal fluid pressure. However, the classic model fails to explain the field observation of extremely closely spaced fracture set in some sedimentary rocks. A new mechanism, natural hydraulic fracturing, is introduced into the classic fracture mechanics model to investigate the combing influences from fluid flow and mechanical interaction between multiple fractures. The numerical results obtained with this new model for high-permeability rocks agree with the classic model results where constant fluid pressure is assumed. As the permeability of host rock decreases, more fractures propagate and fracture spacing is smaller. The simulation results indicate low permeability creates a small pressure depletion area and less pressure interference between fractures, which slows down fracture propagation and prevents any long fracture from dominating the fracture pattern. As a result, more fractures are able to propagate at similar speed and a

smaller fracture spacing is achieved for the given multiple fracture pattern in rocks with low permeability. Other factors, such as boundary condition and initial fracture length, have considerable influences on fracture spacing as well. The new model provides insights into multiple fracture propagation process under the combined influences from pressure interference and mechanical interaction between neighboring fractures. Based on the numerical simulation results, an extremely close-spaced fracture pattern is possible in low-permeability rocks with certain settings of reservoir and geomechanical parameters.

Another topic of interest is how the fluid flow affects the fracture pattern development and the attribute distribution for multiple randomly distributed fractures. Most studies on natural fracture pattern characterization is either conducted in the field or performed by geomechancial modeling work. As natural hydraulic fracturing mechanism has shown significant influences on fracture propagation timing and relative spacing, the current geomechanical models should include this mechanism for a better representation of the underlying process and more accurate prediction of fracture attribute distribution. The new model developed in Chapter 3 is capable of studying how the reservoir and geomechanical properties simultaneously affect the fracture pattern development in poroelastic media. Thus, this model is applied to predict the pattern development and analyze the fracture attribute distribution under various reservoir and geomechanical conditions. The sensitivity study shows that permeability is a dominating factor which controls the pattern development, especially with high subcritical index and large layer thickness, which is very typical condition for shales. In low-permeability rocks, more fractures have intermediate length and aperture. There is no fracture clustering observed in the patterns, though fractures are spaced very closely to each other. On the other hand, the fracture pattern generated in high-permeability rocks has fracture clustering, very similar to those predicted by classic geomechanical models. In addition, the influences of

boundary condition, layer thickness, subcritical index and fracture pattern development stage cannot be ignored on fracture pattern development and the statistics of fracture attributes. Generally, the effective porosity of naturally fractured low-permeability rock is lower than that of high-permeability ones. From the fracture aperture distribution curve, fracture opening rate can be estimated and compared to the quartz precipitation rate. The competition between fracture opening and quartz precipitation will determine whether the fracture will be open or partially open or totally sealed by the cement. This will dramatically change the effective permeability and porosity of the naturally fractured rock, especially in low-permeability rocks, like shales.

In sum, the numerical simulation work in this study has shown that reservoir permeability has a large influence on fracture propagation timing, fracture spacing to layer thickness ratio and fracture attribute distributions for a set of multiple natural hydraulic fractures. Other factors, such as reservoir boundary condition, layer thickness and subcritical index, also affect the fracture pattern development. Moreover, the results indicate the natural hydraulic fracturing mechanism can explain the extremely long fracture growth duration and the closely-spaced fracture patterns in low-permeability rocks, which are massively observed in field and cannot be explained by classic geomechanical models. Lastly, this study provides a practical and robust approach to characterize natural hydraulic fracture pattern and predict the fracture attributes distribution with realistic settings of reservoir properties and geomechanical conditions.

The following recommendations are proposed for future research:

1. The current model only considers planar fracture propagation. The next step is to extend the model to non-planar fractures. It has been reported that fracture propagation path depends on remote differential stress, and fracture spacing and layer thickness given the fluid pressure is unchanged. It is necessary to examine the fluid flow effect on non-

planar fracture propagation path and the fracture pattern development. Possible stress rotations are expected in local stress field around non-planar fractures due to the fracture fluid pressure variations, especially in low-permeability rocks.

2. The effect of cement precipitation during the fracture opening process is not considered in the current model. Fracture growth and pattern development will be highly influenced by the cement growth during fracture opening process. As it is demonstrated in chapter 4 that quartz growth rate is comparable to fracture opening rate in low-permeability rocks, the diagenesis process are expected to have more significant impacts in low-permeability rocks. Therefore, it is desired to couple current model with cement growth model inside the opening fractures. Fractures can be sealed or partially open or totally open based on the competition between fracture opening and cement precipitation rates. This may explain the power-law distributions of fracture apertures which are massively observed from field data.

3. The fluid pressure distribution over the whole reservoir is updated every time step implicitly, which assures an accurate calculation for fracture fluid pressure. However, the fluid flow model is computationally heavy. There exists a tradeoff between computation speed and accuracy. A semi-analytical expression of fracture fluid pressure should be proposed as a function of time and fracture to replace the 2D fluid flow model. The semi-analytical expression should speed up the overall computation speed and provide an estimation of fracture fluid pressure, as long as the computation accuracy is maintained within an acceptable range. The new method of fluid pressure calculation will also enable the study on fracture systems of larger populations and complexities.

Appendices

APPENDIX A: DISCRETION OF THE GOVERNING EQUATIONS AND MODELING FLOW CHART FOR CHAPTER 2

Discretion of the governing equations

Reservoir fluid part:

Based on mass conservation, the governing equation for slightly compressible single phase flow is expressed in the general strong form as equation (A.1a:

$$\phi C_t \frac{dP}{dt} + \vec{\nabla} v = \vec{q}, \tag{A.1a}$$

On the left hand side, the first term is related to the rate of mass accumulation in the system and the second term is correlated to the rate of mass flow through the system. The right hand side represent the source term in the system. This equation is also expressed in the Cartesian form as:

$$\phi C_t \frac{dP}{dt} + \frac{\partial \vec{v}}{\partial x} + \frac{\partial \vec{v}}{\partial y} = \vec{q}. \tag{A.1b}$$

Assuming the fluid flow function $\vec{v}$ is single-valued in the control volume V, divergence theorem can be used to rewrite equation (A.1a) in the weak form:

$$\phi C_t V \frac{d\bar{P}}{dt} + \int\int v(x,y)dxdy = \int q dV, \tag{A.2}$$

where the source term q accounts for the fracture's effect in this study (details are discussed in the next section). The fluid flow $\vec{v}$ is calculated by Darcy's law as

$$\vec{v} = \frac{\vec{\vec{k}}}{\mu} \cdot \nabla P, \tag{A.3}$$

whose Cartesian form is $\begin{pmatrix} v_x \\ v_y \end{pmatrix} = \frac{k}{\mu}\begin{pmatrix} \frac{\partial P}{\partial x} \\ \frac{\partial P}{\partial y} \end{pmatrix}$. This leads to the diffusivity equation as $\frac{\phi \mu C_t}{k}\frac{dP}{dt} = \frac{\partial^2 P}{\partial x^2} + \frac{\partial^2 P}{\partial y^2} + q_f$, for a slightly compressible fluid in 2D Cartesian coordinates.

For any grid cell centered at (i, j) as shown in Fig 2.7, the x- and y-coordinates of the cell (i, j) are given by $x_{i,j} = \frac{1}{2}\left(x_{i+1/2,j} + x_{i-1/2,j}\right)$ and $y_{i,j} = \frac{1}{2}\left(y_{i,j+1/2} + y_{i,j-1/2}\right)$. The time derivative term is expressed as:

$$\frac{dP_{ij}}{dt} = \lim_{\Delta t \to 0}\left(\frac{P_{ij}(t+\Delta t)-P_{ij}(t)}{\Delta t}\right) \cong \frac{{P_{ij}}^{n+1}-{P_{ij}}^{n}}{\Delta t}, \quad \text{(A.4)}$$

where Δt is the time step size, n is the 'old' time level, n+1 is the 'new' time level and P_{ij} is the average pressure in cell (i, j). Similar differencing process is applied to the space derivatives in equation (A.2) and (A.3). The diffusivity equation becomes

$$C_{tij}V_{ij}\left(P_{ij}^{n+1} - P_{ij}^{n}\right) =$$
$$\Delta t\left((T_x)_{i+1/2,j}\left(P_{i+1,j} - P_{i,j}\right)^{n+1} - (T_x)_{i-1/2,j}\left(P_{i,j} - P_{i-1,j}\right)^{n+1}\right) +$$
$$\Delta t\left(\left(T_y\right)_{i,j+1/2}\left(P_{i,j+1} - P_{i,j}\right)^{n+1} - \left(T_y\right)_{i,j-1/2}\left(P_{i,j} - P_{i,j-1}\right)^{n+1}\right) + q_f \cdot \Delta t. \quad \text{(A.5)}$$

Equation (A.5) is arranged in the implicit form of $\vec{\vec{A}} \cdot \vec{P}^{n+1} = \vec{B}$, where $\vec{B}$ is the forcing function depending on the pressure history ($B_{ij} = C_{tij}V_{ij}P_{ij}^{n} + q_f \cdot \Delta t$), $\vec{\vec{A}}$ is the transmissibility matrix and $\vec{P}^{n+1}$ is the unknown pressure to be solved. The elements in matrix $\vec{\vec{A}}$ are described as:

$$A_{i+1,j} = -\Delta t(T_x)_{i+\frac{1}{2},j},\ A_{i-1,j} = -\Delta t(T_x)_{i-\frac{1}{2},j},\ A_{i,j+1} = -\Delta t\left(T_y\right)_{i,j+\frac{1}{2}},\ A_{i,j-1} =$$
$$-\Delta t\left(T_y\right)_{i,j-\frac{1}{2}},\ A_{i,j} = -\left(A_{i+1,j} + A_{i-1,j} + A_{i,j+1} + A_{i,j-1}\right) + C_{tij}V_{ij}, \quad \text{(A.6)}$$

where $(T_x)_{ij}$ and $\left(T_y\right)_{ij}$ are the transmissibility indexes of neighboring cells in the form of $(T_x)_{i+\frac{1}{2},j} = 2\left(\frac{1}{\left(\frac{k_x h\Delta y}{\mu\Delta x}\right)_{i,j}} + \frac{1}{\left(\frac{k_x h\Delta y}{\mu\Delta x}\right)_{i+1,j}}\right)^{-1}$, $(T_x)_{i-\frac{1}{2},j} = 2\left(\frac{1}{\left(\frac{k_x h\Delta y}{\mu\Delta x}\right)_{i,j}} + \frac{1}{\left(\frac{k_x h\Delta y}{\mu\Delta x}\right)_{i-1,j}}\right)^{-1}$,

$$\left(T_y\right)_{i,j+\frac{1}{2}} = 2\left(\frac{1}{\left(\frac{k_y h\Delta x}{\mu\Delta y}\right)_{i,j}} + \frac{1}{\left(\frac{k_y h\Delta x}{\mu\Delta y}\right)_{i,j+1}}\right)^{-1}, \left(T_y\right)_{i,j-\frac{1}{2}} = 2\left(\frac{1}{\left(\frac{k_y h\Delta x}{\mu\Delta y}\right)_{i,j}} + \frac{1}{\left(\frac{k_y h\Delta x}{\mu\Delta y}\right)_{i,j-1}}\right)^{-1}. \quad \text{(A.7)}$$

For a homogeneous and isotropic reservoir, $k_x = k_y = k$. The new time step pressure can be calculated as $\vec{P}^{n+1} = \vec{\vec{A}}^{-1} \cdot \vec{B}$. (A.8)

The initial condition is mathematically described as $P(x, y, t = 0) = P_{initial}$, indicating the pressure is uniformly distributed throughout the reservoir at the valve of $P_{initial.}$ The constant pressure boundary condition is expressed as $P|_{|x| = Lx/2,\ |y| = Ly/2}\ (t > 0) = P_{initial}$, illustrating the reservoir boundaries are kept at constant value of $P_{initial.}$ For no flow

boundary condition, the expressions are: $\frac{\partial P}{\partial x}|_{|x| = Lx/2}(t > 0) = 0$ and $\frac{\partial P}{\partial y}|_{|y| = Ly/2}(t > 0) = 0$, indicating the flow across the boundaries is always zero.

Fracture internal fluid pressure part:

As explained in Section 2.4.1, the fracture is parallel to the *x*-axis and it is divided into N_f elements by *dx* (length of grid cell in *x*-axis): $N_f = L/dx$ for a fracture length of *L* (=2*a*). The grid cells, where the fracture is located, are called fracture cells. The fracture cells only represent the fracture location, not fracture width. The fracture volume is expressed as $V_f = \frac{\pi(1-\gamma^2)h}{2E}\left(P_f - S_{hmin}\right)L^2$. (A.9)

The fluid pressure inside the same fracture (P_f) is assumed constant along the fracture at the same timestep. S_{hmin} is the minimum horizontal stress and expressed as the function of $S_{hmin}(t) = S_{hmin,0} + \frac{E^*(\dot{\varepsilon}\cdot t)}{1-\frac{\nu^2 E^*}{E}}$, which is basically the equation (9) in Segall (1984). E^* is the effective modulus and $\dot{\varepsilon}$ is the remote tectonic strain rate.

Once the pressure value is updated for each grid cell by equation (A.8), the pressure profile (P^{n+1}) can be applied in equation (2.15) to calculate the fracture internal fluid pressure (P_f). Equation (2.15) is expressed as $\frac{k_y h}{\mu}\int_{-a}^{a}\left(\frac{\partial P}{\partial y}\right)\Big|_{y=0} dx = \frac{dV_f}{dt}$, which can be discretized in the space and time domain as $\frac{k_y h}{\mu}\sum_{i=1}^{N_f}\frac{p_i^{n+1} - P_f^{n+1}}{\Delta y}\Delta x = \frac{V_f^{n+1} - V_f^n}{\Delta t}$, (A.10) where V_f^{n+1} and V_f^n are expressed by equation (A.9) and P_i^{n+1} is the pressure value in the fracture neighboring grid cells. P_f^{n+1} is solved iteratively from equation (A.10). The pressure of the corresponding fracture cells is updated to the value of P_f^{n+1}; therefore, those elements in the forcing function $\vec{B}$ are updated as well.

Fracture mechanics part:

With the calculated P_f, the mode I fracture intensity factor (K_I) can be updated from equation (2.14): $K_I = \left(P_f - S_{hmin}\right)\sqrt{\pi L/2}$ and fracture propagation velocity can

be calculated from equation (2.4): $V = Vmax\left({K_I}/{K_{IC}}\right)^n$. If the fracture propagation criterion is met, the fracture will have a fracture growth event; if not, pressure profile at a new timestep is calculated via equation (A.8). The flow chart of the numerical modeling is illustrated below.

Modeling flow chart for Chapter 2

Figure A1 shows the flow chart for the numerical modeling of multiple mode I natural hydraulic fracture propagation under critical propagation condition.

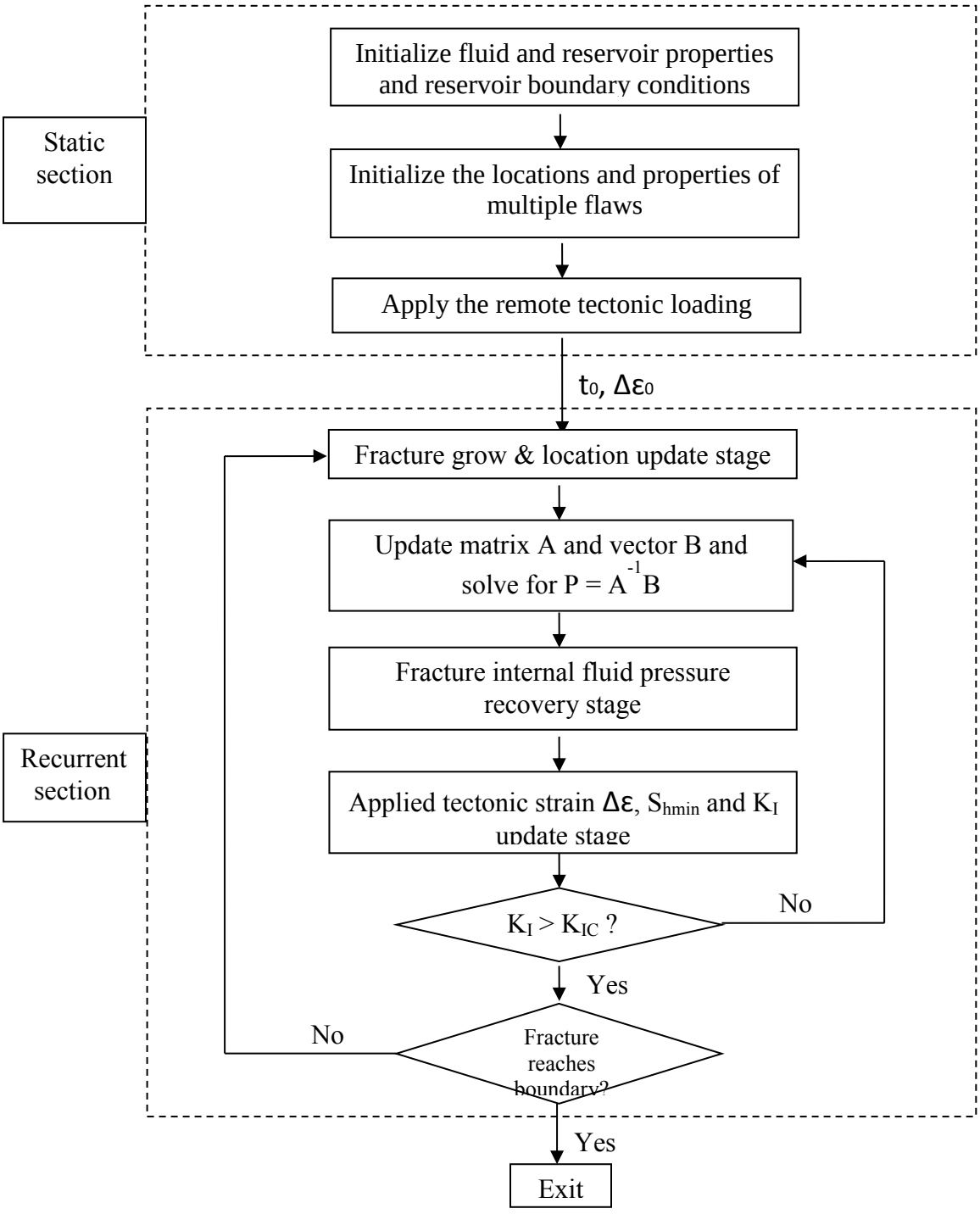

Figure A1 – Numerical modeling flow chart for mode I NHF critical propagation in Chapter 2.

APPENDIX B: THE NUMERICAL RESULTS OF RANDOMLY DISTRIBUTED NHF DEVELOPMENT FOR CHAPTER 2

For rocks and minerals under long-term, slow-cycles of loadings, crack propagation is observed under subcritical growth region where fracture propagation velocity is express in the power-law form of $V = V_{max}\left({K_I}/{K_{IC}}\right)^n$. In addition, most natural fractures are randomly distributed in the field. In this part, the new effective media model developed in Chapter 2 is used to study the timescale of the subcritical growth of randomly distributed natural hydraulic fractures in both high-permeability and low-permeability rocks.

The subcritical index (n) is chosen at 25 and fracture toughness (K_{IC}) at 1.5 MP√m. The reservoir boundary is kept at constant pressure and strain rate is set at 1.2×10^{-18} s^{-1}. A set of five cracks are randomly located within a 10 m by 10 m area. The layer thickness is 1 m. The initial fracture half-length is 0.1 m, corresponding to an initial fracture density of 5×10^{-4}. The initial pressure is uniformly distributed throughout the reservoir and equal to the minimum horizontal stress. At a strain rate of 1.2×10^{-18}, fracture propagation starts at 3.4 my in both 1 D and 1 nD reservoirs; however, the propagation processes vary significantly for these two cases.

The initial fracture pattern is shown in Figure B1. Fracture tip growth termination is considered when the tip reaches the confining boundary inside the reservoir (10% of reservoir length away from the actual boundary). When all the fracture tips reach the boundary, the simulation stops.

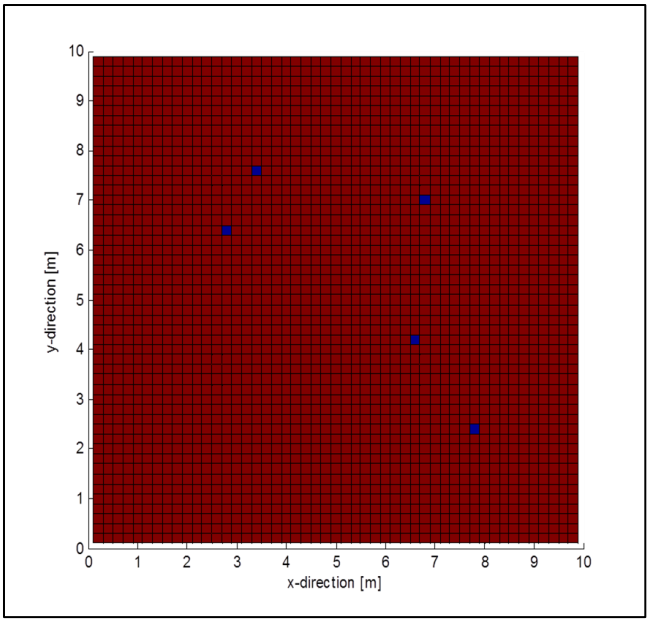

Figure B1 – The geometry of 5 randomly distributed fractures in a 10 m by 10 m by 1 m reservoir.

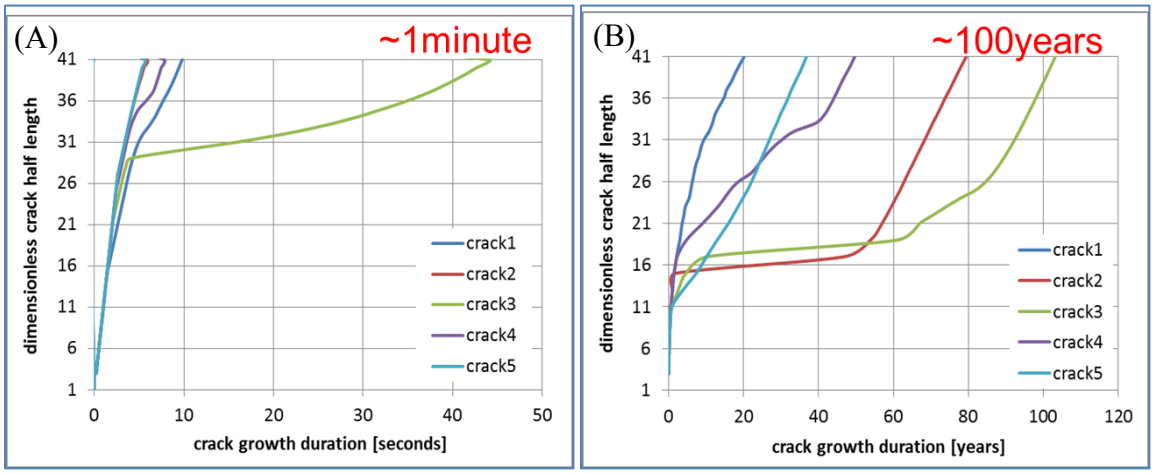

Figure B2 – The fracture propagation curve of dimensionless fracture half-length vs. crack growth duration in (A) 1 D and (B) 1 nD rocks.

As a result of the low initial fracture density, the whole crack growth duration is relatively short as shown in Figure B2: less than 1 minute for 1 D case and around 100 years for 1 nD case. In 1 D case, four cracks have similar propagation velocity and finish

their propagation in less than 10 seconds, leaving only one fracture behind. The situation is quite different in 1 nD case where all cracks have a much slower propagation velocity and they reach boundary in sequence.

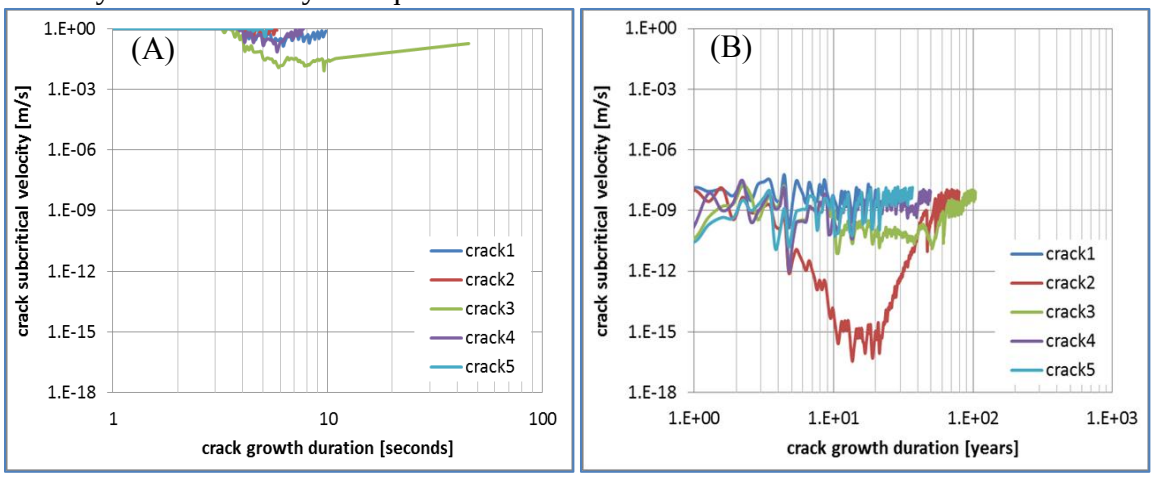

Figure B3 – The fracture subcritical velocity curve of subcritical velocity vs. crack growth duration in (A) 1 D and (B) 1 nD rocks.

Figure B3 records the subcritical velocity profiles of five cracks over the whole growth duration. The velocities in 1 D case are between 1×10^{-3} and 1 m/s, which are generally higher than those in 1 nD case, between 1×10^{-8} to 1×10^{-15} m/s. The difference in velocity value and range is related to the pressure recovery and fluid distribution in different permeable reservoirs. In high-permeability rock with constant pressure boundary, fluid flow is fast and more uniformly distributed inside reservoir, which provides faster fracture internal pressure recovery process and higher subcritical velocity. In the low-permeability rocks, slow fluid flow leads to slow fracture internal recovery process and low subcritical velocity. Meanwhile, the wide range of velocities is related to the non-uniform distribution of fluid inside reservoir. More details of the pressure profiles can be found in Figure B4 for both cases.

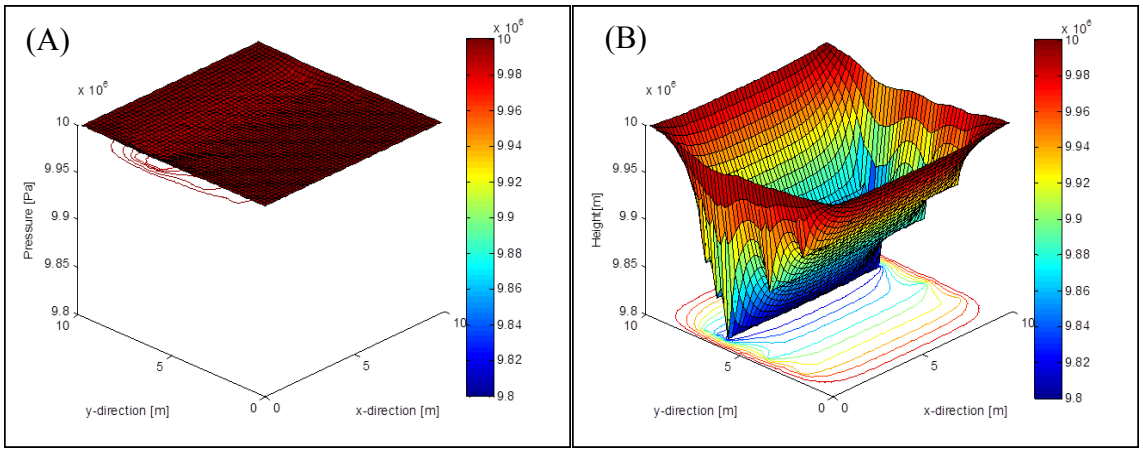

Figure B4 – 3D pressure profile at the end of crack propagation in (A) 1 D and (B) 1 nD rocks.

Figure B4 shows the three-dimensional pressure profile over the whole reservoir at the end of propagation in each case. The average pressure in 1 D rock is almost at the boundary pressure value, indicating fast pressure recovery because of the high permeability. On the other hand, the average pressure in 1 nD rock is much lower than the boundary pressure value and the pressure profile is quite non-uniform over the whole reservoir, indicating the pressure distribution is updated more slowly throughout the whole fracture propagation duration.

In addition to permeability, the subcritical index plays a significant role in controlling crack growth velocity and the overall growth duration. In following section, an investigation will be conducted on how subcritical index n affects the crack growths for the set of five fractures in 1 nD rock at strain rate of 1.2×10^{-18} s^{-1}. Two cases are chosen: $n = 25$ as a typical value for sandstone rock and $n = 80$ for much tighter rocks like Barnett shale (Gale and Holder, 2010).

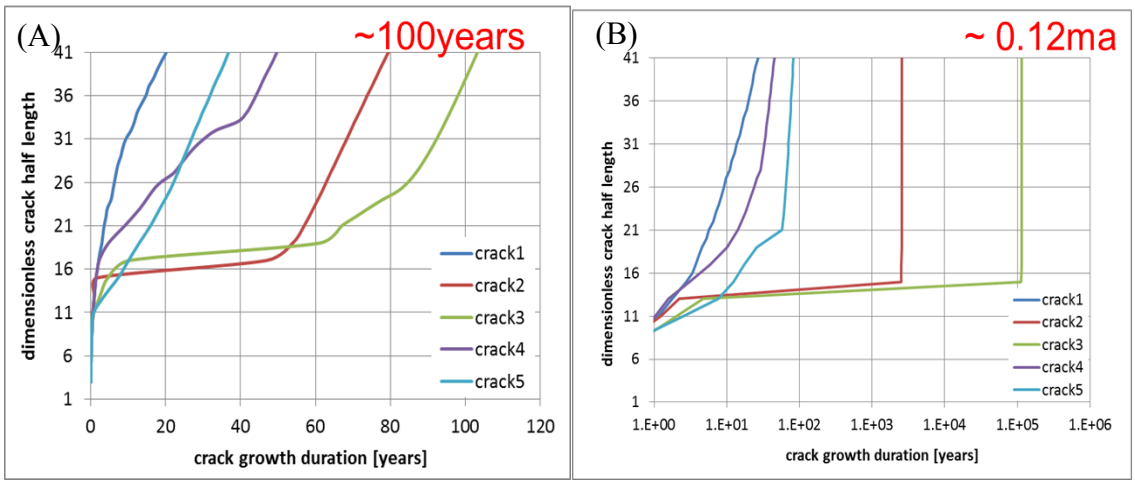

Figure B5 – The fracture propagation curve of dimensionless fracture half-length vs. crack growth duration in 1 nD rock with (A) n = 25, (B) n = 80.

Fractures normally grow much slower in the high *n* case than in the low *n* case. Figure B5 shows the plots of five crack growth profiles with different *n*. For the low *n* case (Figure B5(A)), the whole growth duration is about 100 years, while it becomes as long as 0.12 ma for the high *n* case (Figure B5(B)).

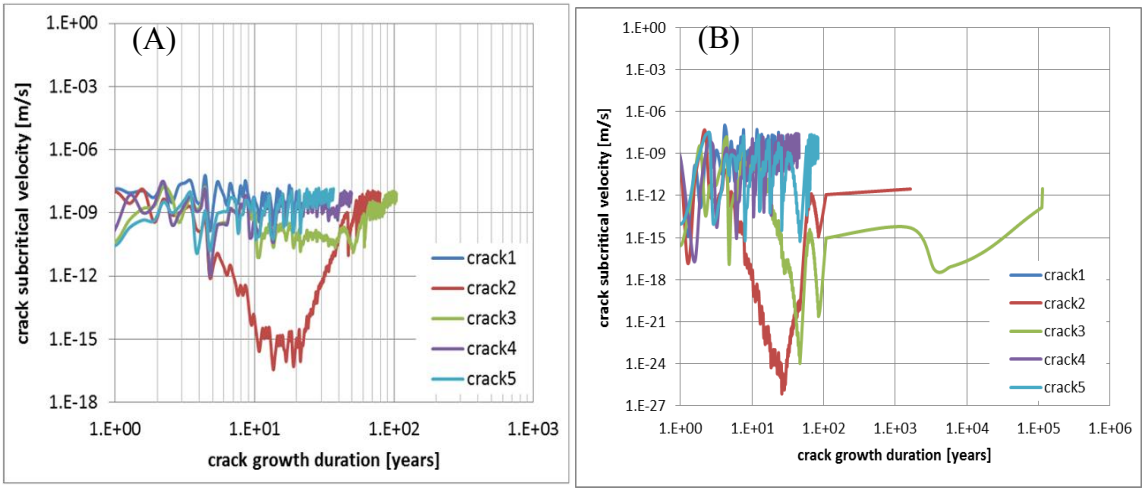

Figure B6 – The fracture subcritical velocity curve of subcritical velocity vs. crack growth duration in 1 nD rock with (A) n = 25, (B) n = 80.

The crack subcritical velocity profiles in Figure B6 reveal more details about the crack growth process for the high and low *n* cases. In the low *n* case, all the fracture velocities (between 1×10^{-8} to 1×10^{-16} m/s) are in a much higher range than those in the high *n* case (between 1×10^{-8} to 1×10^{-26} m/s). The lowest velocity in the low *n* case is around 1×10^{-16} m/s, whereas it is 1×10^{-26} m/s in the high *n* case. The big difference in the fracture subcritical velocity explains the difference in the overall crack propagation duration between both the low and high *n* cases.

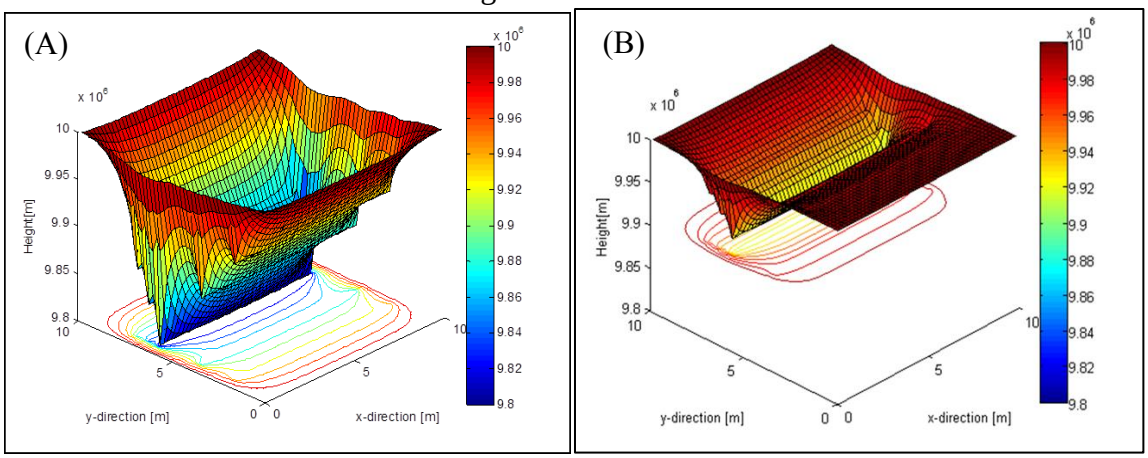

Figure B7 – 3D pressure profile at the end of crack propagation in 1 nD rock with (A) n = 25 after 100 years growth duration; (B) n = 80 after 0.12 my growth duration.

The plots shown in Figure B7 correspond to the 3D pressure profiles at the final stage when all cracks reach the inner confining boundary. Figure B7(A) is the pressure profile after 100 years growth duration for *n* = 25 case, where the pressure distribution is quite non-uniform and the lowest pressure is around 9.8 MPa (0.2 MPa lower than the boundary pressure value). Figure B7(B) is the pressure profile after 0.12 my growth duration for *n* = 80 case, where the lowest pressure is about 9.9 MPa (0.1 MPa lower than the boundary value). The average pressure is higher in *n* = 80 than *n* = 25 case. This is related to the overall growth duration and the reservoir permeability. For the low-

permeability reservoir, it takes a longer time for fluid to flow throughout the reservoir; therefore, a growth duration of 0.12 my in $n = 25$ case provides more time for the whole reservoir area to recover fluid from boundaries; therefore, a higher average pressure is achieved ultimately.

APPENDIX C: COUPLING OF P3D DDM AND FLUID MODEL AND MODELING FLOW CHART FOR CHAPTER 3

Coupling of P3D DDM and fluid model

The fluid model is described in detail in Appendix A. As described in Section 3.4.1, the fluid model is coupled with the P3D displacement discontinuity method (DDM) to incorporate the mechanical interaction between fractures. Once the fracture internal fluid pressure (P_f) is updated from the fluid model, the boundary condition for each fracture element is calculated as $\begin{pmatrix}\sigma_s \\ \sigma_n\end{pmatrix} = \begin{pmatrix}0 - \sigma_s^r \\ P_f - \sigma_n^r\end{pmatrix}$, (C.1)

where σ_s^r, σ_n^r are the shear and normal components of remote stresses acting on the fracture element. Actually, equation (C.1) is the LHS of equation (3.6); therefore, the displacement discontinuity D_n and D_s can be solved from equation (3.6) as $\begin{pmatrix}D_s \\ D_n\end{pmatrix} = \begin{bmatrix}A_{ss} & A_{sn} \\ A_{ns} & A_{nn}\end{bmatrix}^{-1} \cdot \begin{pmatrix}\sigma_s \\ \sigma_n\end{pmatrix}$. The corresponding mode I and II stress intensity factors can be calculated from equation (3.8) as $\begin{pmatrix}K_I \\ K_{II}\end{pmatrix} = 0.806 \left(\frac{E\sqrt{\pi}}{4(1-\gamma^2)\sqrt{\Delta a}}\right) \begin{pmatrix}D_n \\ D_s\end{pmatrix}$.

For mode I fracture subcritical growth, the subcritical velocity obeys the power-law function as shown in equation (2.4). The length of fracture growth during the time increment Δt is calculated from equation (3.10) as $\Delta L = V \times \Delta t$.. Once the total fracture growth length exceeds the prespecified growth increment length, the fracture will have a growth event and one boundary element will be added to the fracture tip. The modeling details are summarized in the flow chart below.

Modeling flow chart for Chapter 3

Figure C1 shows the flow chart for the numerical modeling of multiple mode I natural hydraulic fracture propagation under subcritical propagation condition.

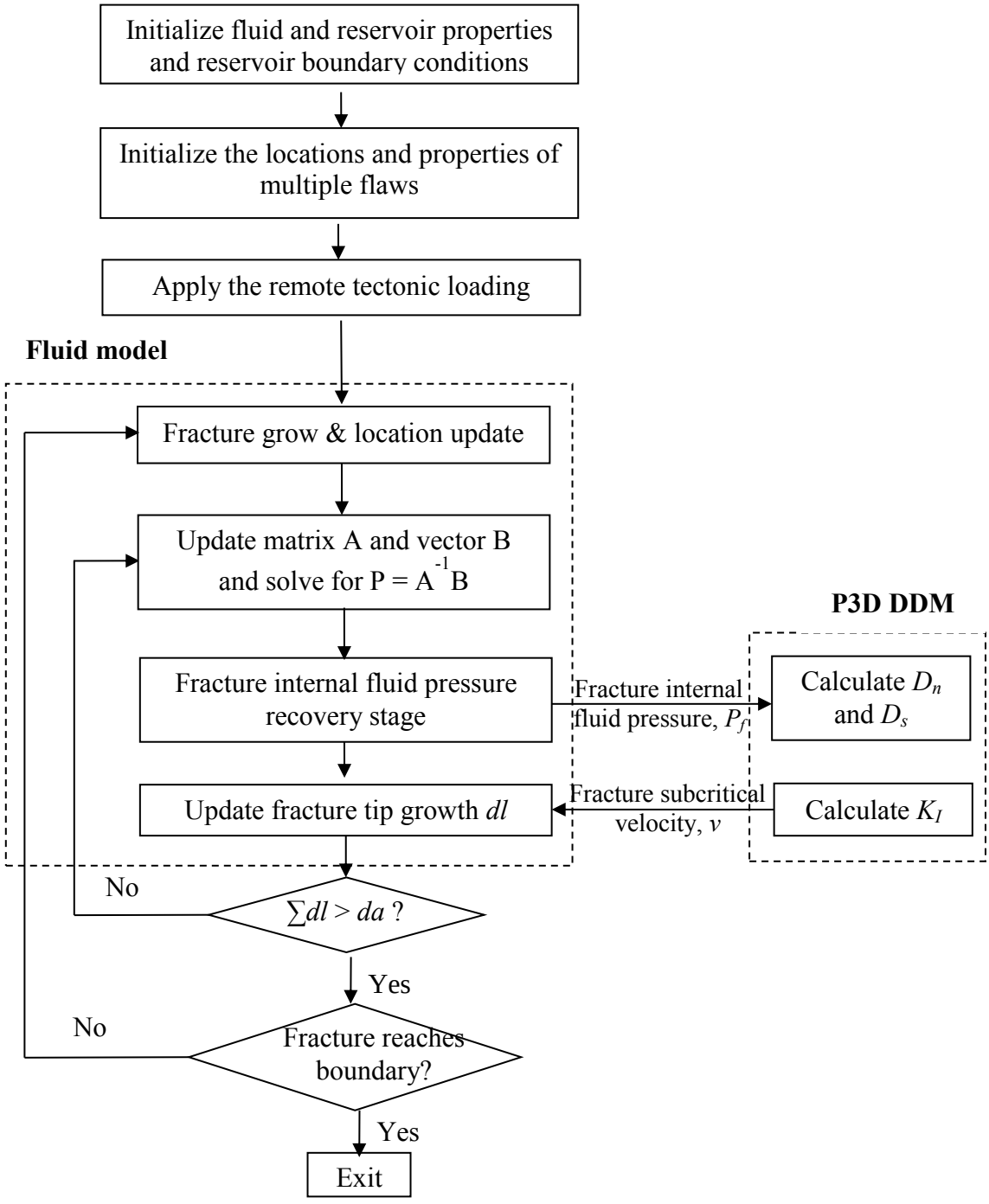

Figure C1 – Numerical modeling flow chart for coupling P3D DDM and fluid model for multiple mode I NHF subcritical propagation in Chapter 3.

APPENDIX D: THE VERIFICATION OF DDM CODE FOR CHAPTER 3

The verification of 2D DDM code

First, the 2D DDM code developed in Chapter 3 is used to verify the single pressurized crack problem with conditions described below. All displacements and stresses are assumed zero at infinity:

$$\sigma_{xy} = 0, -\infty < x < \infty, y = 0$$

$$\sigma_{yy} = -P,\ |x| < b, y = 0$$

$$u_y = 0,\ |x| \geq b, y = 0$$

The analytical solution for the normal displacement distribution along the crack is derived by Crouch and Starfield (1983) as:

$$\hat{u}_y(x) = u_y(x, 0_-) - u_y(x, 0_+) = -\frac{2(1-\gamma)}{G} pb(1 - x^2/b^2)^{1/2}.$$

No matter the crack is divided into 20 (Figure D1(A)) or 100 elements (Figure D1(B)), the plots of displacement discontinuity distribution along the fracture show that the numerical simulation and analytical results match well.

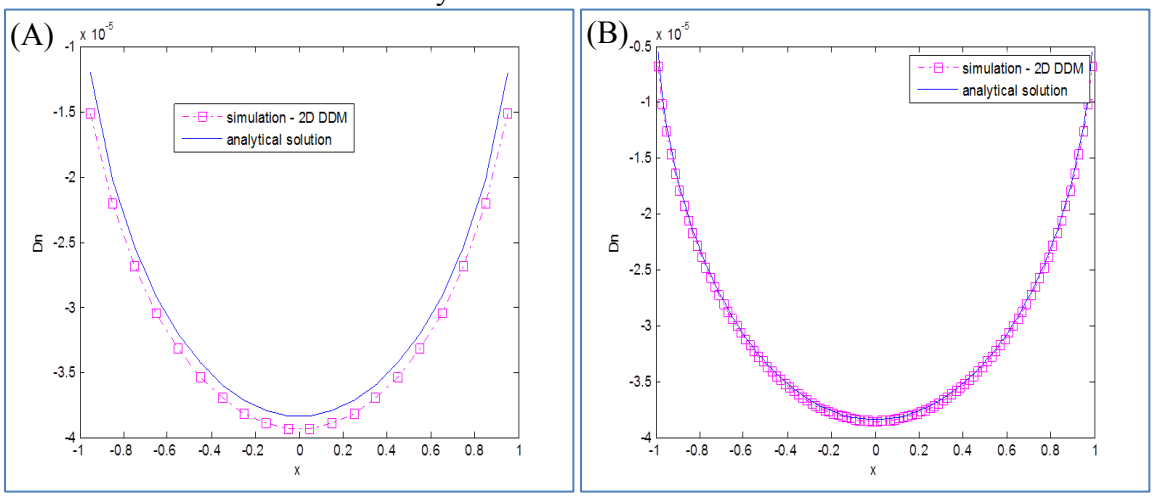

Figure D1 – The numerical and analytical solutions for displacement discontinuity distribution along a crack, which is divided into (A) 20 and (B) 100 elements in the numerical model.

Next, the 2D DDM code is also used to verify the two curving fracture case which was published earlier by Olson (1989).

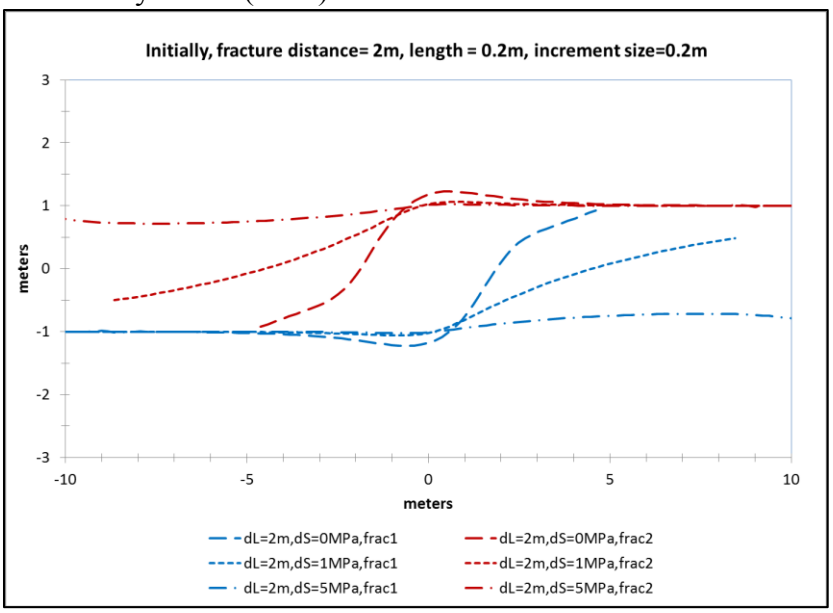

Figure D2 – Crack path for initial crack spacing of 2 m (1/10 of total crack array length) at different remote differential stress conditions, 0, 1, 5 MPa.

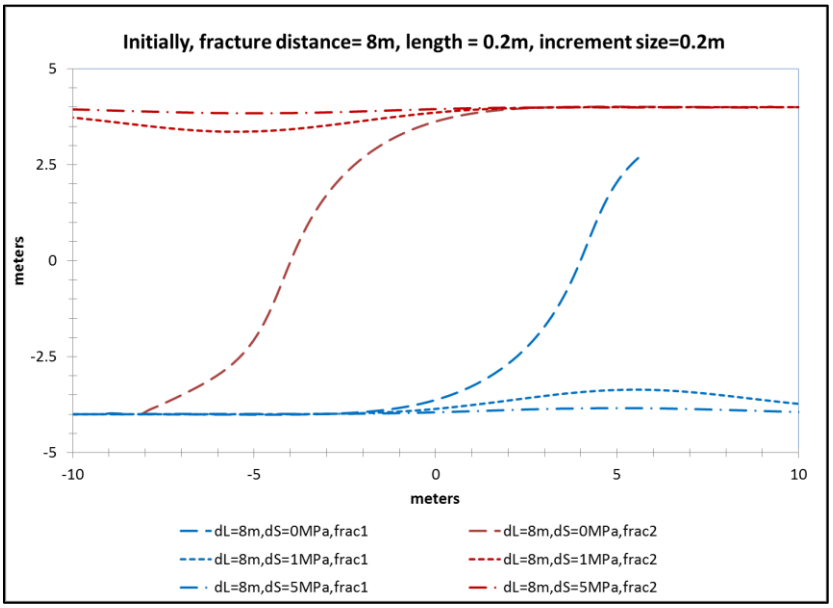

Figure D3 – Crack path for initial crack spacing of 8 m (1/2.5 of total crack array length) at different remote differential stress conditions, 0, 1, 5 MPa.

Fracture distance is fixed at 2 m in Figure D2 and 8 m in Figure D3. In both cases, only the differential stress (the difference between remote S_{Hmax} and S_{hmin}) varies, from 0 MPa to 5 MPa. The plots in both figures verify the published results (Olson, 1989). The results indicate that crack path depends on both the fracture spacing and the differential stress. When the fractures are more distanced from each other or the differential stress is larger, less mechanical interaction exists between fractures and more straight propagation path is observed.

The verification of P3D DDM Code for Chapter 3

A G-factor is introduced in the 2D DDM model to account for the limited fracture height. The P3D DDM model is verified against the analytical solution derived by Pollard and Segall for single isolated fracture under plane strain conditions (infinite height) (Pollard and Segall, 1987).

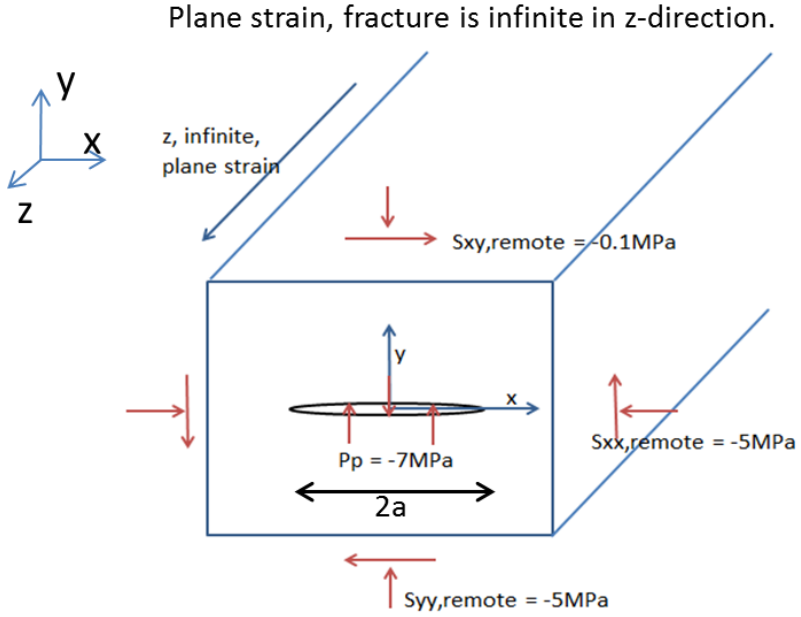

Figure D4 – Diagram of a single fracture located at the center of elastic media under 2D plane strain condition. The fracture half-length is *a*.

The analytical solution for the normalized stresses σ_{xx}, σ_{yy} and σ_{xy} are expressed as $\frac{\sigma_{yy}-\sigma_{yy}^{r}}{\Delta\sigma_I} = \frac{y^3}{(y^2+a^2)^{3/2}} - 1$, $\frac{\sigma_{xx}-\sigma_{xx}^{r}}{\Delta\sigma_I} = \frac{y^3+2ya^2}{(y^2+a^2)^{3/2}} - 1$, $\frac{\sigma_{xy}-\sigma_{xy}^{r}}{\Delta\sigma_{II}} = \frac{y^3+2ya^2}{(y^2+a^2)^{3/2}} - 1$. For the numerical simulation, G factor is chosen with $\alpha = 1$ and $\beta = 2.3$: $G^{ij} = 1 - \frac{d_{ij}^{\beta}}{\left[d_{ij}^2+\left(h/\alpha\right)^2\right]^{\beta/2}}$. With the infinite height assumption, the simulation results obtained with the P3D DDM codes match well with the analytical results, as shown in Figure D5.

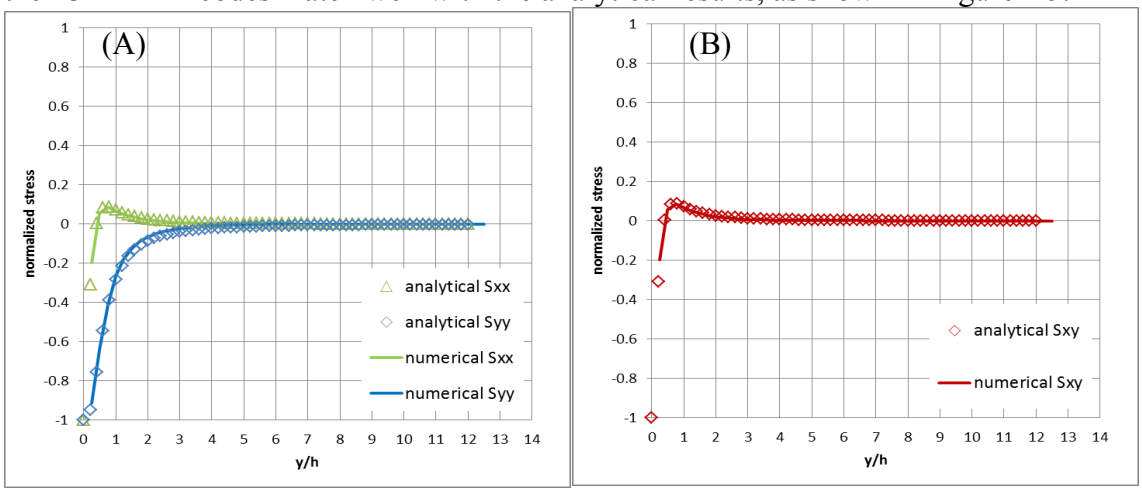

Figure D5 – The numerical and analytical solutions of (A) σ_{xx}, σ_{yy} and (B) σ_{xy} for a single fracture case.

With the infinite permeability assumption, this P3D DDM model is also used to validate the published results for multiple fracture pattern geometry development under uniaxial loading conditions. The G-factor is chosen with $\alpha = 1$ and $\beta = 2.3$. 60 parallel flaws are randomly distributed in the confined reservoir area. Their initial half-length is 0.2 m and the uniaxial loading strain is applied to initiate fracture propagation. Subcritical growth and mixed mode I-II are considered in the model. Fracture termination is considered when it intersects with the inner imaginary boundary between fractures and the unfractured region. The width of imaginary region is chosen at 5 m to eliminate the body's free surface effects on propagation. As shown in Olson's study on joint pattern

development, both the subcritical index and bed thickness effects are investigated (Olson, 1993, 1997, 2004, 2007)

The bed thickness is chosen at 8 m and subcritical index varies from 5, 20 to 80. Strain of 1×10^{-4} is applied in y-direction. The final fracture patterns are shown in Figure D6.

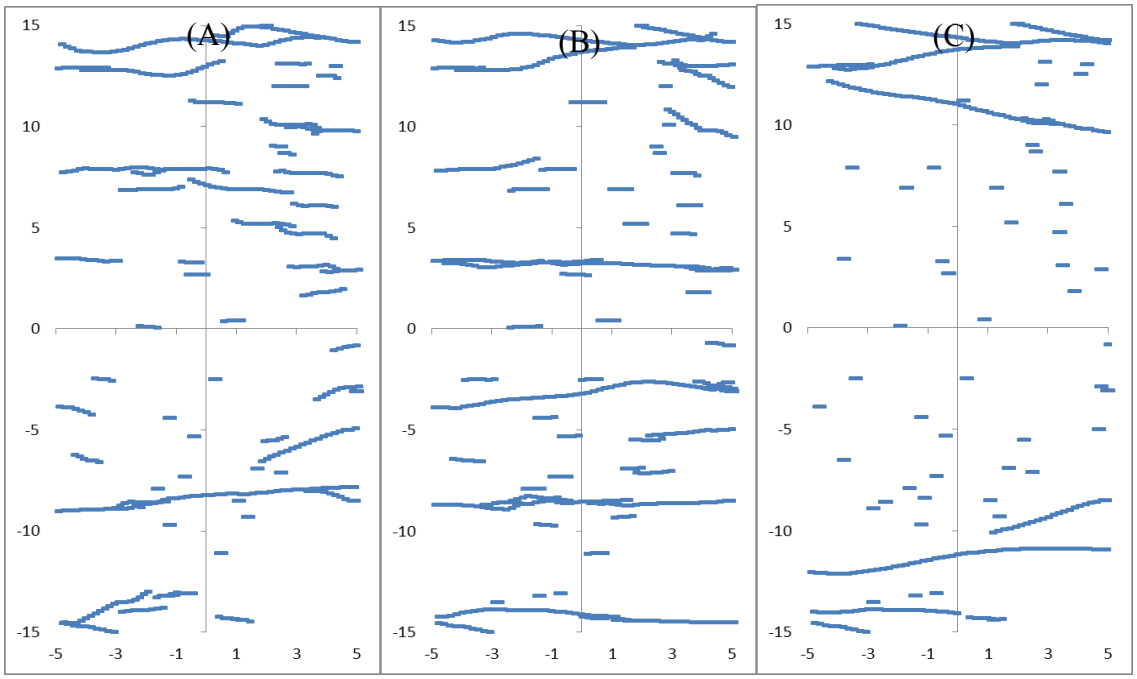

Figure D6 – P3D subcritical fracture growth patterns with subcritical indices of (A) n = 5, (B) n = 20, (C) n = 80.

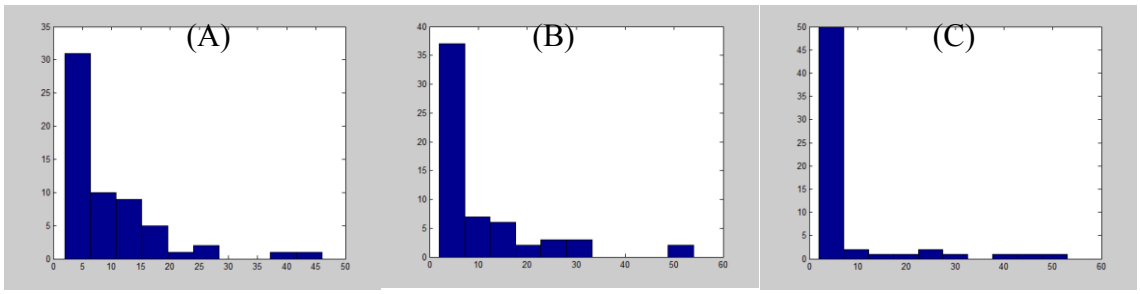

Figure D7 – Fracture element-frequency diagram for fracture patterns in Figure D6. Each fracture element represents length of 0.2 m.

The patterns in Figure D6 show that the fracture spacing increases when the subcritical index increases from 5 to 80. With a low subcritical index, less velocity contrast is emphasized and more fractures can grow at the same time (Figure D6(A)), while large velocity contrast exists for the high subcritical index case and only a few fractures dominate the propagation pattern and leave many flaws closed (Figure D6(C)). This is also confirmed from the fracture length-frequency diagrams in Figure D7. These results are consistent with the previously published data (Olson, 1993, 2004).

In following section, the bed thickness varies form 2, 4 to 8 m and the subcritical index is kept at 20.

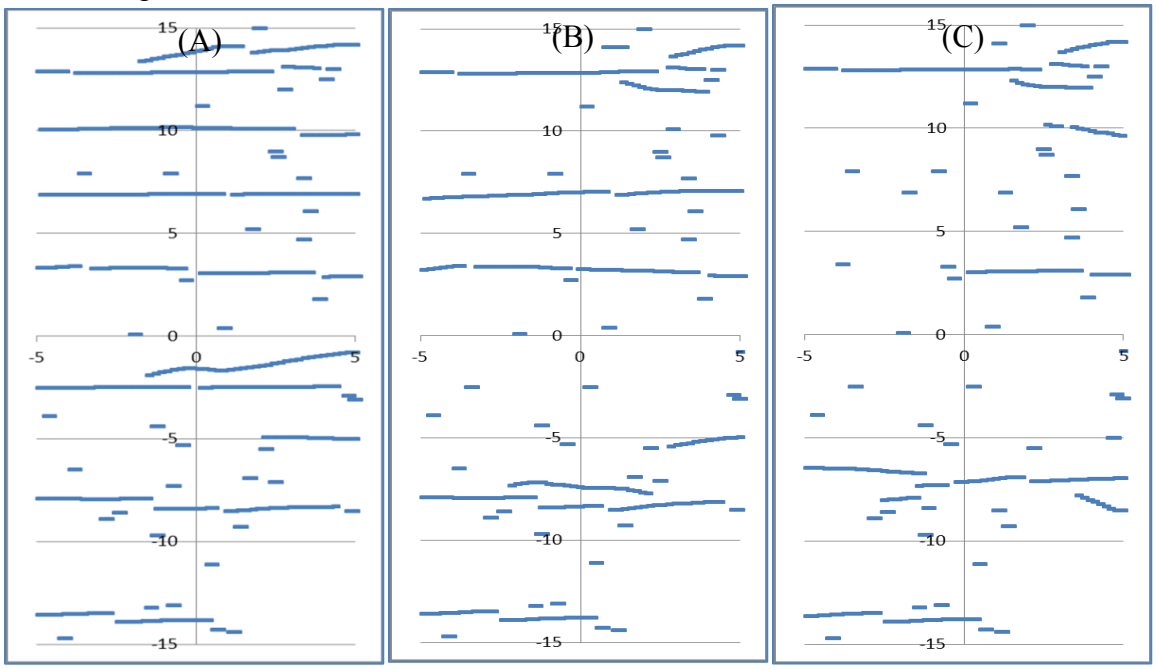

Figure D8 – Pseudo3D subcritical fracture growth patterns with a bed thickness of (A) 2 m, (B) 4 m, (C) 8 m.

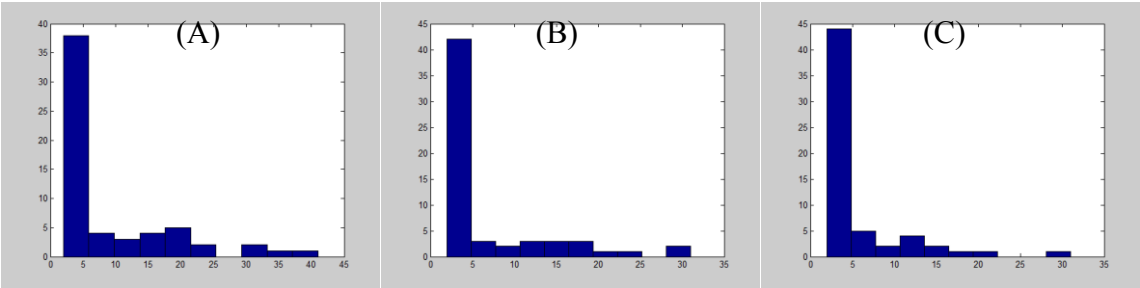

Figure D9 – Fracture element-frequency diagram for fracture patterns in Figure D8. Each fracture element represents length of 0.2 m.

Figure D8 illustrates that the fracture spacing increases with bed thickness. For the thin bed case, the fractures are distributed relatively close to each other (Olson, 1997, 2007). Using the line method to calculate fracture spacing, fracture spacing is 3 m for h = 2 m beds (Figure D8(A)), 5m for h = 4 m beds (Figure D8(B)) and 7 m for h = 8 m beds (Figure D8(C)). The correlation is linear between the fracture spacing and bed thickness. Meanwhile, fewer short fractures are observed in the thin bed than thick bed as shown in Figures D8 and D9. The findings are consistent with the published results (Olson, 1997, 2007).

APPENDIX E: THE NUMERICAL STUDY OF MULTIPLE NHF DEVELOPMENT IN THICK BEDS FOR CHAPTER 4

The stress shadow around a fracture has the radius close to layer thickness (Olson, 2004). Any fracture sitting within this zone is considered under stress shadow. To ensure the same number of fractures under stress shadow, the total number of fractures for the thick bed case will be adjusted to count for the bed thickness effect. The simple correlation between fracture numbers and bed thickness is derived as below:

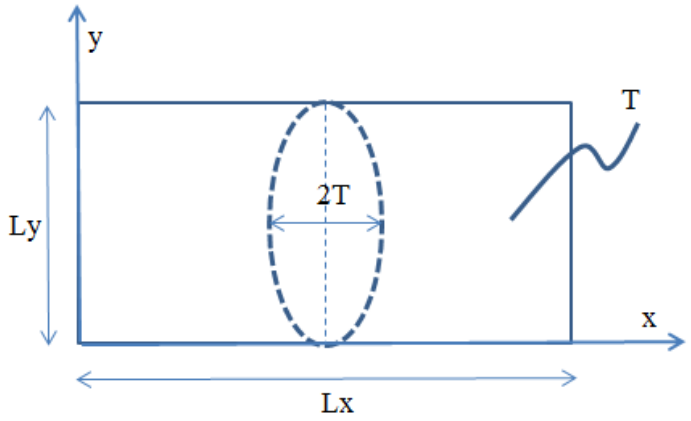

Figure E1 – The demonstration of the dimensions of stress shadow and reservoir area: L_x and L_y is the dimensions in x- and y-directions; T is the bed thickness in z-direction.

As shown in Figure E1, the area of stress shadow is approximated as the product of its diameter ($2T$) and the distance in the y-direction: $A_{shadow} = L_y \cdot (2T)$. Assuming the fractures are randomly distributed in the whole reservoir, the fraction of fractures sitting in the stress shadow area to the total number of fracture is the areal ratio of stress shadow to the whole rock: $\frac{N_{fracs}^{shadow}}{N_{fracs}^{total}} = \frac{A_{shadow}}{A_{total}} = \frac{L_y \cdot (2T)}{L_y \cdot L_x} = \frac{2T}{L_x}$. Therefore, the number of fractures located in the stress shadow can be estimated as: $N_{fracs}^{shadow} = N_{fracs}^{total} \cdot \left(\frac{2T}{L_x}\right)$.

For the case shown in Section 4.3 in Chapter 4 , L_x = 40 m, T = 4 m, $N_{fracs}^{total} = 100$, which leads to $N_{fracs}^{shadow} = 20$. In this section, both L_x and L_y are chosen at 20 m

and T at 8 m, therefore, N_{fracs}^{total} is set as 25 to keep N_{fracs}^{shadow} at 20. The initial half-length of the 25 cracks is 0.2 m. All cracks are confined to an area of 17 by 17 m^2. Bedding thickness is kept at 8 m. The other settings are the same as those in Section 4.3.

Permeability effect

Reservoir permeability varies from zero, 1 nD, 1 mD to infinitely large large (referred as constant pressure case) to evaluate the permeability effect on fracture spacing in thick beds. The base case is chosen with subcritical index of 80, bed thickness of 8 m and boundary at constant pressure condition. On each fracture pattern, a reference bubble with radius of $1x10^{-3}$ is located at the corner of each plot.

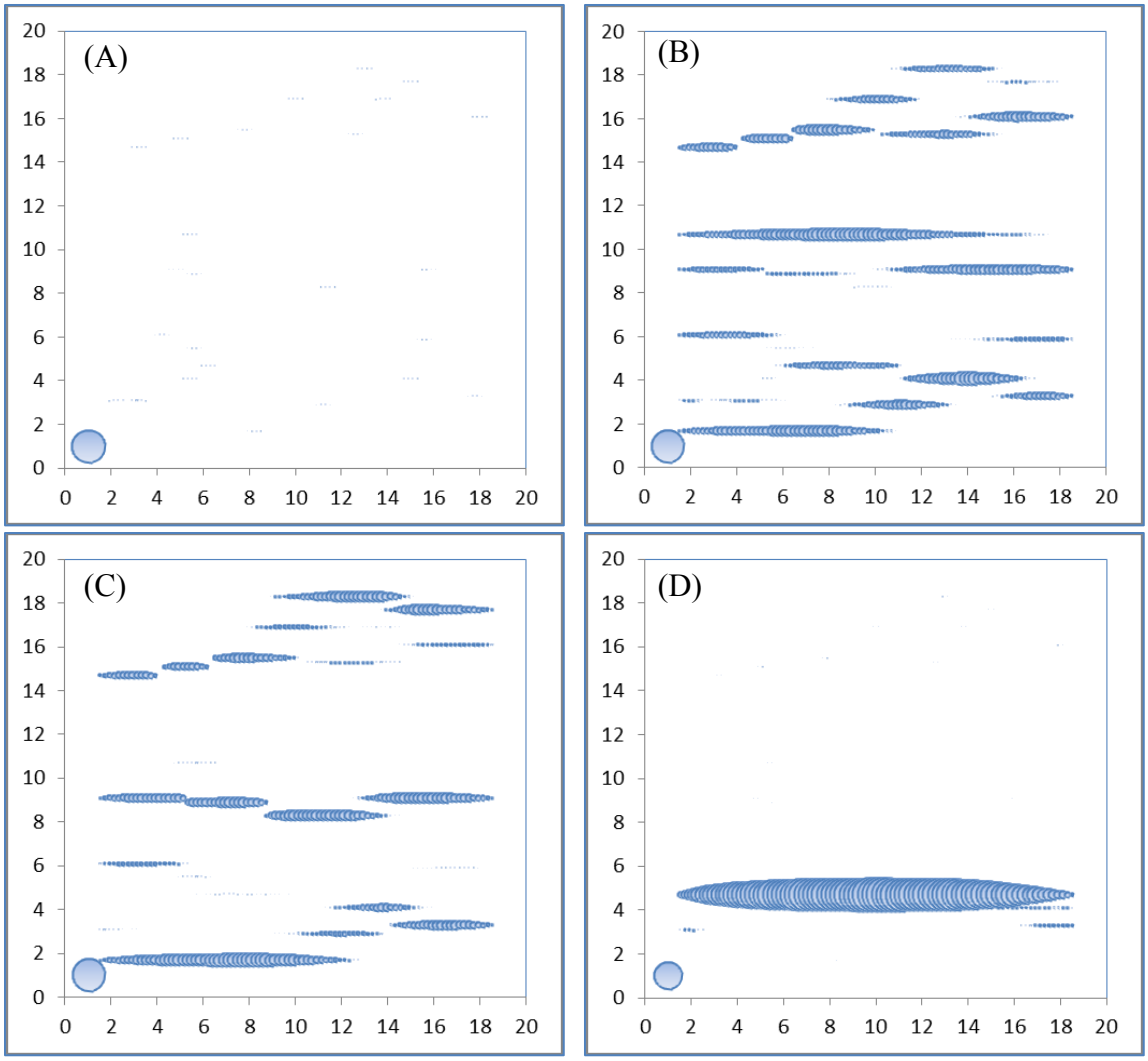

Figure E2 – At 11 my, the subcritical fracture growth patterns in 8 m layer with permeability of (A) 0, (B) 1 nD, (C) 1 mD, (D) infinite large.

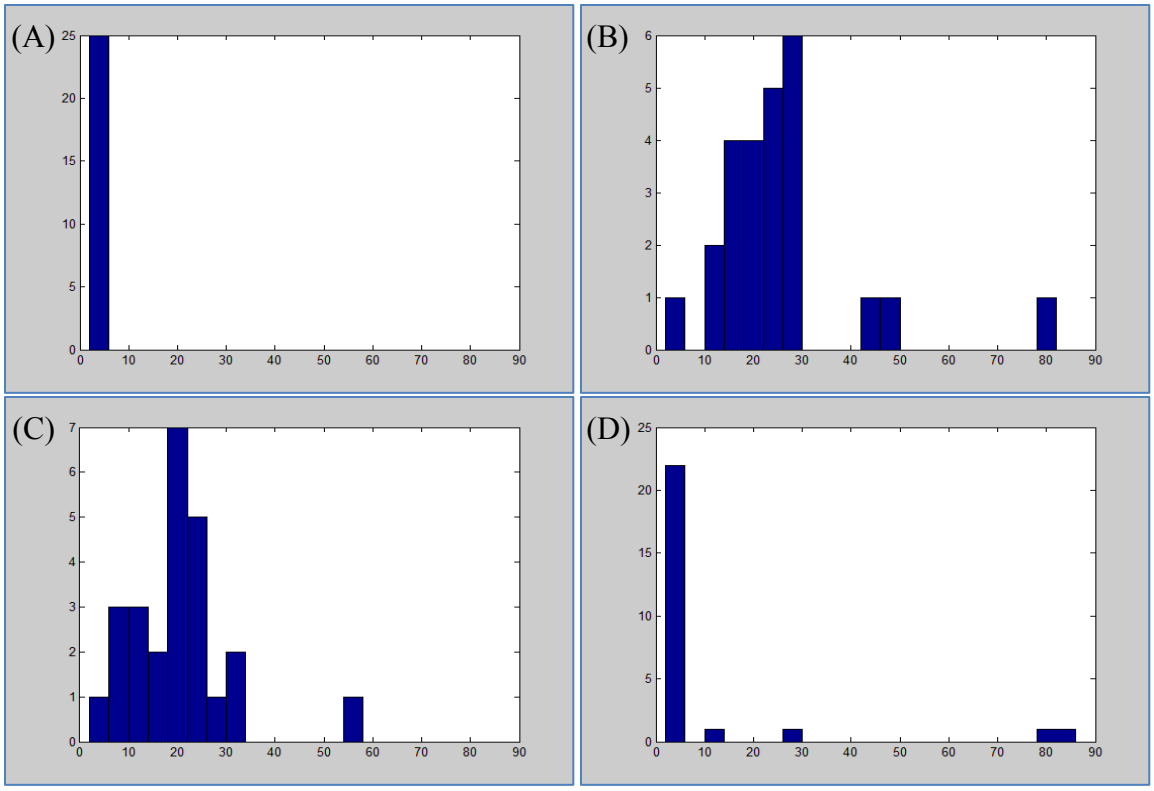

Figure E3 – At 11 my, fracture element-frequency diagram for fracture patterns in Figure E2. Each fracture element represents length of 0.2 m.

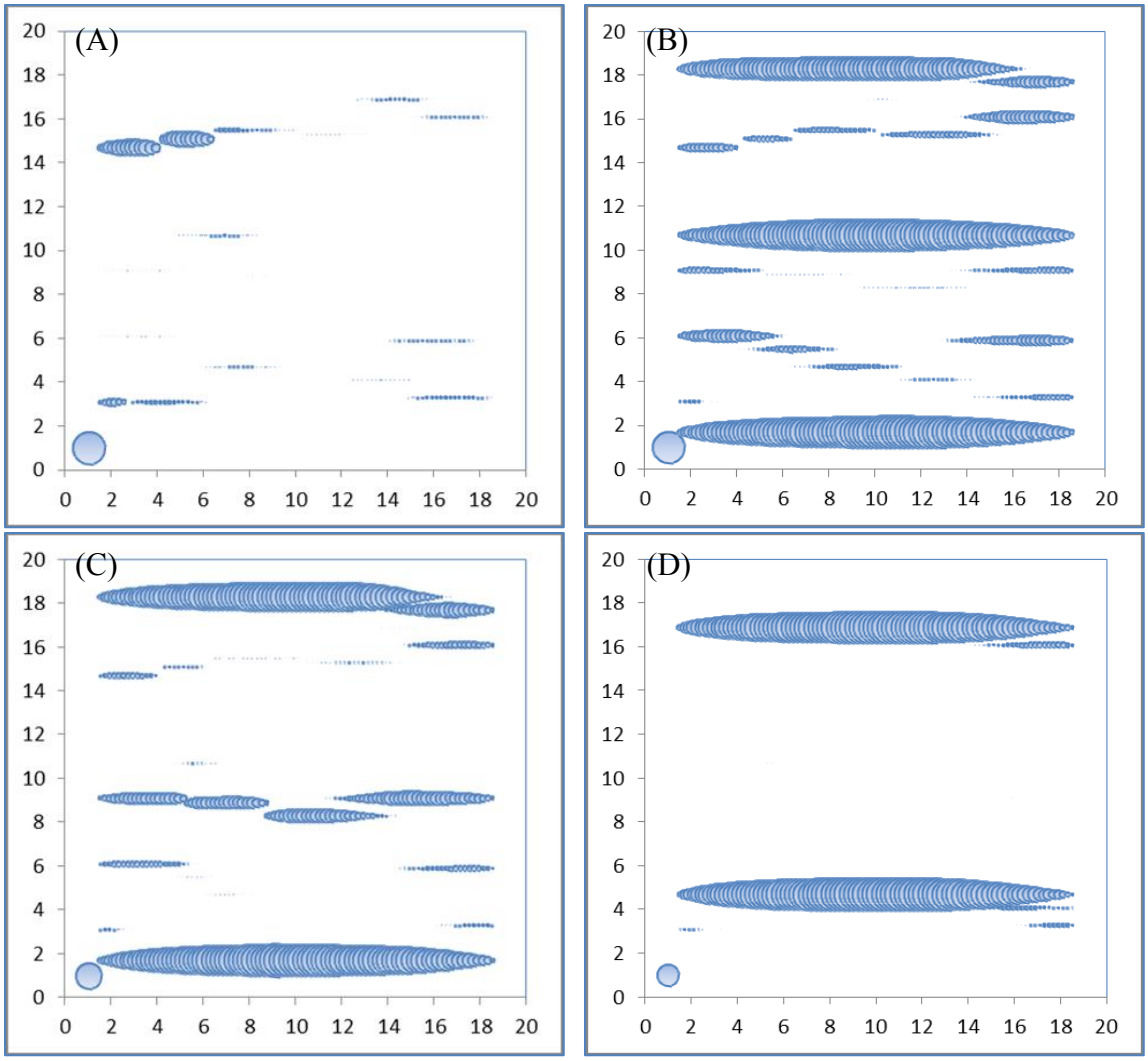

Figure E4 – At 21 my, the subcritical fracture growth patterns in 8 m layer with permeability of (A) 0, (B) 1 nD, (C) 1 mD, (D) infinite large.

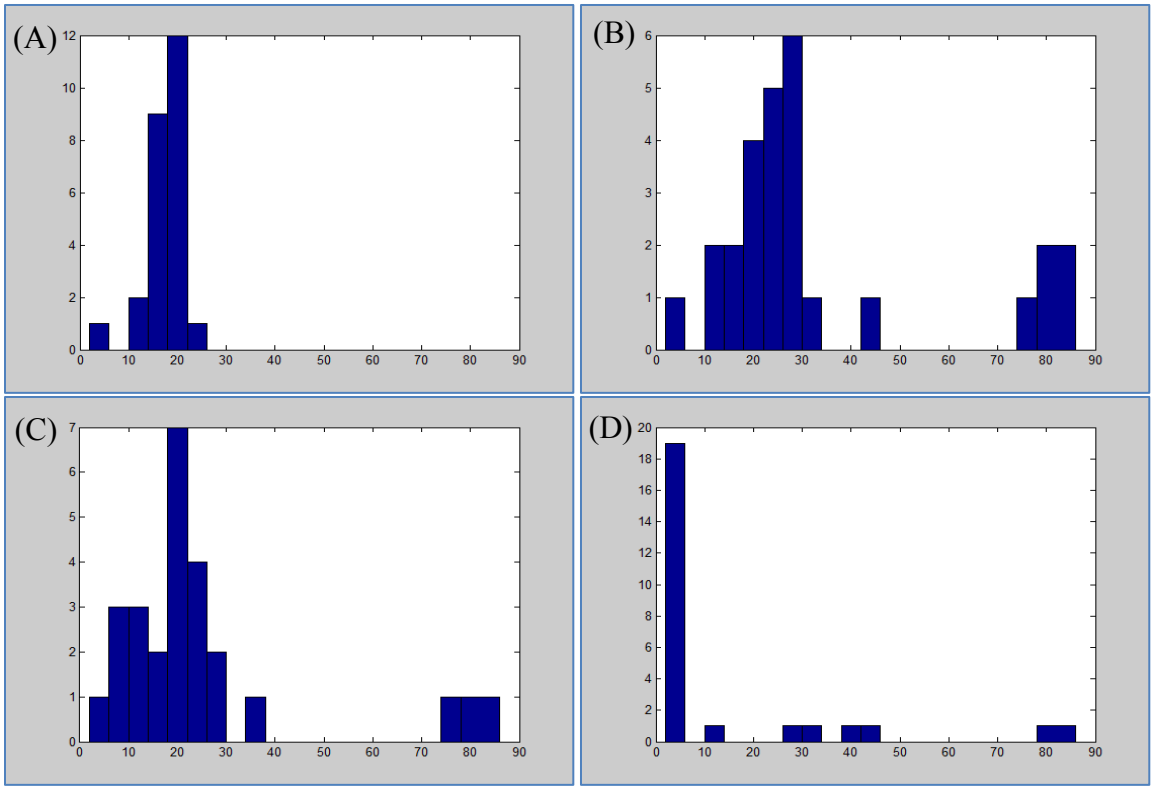

Figure E5 – At 21 my, fracture element-frequency diagram for fracture patterns in Figure E4. Each fracture element represents length of 0.2 m.

Figures E2 and E4 are the fracture patterns in 4 different permeable rocks at 11 my and 21 my respectively. Figures E3 and E5 are the corresponding histogram plots of fracture length in Figures E2 and E4. At the early stage shown in Figure E2, no fracture propagation is observed in zero-permeability rock (Figure E2(A)), whereas in the infinitely permeable rock, one extremely long and fat fracture dominates the whole pattern (Figure E2(D)). In 1 nD and 1 mD rocks, fractures are relatively shorter and skinnier compared to those in infinite permeable rock (Figure E2(B, C)). At the late stage shown in Figure E4, a few short and skinny fractures propagate in zero-permeability rock (Figure E4(A)) and only two long fractures dominate the infinite permeable rock (Figure E4(D)). More fractures propagate in the intermediate permeability rocks and their

fracture length distributions look similar (Figure E2(B, C)). Compared to the reference bubble at corner of each plot, the apertures of fractures in the high-permeability rock are much larger than those in the low-permeability rocks. On a closer look, fractures are more closely spaced and the average fracture length is higher in the low-permeability than in the high-permeability rocks. The fracture spacing data is summarized in Table E1.

Boundary condition effect

The above results show that fractures are more closely spaced in low-permeability rocks. In this section, reservoir boundary condition will be investigated for 1 nD rock with all other parameters the same as above. The results are shown in Figures E6 and E7.

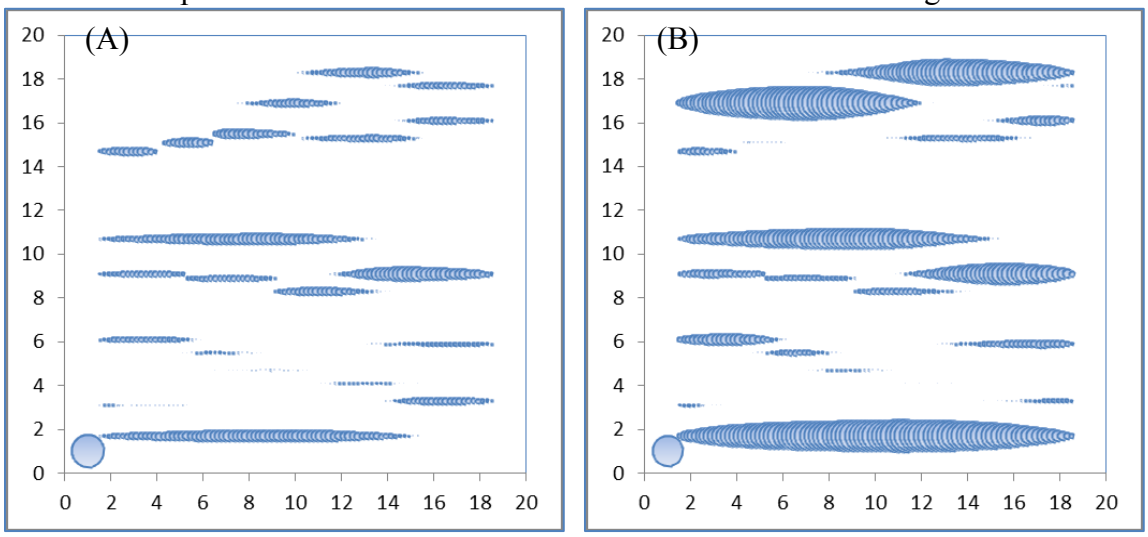

Figure E6 – The subcritical fracture growth patterns with no flow condition in 8 m thickness, 1 nD rock at (A) 11 and (B) 21 my.

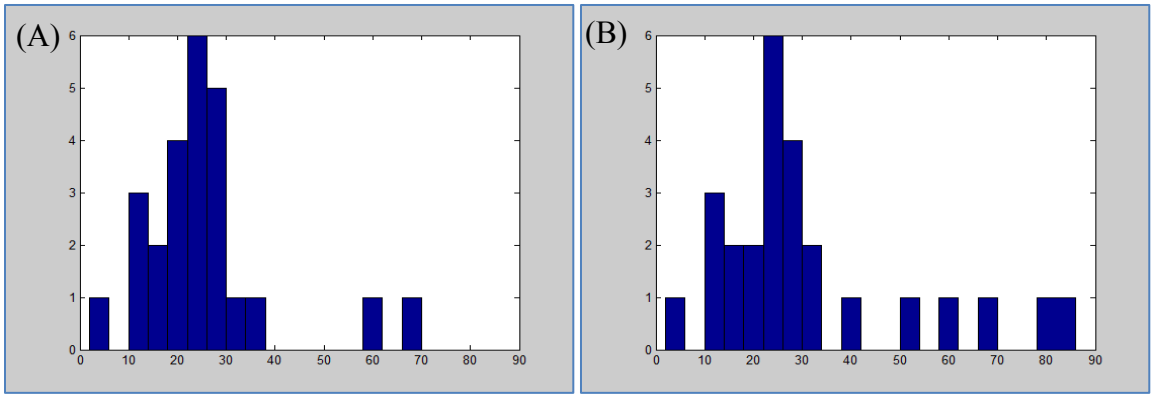

Figure E7 – The fracture element-frequency diagram for fracture patterns in 1 nD rock with no flow condition at (A) 11 and (B) 21 my. Each fracture element represents length of 0.2 m.

As shown in Figure E6, at the early stage, fracture patterns developed with no flow boundary condition (Figure E6(A)) look similar to the pattern developed with constant pressure condition shown in Figure E2(B) for 1 nD rock. At the late stage, fewer very long fractures developed with no flow boundary (Figure E6(B)) than with constant boundary as shown in Figure E4(B), though the overall patterns look similar. At no flow condition, there are more fractures with intermediate length in 1 nD rock at late stage. Overall, the fracture spacing is slightly larger with no flow boundary than constant pressure boundary. The fracture spacing data is summarized in Table E1. The results indicate reservoir boundary condition has certain, but not very a significant, influence on fracture spacing and fracture pattern development in low-permeability rocks.

Subcritical index effect

In this section, sensitivity test is conducted to examine the effect of subcritical index on fracture growth in low-permeability rocks. Subcritical index is chosen at 20 and other parameters are the same as before. Results are shown in Figures E8 and E9.

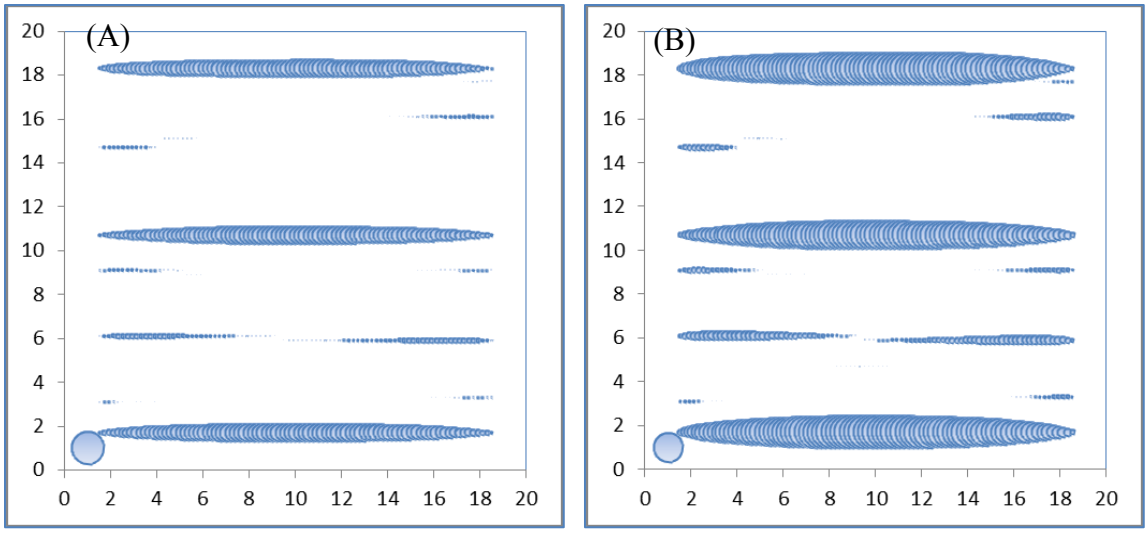

Figure E8 – The subcritical fracture growth patterns in 8 m layer with subcritical index at 20 in 1 nD rock at (A) 11 and (B) 21 my.

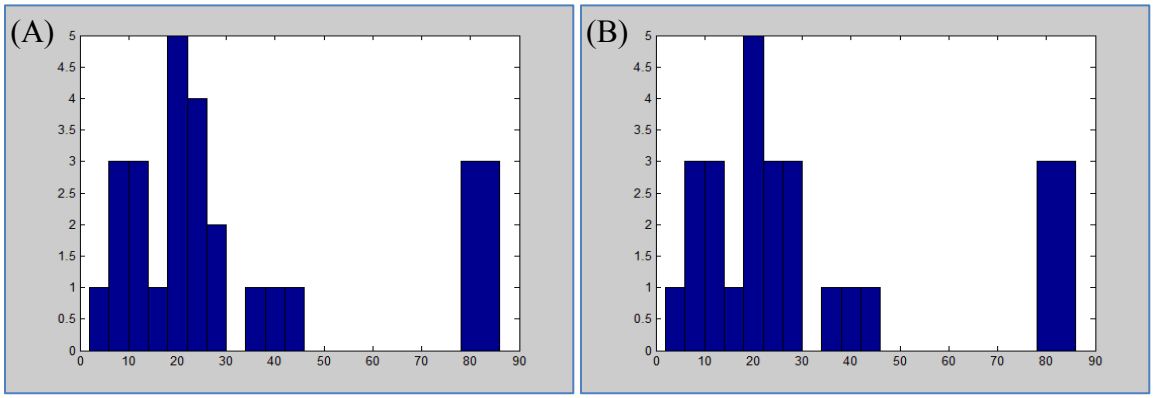

Figure E9 – The fracture element-frequency diagram for fractures in 1 nD rock with subcritical index at 20 at (A) 11 and (B) 21 my. Each fracture element represents length of 0.2 m.

When the subcritical index decreases from 80 in Figures E2 and E4 to 20 in Figure E8 for 1 nD rock, more long and fat fractures are developed with n = 20, sacrificing the growth of other short and skinny fractures. In addition, for n = 20 case, the fracture spacing stays at 2 m since 11 my, indicating the fracture pattern gets saturated very fast with low subcritical index. At the late stage, the ultimate fracture spacing is

slightly lower with lower subcritical index, D = 2 m for n = 20 and D = 2.2 m for n = 80 (Table E1).

Fracture aperture and half-length analysis

The distributions of fracture aperture and half-length are summarized in this section to better evaluate the fracture patterns shown above.

The figures in Figure E10 are the plots of fracture aperture and half-length distribution in rocks with different permeabilities. At the early stage (Figures E10(A, B)), the fractures in 1 nD rock have similar fracture aperture distribution as in 1 mD rock, but the fracture half-lengths are generally larger in 1 nD rock than 1 mD rock. In zero-permeability rock, not much fracture growth is observed; whereas in the infinite permeable rock, one fracture is much fatter and longer than the other fractures. At the late stage (Figures E10(C, D)), the higher permeability the rock has, the broader aperture range the fracture pattern covers. The infinite permeable rock has a lot of short and skinny flaws and several very long and fat fractures; however, in 1 nD rock, almost all the fracture grow and the range of fracture aperture is relatively narrower than that in the high-permeability rocks. Though fractures are relatively skinnier in 1 nD rock, the overall fracture length in low-permeability rock is larger than high-permeability rock. This explains the large fracture population and small fracture spacing observed in the fracture patterns developed in low-permeability rocks.

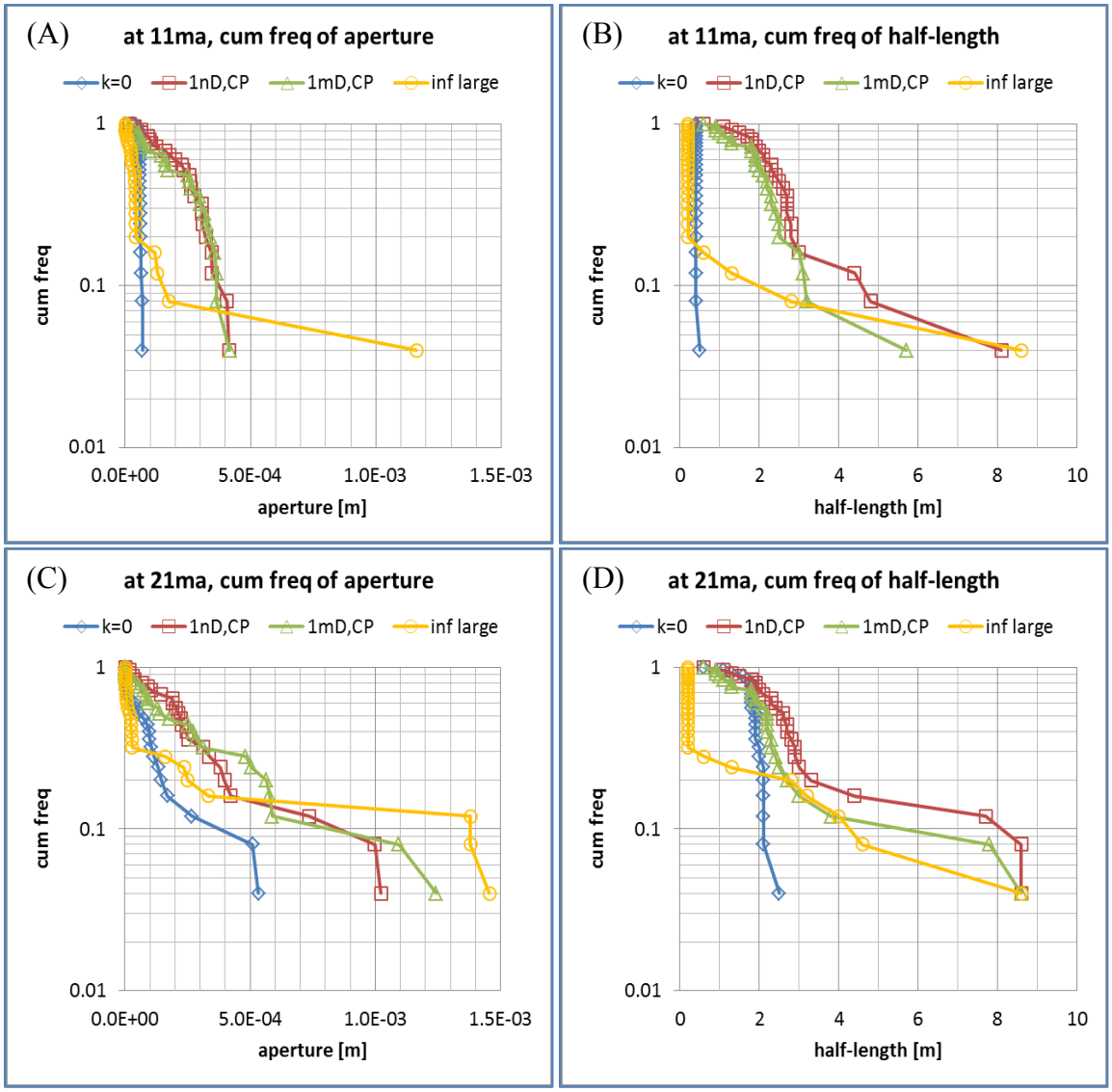

Figure E10 – The cumulative frequency plots of fracture attributes with subcritical index of 80, layer thickness of 8 m and constant pressure boundary condition: (A) aperture (B) half-length plots at 11 my (ma); (C) aperture (D) half-length plots at 21 my (ma).

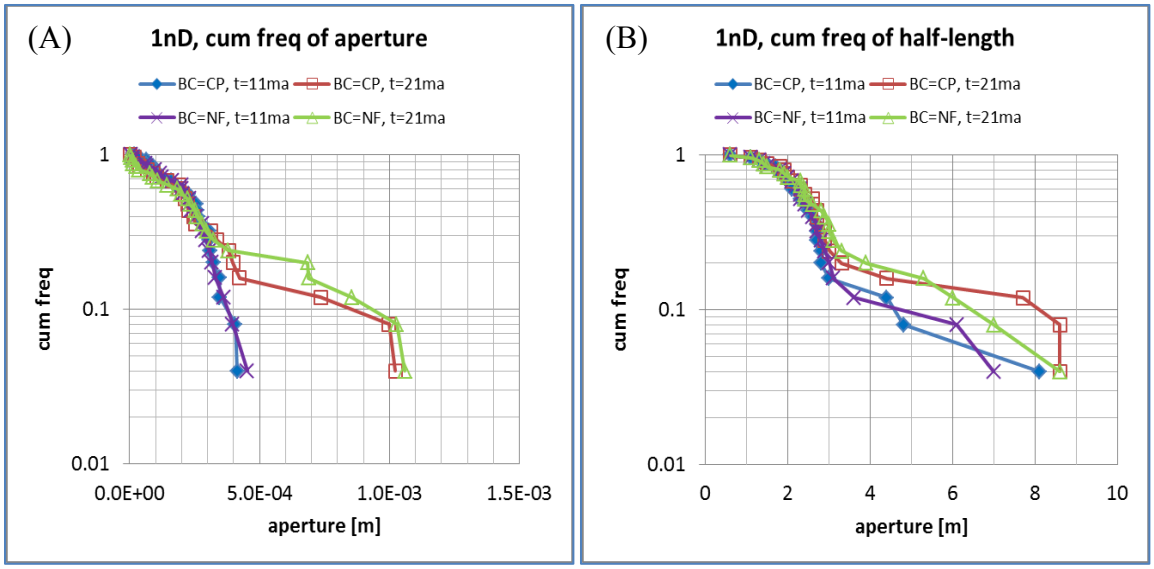

Figure E11 – The cumulative frequency plots of fracture attributes with subcritical index at 80, 8 m thickness in 1 nD rock: (A) aperture (B) half-length plots with BC = CP or NF at 11 or 21 my (ma).

Plots in Figure E11 are used to examine the effects of reservoir boundary condition for fracture growth in 1 nD rock at both early and late stages. The results show that the fracture aperture and half-length distributions are not very sensitive to reservoir boundary conditions in the low-permeability rocks, especially at early stage when the pressure wave has not reached the boundary yet. As fracture propagation continues, fewer fractures have extremely long length and larger apertures with no flow boundary condition. The results in Figure E11 indicate that the reservoir boundary condition will affect the late time fracture length distribution for low-permeability rocks confined by thick bed; however, the influence on fracture attribute distribution is negligible.

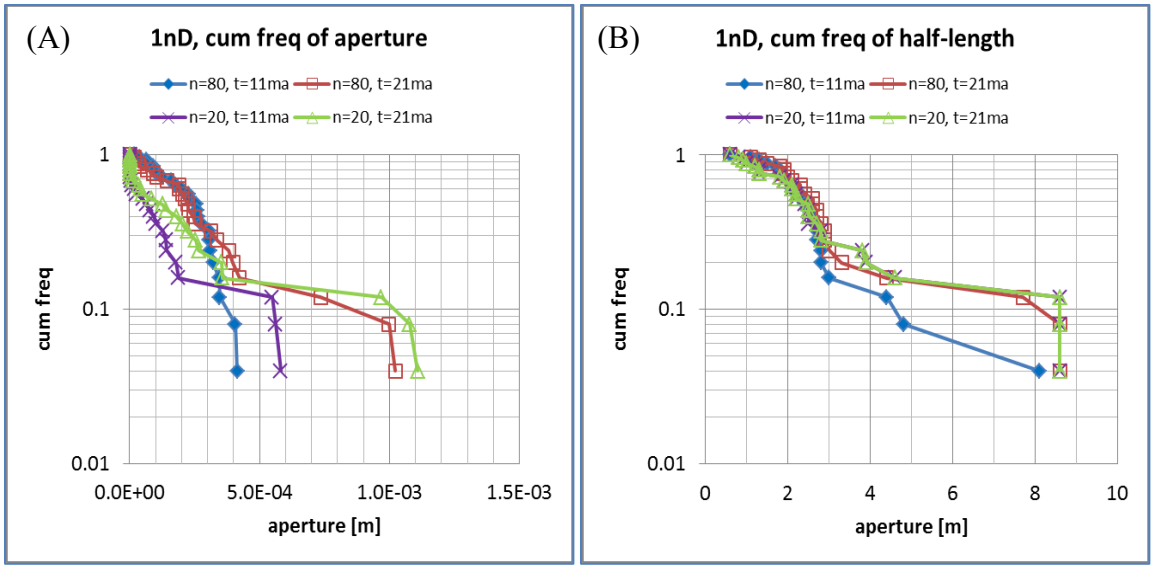

Figure E12 – The cumulative frequency plots of fracture attributes with constant pressure boundary condition and layer thickness of 8 m in 1 nD rock: (A) aperture, (B) half-length plots with BC at CP or NF at 11 or 21 my (ma).

Plots in Figure E12 show the influence of the subcritical index on the fracture attribute distribution in 1 nD rock. As the subcritical index decreases from 80 to 20, the aperture range becomes broader at both early and late stage in 1 nD rock. With low subcritical index (n = 20), fracture length distribution does not change beyond 11 my, indicating fracture pattern reaches saturation level at 11 my. With high subcritical index (n = 80), the distribution curves of fracture half-length are quite different at early and late stages, though the curve at late stage is similar to that the one with n = 20. Overall, for the given setup of simulation conditions, subcritical index seems to have a stronger influence on fracture aperture distribution and negligible influence on fracture half-length distribution in low-permeability rock confined by thick beds.

Fracture spacing analysis

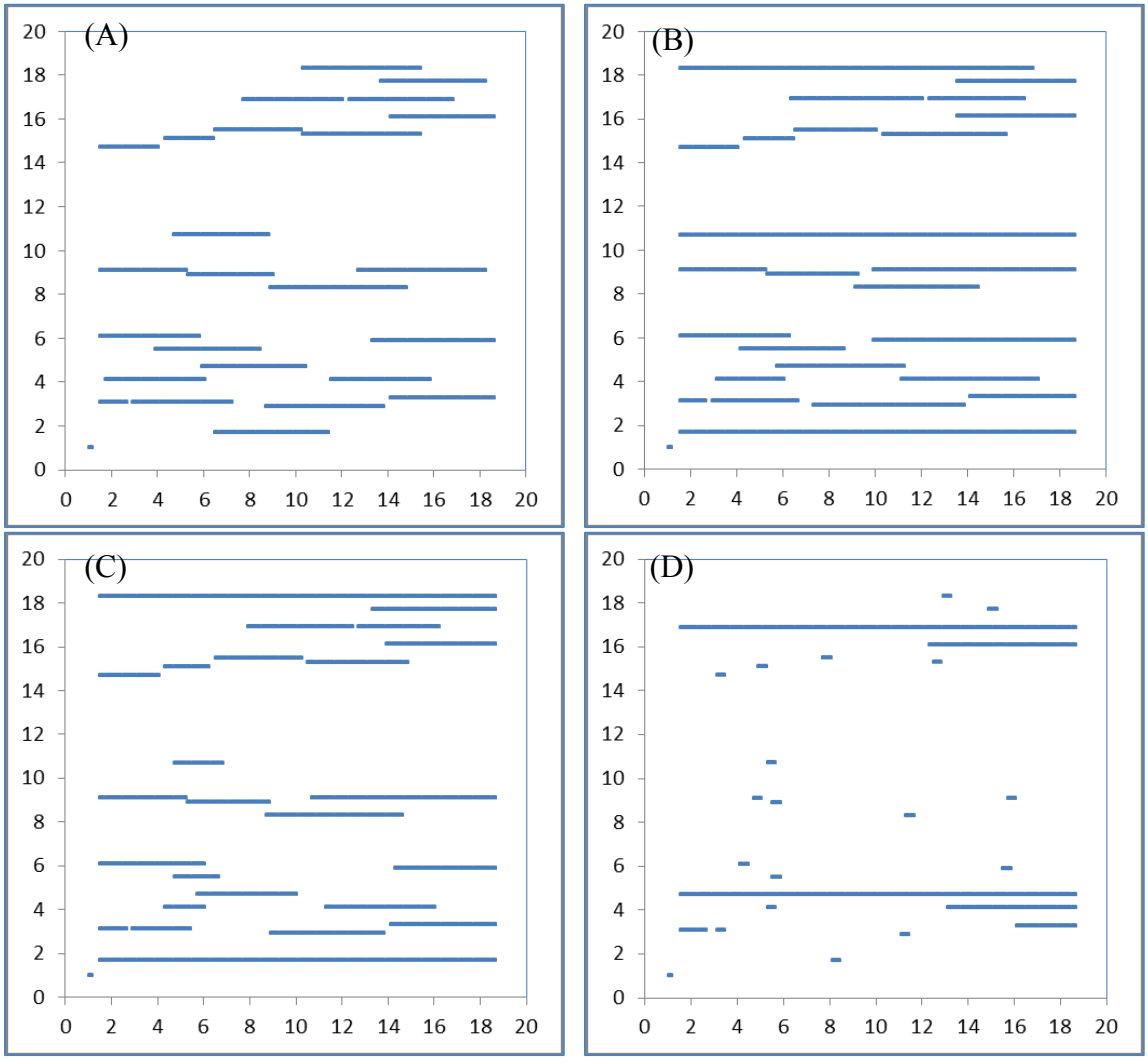

Figure E13 – Tracer plot of fracture pattern at 26 my in rocks with permeability of (A) 0 (B) 1 nD (C) 1 mD (D) infinite large.

Plots in Figure E13 are the tracer maps of fracture patterns in 8 m thick rock layers with various permeabilities at 26 my. The short segments are flaws which have not propagated. It seems that the lower the rock permeability is, the closer the fractures are spaced to each other. Line method is used to calculate fracture spacing.

Table E1 Summary of the fracture spacing calculated with line method for Appendix E.

Permeability	Bed thickness [m]	Boundary condition	Subcritical index	S @ 11 my	S @ 21 my
0	8	CP	80	10	3.3
1 nD	8	CP	80	2.5	2.2
1 mD	8	CP	80	2.9	2.9
Infinite	8	CP	80	10	6.7
1 nD	8	NF	80	2.9	2.5
1 nD	8	CP	20	2	2

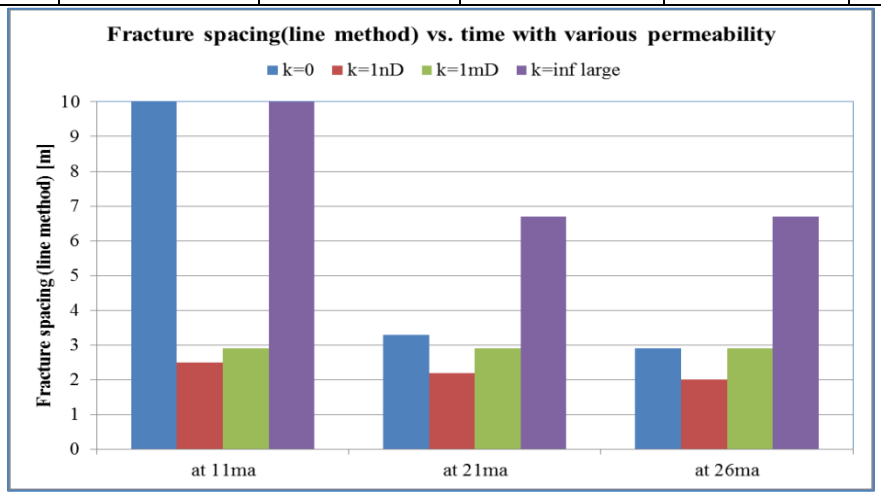

Figure E14 – Fracture spacing calculated with line method vs. fracture growth duration with various rock permeability for bed thickness = 8 m, subcritical index = 80 and BC = CP.

In Figure E14, permeability is the only variable and all other parameters are the same. Fracture spacings in four rock types are plotted at 3 different propagation stages. The numbers in Table E1 show that fracture spacing varies significantly with reservoir permeability in the thick bed (8 m). In infinitely permeable rocks, fracture spacing is 6.7 m at 21 my, roughly proportional to bed thickness. Beyond 21 my, no more fracture propagation is observed in high-permeability rocks. While in 1 nD rock, fractures continue propagation with time and the pattern has not reached the saturation level yet.

The fracture spacing decreases from 2.5 m at early stage to 2 m at 26 my, about ¼ of bed thickness. Fractures are more closely spaced in low-permeability than high-permeability rocks in thick beds.

Glossary

a	Fracture half-length
a_0	Initial fracture half-length
A	Reservoir area
A_{ss}, A_{sn} ... A_{nn}	Influence coefficients
$\vec{\vec{A}}$	Transmissibility matrix
$\vec{B}$	Forcing function
C_t	Fluid compressibility
d_{max}	Fracture aperture
d_{ij}	Distance between fracture elements
D_n	Normal displacement discontinuity
D_s	Shear displacement discontinuity
E	Young's modulus
E^*, $\tilde{E}$, E_{eff}	Effective modulus
$f(x)$	Probability distribution function
G	Energy release rate
G^{ij}	Fracture height effect correction factor
h	Reservoir layer thickness
k	Reservoir permeability
K_I	Mode I stress intensity factor
K_{II}	Mode II stress intensity factor
K_{IC}	Fracture toughness
K_{tip}	Stress intensity factor at fracture tip
L	Fracture length

n	Power-law exponent (subcritical index)
N	Total number of fractures
S/T	Fracture spacing to layer thickness ratio
P-T-X	Pressure-temperature-composition
P_f	Fracture internal fluid pressure
P_i	Initial reservoir fluid pressure
$S_{hmin}(S_3)$	Least compressive remote stress
$S_p^{'}$	Reservoir storage
t_D	Dimensionless time
$T_x,\ T_y$	Transmissibility index
$V(v)$	Crack subcritical velocity
V_f	Fracture volume
V_{max}	Constant velocity
$\Delta\sigma$	Driving stress
$\Delta\sigma_{IC}$	Critical driving stress
ΔL	Fracture growth increment
Δt	Time step
$\Delta\varepsilon$	Applied strain
α, β	Fitting constants
γ	Poisson's ratio
$\dot{\varepsilon}$	Strain rate
θ	Fracture propagation direction
ρ	Fracture density
ρ_0	Initial fracture density
Γ^*	Fracture surface energy reduced by adsorption

κ_I, κ_{II}	Dimensionless stress intensity factor
ϕ	Reservoir porosity
μ	Fluid viscosity
κ	Hydraulic conductivity
σ_n	Normal stress
σ_s	Shear stress
BC	Reservoir boundary condition
CP	Constant pressure boundary condition
DDM	Displacement discontinuity method
LEFM	Linear elastic fracture mechanics
my (ma)	Millions of years
NHF	Natural hydraulic fracture
NF	No flow boundary condition

References

Andersson, J. and Dverstorp, B., 1987, Conditional simulations of fluid flow in three-dimensional networks of discrete fractures, Water Resources Research, 23(10):1876-1886.

Arash, D.T. and Olson, J.E., 2009, Numerical modeling of multi-stranded hydraulic fracture propagation: Accounting for the interaction between induced and natural fractures, SPE 124884.

Atkinson, B.K., 1984, Subcritical crack growth in geological minerals, Journal of Geophysical Research, 89(B6):4077-4114.

Atkinson, B.K. and Meredith, P.G., 1987a, The theory of subcritical crack growth with applications to minerals and rocks, Fracture Mechanics of Rocks, Academic Press, pp.111-166.

Atkinson, B.K. and Meredith, P.G., 1987b, Experimental fracture mechanics data for rocks and minerals, Fracture Mechanics of Rocks, Academic Press, pp.477-525.

Bahat, D. and Engelder, T., 1984, Surface morphology on cross-fold joints of the Appalachian Plateau, New York and Pennsylvania, Tectonophysics, 104:299-313.

Bai, T. and Pollard, D.D., 2000a, Fracture spacing in layered rocks: a new explanation based on the stress transition, Journal of Structural Geology, 22:43-57.

Bai, T. and Pollard, D.D., 2000b, Closely spaced fractures in layered rocks: initiation mechanism and propagtion kinematics, Journal of structural geology, 22:1409-1425.

Barton, C.A. and Zoback, M.D., 1992, Self-similar distribution and properties of macroscopic fractures at depth in crystalline rock in the Cajon Pass scientific hole, Journal of Geophysical Research, 97(B4):5181-5200.

Beach, A., 1977, Vein arrays, hydraulic fractures, and pressure solution structures in a deformed flysch sequence, S.W. England, Tectonophysics, 40:201-225.

Becker, S.P., Eichhubl, P., Laubach, S.E., Reed, R.M., Lander, R.H. and Bodnar, R.J., 2010, A 48 m.y. history of fracture opening, temperature and fluid pressure: Cretaceous Travis Peak Formation, East Texas basin, GSA Bulletin, 122(7/8):1081-1093.

Becker, A. and Gross, M.R., 1996, mechanism for joint saturation in mechanically layered rocks: an example from southern Israel, Tectonophysics, 257:223-237.

Biot, M.A., 1941, General theory of three-dimensional consolidation, Journal of Applied Physics, 12:155-164.

Bloomfield, J., 1996, Characterization of hydrogeologically significant fracture distributions in the chalk: an example from the Upper Chalk of Southern England, Journal of hydrology, 184:355-379.

Cobbold, P.R., 1979, Origin of periodicity: saturation or propagation?, J. Struct. Geol. 1:96-97.

Cherepanov, G.P., 1997, On the origin of joints in sedimentary rocks. Advances in Fracture Research, Proceedings of the ninth international Conference of Fracture, Australia, 4:1757:1766.

Clark, M.B., Brantley, S.L. and Fisher, D.M., 1995, Power-law vein-thickness distributions and positive feedback in vein growth, Geology, 23:975-978.

Close, J.C. and Mavor, M.J., 1991, Influence of coal composition and rank on fracture development in Fruitland coal gas reservoirs of San Juan Basin, Coalbed Methane of Western North America. Rocky Mountain Association of Geologists, pp.109-121.

Cotterell, B. and Rice, J.R., 1980, Slightly curved or kinked cracks, International Journal of Fracture, 16:155-169.

Cox, H.L., 1952, The elasticity and strength of paper and other fibrous materials, British Journal of Applied Physics, 3:72-79.

Crouch, S.L., 1976, Solution of plane elasticity problems by the displacement discontinuity method, International Journal for Numerical Methods in Engineering, 10:301-343.

Crouch, S.L, 1979, Computer simulation of mining in faulted ground, Journal of the South African Institute of Mining and Metallurgy, pp.159-174.

Crouch, S.L. and Starfield, A.M., 1983, Boundary element methods in solid mechanics, George Allen and Unwin, London.

Dawson, G.K.W. and Esterle, J.S., 2010, Controls on coal cleat spacing, International Journal of Coal Geology, 82:213-218.

Degraff, J.M. and Aydin, A., 1993, Effect of thermal regime on growth increment and spacing of contraction joints in basaltic lava, Journal of Geophysical Research, 98(B4):6411-6430.

Delaney, P.T. and Pollard, D.D., 1981, Deformation of host rocks and flow of magma during growth of minette dikes and breccia-bearing intrusions near Ship Rock, New Mexico, U.S. Geol. Surv. Prof., 1202.

Dron, R.W., 1925, Notes on cleat in the Scottish coalfield, Trans. Inst. Min. Eng., 70:115-117.

Dverstorp, B. and Andersson, J., 1989, Application of the discrete fracture network concept with field data: possibilities of model calibration and validation, Water Resources Research, 25(3):540-550.

Dyer, R., 1988, Using joint interactions to estimate paleostress ratios, J. Struct. Geol., 10:685-699.

Einarsson, P., 1991, Earthquakes and present-day tectonism in Iceland, Tectonophysics, 189:261-279.

Engelder, T. and Oerrel, G., 1985, The correlation between undercompaction and tectonic jointing within the Devonian Catskill Delta, Geology, 13:863-866.

Engelder, T. and Lacazette, A., 1990, Natural hydraulic fracturing, Rock Joints, Barton & Stephansson(eds), 35-43.

Engelder, T. and Fischer, M.P., 1996, Loading configurations and driving mechanisms for joints based on the Griffith energy-balance concept, Tectonophysics, 256:253-277.

Engelder, T., Lash, G.G. and Uzcategui, R.S., 2009, Joint sets that enhance production from Middle and Upper Devonian gas shales of the Appalachian basin, AAPG Bulletin, 93(7):857-889.

Evans, A.G., 1972, A method for evaluating the time-dependent failure characteristics of brittle materials – and its application to Polycrystalline Alumina, Journal of Materials Science, 7:1137-1146.

Fall, A., Eichhubl, P., Cumella, S.P., Bodnar, R.J., Laubach, S.E. and Becker, S.P., 2012, Testing the basin-centered gas accumulation model using fluid inclusion observations: Southern Piceance Basin, Colorado, AAPG Bulletin, 96(12):2297-2318.

Fischer, M.P., Gross, M.R., Engelder, T. and Greenfield, R.J., 1995, Finite-element analysis of the stress distribution around a pressurized crack in a layered elastic medium; implications for the spacing of fluid-driven joints in bedded sedimentary rock, Tectonophysics, 247:49-64.

Gale, J.F.W., 2002, Specifying lengths of horizontal wells in fractured reservoirs, Society of Petroleum Engineers Reservoir Evaluation and Engineering, 5:266-272.

Gale, J.F.W., Laubach, S.E., Marrett, R.A., Olson, J.E., Holder, J.T. and Reed, R.M., 2004, Predicting and characterizing fractures in dolomite reservoirs: using the link between diagenesis and fracturing, Geological Society of London Special Publication, 235:177-192.

Gale, J.F.W., Reed. R.M. and Holder, J., 2007, Natural fractures in the Barnett Shale and their importance for hydraulic fracture treatments, AAPG Bulletin, 91:603-622.

Gale, J.F.W. and Holder, J., 2008, Natural fractures in Barnett Shale: Constraints on spatial organization and tensile strength with implications for hydraulic fracture treatment in shale-gas reservoirs, Proceeding of the 42nd US Rock Mechanics Symposium, ARMA 08-96.

Gale, J.F.W. and Laubach, S.E., 2009, Natural fractures in the New Albany shale and their importance for shale-gas production, 2009 International Coalbed & shale gas symposium.

Gale, J.F.W. and Holder, J., 2010, Natural fractures in some US shales and their importance for gas production, Petroleum Geology Conference series, 7:1131-1140.

Geertsma, J. and Klerk, de. F., 1969, A rapid method of predicting width and extent of hydraulically induced fractures, Journal of Petroleum Technology, 21:1571-1581.

Germanovich, L.N. and Astakhov, D.K., 2004, Fracture closure in extension and mechanical interaction of parallel joints, Journal of Geophysical Research, 109(B2).

Gillespie, P.A., Johnston, J.D., Loriga, M.A., McCaffrey, K.J.W., Walsh, J.J. and Watterson J., 1999, Influence of layering on vein systematics in line samples, Fractures, Fluid flow and Mineralization, Geological Society, London, Special Publications, 155:35-36.

Gross, M.R., 1993, The origin and spacing of cross oints: examples from Monterey Formation, Santa Barbara Coastline, California, Journal of structural geology, 15:737-751.

Gross, M.R., Fisher, M.P., Engelder, T. and Greenfield, R.J., 1995, Factors controlling joint spacing in interbedded sedimentary rocks: integrating numerical models with field observations from the Monterey formation, USA., Geological Society, London, Special Publications, 92:215-233.

Gross, M.R. and Engelder, T., 1995b, Strain accommodated by brittle failure in adjacent units of the Monterey formation, U.S.A: scale effects and evidence for uniform displacement boundary conditions, Journal of Structural Geology, 17(9):1303-1318.

Gudmundsson, A., 1987, Tectonics of the Thingvellir fissure swarm, SW Iceland, Journal of Structural Geology, 9(1):61-69.

Gudmundsson, A., 2000, Fracture dimensions, displacement and fluid transport, Journal of Structural Geology, 22:1221-1231.

Halliburton, 2007, Trends in unconventional gas, Drilling and Production, Oil and gas Journal, link: www.halliburton.com/public/common/trends.pdf.

Hanks, C.L., Parris, T.M., and Wallace, W.K., 2006, Fracture paragenesis and microthermometry in Lisburne Group detachment folds: Implications for the

thermal and structural evolution of the northeastern Brooks range, Alaska, AAPG Bulletin, 90:1-20.

Hatton, C.G., Main, I.G. and Meredith, P.G., 1994, Non-universal scaling of fracture length and opening displacement, Nature, 367:160-162.

Helgeson, D.E. and Aydin, A., 1991, Characteristics of joint propagation across layer interfaces in sedimentary rocks, Journal of Structural Geology, 13(8):897-911.

Hennings, P.H., Olson, J.E. and Thompson, L.B., 2000, Combining outcrop and 3d structural modeling to characterize fractured reserovirs: an example from Wyoming. AAPG Bulletin, 84:830-849.

Hobbs, D.W., 1967, The formation of tension joints in sedimentary rocks: an explanation, Geol. Mag., 104:550-556.

Hodgson, R.A., 1961, Regional study of jointing in Comb Ridge–Navajo Mountain area, Arizona and Utah, Am. Asso. Pet. Geol. Bull., 45:1-38.

Hubbert, M.K. and Rubey, W.W., 1959, Role of fluid pressure in the mechanics of overthrust faulting, Bull. Geo. Sco. Am., 70:115-166.

Ingraffea, A.R., 1981, Mixed-mode fracture initiation in Indiana limestone and Westerly Granite, Proc. 22nd Symp. Rock Mech., pp.186-191.

Jamison, R.W., 1997, Quantitative evaluation of fractures on Monkshood Anticline, a detachment fold in the foothills of Western Canda, AAPG Bulletin, 81(7):1110-1132.

Khristianovic, S.A. and Zheltov, Y.P., 1955, Formation of vertical fractures by means of highly viscous liquid, Proceedings of the fourth world petroleum congress, Rome, pp. 579-586.

Kranz, R.L., 1979, Crack-crack and crack-pore interactions in stressed granite, Int. J. Rock Mech. Min. Sci., 16:37-47.

Kulatilake, P.H.S.W., Wathugala, D.N. and Stephansson, O., 1993, Joint network modeling with a validation exercise in Stripa Mine, Sweden, Intl. J. Rock Mech. Min. Sci. and Geomech. Abstr., 30(5):503-526.

Lacazette, A. and Engelder, T., 1992, Fluid-driven cyclic propagation of a joint in the Ithaca siltstone, Appalachian Basin, Fault Mechanics and Transport Properties of Rocks, Academic Press, London, pp. 297-324.

Lachenbruch, A.H., 1961, Depth and spacing of tension cracks, J. Geophys. Res., 66:4273-4292.

Ladeira, F.L. and Price, N.J., 1981, Relationship between fracture spacing and bed thickness, J. Struct. Geol., 3:179-183.

Lander, R.H. and Walderhaug, O., 1999, Predicting porosity through simulating sandstone compaction and quartz cementation, AAPG Bulletin, 83:433-449.

Lander, R.H., 1998, Effect of sandstone diagenesis on fluid overpressure development, AAPG Annual Convention Program Extended Abs., 2:A383.

Lander, R.H., gale, J.F.W., Laubach, S.E. and Bonnell, L.M., 2002, Interaction between quartz cementation and fracturing in sandstone, American Association of petroleum Geologists Annual Convention Program, 11:A98-A99.

Lander, R.H., Larese, R.E. and Bonnell, L.M., 2008, Toward more accurate quartz cement models – the importance of euhedral vs. no-euhedral growth rates, AAPG Bulletin, 92:1537-1564.

Lash, G.G. and Engelder, T., 2007, Jointing within the outer arc of a forebulge at the onset of the Alleghanian Orogeny, Journal of Structural Geology, 29:774-786.

Law, B.E., 1993, The relationship between coal rank and cleat spacing: implications for the prediction of permeability of coal, Proceedings of the International Coalbed Methane Symposium, 2:435-442.

Lawn, R., and Wilshaw, R., 1975, Review indentation fracture: principles and applications, Journal of Material Science, 10(6):1049-1081.

Laubach, S.E., 1988, Subsurface fractures and their relationship to stress history in East Texas Basin sandstone, Tectonophysics, 156:37-49.

Laubach, S.E., 1991, Fracture patterns in low-permeability sandstone gas reservoir rocks in the Rocky Mountain region, SPE 21853, pp.501-510.

Laubach, S.E., Schultz-Ela, D.D. and Tyler, R., 1993, Analysis of compaction effects on coal fracture patterns, Upper Creaceous Rock Springs Formations, southwestern Wyoming. Mt. Geol., 30:95-110.

Laubach, S.E., 1997, A method to detect natural fracture strike in sandstones, AAPG Bulletin, 81(4):604-623.

Laubach, S.E., Marrett, R.A., Olson, J.E. and Scott, A.R., 1998, Characteristics and origins of coal cleat: A review, International Journal of Coal Geology, 35:175-207.

Laubach, S., Marrett, R. and Olson, J., 2000, New directions in fracture characterization, The Leading Edge, 19(7):704-711.

Laubach, S.E., 2003, Practical approaches to identifying sealed and open fractures, Bulletin of the American Association of Petroleum Geologists, 87:561-579.

Laubach, S.E., Lander, R.H., Bonnell, L.M., Olson, J.E. and Reed, R.M., 2004, Opening histories of fractures in sandstone, Geological Society, London, Special Publications, 231:1-9.

Laubach, S.E., Reed, R.M., Olson, J.E., Lander, R.H. and Bonnell, L.M., 2004, Coevolutoin of crack-seal texture and fracture porosity in sedimentary rocks:

cathodoluminescence observations of regional fractures, Journal of Structural Geology, 26:967-982.

Long, J.C.S., Remer, J.S., Wilson, C.R. and Witherspoon, P.A., 1982, Porous media equivalents for networks of discontinuous fractures, Water Resources Research, 18(3):645-658.

Marrett, R. and Peacock, D., 1997, Stain and Stress, Journal of Structural Geology, Aug:2-16.

Marrett, R., Ortega, O.J. an Kelsey, C.M., 1999, Extent of power-law scaling for natural fractures in rocks, Geology, 27:799-802.

McCaffrey, K.J.W., Johnston, J.D. and Loriga, M.A., 1994, Variation of fractal dimension in vein systems, Tectonic studies group special meeting, fault populations, 103-105.

McQuillan, H., 1973, Small-scale fracture density in Asmari Formation of Southwest Iran and its relation to bed thickness and structural setting, Bull. Am. Ass. Petrol. Geol., 57:2367-2385.

Meyer, B.R. and Bazan, L.W., 2011, A discrete fracture network model for hydraulically induced fractures: Theory, parametric and case studies, SPE 140514.

Milliken, K.L. and Laubach, S.E., 2000, Brittle deformation in sandstone diagenesis as revealed by cathodoluminescence imaging with application to characterization of fractured reservoirs, Cathodoluminescence in geosciences, Heidelburg, Springer-Verlag, pp.225-244.

Miller, N., 1993, Predicting flow characteristics of a Lixiviant in a fractured crystalline rock mass, Report of investigations, 9457, Bureau of mines, 24.

Moros, J.G., 1999, Relationship between fracture aperture and length in sedimentary rocks, M.A. thesis, The University of Texas at Austin, Department of Geological Sciences.

Narr, W. and Currie, J.B., 1982, Origin of fracture porosity – examples from Altamont Field, Utah, AAPG Bulletin, 66:1231-1247.

Narr, W. and Lerche, I., 1984, A method for estimating subsurface fracture density in core, American Association of Petroleum Geologists Bulletin, 66:637-648.

Narr, W. and Suppe, J., 1991, Joint spacing in sedimentary rocks, Journal of Structural Geology, 13:1037-1048.

Narr, W., 1991, Fracture density in the deep subsurface: techniques with application to Point Arguello oil field, Bull. Am. Ass. Petrol. Geol., 75:1300-1323.

Narr, W., 1996, Estimating average fracture spacing in subsurface rocks, AAPG Bulletin, 80(10):1565-1586.

NPC report, 2007, Unconventional gas subgroup of the technology task group of the NPC Committee on global oil and gas, link: www.npc.org/study_topic_papers/29-ttg-unconventional-gas.pdf.

Odling, N.E., 1997, Scaling and connectivity of joint systems in sandsotnes from Western Norway, Journal of Structural Geology, 19(10):1257-1271,

Olson, J.E. and Pollard, D.D., 1989, Inferring paleostresses from natural fracture patterns: A new method, Geology, 17:345-348.

Olson, J.E. and Pollard, D.D., 1991, The initiation and growth of en echelon veins, Journal of Structural Geology, 13:595-608.

Olson, J.E., 1993, Joint pattern development: effects of subcritical crack growth and mechanical crack interaction, Journal of Geophysical Research, 98(B7):12251-12265

Olson, J.E., 1997, Natural fracture pattern characterization using a mechanically-based model constrained by geological data-moving closer to a predictive tool, Int. J. Rock Mech. & Min. Sci., 34:3-4, Paper NO.237.

Olson, J.E., Qiu, Y., Holder, J. and Rijken, P., 2001, Constraining the spatial distribution of fracture networks in naturally fractured reservoirs using fracture mechanics and core measurements, SPE 71342.

Olson, J.E., 2004, Predicting fracture swarms – the influence of subcritical crack growth and the crack-tip process zone on joint spacing in rock, Geological Society, London, Special Publications, 231:73-88.

Olson, J.E., Laubach, S.E. and Lander, R.H., 2009, Natural fracture characterization in tight gas snadstones: Integrating mechanics and diagenesis, AAPG Bulletin, 93(11):1535-1549.

Ortega, O. and Marrett, R., 2000, Prediction of macrofracture properties using microfracture information, Mesaverde Group sandstones, San Juan Basin, New Mexico, Journal of Structural Geology, 22:571-588.

Parker, J.M., 1942, Regional systematic jointing in slightly deformed sedimentary rocks, Geol. Soc. Am. Bull., 53(3):381-408.

Parris, T.M., Burruss, R.C. and O'Sullivan, P.B., 2003, Deformation and the timing of gas generation and migration in the eastern Brooks Range foothills, Arctic National Wildlife Refuge, Alaska, AAPG Bulletin, 87:1823-1846.

Perkins, T.K. and Kern, L.R., 1961, Widths of hydraulic fractures, Journal of Petroleum Technology, 13(9):937-949.

Philip, Z., Jennings, J., Olson, J., Laubach, S. and Holder, J., 2005, Modeling coupled fracture-matrix fluid flow in geomechanically simulated fracture networks, SPE Reservoir Evaluation and Engineering, v. 8(4):300-309.

Pollard, D.D., Segall, P. and Delaney, P.T., 1982, Formation and interpretation of dilatant echelon cracks, Geological Society of America Bulletin, 93:1291-1303.

Pollard, D.D. and Segall, P., 1987, Theoretical displacements and stresses near fractures in rock: with applications to faults, joints, veins, dikes and solution surfaces, Fracture Mechanics of Rock, Academic Press, London, 277-350.

Pollard, D.D. and Aydin, A., 1988, Progress in understanding jointing over the past century, Geological Society of American Bulletin, 100:1181-1204.

Price, N.J. and Cosgrove, J.W., 1990. Analysis of geological structures, Cambridge University Press.

Qiu, Y., 2002, Natural fracture modeling and characterization, Ph.D. Thesis, The University of Texas at Austin, Department of Petroleum and Geosystems Engineering.

Ramsay, J.G., 1980, The crack-seal mechanism of rock deformation, Nature, 284:135-139.

Renshaw, C.E., 1993, Modeling fluid migration through physically-based fracture networks, Ph.D. Dissertation, Stanford University.

Renshaw, C.E. and Harvey, C.F., 1994, Propagation velocity of a natural hydraulic fracture in a poroelastic medium, Journal of Geophysical Research, 99(B11):21667-21677.

Renshaw, C.E. and Pollard, D.D., 1994, Numerical simulation of fracture set formation: A fracture mechanics model consistent with experimental observations, Journal of Geophysical Research, 99(B5):9359-9372.

Renshaw, C.E. and Park, J.C., 1997, Effect of mechanical interactions on the scaling of fracture length and aperture, Nature, 386:482-484.

Rice, J.R. and Cleary, M.P., 1976, some basic stress diffusion solutions for fluid-saturated elastic porous media with compressible constituents, Rev. Geophys., 14:227-241.

Rives, T., Pazack, M., Petit, J.P. and Rawnsley, K.D., 1992, Joint spacing: analogue and numerical simulations, J. Struct. Geol., 14:925-937.

Rouleau, A., and Gale, J.E., 1985, Statistical characterization of the fracture system in the Stripa Granite, Sweden, Int. J. of Rock Mech. And min. Sci. & Geom. Abstr., 22(6):353-367.

Ruf, J.C., Rust, K.A. and Engelder, T., 1998, Investigating the effect of mechanical discontinuities on joint spacing, Tectonophysics, 295:245-257.

Secor, D.T., 1965, Role of fluid pressure in jointing, American Journal of Science, 263:633-646.

Secor, D.T., 1969, Mechanics of natural extension fracturing at depth in the earth's crust, Research in tectonics: Geological Survey of Canada Paper, 68-52:3-47.

Segall, P. and Pollard, D.D., 1983, Joint formation in granitic rock of the Sierra Nevada, Geological Society of America Bulletin, 94:563-575.

Segall, P. and Pollard, D.D., 1984, Rate-dependent extensional deformation resulting from crack growth in rock, Journal of Geophysical Research, 89(B6):4185-4195.

Segall, P., 1984, Formation and growth of extensional fracture sets, Geological Society of American Bulletin, 95:454-462.

Sneddon, I.N, and Elliot, H.A., 1946, The opening of a Griffith crack under internal pressure, Q. Appl. Math., 4:262-267.

Snow, D.T., 1970, The frequency and apertures of fractures in rocks, International Journal of Rock Mechanics and mining sciences, 7:23:40.

Soeder, D.J., 1988, Porosity and permeability of Eastern Devonian gas shale, SPE Formation evalution, 3(1):116-124.

Sonnenberg, S.A., 2011, Core Analysis and Unconventional Reservoirs, online material, Colorado School of Mines, http://www.tight-oil-shale-plays.com/media/downloads/inline/steve-sonnenberg-colorado-school-of-mines.1295453329.pdf

Sowers, G.M., 1973, Thoery of spacing of extension fracture, Eng. Geol. Case Hist., 9:27-53.

Swanson, P.L., 1984, Subcritical crack growth and other time- and environment-dependent behavior in crustal rocks, Journal of Geophysical Research, 89:4137-4152.

Tapponier, P. and Brace, W.F., 1976, Development of stress induced microcracks in Westerly granite, Int. J. Rock Mech. Min. Sci., 13:102-112.

Terzaghi, K.V., 1943, Theoretical soil mechanics, New York, Wiley.

Thomas, A.L. and Pollard, D.D., 1993, The geometry of echelon fractures in rock: implications from laboratory and numerical experiments, J. Struct. Geol., 15:323-334.

Tremain, C.M., Laubach, S.E. and Whitehead, N.H., 1991, Coal fracture cleat pattern in Upper Cretaceous Fruitland formation, San Juan Basin, Colorado and New Mexico: implications for exploration and development, Coalbed Methane of Western North America. Rocky Mountain Association of Geologists, pp.49-59.

Vermilye, J.M. and Scholz, C.H., 1995, Relation between vein length and aperture, Journal of Structural Geology, 17(3):423-434.

Walderhaug, O.,1994, Precipitation rates for quartz cement in sandstones determined by fluid-inclusion microthermometry and temperature-history modeling, Journal of Sedimentary Research, A64:324-333.

Walderhaug, O., 2000, Modeling quartz cementation and porosity loss in Middle Jurassic Brent Group sandstones of the Kvitebjorn field, northern North Sea, AAPG Bulletin, 84:1325-1339.

Walsh, J.B., 1965, The effect of cracks on the compressibility of rock, Journal of Geophysical Research, 70(2):381-389.

Warpinski, N. R. and Teufel, L. W., 1987, Influence of geologic discontinuities on hydraulic fracture propagation, Journal of Petroleum Technology, 39:209-220.

Wiederhorn, S.M., 1967, Influence of water vapor on crack propagation in Soda-Lime glass, J. Am. Ceram, Soc., 50:407-414.

Woodworth, J.B., 1896, On the fracture system of joints, with remarks on certain great fractures, Boston Soc. Nat. His. Proc., 27(1):63-183.

Wu, H. and Pollard, D.D., 1991, Propagation of a set of opening-mode fractures in layered brittle materials under uniaxial strain cycling, J. Geophys. Res., 97:3381-3396.

Wu. H. and Pollard, D.D., 1992, Modeling a fracture set in a layered brittle material, Eng. Frac. Mech., 42:1011-1017.

Wu, H. and Pollard, D.D., 1995, An experimental study of the relationship between joint spacing and layer thickness, Journal of Structural Geology, 17:887-905.

Wu, K., and Olson, J.E., 2013, Investigation of critical In Situ and injection factors in multi-frac treatments: guidelines for controlling fracture complexity, SPE 163821.

Zeller, S.S. and Pollard, D.D., 1992, Boundary conditions for rock fracture analysis using the boundary element method, J. Geophys. Res., 97:1991-1997.

Zhang, X., Harkness, R.M. and Last, N.C., 1992, Evaluation of connectivity characteristics of naturally jointed rock masses, Engineering Geology, 33:11-30.